Turbulent Exchange of Carbon Dioxide in a Complex Urban Environment: Results from Long-term Eddy Covariance Measurements

Inauguraldissertation

zur
Erlangung der Würde eines Doktors der Philosophie
vorgelegt der
Philosophisch-Naturwissenschaftlichen Fakultät
der Universität Basel

von
Michael Schmutz
aus Basel BS

BASEL, 2019

Genehmigt von der Philosophisch-Naturwissenschaftlichen Fakultät

auf Antrag von:

Prof. Dr. Eberhard Parlow
Fakultätsverantwortlicher und Dissertationsleiter
Meteorologie, Klimatologie und Fernerkundung
Departement Umweltwissenschaften
Universität Basel
Schweiz

und

Prof. Dr. Andreas Christen
Korreferent
Umweltmeteorologie
Albert-Ludwigs-Universität Freiburg
Deutschland

Basel, den 27.03.2018

Prof. Dr. Martin Spiess
Dekan

Acknowledgments

"If I have seen further it is by standing on ye sholders of Giants."

Isaac Newton (1676)

I would like to thank Prof. Dr. Eberhard Parlow who gave me the chance to work in his research group for many years. Being part of the MCR-Lab gave me the chance to benefit in many different ways from all team members. My special thanks go to Dr. Roland Vogt who encouraged me to become a member of the MCR-Lab as a research assistant during my bachelor studies and always supported me during the following years. His profound knowledge in the field of micrometeorology and his fascination for many facets of natural sciences made field trips always a great experience and turned discussions into conversations rich in content.

Part of my work is based on the previous efforts of other scientists, especially Dr. Björn Lietzke and Dr. Christian Feigenwinter who shared their knowledge and ideas which helped me greatly to gain deep insights into the research field of urban climatology. I also enjoyed the fellowship and support of other team members, namely Patrick Koller, Ambros Werner, Dr. Dominik Michel, Dr. Andres Gartmann, Thomas Meuli, Samuel Diethelm, Serafin Bieder, Iris Feigenwinter, Mihal Rütimann, Robert Spirig and Dr. Andreas Wicki. I could always rely on the IT support of Günter Bing and the technical expertise of Hans-Rudolf Rüegg which is why they both earn my special thanks. Not to forget the exceptional administrative work of Josette Pfefferli-Stocky.

The funding of my PhD was made possible by the Romanian-Swiss Research Program which led to the project "Urban Climate Study of Bucharest". It was a great experience to install two flux towers in the city center of Bucharest and I would like to address special thanks to Prof. Dr. Florian Petrescu, Dr. Florian Gaman, Dr. Mihai Sercaianu and Mihaela Aldea for their support by communicating with the local authorities during my stays in Bucharest.

My greatest thanks go to my parents and to my parents-in-law who supported me in every way the could. And I would like to express my deepest gratitude to my wife and my children for their patience and their love.

Abstract

Within this thesis, characteristics of the turbulent exchange within the urban boundary layer, as well as long-term trends and tendencies of the carbon dioxide flux (F_C) and concentration (ρ_C) are presented. Prevailing transport processes, the transfer and transport efficiencies of the turbulent exchange of momentum, heat, CO_2 and H_2O and the importance of coherent turbulent motions within the urban boundary layer are studied by applying the quadrant analysis technique. The behavior of F_C and ρ_C in the urban environment is investigated on daily, seasonal, and inter-annual scales as well as in comparison to regional background concentration records of the atmospheric CO_2 concentration.

The dependence of the passive scalars CO_2 and H_2O on atmospheric stability (ζ) differs distinctly in comparison to momentum and heat. The vertical fluxes of momentum (τ) and heat (Q_H) are actively generating mechanically and buoyantly driven turbulence, respectively. Due to the strong coupling between τ, Q_H and ζ, each stability class is characterized by a distinctive turbulence regime. In contrast, the turbulent exchange of CO_2 and H_2O is not primarily controlled by the existence of transporting eddies, but also heavily influenced by the activity and the composition of the corresponding scalar sources (e.g. traffic, heating etc.) and thus, the heterogeneity of the local surrounding. Models represent the transfer efficiencies of momentum and heat accurately while the prediction for CO_2 and H_2O mostly fails. Other factors, like the interplay between the activity of sources and sinks are more important and accordingly, the transfer efficiency of CO_2 can be consulted to identify times or wind sectors where the source/sink regime is altered by e.g. photosynthetic activity. The inter-comparison of the transport characteristics of heat, CO_2 and H_2O leads to the assumption of scalar dissimilarity. By applying the quadrant analysis framework to the long-term time series, dominant turbulent structures responsible for efficient vertical exchange, i.e. coherent structures, can be identified. The length of the time series allows to extend the analysis to the stable range, which usually rarely occurs in urban areas.

The variability of local urban ρ_C is investigated in comparison to regional background concentration records. While patterns on daily and seasonal scales are similar, the vicinity to the ground sources of the local measurements leads to a stronger sensitivity to changes on small temporal scales. The height above ground of the background concentration measurements and thus the larger distance from the ground sources results in a phase shift of up to three months compared to the local seasonal course of ρ_C. While ρ_C in the urban area is also clearly elevated by $10\,\mathrm{ppm}$ on average, the behavior of ρ_C in the urban environment reveals good consistency with background concentration measurements in terms of seasonality and long-term trend. The calculated local linear trend for the time period between 2005 and 2014 is around $2\,\mathrm{ppm\,y^{-1}}$, which also coincides well with the global average trend.

The coupling between F_C and anthropogenic activity in the urban area is apparent from

considerable differences in weekday and weekend fluxes, the diurnal cycle as a result of traffic volume or the seasonality caused by additional heating activity in wintertime. The variability of F_C scales with the source activity and a long-term decrease of F_C around $5\,\%$ is observed locally as a result of a decrease in traffic activity during the investigation period. However, variabilities on all temporal scales are clearly larger than the observed long-term tendencies. For the investigation of F_C in the heterogeneous urban environment an appropriate weighting between individual wind sectors is shown to be necessary due to the unequal frequency distribution of wind directions. The application of a refined methodology for the calculation of horizontally averaged fluxes of CO_2 significantly improves the representativity of the data for the investigation area and also enhances the comparability of the data to results from other studies. The length of the current dataset allows to estimate the significance of the observed long-term behavior. While up to six years are potentially needed to calculate a significant inter-annual trend of ρ_C, statistics of F_C still benefit from even longer data records due to the larger variability. This gives evidence, that long-term time series of urban CO_2 can help to add valuable knowledge to the current understanding of the urban ecosystem and its role in the global carbon balance.

Contents

List of Figures

List of Tables

Acronyms

BAES	Basel Aeschenplatz
BKLI	Basel Klingelbergstrasse
EC	eddy covariance
GPP	Gross primary production
HDD	heating degree days
IPCC	Intergovernmental Panel on Climate Change
ISL	inertial sublayer
JFJ	Jungfraujoch
LUT	look-up table
MCR	Meteorology, Climatology and Remote Sensing
ML	mixed layer
mLUT	moving look-up table
NEE	net ecosystem exchange
<NEE>	horizontally averaged net ecosystem exchange
PAR	photosynthetically active radiation
PBL	planetary boundary layer
RSL	roughness sublayer
SAL	Schauinsland
SL	surface layer
TZ	transition zone
UBL	urban boundary layer
UCL	urban canopy layer

CHAPTER 1

Introduction

1.1 Preface

When looking at the day side of the Earth's surface from the orbit of the international space station, surprisingly little evidence of human live remains visible to the eye. Only large urban areas may be localized as grayish islands within the endless green-brown cover of the continents. However, the picture changes when the planet reveals its night side and human settlements start to pop up as a complex network of strings of lights all over the Earth. The nocturnal view nicely illustrates the role of cities as hot spots of anthropogenic activity by providing home to more than half of human population but yet covering only around $1\,\%$ of the Earth's surface. The fact, that millions of people are concentrated on such a small area, raises a complex socio-economic scenario, within which vast flows of goods and energy are necessary to meet the requirements of the whole system. This leads to an unique environmental system sometimes referred to as the "urban metabolism" [Wolman, 1965]. Their large spatial extension, the modulated surface properties, the patchy composition of many different materials, the complex three dimensional structure as well as the abnormal consumption of energy and emission of air pollutants gives cities an unique climate which is distinctively different from the rural surrounding.

Urban climatology is a research field which focuses on the interactions between urban surfaces and the overlaying atmosphere. Many meteorological facets like the emission and dispersion of air pollutants, the energy and water balance or the urban heat island effect and their influence on the human welfare are studied. From todays perspective urban air pollution became a major topic for the first time during the Industrial Revolution in the eighteenth and nineteenth century, when the rapid growth of industrial and domestic wood and coal burning led to a dirty atmosphere filled with smoke. It was during this time, when the urban climate was first studied scientifically by Luke Howard who presented his results in the famous publication entitled "The Climate of London" [Howard, 1818, 1820]. With simple measurements of the air temperature he has been able to quantify and explain the anomalous warmth of the urban atmosphere, which is known today as the urban heat island. His findings, which he later presented in a more extended version [Howard, 1833], are nowadays seen as the foundation stone for the evolution of research on the urban climate and environment. Despite advances in meteorological survey and

measurement techniques in the nineteenth century, it took until the end of World War II when research on the local urban climate received a new boost. In the second half of the twentieth century descriptive models were more and more accompanied by numerical simulations - made possible by the increasingly available computer technology. But it was not before the 1980s when researchers started to apply micro-meteorological measurement techniques to cities in order to reliably characterize the urban energy balance with in-situ experiments. In the 1990s the applicability of the eddy covariance method over the complex and heterogeneous urban landscape could be demonstrated [e.g. Roth and Oke, 1993; Roth, 1993; Schmid, 1994]. This can be seen as an important mile stone for the development of experimental urban micro-meteorology, because it became possible to investigate turbulent transport processes not only from wind tunnel studies but from real experimental setups. Large research campaigns like the Basel Urban Boundary Layer Experiment (BUBBLE) in Basel, Switzerland [Rotach et al., 2005] helped to develop a valuable database of parameterizations and a solid understanding of the urban system in general. This is important for the development and validation of local urban models, as well as global climate models.

Due to the extremely fast development of computational power during the last decade, it became now possible to model complex turbulence structures and exchange processes with high temporal and spatial resolution with no need for sophisticated experimental setup. This might be one of the reasons why results from urban modeling studies prevail during the last decade and the experimental urban climatology is still under-developed compared to the current state of micro-meteorology in general. Together with the demanding logistical and technical requirements of an urban micro-meteorological site, this leads to a comparatively sparse availability of long-term measurements above representative urban areas. Thus, it is desirable to increase the availability of datasets from cities and to develop advanced methodologies for the interpretation of data above the complex urban landscape.

At the same time, there is an increasing interest in meteorological information from cities in general. For example the investigation of the exchange processes in the urban atmosphere is not only of interest for natural scientists, but also helps to improve research on public health, sustainable development or even the decision and policy making of local authorities. On the one side the data might indicate hot spots of need for action and on the other side it additionally provides the possibility to validate the actions of city developers or to proof the impacts of political decisions. The fact, that the Intergovernmental Panel on Climate Change (IPCC) announced to give cities a special focus in its work program towards 2028 is a clear signal, that more attention should be payed on research about the manifold facets of the urban ecosystem. This can be seen as a great opportunity to significantly increase evidence on the impact of urban areas on the global climate change scenario.

1.2 Aims and Objectives

The focus of this thesis was to analyze the turbulent exchange of carbon dioxide in a complex urban environment from long-term eddy covariance measurements. The investigation can be split in two thematic research areas:

(a) Turbulent exchange processes and transport mechanisms

The instrumentation and computational power to perform field experiments on turbulent exchange processes within the planetary boundary layer became available in the second half of the twentieth century and first comprehensive studies within urban areas only started in the last decade of the previous millennium. While the applicability and partial validity of the eddy covariance method could be proofed within the urban boundary layer, the transport mechanisms and turbulent processes leading to the average eddy covariance fluxes are not yet studied conclusively. The length of the current dataset used in this thesis provides a solid database, covering the entire stability range. This enables the generation of valuable information for the understanding of turbulent exchange processes on different temporal and spatial scales. By applying the quadrant analysis framework, information about prevailing turbulent structures, the importance of specific temporal scales and the influence of coherent turbulent motions is acquired.

(b) Long-term tendencies and variabilities of carbon dioxide flux and concentration

While during the last decade many studies have been published which focus on the determination of controlling factors of carbon dioxide fluxes or the spatial heterogeneity of the source/sink pattern, only few investigations cover a sufficient period of time to generate significant results concerning the long-term behavior of urban carbon dioxide. Many time series of carbon dioxide fluxes cover at most a couple of years or are incomplete and not continuous. However, given the large variability within the urban area e.g. changes in traffic volume, population increase or the construction of new buildings, many years of data are necessary to create a complete picture of the urban system. Otherwise the results are only valid for a short snapshot and the comparability between studies is not given. Even for the concentration of carbon dioxide, which is monitored widely, comparative results from cities occur in a much smaller number in contrast to natural environments. The current dataset allows to gain increased knowledge about long-term trends and variabilities of both carbon dioxide fluxes and carbon dioxide concentration in urban areas.

Both topics are not yet studied extensively in cities due to a lack of sufficient data to provide

solid analysis. The dataset processed within this thesis (2004-2016) is one of the longest continuous eddy covariance time series available that has been reported in literature for an urban area. The investigation of each topic led to a peer-reviewed publication in a scientific journal which are presented in section 3 - P1 and section 5 - P2. Both studies are accompanied by additional results and explanations. Supplementary, the processing of the current dataset helped to provide substantial information for three more scientific publications where the author of this thesis is listed as a co-author. These articles are appended separately in the appendix of this thesis (section A).

1.3 The Urban Boundary Layer

1.3.1 Vertical Structure

The Earth's atmosphere forms a layer around the globe with a thickness of several hundred kilometers, which is around $10\,\%$ of the Earth's radius. Interaction between the atmosphere and the surface however, takes mostly place within the lowest $10–15\,\mathrm{km}$ known as the troposphere. While the vertical extension of the troposphere is modulated by variation of the solar input at the surface with season and latitude, the direct influence of the ground is restricted to the lowest $\sim$100–1000 m over time periods of one day or less. In analogy to fluid mechanics, this thin layer next to the bounding surface is defined as the planetary boundary layer (PBL) [Oke, 1987]. Over the course of a day, the height of the PBL varies significantly. The generation of convective motions leads to an upward transport of heat and to an extension of the PBL height up to $1–2\,\mathrm{km}$. After sunset, the surface loses energy by thermal radiation, which leads to a rapid cooling of the ground and successively the overlaying air layer. Soon, the surface becomes cooler than the air and the stable stratification prevents high reaching vertical motions. As a result, the vertical extension of the PBL often shrinks to a height in the order of magnitude of

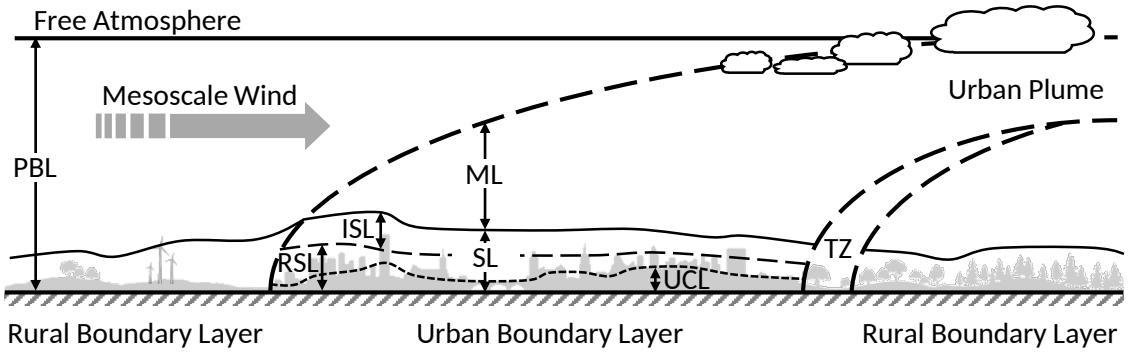

Figure 1.1. Schematic illustration of the urban boundary layer (UBL). PBL: planetary boundary layer, RSL: roughness sublayer, ISL, inertial sublayer, SL: surface layer, ML: mixed layer, UCL: urban canopy layer, TZ: transition zone [adapted from Oke, 2006; Feigenwinter et al., 2012].

100 m. Synoptic events and local surface characteristics (e.g. mountains or water) may also influence the shape of the PBL.

In close vicinity to the ground, the PBL is strongly influenced by local surface properties. Due to the high friction, the vertical transport within the lowest few millimeters, known as the laminar sublayer, takes exclusively place by molecular diffusion. The strong influence of surface friction vanishes steadily with increasing height and a roughness sublayer (RSL) is distinguished up to a height z_r of 1–3 times the average height of the roughness elements z_h. The RSL is embraced by the (turbulent) surface layer (SL), which is characterized by small-scale turbulence which reaches a thickness of 50–100 m with time scales of less than 30–60 min.

The urban boundary layer (UBL) (Fig. 1.1) follows the basic concept of a PBL but adds some additional features [Oke et al., 2017]. In analogy to the PBL over plant canopies, commonly an urban canopy layer (UCL) is defined, which extends up to z_h, i.e. the average height of the buildings. Below z_h the air is often decoupled from the layers above and within street canyons complex micro-climates form and can have significant influence on the way energy and mass is transferred horizontally and vertically. The overlaying RSL is then followed by an inertial sublayer (ISL) which starts at a height of approximately 1–3 times the average building height z_h. Within the ISL, fluxes are nearly constant with height (also constant flux layer) and represent a mixed signal from the individual surface elements with a representative footprint of several hundred meters in upwind direction. This is sometimes also referred to as the blending height. Further up within the mixed layer (ML), the fluxes have a much larger footprint and atmospheric properties are uniformly mixed. The top of the ML is usually capped by an inversion. At the city border the transition zone (TZ) forms the intersection between the UCL and the rural PBL with different roughness characteristics and length scales.

In practice differentiation of sublayers is not always straightforward, especially in cities, where the height of the roughness elements varies largely. Compared to natural canopies, the UCL consists mostly of impermeable structures which do not form a continuous cover as can be found in e.g. forests. Hence, the distance between buildings and their height (i.e. the sky view factor) manipulates the UCL in a complex way. Furthermore, due to the generally heterogeneous structural composition of a city, roughness characteristics around a station can vary largely with wind direction.

1.3.2 Temporal and Spatial Scales

Processes in atmospheric sciences are traditionally divided into micro-scale (10^{-2}–10^{3}), local scale (10^{2}–5×10^{4}), meso-scale (10^{4}–2×10^{5}) and macro-scale (10^{5}–10^{8}) in terms of horizontal extension (m) and duration (s) [Oke, 2006]. In Fig. 1.2 prevailing scales in the PBL are depicted in conjunction with examples related to urban climate processes. For urban climate studies only processes up to the meso-scale are of major relevance and an adapted nomenclature suitable for the processes within the UBL is used, i.e. street scale ($<10^{2}$ m),

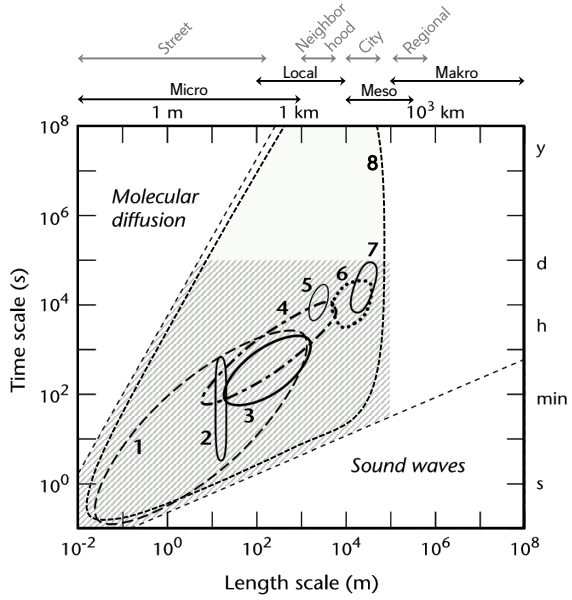

Figure 1.2 Temporal and spatial scales in urban boundary layer meteorology [adapted from Oke, 2006]. 1: mechanical eddies shed by obstacles, 2: cross-canyon vortex, 3: individual building wake, 4: chimney stack plume, 5: urban park breeze circulation, 6: urban-rural breeze system / urban heat island circulation, 7: uplift in city 'plume', 8: frame of relevant scales within current studies. The shaded area represents the scales of classical boundary-layer meteorology.

neighborhood scale ($\sim 10^3$ m), city scale ($\sim 10^4$ m), regional scale ($\sim 10^5$ m) [Britter and Hanna, 2003]. The numbers stated in brackets, especially the order of magnitude for city scale, may vary with the size of the investigated city and the numbers should be adapted correspondingly. Street scale can be referred to processes that are observed within the UCL or the RSL and thus very close to the surface. Neighborhood scale processes represent a mixed signal from a larger area of hundreds of meters. This is primarily the scale which is covered by the footprint (source area) of ground based measurements carried out within the ISL and the denotation "footprint scale" is often used synonymously. The city scale embraces all processes within the area of a city and thus, summarizes the overall impact of a city on the PBL. Finally, the regional scale connects the city to its surrounding and the larger synoptic processes and describes e.g. the general meteorological situation in terms of wind systems or climate characteristics.

Spatial and temporal scales are often interconnected linearly as demonstrated in Fig. 1.2, but this direct relation is mostly one-sided. While processes happening on small spatial e.g. micro or street scale can be subject to variation over the course of days, month or even years, processes on large spatial scales are rarely changing faster than their corresponding temporal order of magnitude. As such, ground based observations with relatively small spatial scales of interest can benefit largely if the observations are carried out over a much longer temporal scale, i.e. long-term measurements.

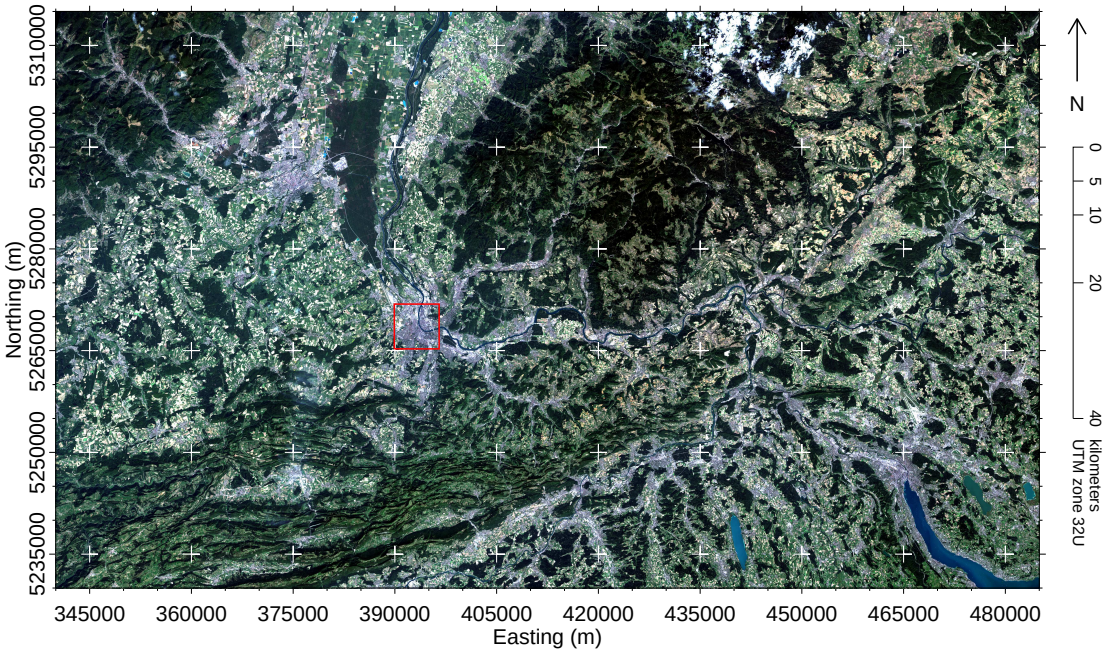

Figure 1.3. LANDSAT 8 pseudo true-color composite based on channels 4, 3 & 2 (RGB) dated from 30 August 2015 at 10:16 UTC. The red box indicates the location of Basel at 47.561 73 °N / 7.580 49 °E (393 218.17 N / 5 268 566.51 E, UTM 32U) [U.S. Geological Survey, 2017].

1.4 Investigation Area

Basel is a central European city located in northern Switzerland at the border triangle of Germany, France and Switzerland also known as the "Rhine's knee". Geographically Basel is separated from the rest of Switzerland to the south by the Jura mountains with a height of up to 1000 m a.s.l., whereas the city itself lies at approximately 270 m a.s.l. and marks the southern end of the Upper Rhine Rift Valley (overview in Fig. 1.3). On a synoptic scale, Basel lies within the west wind drift of the northern mid-latitudes. Due to the considerable distance from the Atlantic ocean of around 1000 km towards the center of the European continent, the local climate shows alternately characteristics of oceanic and continental climate conditions and can be specified as a Cfb-climate according to the Köppen classification (comp. Fig 1.5). Currently, the canton of Basel is home to around 198 000 inhabitants, whereas approximately 176 000 people are living within the city of Basel. The city itself covers an area of 2389 m^2 which is 64.8 % of the area covered by the canton of Basel (3698 m^2). This results in a population density of 7380 pop km^{-2} within the city boundaries and 5360 pop km^{-2} within the entire canton, respectively.

Research on urban climatology at the University of Basel is conducted by the Meteorology, Climatology and Remote Sensing (MCR) Lab by (i) analyzing satellite imagery, by (ii) developing and applying numerical models as well as by (iii) ground-based field measurements with

Figure 1.4. Aerial image (3.7 km × 3.2 km) dated from April 2015. The red box indicates the location of BKLI at 47.561 73 °N / 7.580 49 °E (2 610 677 N, 1 267 900 E, LV95) and the blue box indicates the location of BAES at 47.551 30 °N / 7.595 57 °E (2 611 814 N, 1 266 743 E, LV95) [Geodaten Kanton Basel-Stadt, 2017].

micro-meteorological equipment. While all three perspectives provide an unique approach to research questions related to urban climatology, in-situ measurements are probably closest to the ongoing micro-meteorological processes within the investigation area and are inevitable for the basic understanding of the ecosystem as well as for validation purposes of models or inventory approaches. The unique structural composition as well as the complex combination of chemical and biological processes confront researchers with a sophisticated challenge when it comes to the sensor placement. As for many investigation areas an optimal compromise between the conflicting priorities of theoretical, technical, logistical and scientific requirements needs to be found [Munger et al., 2012]. Since the MCR-Lab has moved to the current location at the Basel Klingelbergstrasse (BKLI) in 2003, the heart of the micro-meteorological measurements is an 18 m tall tower construction mounted to the rooftop of the new MCR-Lab

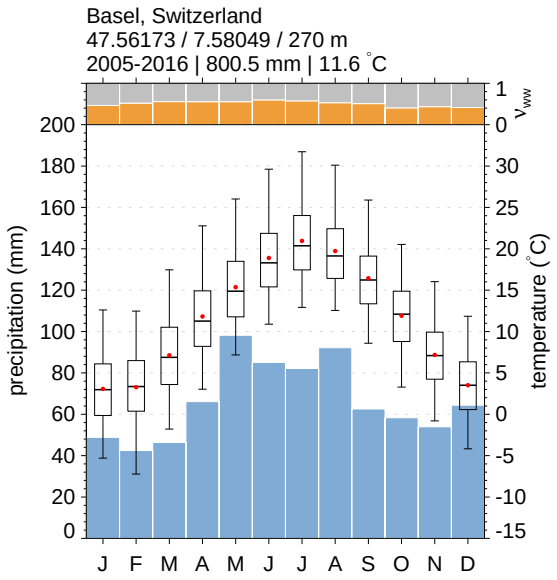

Figure 1.5 Climate diagram for Basel calculated with meteorological data derived at BKLI between 2005 and 2016. Blue bars indicate average monthly precipitation sums and box plots present the average monthly statistics for air temperature calculated from 30 min averages. The orange bars at the top show the west wind frequency ν_{wwf} as introduced in sec. 5 - P2.

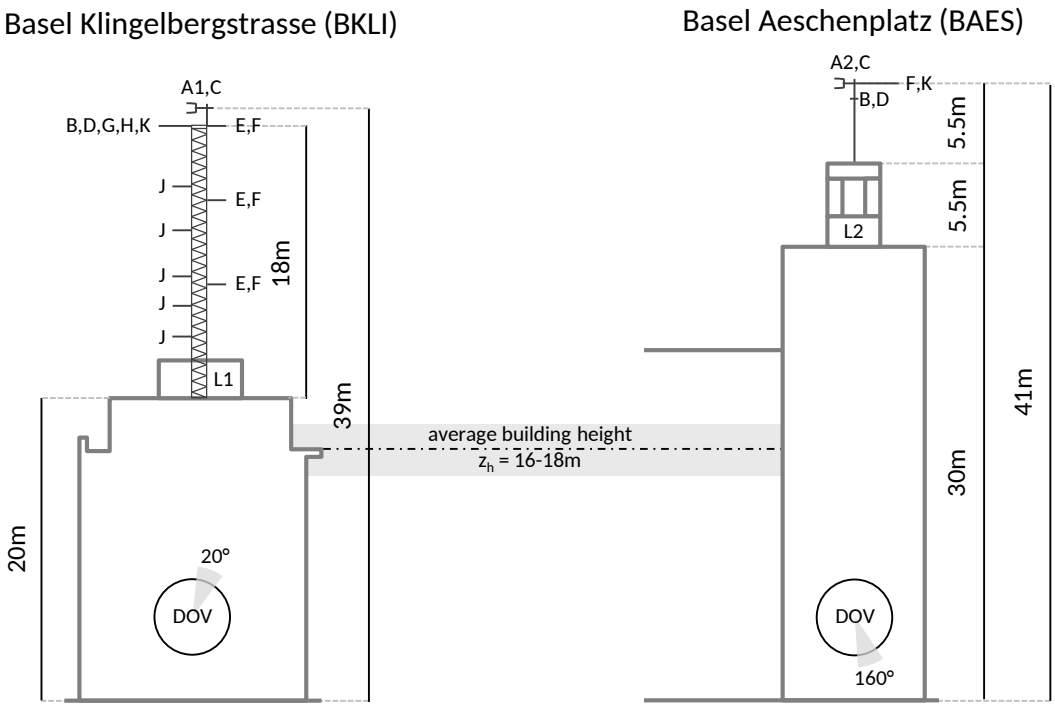

A1: Gill HS-50 Ultrasonic Anemometer, **A2:** CSAT3 Ultrasonic Anemometer **B:** Sonic Electronics Box, **C:** LI-7500 CO_2/H_2O Analyzer Sensor Head, **D:** LI-7500 Control Box, **E:** Aspirated Thermocouple, **F:** HMP155 Humidity and Temperature Probe, **G:** THYGAN Thermohygrometer, **H:** WA15 Crossarm, **J:** WAA151 Cup Anemometer, **K:** CNR1 Net Radiometer, **L1:** CR5000 Datalogger, **L2:** CR1000 Datalogger

Figure 1.6. Side view (direction of view as indicated) of the institute building and the flux tower at BKLI (left) as well as of the "Turmhaus" at BAES. The indicated instrumentation represents the status by the end of 2017.

building at 20 m above street level. The resulting total measurement height of 38 m reaches into the ISL and gives access to transport processes between surface and atmosphere on a neighborhood scale. The assumption of a well defined ISL is feasible, because the building height for the larger area around BKLI is relatively constant around 15–20 m and as a result, z_r, which marks the bottom level of the ISL, is expected to be around 25–30 m ($\approx 1.5\, z_h$ with $z_h = 16.7$ m). For validation purposes and to gain more information about the spatial heterogeneity of meteorological parameters across the city, a second flux tower has been equipped in 2009 1.6 km southeast at Basel Aeschenplatz (BAES). Next to a busy crossroad where five major roads come together, the sensors are mounted to a pole on the top of a tower-like building (Turmhaus) allowing for a total measurement height of 41 m above street level. At both stations CO_2 mole fractions and fluxes are measured by ultrasonic anemometers combined with open-path CO_2/H_2O gas analyzers. To provide additional information about the meteorological conditions, accompanying measurements of air temperature, relative humidity and solar as well as terrestrial radiation are carried out at both stations. At BKLI profiles of wind speed, air temperature and relative humidity as well as precipitation are measured additionally. Figure 1.4 shows the location of the two flux towers within the city of Basel, Fig. 1.6 provides a side view of both measurements sites including measures and instrumentation and Fig. 1.7 presents some photographs of the BKLI tower. Further details about the structural composition of the investigation area are available in sec. 5 - P2 or in Lietzke et al. [2015]. Within this thesis primarily data from BKLI is used. The time series from BAES is taken as a reference to validate the results and the applied methodologies.

Figure 1.7 Photograph of the BKLI measurement site: the 18 m tower on the rooftop of the MCR building. The location of the tower (orange marker) and the viewpoints of the photographs (A,B,C) are indicated in the overview map [Geodaten Kanton Basel-Stadt, 2017, Photographs by M. Schmutz].

CHAPTER 2

Turbulent Transport in the Urban Boundary Layer

Research on turbulence can be traced back at least to Leonardo da Vinci who studied the velocity streamlines of fluids back in 1510. Aside a sketch of water pouring into a pond, he formulated the words:

> *"Observe the motion of the surface of the water, which resembles that of hair, which has two motions, of which one is caused by the weight of the hair, the other by the direction of the curls; thus the water has eddying motions, one part of which is due to the principal current, the other to the random and reverse motion"*
>
> Leonardo da Vinci (1510), *Trans. Piomelli in Lumley [1992]*

Seemingly, this is a metaphorical description of the theoretical concept devised later by Sir Osborne Reynolds in 1895 known as the Reynolds decomposition

$$x(t) = \overline{x} + x(t)', \tag{2.1}$$

which separates an instantaneous value $x(t)$ at time t into its average part

$$\overline{x} = \frac{1}{N}\sum_{t=1}^{N} x(t), \tag{2.2}$$

representing the principal current and its turbulent part

$$x(t)' = x(t) - \overline{x}, \tag{2.3}$$

representing the random motion.

While turbulence can nicely be observed when leaves on the ground get swirled by a wind gust or smoke from an extinguished candle evolves from a thin line to complex ever-changing patterns, experimental setups capable to deliver quantitative measures of the turbulence field have long not been available. In the early 20th Century, several physicists like Ludwig Prandtl, Ira S. Bowen or Sir Geoffrey Ingram Taylor have made some major contributions to the concept of estimating fluxes of momentum, energy and mass by the flux-gradient approach. The latter of these three researchers also became famous for his hypothesis of "frozen turbulence", which is commonly denoted as Taylor's Hypothesis. The concept of the "frozen turbulence" is based

upon the idea, that eddies of different sizes are responsible for the vertical transport with their up-welling and down-welling branches. The eddies are coupled in such a way, that smaller eddies feed on the energy of the larger ones, which leads to a cascade of energy and a continuous breakdown of eddies into smaller whirls until they dissipate due to increasing viscosity. Over certain time scales - usually 30–60 min for most PBL - the spectrum of eddies is thought to be transported past the station without considerable changes in frequency distribution, hence the term "frozen". As such, it is possible to determine the turbulent transport on top of the main stream by just waiting long enough, which substitutes the much more complex approach of having many measurements distributed all over the investigation area but at just one specific moment in time. With this conceptual background about the nature of turbulence the base for the eddy covariance (EC) method was given. Some early applications of the EC method are reported by Scrase [1930] or Schmidt [1928] but the technical equipment has not yet been capable of delivering the necessary high frequency data nor has there been enough computing power to process the statistics. It was only around the 1950s when major advances were made in the EC method by proceedings of e.g. Montgomery [1948], Swinbank [1951] or Obukhov [1951]. During these times basic concepts and equations for sonic anemometry were discussed by e.g. Barrett and Suomi [1949] or Schotland [1955] which made it possible to derive first results from field campaigns like the O'Neill [Lettau, 1957] or later the Kansas experiment [Businger et al., 1971]. Besides other field campaigns, these datasets are important sources of information and are still in use for atmospheric surface layer parameterizations. With the availability of sonic anemometers the research field of micro-meteorology gained access to the fundamental transport processes within the PBL. While at the beginning mainly profile approaches were used to determine vertical transfer, towards the end of the twentieth century the EC method became more and more the state of the art technique for the calculation of turbulent fluxes.

2.1 Eddy Covariance Method - Theory

The speed of an air flow is generally expressed in units of meters per second, which describes the average downstream velocity of all air particles. To establish a measure for the vertical transport of any property of the air, the vertical wind speed w can simply be expressed as a volume flux density Q_V by converting the units of w

$$w[\frac{m}{s}] = Q_V[\frac{m^3}{m^2 s}]. \tag{2.4}$$

By multiplying Q_V by the density of air ρ_a one derives the mass flux density of air Q_M

$$Q_M = w\rho_a[\frac{kg}{m^2 s}]. \tag{2.5}$$

Because the transport of any scalar property e of the air is related to Q_M a scalar flux density Q_e

can be defined as

$$Q_e = w\rho_a e. \tag{2.6}$$

Following the Taylor Hypothesis, which assumes conditions of temporal stationarity

$$\frac{d\overline{e}}{dt} = 0 \tag{2.7}$$

and horizontal homogeneity

$$\frac{d\overline{e}}{dx} = \frac{d\overline{e}}{dy} = 0, \tag{2.8}$$

an averaging operator can be applied to Q_e like

$$Q_e = \overline{w\rho_a e}. \tag{2.9}$$

This is also known as frozen turbulence and means, that the transporting motion of the eddies is much smaller than the mean flow and the field of turbulence is thus transported past the station without changing considerably over the investigated period of time. Subsequently, the Reynolds decomposition allows the separation of the averages in their mean value and their fluctuating part

$$Q_e = \overline{w\rho_a e} = (\overline{w} + w')\,(\overline{\rho_a} + \rho_a')\,(\overline{e} + e'). \tag{2.10}$$

By expanding the above equation and assuming that (i) mean values of fluctuating parts are zero, (ii) the air density is constant and thus fluctuating parts of ρ_a are zero and (iii) the mean vertical wind speed is zero over time, the final scalar flux density can be written like

$$Q_e = \overline{\rho_a}\,\overline{w'e'}, \tag{2.11}$$

where term $\overline{w'e'}$ is the covariance of the variables w and e. Because the turbulent fluctuation of ρ_a is negligible the Reynolds decomposition is not applied to this term (also not to λ_L for Q_E). This is the basic definition of the EC method which can then be applied to derive the sensible heat flux

$$Q_H = \overline{\rho_a}\,c_p\,\overline{w'\theta'}, \tag{2.12}$$

the latent heat flux

$$Q_E = \overline{\rho_a}\,\overline{\lambda_L}\,\overline{w'q'}, \tag{2.13}$$

the momentum flux

$$\tau = \overline{\rho_a}\,\overline{u'w'}, \tag{2.14}$$

or the carbon dioxide flux

$$F_C = \overline{\rho_a}\,\overline{w'c'}, \tag{2.15}$$

where c_p is the specific heat capacity at constant pressure, θ is the potential air temperature and λ_L is the latent heat of vaporization [overview in Aubinet et al., 2012].

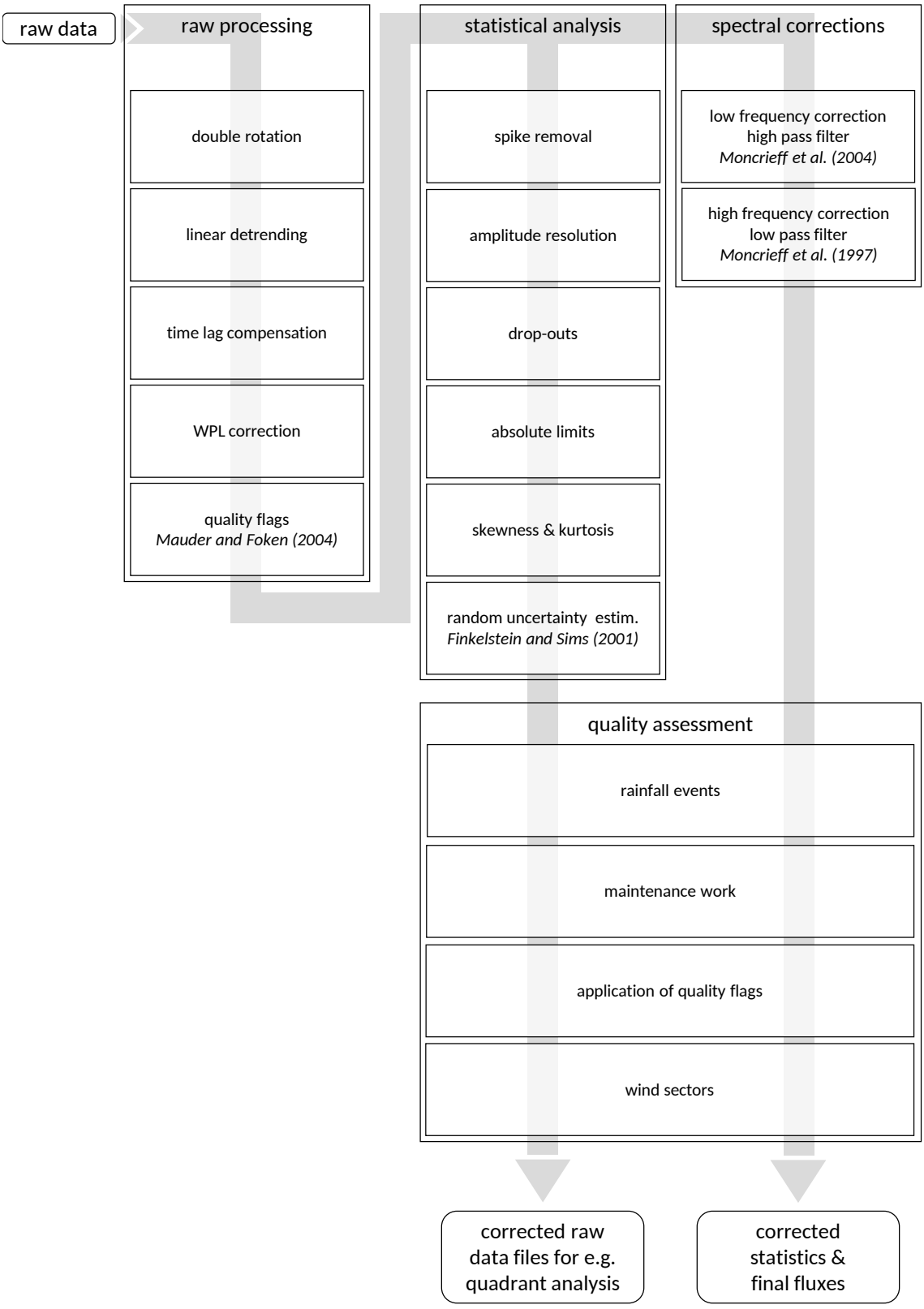

Figure 2.1. Basic post-processing steps of the data. Listed are the major processing steps performed by EddyPro (LI-COR Inc.) as well as site specific quality assessments [comp. Mauder and Foken, 2004; Finkelstein and Sims, 2001; Moncrieff et al., 1997, 2004].

2.1.1 Corrections and Quality Assessment

The EC method is the state of the art technique to measure land-atmosphere exchange of momentum, energy and mass. However, the above-mentioned theoretical assumptions only apply to a flat and homogenous surface and the implementation of the EC method for complex and heterogeneous environments like urban landscapes lead to rigorous restrictions concerning sensor placement and data interpretation [Feigenwinter et al., 2012]. Data post-processing is necessary and has been done with the EddyPro (LI-COR Inc.) toolkit within this thesis. Figure 2.1 presents the general workflow to derive data ready for interpretation. The last processing step named "quality assessment" includes site specific exclusion criteria like specific wind sectors (mast effect) or maintenance and rainfall events.

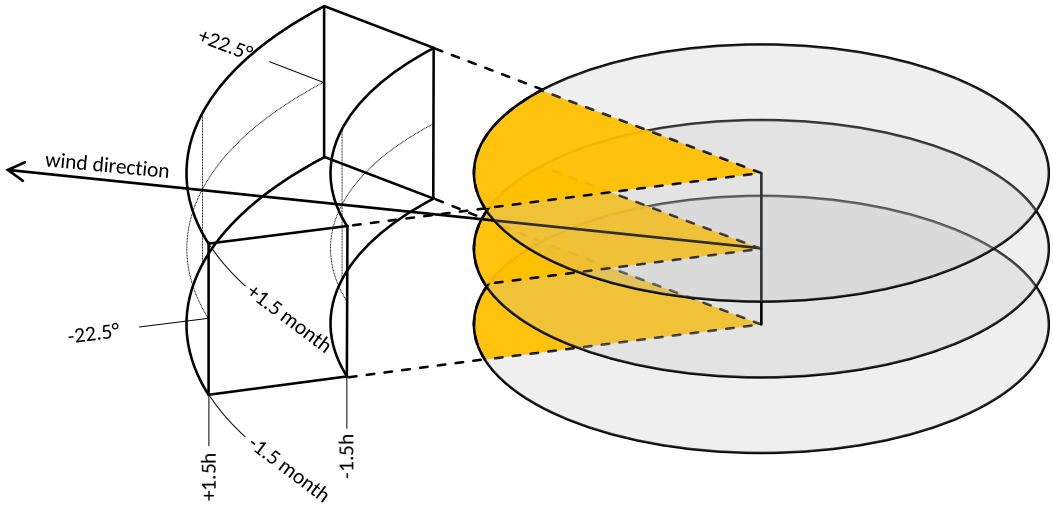

Figure 2.2. Gap-filling scheme showing the boundaries of the moving look-up table (mLUT).

2.1.2 Gap-Filling

To analyze EC time series and in order to calculate significant statistics, gaps in the data need to be filled. Missing values might occur due to different reasons, i.e. rejection by quality criterion during post-processing, malfunction of the EC system, bad weather conditions, maintenance or manual exclusion of data due to user-defined criterions (e.g. wind direction). At BKLI most data are rejected during post-processing algorithms or excluded during rainfall events ± 1 h and during maintenance work. This leads to an average data availability for EC fluxes around 70 %. Because some influence on the airflow must be expected from the south sector due to the mast and the mounting structure, these data are analyzed and treated with special care by manual inspection. For each missing value a three dimensional moving data frame (mLUT) is generated

with boundaries of $\pm 22.5^\circ$ in wind direction, ± 1.5 h in daytime and 45 days forth and back in time (Fig. 2.2). Additionally, weekend and working day gaps are only filled with values from corresponding weekdays. Wind data is taken from accompanying meteorological measurements at the BKLI tower with high availability ($>99\,\%$). The usage of mLUT has the advantage over static look-up table (LUT) that the variability over time is better preserved and no convergence of the overall statistics towards the LUT values occurs. Furthermore, the gap-filling frame is always centered over the gap which improves the representativity by avoiding uncertainties towards the border of the look up frame.

CHAPTER 3 - P1

Flux Similarity and Turbulent Transport of Momentum, Heat and Carbon Dioxide in the Urban Boundary Layer

The following chapter is published as a research article in Boundary-Layer Meteorology:

M. Schmutz[1], R. Vogt[1] (2019): Flux Similarity and Turbulent Transport of Momentum, Heat and Carbon Dioxide in the Urban Boundary Layer. *Boundary-Layer Meteorology 172*(45), 45-65.

[1]Research Group Meteorology, Climatology, and Remote Sensing, University of Basel, Switzerland

Boundary-Layer Meteorology (2019) 172:45–65
https://doi.org/10.1007/s10546-019-00431-w

RESEARCH ARTICLE

Flux Similarity and Turbulent Transport of Momentum, Heat and Carbon Dioxide in the Urban Boundary Layer

M. Schmutz[1] · **R. Vogt**[1]

Received: 12 March 2018 / Accepted: 15 January 2019 / Published online: 30 January 2019

Abstract
Turbulence characteristics in the urban boundary layer of a mid-latitude European city are investigated using a quadrant analysis of more than 12 years of eddy-covariance measurements at 39 m above street level. To describe the ongoing turbulent-exchange processes, particularly the properties of ejection and sweep events, presented here are the transfer efficiency and the similarity of momentum, heat, CO_2 and H_2O fluxes. In addition, an event-detection algorithm is applied to derive information on the importance of organized structures for the turbulent exchange, finding that momentum and heat fluxes are primarily controlled by atmospheric stability, whereas CO_2 and H_2O fluxes are more affected by the presence of active sources of the corresponding scalars (e.g. traffic for CO_2 fluxes). The transfer efficiencies of momentum and heat can thus be modelled accurately, but the prediction for CO_2 and H_2O fluxes fails because of scalar dissimilarity. Generally, ejections are more important under buoyancy-driven unstable conditions and responsible for large structures, and sweeps are more characteristic of stable cases and smaller structures. The quadrant statistics enable the identification of scales between a hole-size factor of 10 and 20 where turbulent exchange is especially efficient and almost solely takes place by ejection–sweep cycles. This information is used to apply an event-detection algorithm, which quantifies flux fractions of such reoccurring structures to be around 0.5–0.8, with the time fraction being usually around 0.1.

Keywords Flux similarity · Long-term measurements · Quadrant analysis · Transport and transfer efficiency · Urban boundary layer

1 Introduction

Numerical models focusing on land–atmosphere exchange or the dispersion of air pollutants require information about the processes responsible for the exchange of heat, mass and momentum close to the surface. The parametrizations of turbulent-exchange processes mostly rely on traditional micrometeorological approaches, such as Monin–Obukhov

✉ M. Schmutz
mi.schmutz@unibas.ch

[1] Department of Environmental Sciences, Atmospheric Sciences, Research Group Meteorology, Climatology, and Remote Sensing, University of Basel, 4056 Basel, Switzerland

similarity theory, which requires idealized conditions rarely existing in most ecosystems, such as horizontal homogeneity and stationarity. For urbanized areas, the characterization of turbulent exchange becomes an even more sophisticated task due to the increased roughness and structural complexity of the environment. Nonetheless, it is of particular interest to investigate the mechanisms controlling exchange processes to better understand and improve the forecasts of air pollution—especially in cities. Despite this, the amount of available data from urban areas on which to develop parametrizations is still small compared with natural ecosystems, since the deployment of eddy-covariance systems capable of measuring turbulence statistics in densely-urbanized areas is technically and logistically demanding.

Many studies over vegetated complex terrain have shown that, for example, coherent structures play a major role in the transport of momentum and scalars (e.g. Shaw et al. 1983; Katul et al. 1997a; Li and Bou-Zeid 2011; Dupont and Patton 2012; Francone et al. 2012; Tyagi and Satyanarayana 2014; Mohr and Schindler 2016). Results suggest similarities between plant canopies and urban areas in terms of flow characteristics (e.g. Roth 2000) and, as such, organized turbulent events are expected to play an important role in cities as well. However, the direct comparison of flow above and within plant canopies and urban landscapes is mostly not feasible, because solid buildings alter the turbulent flow differently compared with semi-permeable plant canopies, and there is no analogy for distinct urban structures, such as street canyons in, for example, forest ecosystems. For more than three decades, research on urban turbulence has been active (e.g. Roth and Oke 1995; Feigenwinter et al. 1999; Moriwaki and Kanda 2005; Christen et al. 2007; Wood et al. 2010), and the influence and importance of ejection–sweep interactions, intermittent turbulence, and coherent structures have been discussed (see the comprehensive reviews in Roth 2000; Arnfield 2003). Still, there is no detailed common understanding of all features involved in turbulent exchange over urban areas, and the significant heterogeneity between and within cities underlines the necessity for more valuable datasets to gain a deeper insight. Besides the unique structural composition, urban areas often also distinctly differ in terms of atmospheric stability, which is a major modulator of turbulent exchange. In mid-latitude dense urban environments, the large amount of stored heat in buildings, as well as the additional input of energy from anthropogenic activities, alters the atmospheric stability towards a regime mostly characterized by unstable conditions—even during the night. Although stability regimes may vary considerably between cities, the shift towards unstable stratification is a common theme (e.g. Wood et al. 2010; Lietzke and Vogt 2013; Schmutz et al. 2016), making it crucial for the understanding of turbulent transport because of the potential to change the ejection–sweep relationship significantly. While transport dissimilarity between momentum and scalars for different stability regimes can be deduced from the alternating influence of momentum and sensible heat fluxes on atmospheric stability, less is known about scalar-transport dissimilarity, which is attributed to, for example, advection (Lee et al. 2004), entrainment into the boundary layer (Sempreviva and Højstrup 1998), atmospheric stability (Li and Bou-Zeid 2011) or, more generally, differences in the distribution of sources and sinks (Williams et al. 2006). However, since many such studies were carried out above very different ecosystems, the above-mentioned reasons for scalar dissimilarity may be of varying importance.

We assess here the turbulence characteristics of a mid-latitude European city by analyzing more than 12 years of eddy-covariance measurements collected at a height of 39 m above street level in Basel, Switzerland. We use the quadrant-analysis framework to extract statistics from the turbulence time series to infer ejection–sweep interactions, as well as the importance and composition of organized turbulent events. We also examine the

transport and transfer efficiencies of momentum, heat, H_2O and CO_2, the modulation of these properties as a function of atmospheric stability, and investigate the transport similarity between these variables. We expect atmospheric stability to be a major modulator of turbulence intensity and the occurrence of organized turbulence, and assume the patchy complex distribution of individual sources of sensible heat, CO_2 or H_2O fluxes to be the major influence on scalar dissimilarity (Moriwaki and Kanda 2005; Nordbo et al. 2012; Wang et al. 2013; Kurppa et al. 2015).

2 Methods

2.1 Measurements

The eddy-covariance system in operation since May 2004 consists of a Gill HS three-dimensional sonic anemometer and a LICOR–7500 open-path gas analyzer. The instruments were mounted at 39 m above street level, on a 19-m tall tower that is installed permanently on the rooftop of a 20-m tall building in the centre of Basel, Switzerland (47.56173°N, 7.58049°E). To the east of the station, the inner ring road Klingelbergstrasse of high traffic density (15,000–20,000 vehicles day^{-1}) passes the station, and there are residential buildings with green spaces and small minor streets to the west. The eddy-covariance system samples at 20.83 Hz, raw data are stored at full resolution as 30-min files, and post-processing is done using EddyPro® 6.1.0 (LICOR Inc.) software. Data collected between May 2004 and December 2016 have been analyzed, with overall data availability for flux data after post-processing approximately 70%. Further details on the instrumental set-up and the data processing are available in Schmutz et al. (2016).

2.2 Turbulent Transport and Flux Dissimilarity

Within the inertial sublayer, the dominant process for transporting momentum, energy and mass is turbulence. Following the basic principle of turbulent transport by eddy motions, the transport of any property of the air is related to the vertical velocity component or its fluctuation. Rewriting the units of the vertical velocity component w (m s^{-1}) as

$$w = Q_V \tag{1}$$

gives the transport of a volume per unit area and unit time Q_V (m^3 m^{-2} s^{-1}), which may be multiplied by the density of air to give the mass-flux density of air as

$$Q_M = \rho_A Q_V = \rho_A w. \tag{2}$$

The transport of any scalar property a of the air can be multiplied by the mass-flux density Q_M to give the flux density of the scalar property a as

$$Q_a = \rho_A w a. \tag{3}$$

By applying Reynolds decomposition to the flux density Q_a, then

$$Q_a = \overline{\rho_A}\,\overline{w'a'}, \tag{4}$$

where primes ($'$) denote fluctuating quantities, and an overbar ($^-$) is an averaged quantity. Known as the eddy-covariance method, the derivation of flux densities implies that all of the transport is directly related to the vertical velocity component and, thus, all of the scalar properties of the air are potentially subject to the same transporting motions. Nevertheless,

it is not necessarily true that all fluctuations of the scalar properties are related to the same eddies because the fluctuation of each scalar property is independent as far as the scalar sources are independent, which is also known as flux dissimilarity.

According to Li and Bou-Zeid (2011), the dissimilarity of the flux densities of momentum, energy and mass can be investigated by calculating the correlation coefficient between the fluxes $\overline{w'a'}$ and $\overline{w'b'}$ as

$$r_{\overline{w'a'},\overline{w'b'}} = \frac{\overline{\left(w'a' - \overline{w'a'}\right)\left(w'b' - \overline{w'b'}\right)}}{\sigma_{wa}\sigma_{wb}}, \tag{5}$$

where a' and b' can either be fluctuations of the longitudinal velocity component u, sonic temperature T, specific humidity q, or CO_2 concentration c.

2.3 Quadrant Analysis

Quadrant analysis is widely used to identify turbulent structures in eddy-covariance time series (Shaw et al. 1983) by separating the instantaneous flux $w'a'$ into four quadrants in the $w' - a'$ plane according to the sign of the fluctuating components as follows:

quadrant 1: $a' > 0, w' > 0$, ejections for $\overline{w'a'} > 0$, outward interactions for $\overline{w'a'} < 0$
quadrant 2: $a' < 0, w' > 0$, outward interactions for $\overline{w'a'} > 0$, ejections for $\overline{w'a'} < 0$
quadrant 3: $a' < 0, w' < 0$, sweeps for $\overline{w'a'} > 0$, inward interactions for $\overline{w'a'} < 0$
quadrant 4: $a' > 0, w' < 0$, inward interactions for $\overline{w'a'} > 0$, sweeps for $\overline{w'a'} < 0$

Motions contributing to the same sign as the net flux are always labelled ejections and sweeps, whereas counter-gradient structures are named outward interactions and inward interactions, respectively (Fig. 1). This definition ensures that ejections and sweeps always refer to the dominant turbulent structures that produce fluxes within the averaging period. Note that some studies use different definitions for the quadrants. Furthermore, the vertical

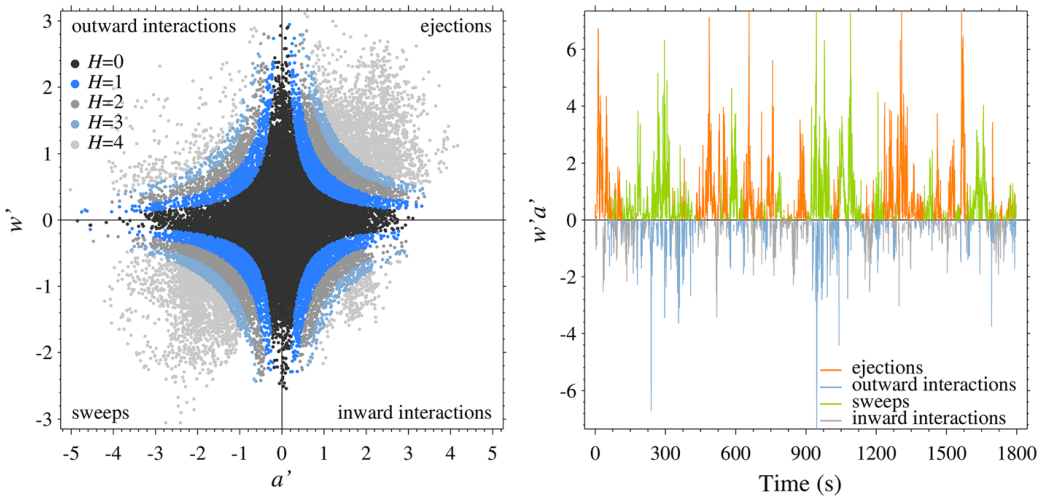

Fig. 1 Illustration of quadrant definitions in the quadrant framework (left) and in time (right) for $\overline{w'a'} > 0$

velocity component w is always plotted here on the y-axis and scalars on the x-axis to aid visualization of the actual turbulence processes.

We characterize the flux contribution of each quadrant by calculating the flux fraction

$$S_{i,H} = \frac{\overline{w'a'}_{i,H}}{\overline{w'a'}}, \tag{6}$$

with

$$\overline{w'a'}_{i,H} = \frac{1}{t_{avg}} \int_0^{t_{avg}} I(t) O\left(w', a'\right) w'a' dt, \tag{7}$$

where i denotes the quadrant number, t_{avg} is the averaging period, $I(t)$ is an indicator function

$$I(t) = \begin{cases} 1 & \text{if } w'a' \text{is in quadrant } i \\ 0 & \text{otherwise,} \end{cases}, \tag{8}$$

$O\left(w', a'\right)$ is a hole-size function defining a hyperbolic hole,

$$O\left(w', a'\right) = \begin{cases} 1 & \text{if } |w'a'| \geq H\left|\overline{w'a'}\right| \\ 0 & \text{otherwise,} \end{cases}, \tag{9}$$

and H is the hole-size factor. Note that Lu and Willmarth (1973) originally defined the hole size as a multiple of the root mean square of the quantities w' and a', but both definitions are commonly found in the literature. Raupach et al. (1986) defined a variable hole size for each averaging period above which 50% of the flux density occurs. The introduction of such a hyperbolic hole allows the exclusion of small near-isotropic structures to identify those large and infrequent structures contributing significantly to the total flux. In addition to the flux fraction, it is also of interest to evaluate the time fraction $\vartheta_{i,H}$ covered by those turbulent structures,

$$\vartheta_{i,H} = \frac{1}{t_{avg}} \int_0^{t_{avg}} I(t) O\left(w', a'\right) dt. \tag{10}$$

2.4 Organized Turbulence

The application of the eddy-covariance method assumes a stationary signal from sources distributed homogenously in space, which is a basic requirement challenged by the complex structural composition and source/sink configuration of urban landscapes. Line (streets), point (chimneys) and even moving sources (vehicles) lead to a spatially- and temporally-heterogeneous signal, while tall and massive building structures enforce the generation of complex turbulence structures, which may lead to reoccurring vortexes or the increase of, for example, CO_2 concentration within a street canyon (Lietzke and Vogt 2013). In addition to natural processes, such as free convection, downdrafts, breaking gravity waves or entrainment, certain properties of the urban boundary layer facilitate the formation of organized events likely responsible for a substantial amount of the net flux

density. Organized events, which are usually called coherent structures and occur as intermittent patterns with dimensions that scale with the density and depth of the underlying roughness elements (Thomas et al. 2017), are generally accepted to be responsible for large parts of the surface–atmosphere exchange. Still, there is no common agreement about the constitution and shape of such turbulent structures and, hence, detection algorithms and criteria vary from study to study. Our approach is not to differentiate between different types of organized motions or to investigate the reason for each occurrence, but to quantify their flux contribution and emphasize the importance of conditional sampling within complex urban environments.

Organized events can be investigated within the frequency domain by, for example, wavelet analysis, since turbulent motions are expected to occur as single units of specific time scales (Thomas and Foken 2007). Such structures can also be investigated within a quadrant-analysis framework, which assumes a signal is produced by events significantly larger than a predefined threshold value. Quadrant analysis generally leads to a larger number of detections compared with wavelet analysis, because events are often chopped into multiple parts whenever the value of $w'a'$ drops below the threshold value given by the hyperbolic hole. To overcome this issue, Luchik and Tiederman (1987) use a time frequency parameter τ_E, which defines the maximum time allowed to elapse between individual sweeps and ejections to still count as one burst event. To find a reasonable value for τ_E, we calculated the histogram and the cumulative distribution function of the parameter τ_E for single 30-min periods to distinguish between a region of ejections and sweeps from the same burst, and ejections and sweeps from different burst events (Steiner et al. 2011). Furthermore, we conducted a sensitivity analysis of the final statistics, including the average and total durations, and the total number of organized structures per 30 min as a function of different τ_E values. The number of detected events per 30-min run decreases exponentially with increasing values of τ_E and the variance becomes smaller. Finally, the frequency parameter τ_E is fixed to the value where the rate of change between the number of detected events, represented by the modus of the distribution, falls below a threshold value of 5%, and leads to an average frequency parameter of $\tau_E = 0.8$ s, which we use for all variables. The total event duration is defined as the elapsed time between the first and the last fluctuation of $w'a'$, whereas the flux fraction of the event is derived from all values of $w'a'$ that lie within this time frame, but outside the hyperbolic hole. To improve the results from the detection algorithm, the time series is filtered by a 1-s moving average; flux fractions are, however, calculated from the original high-frequency data. An illustration of the detection algorithm is given in Fig. 2.

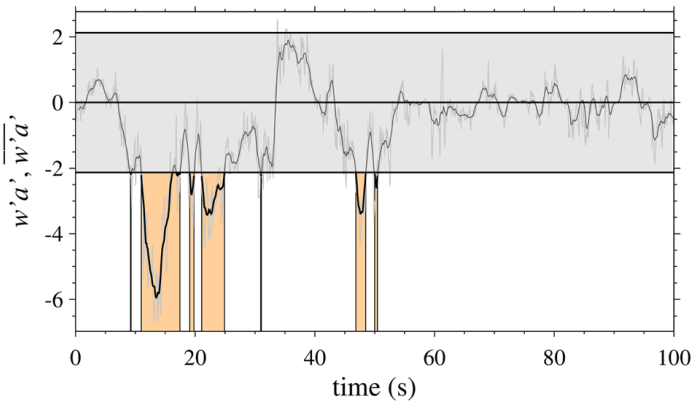

Fig. 2 Demonstration of the event-detection algorithm. Depicted is a 100-s extract from an arbitrary time series. The grey shaded area is the hyperbolic-hole representation in time, the light grey line is the raw time series, and the dark grey line shows the 1-s moving averages. The orange area and the black lines mark detected events

2.5 Atmospheric Stability

Atmospheric stability is classified according to the dimensionless stability parameter

$$\zeta = \frac{z - z_d}{L}, \tag{11}$$

where z is the measurement height, z_d is the displacement height, and L is the local Obukhov length,

$$L = -\frac{u_*^3}{\kappa \frac{g}{\overline{\theta_v}} \overline{w'T'_v}}, \tag{12}$$

where u_* is the friction velocity, $\kappa = 0.4$ is the von Kármán constant, g is the acceleration due to gravity, $\overline{(\theta_v)}$ is the average virtual potential air temperature, and T_v is the virtual air temperature, which can be approximated by the sonic temperature (Kaimal and Gaynor 1991). The displacement height is derived from the empirical relation

$$z_d = 0.67 z_h, \tag{13}$$

where z_h is the mean building height (16.6 m) calculated from a three-dimensional city model (Grimmond and Oke 1999; Schmutz et al. 2016; Foken 2017). We classify stable conditions as $\zeta > 0.05$, near-neutral conditions as $|\zeta| \leq 0.05$, and unstable conditions as $\zeta < -0.05$. Because the transport of momentum and sensible heat is the driving force for turbulence generation in Eq. 12, there is significant correlation between these two fluxes and the stability parameter ζ. Even though CO_2 and H_2O fluxes may also influence the transport processes by altering, for example, the air density (Webb et al. 1980), they are referred to as passive scalars here.

Atmospheric stability largely modulates the turbulent-transport processes within the atmospheric boundary layer, mainly because of the varying influence of buoyancy- and mechanically-driven turbulence under different stability conditions. While both thermal turbulence and mechanical turbulence produce eddies capable of transporting properties of the air vertically, the shape and the scale of these structures are not the same. There is a general consensus in the literature that coherent structures are produced by different types of turbulent motions (Li and Bou-Zeid 2011). From observations of laboratory flows, it is known that hairpin vortices form under near-neutral conditions and coherent structures can primarily be attributed to these three-dimensional motion types. With increasing positive buoyancy, there is a transition from wall-bounded hairpin structures to uplifted organized motions (e.g. Hommema and Adrian 2003). While combined shear and buoyant effects may be responsible for the horizontal roll vortices in the weakly unstable boundary layer, vertical motions in the form of thermal plumes increasingly dominate the turbulent transport towards more unstable conditions (Mason and Sykes 1980; Etling and Brown 1993; Boppe et al. 1999; Hutchins and Marusic 2007; Li and Bou-Zeid 2011).

2.6 Transport Efficiency

The transport efficiency E_{Tp} introduced by Wyngaard and Moeng (1992) describes the ratio between the total covariance and the motions contributing to the same sign (down-gradient)

as the final flux, i.e. ejections and sweeps. In other words, the efficiency E_{Tp} compares the net transport to what is effectively transported down-gradient,

$$E_{Tp} = \frac{\text{net flux}}{\text{direct flux}} = \frac{\overline{w'a'}}{\overline{w'a'}_{EJ} + \overline{w'a'}_{SW}}. \tag{13}$$

Due to the definition of ejection and sweeps as positive flux contributions, the condition $E_{Tp} \leq 1$ is always true for hole sizes $H = 0$, and $1 - E_{Tp}$ is the amount of counter-gradient transport. Within the quadrant analysis, the transport efficiency is sometimes referred to as the exuberance E_x, which balances the counter-gradient transport against the down-gradient transport,

$$E_x = \frac{\overline{w'a'}_{OI} + \overline{w'a'}_{II}}{\overline{w'a'}_{EJ} + \overline{w'a'}_{SW}}, \tag{14}$$

where E_{Tp} and E_x are negatively correlated; here, we use the parameter E_{Tp} to quantify the transport efficiency.

2.7 Transfer Efficiency

The transfer efficiency E_{Tf} is a measure of the correlation between the vertical velocity component w and a scalar a, and is given by the covariance scaled by the product of the standard deviations σ_w and σ_a of the two variables,

$$E_{Tf} = \frac{\overline{w'a'}}{\sigma_w \sigma_a} = R_{w'a'}, \tag{15}$$

where E_{Tf} takes values between -1 and 1, and the variables are said to be positively correlated when $E_{Tf} > 0$, negatively correlated when $E_{Tf} < 0$, and uncorrelated when $E_{Tf} = 0$. This implies that the transport of a scalar a becomes more efficient as $\left|E_{Tf}\right| \to 1$, when the values of the fluctuations a' and w' coincide.

3 Results and Discussion

3.1 Influence of Atmospheric Stability on the Mechanism of Turbulent Transport

To characterize the impact of different stability conditions on turbulent transport, Fig. 3 presents the general behaviour of the vertical transport of momentum, heat, CO_2 and H_2O as a function of the stability parameter ζ. As expected, neutral conditions are characterized by the dominance of mechanical turbulence represented by the momentum transport, whereas thermal turbulence vanishes. In the unstable range ($-0.05 > \zeta > -1$), mechanical turbulence and thermal turbulence are in balance, whereas for strongly unstable conditions ($\zeta < -1$), turbulence is almost solely produced by buoyancy. For stable stratification, the mechanical turbulence also vanishes quickly as $\zeta \to 1$, and there is a weak influence of negative buoyancy throughout the stable range. The passive scalars CO_2 and H_2O do not show a direct relationship to atmospheric stability. While both variables do not respond to a change in atmospheric stability under unstable conditions, H_2O fluxes decrease from the

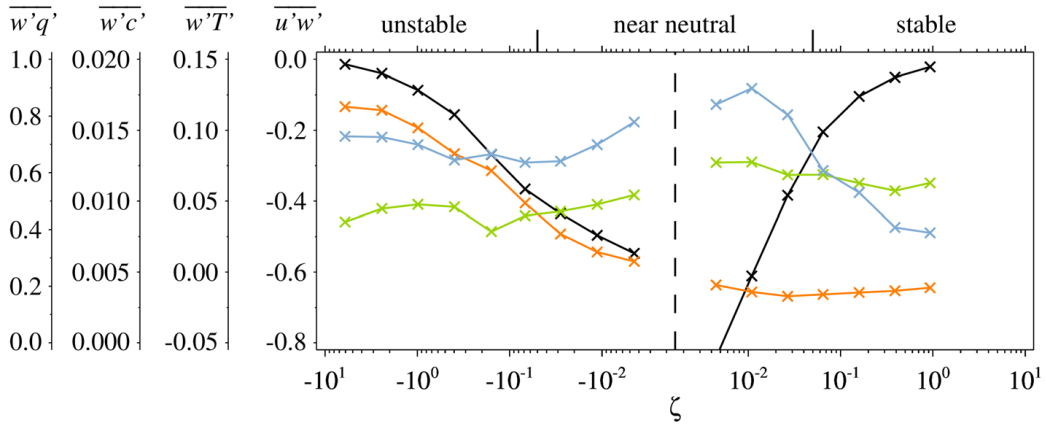

Fig. 3 Covariances of momentum (black, [m^2 s^{-2}]), sensible heat (orange, [m K s^{-1}]), CO_2 (green, [mmol m^{-2} s^{-1}]) and H_2O (blue, [mmol m^{-2} s^{-1}]) as a function of atmospheric stability ζ

near-neutral range towards stable stratification. The behaviour of the momentum and sensible heat fluxes in relation to the stability conditions has been well studied, and it has to be mentioned at this point that there is an autocorrelation between the Obukhov length and these two variables.

As net fluxes are of great interest for the quantification of the transported property, but only give little information about the underlying processes, the transfer and transport efficiencies reveal the ongoing processes hidden behind the net flux density. The efficiency of turbulent exchange is not directly coupled to the magnitude of the net flux and, as such, processes that lead to weak fluxes (e.g. plant uptake) can be detected by an altered (e.g. weakened) correlation. Very often, fluxes near zero do not imply that there is no ongoing vertical transport, but only that the amount transported upwards is equal to that transported downwards. Whereas this may not be of particular interest for the characterization of the net exchange for a specific environment, the effective transport processes become more important in complex areas. Even though the net transport at a specific height may approximate zero, a higher chance exists for CO_2 in a street canyon to settle horizontally if there is absolutely no vertical transport compared with a situation where there is a very effective (but not efficient) vertical exchange, but an equilibrium of upwards and downwards transport. The same is of course valid for other scalars, and may be of interest when investigating the propagation of air pollutants or constituents in general. In Fig. 4, the transfer efficiencies of all four investigated variables are depicted as a function of atmospheric stability, and fitted with functions from De Bruin et al. (1993) derived over a horizontal, uniform terrain in France, and from Wood et al. (2010) for measurements in London, U.K. Both studies propose a separate function for momentum and heat, whereas the function for the heat flux is used to check scalar similarity between heat, CO_2 and H_2O fluxes.

The transfer efficiency for momentum follows relatively well the function proposed by De Bruin et al. (1993) for unstable cases, which reflects the near-neutral and free-convective limits well, but the linear function is too simplistic under stable conditions, with the fit derived from the urban environment in London better representing the slight decrease (absolute) in transfer efficiency for momentum with increasing atmospheric stability. The transfer efficiency of the sensible heat flux clearly follows more closely the fit of Wood et al. (2010) for both stable and unstable cases in terms of shape, as well as in the free-convective, near-neutral and stable limits. Compared with the momentum flux, the linear

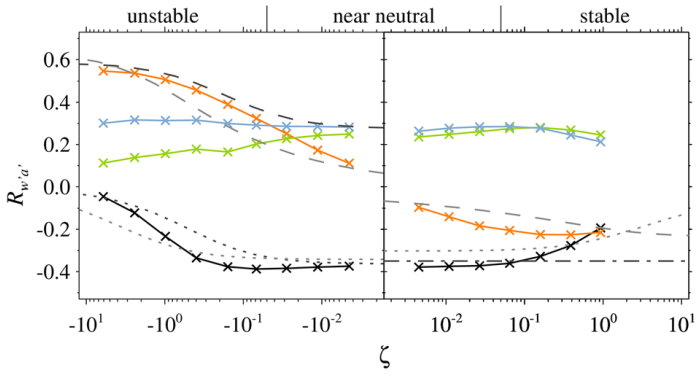

Fig. 4 Transfer efficiency of momentum (solid black), heat (solid orange), CO_2 (solid green) and H_2O (solid blue) as a function of atmospheric stability fitted with functions from De Bruin et al. (1993) (dark grey, dashed for scalars, dotted for momentum, dash–dotted for both) and Wood et al. (2010) (light grey, dashed for scalars, dotted for momentum). Note that the logarithmic *x*-axis is non-continuous in the neutral range

fit for stable cases not only misses the dependence on atmospheric stability, but also clearly overestimates the transfer efficiency of the sensible heat flux under stable conditions. In contrast to the assumption of scalar similarity given by the fitted functions, the two passive scalars CO_2 and H_2O do not follow the same relationship. It is often assumed that heat and other scalars such as water vapour are transported by the same mechanisms (De Bruin et al. 1993), but this is likely not the case as demonstrated by our data, as well as that reported in literature (Wang et al. 2013). While the transfer efficiency for scalars is expected to increase under unstable conditions, there is in fact no real dependence on atmospheric stability. Interestingly, CO_2 is transported less efficiently under unstable conditions in comparison with H_2O, whereas the transfer efficiency becomes increasingly similar towards near-neutral and stable conditions. The linear relationship between the transfer efficiency of the scalars CO_2 and H_2O under stable conditions corresponds well to our data, but because of the unrelated source activity of both scalars, the flux direction cannot easily be determined as a function of atmospheric stability, which was also found by Wang et al. (2013), who compared their data from the Beijing tower to the same functions.

The transfer efficiencies reveal differences between the transporting mechanism of energy, and the scalars CO_2 and H_2O. In many approaches to the characterization of turbulent transport, scalar similarity between these variables is assumed, which implies that the same turbulent structures or motions are responsible for the transport of all scalars. While this may apply for uniform terrain, the heterogeneous and complex urban environment does certainly not allow for this simplification. Cities are a patchy representation of heat, CO_2 and H_2O sources and sinks, and their locations are not implicitly congruent. Furthermore, as the sources of heat, H_2O and especially CO_2 also undergo temporal variations mostly linked to diurnal human activities (e.g. traffic, heating activity, industrial production) in urbanized areas, we expect spatial and temporal scalar dissimilarity because of the heterogeneous environment.

Figure 5 presents the correlation coefficients between the individual fluxes as a function of atmospheric stability to assess their similarity. During very unstable, neutral and very stable conditions, the correlation between the momentum and sensible heat fluxes (black line) is negligibly small because, under these conditions, either the buoyant or mechanical production of turbulence approaches zero; only at the transition to near-neutral conditions are both fluxes partially correlated. If the momentum flux is compared with passive scalars

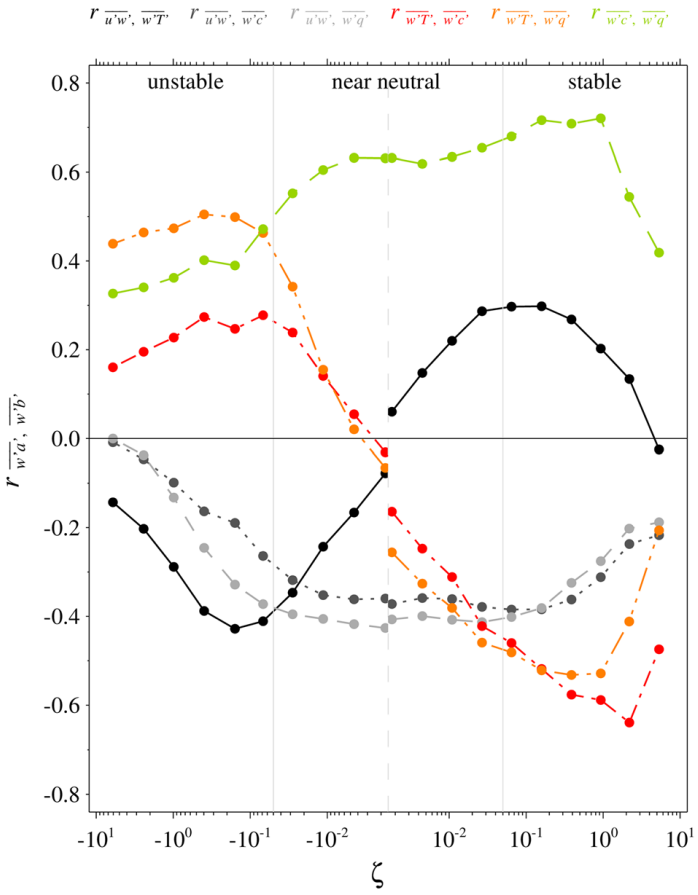

Fig. 5 Flux similarity for all combinations of measured covariances as a function of atmospheric stability is the correlation coefficient (see Eq. 5). Note that the logarithmic *x*-axis is non-continuous in the neutral range

(grey lines), the correlation is again small for unstable conditions when there is almost no mechanically-driven turbulence. When approaching near-neutral conditions, similarity between momentum and scalars increases to around −0.4 for H_2O and −0.35 for CO_2. For stable conditions, the similarity decreases again, but the fluxes are still better correlated than for unstable conditions. If we consider the correlation between the active scalar of sensible heat and the two passive scalars (red and orange lines), we find a correlation coefficient of between 0.35 and 0.4 for water vapour, and 0.15–0.25 for CO_2 under unstable conditions, with a maximum in the unstable range ($-0.05 > \zeta > -1$). The better correlation between the sensible heat flux and water vapour compared with CO_2 may be explained by the fact that water vapour also has a positive effect on buoyancy and, furthermore, that the sources of sensible heat and H_2O are less patchy and likely more congruent than the locations of CO_2 emission and uptake. Furthermore, we assume that, during unstable conditions (primarily daytime conditions), photosynthesis weakens the correlation between the net transport of CO_2 and heat or momentum, because a counter-gradient component (sink) is introduced by plant uptake. In the near-neutral range where the sensible heat flux vanishes, the correlation is accordingly near zero because the passive scalars are still transported mechanically. For stable conditions when the influence of negative buoyancy increases, we find even higher similarity, whereas for very stable conditions, the correlation between sensible heat and CO_2 (−0.6) fluxes exceeds that of water vapour (−0.5). It is interesting that, under stable conditions when both mechanically- and buoyancy-driven turbulence are active, the similarity between the sensible heat flux and passive scalars is

larger compared with unstable cases, where we find dominant buoyancy-generated turbulent motion. However, this may also be an indicator that, during daytime during predominantly unstable conditions, we also observe the largest variability in the spatial and temporal source/sink distributions of the sensible heat, CO_2 and H_2O fluxes. In contrast, during the night when stable cases occur, we expect more constant emissions of these three scalars and, thus, an enhanced similarity of transport processes. By inspecting the similarity between the passive scalars, we observe increasingly greater correlation between the scalars CO_2 and H_2O with increasing stability. The similarity between CO_2 and H_2O is largest compared with the correlation to the sensible heat or momentum fluxes, except for water vapour under unstable conditions, which correlates better to the sensible heat flux due to the above-mentioned reasons. The large decrease of the correlation coefficient for very stable conditions can partially be explained by the complete breakdown of turbulent transport for very stable conditions, but it also has to be mentioned that very stable cases are extremely rare in the urban boundary layer and, thus, the smaller database should also be considered when interpreting the results.

3.2 Locating Dominant Turbulent Structures

To examine the dominant turbulence structures responsible for the transport of momentum, sensible heat, CO_2 and H_2O over the urban canopy, we analyze the quadrant statistics by investigating the flux fractions, ejections, outward interactions, sweeps and inward interactions. For comparability with other studies and for historical reasons, Fig. 6 shows the classical presentation of the flux fraction $S_{i,H}$ for each quadrant i as a function of increasing hole size H. By definition, ejections and sweeps are dominant over outward interactions and inward interactions for non-zero fluxes, as they refer to down-gradient transport. As such, first and third quadrant flux fractions $S_{1,H}$ and $S_{3,H}$ are given as positive, and the second and fourth quadrant flux fractions $S_{2,H}$ and $S_{4,H}$ are negative when summed to achieve the net transport ($S_0 = 1$).

In Fig. 7, the statistical properties from Fig. 6 are compiled to emphasize the ongoing processes. The introduction of a hyperbolic hole into the quadrant analysis enables the separation of different scales of turbulent fluctuations, and the identification of areas in the covariance plane that are of higher or lower importance for the net transport. While the traditional definition of the hole size H gives cumulative information about all structures, where $|w'a'| \geq H\left|\overline{w'a'}\right|$, the bars in Fig. 7 indicate the increment in the flux fraction between adjacent hole sizes, i.e. the amount of flux produced within the area between two hole sizes. For all variables and all stability regimes, a similar pattern occurs. For $H < 1$, a nearly isotropic area can be observed where down-gradient and counter-gradient motions transport almost an equal amount of mass, sensible heat, CO_2 or H_2O upwards and downwards, thus resulting in no effective transport. By increasing the hole size, both ejections/sweeps and outward interactions/inward interactions transport more of the particular property, but down-gradient transport increases more rapidly. The maximum transport per hole size for counter-gradient motions is reached at $1 < H < 2$ or $2 < H < 3$ ($\overline{w'T'}$, neutral), respectively. For ejections and sweeps, the maxima occur at $2 < H < 3$ and $3 < H < 4$ ($\overline{w'T'}$, stable and neutral, respectively). While the influences of outward and inward interactions decrease rapidly as $H \to 10$, ejections and sweeps become more dominant while still producing a significant down-gradient flux up to at least $H = 15$. Generally, this allows us to roughly separate two areas of major interest: (i) $H < 10$ where both counter-gradient and down-gradient motion transport a significant amount of each property, (ii) $H > 10$

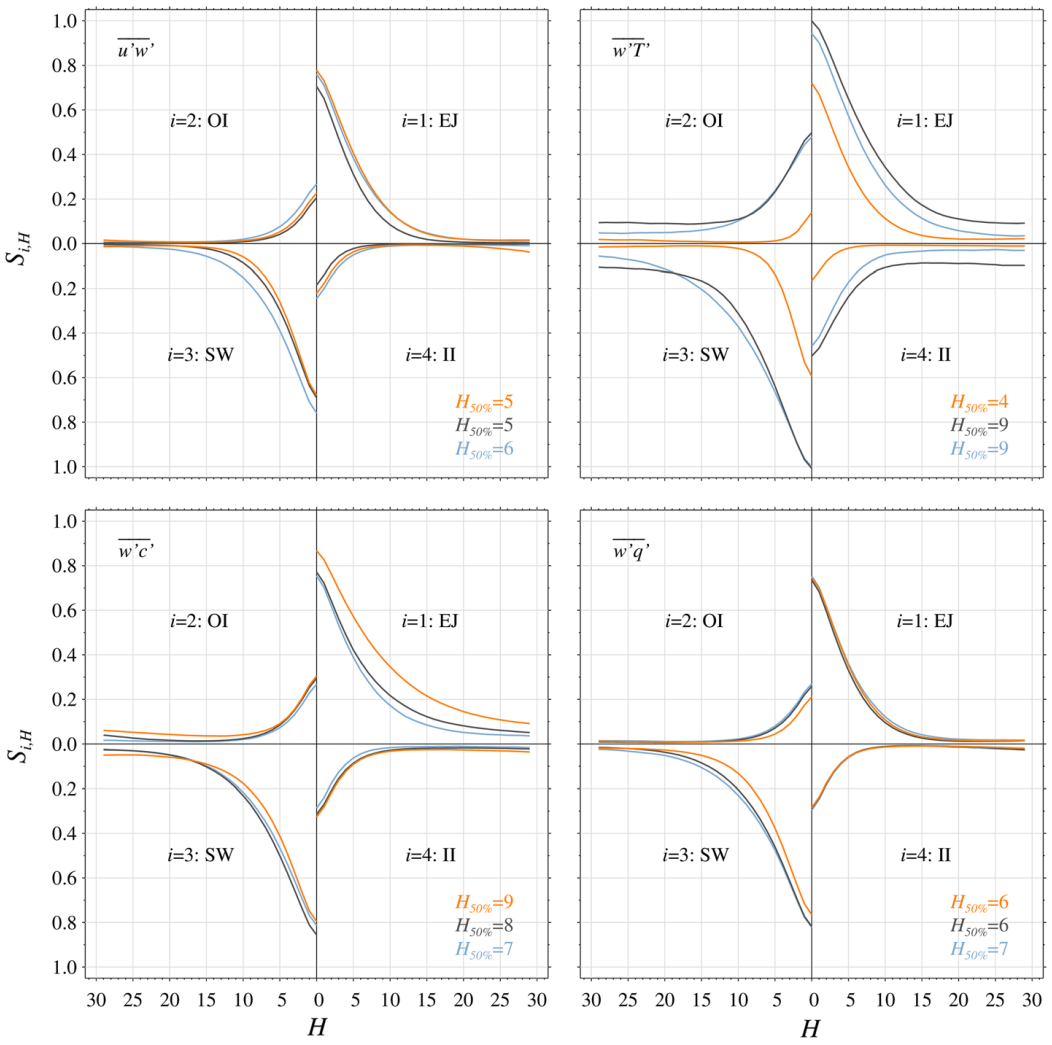

Fig. 6 Flux fractions $S_{i,H}$ for momentum, heat, CO_2 and H_2O fluxes as a function of hole size H separated by stability for each quadrant. Indicated bottom right is the hole size $H_{50\%}$ above which at least 50% of the final flux occurs. Atmospheric stability is classified as stable for $\zeta > 0.05$ (blue), near-neutral for $|\zeta| \leq 0.05$ (black), and unstable for $\zeta < -0.05$ (orange)

where predominantly down-gradient transport takes place and counter-gradient motion mostly vanishes. This area coincides well with the transport efficiency (dotted line) reaching its maximum values around these hole sizes.

The solid lines in Fig. 7 show the cumulative flux fraction of each quadrant and the overall flux fraction similarly to the curves in Fig. 6. By considering the build-up of the overall flux fraction as a function of hole size H (solid black line), a stability dependency is evident for all variables except for CO_2. For momentum, heat and H_2O fluxes, the total flux is on average achieved at smaller hole sizes for unstable conditions, and larger hole sizes become increasingly more important under near-neutral and stable conditions. This effect is most apparent for the covariance $\overline{w'T'}$ where the maximum relevant hole size shifts from $H = 18$ during unstable cases to $H = 28$ during stable conditions. For momentum, the maximum hole size still shifts from $H = 19$ to $H = 28$ and from $H = 20$ to $H = 25$ for H_2O. Simultaneously with the shift towards larger turbulence structures under stable

Fig. 7 Quadrant statistics for momentum, sensible heat, CO_2 and H_2O fluxes separated by unstable, near-neutral and stable conditions. The bars (orange: ejections, green: sweeps, blue: outward interactions, grey: inward interactions) indicate flux-fraction increments between each hole size. Solid lines represent the cumulative flux fraction for each quadrant, as well as the overall flux fraction as a function of the hole size (solid black line). The dotted line shows the transport efficiency ▶

conditions, we also observe a significant difference concerning the interplay between ejections is sweeps. While for all variables the sum of ejections is more ($\overline{u'w'}, \overline{w'T'}, \overline{w'c'}$) or at least equally ($\overline{w'q'}$) important for the overall flux under unstable conditions, sweeps become slightly dominant ($\overline{w'T'}, \overline{w'c'}, \overline{w'q'}$) or equally important ($\overline{u'w'}$) compared with ejections towards stable stratification. The general dominance of ejections over sweeps under unstable conditions is explained by buoyancy-driven thermal plumes leading to strong upwelling motions, which is a known feature of the unstable atmosphere reported for many different surface types (e.g. Maitani and Ohtaki 1987; Katul et al. 1997b; Feigenwinter et al. 1999; Christen et al. 2007; Li and Bou-Zeid 2011; Dupont and Patton 2012; Francone et al. 2012). Interestingly, this is not true throughout the range of hole sizes. For momentum, sensible heat and CO_2 fluxes, sweeps dominate ejections under unstable conditions up to $H = 7$ ($\overline{u'w'}, \overline{w'T'}$) and $H = 22$ ($\overline{w'c'}$). As such, downward motions dominate the vertical exchange at smaller scales, but ejections are finally more important as they add significantly to the net flux at larger scales. For the H_2O flux, the upwards and downwards transport by ejections and sweeps is equally important. Towards stable conditions, the interplay between ejections and sweeps changes and for sensible heat, CO_2 and H_2O fluxes, ejections dominate the smaller scales, whereas sweeps overcompensate ejections by adding more to the overall flux at larger scales.

The differences in the importance of ejections and sweeps are most likely the result of different mixing scenarios in the unstable, near-neutral and stable boundary layers. During the day, we generally expect a downwards transport of momentum from the overlaying air into the lower boundary layer, resulting in increasingly higher wind speeds over the course of a day. However, due to the vicinity of the measurements to the ground, the change in wind speed between the ground and the measurement level is much larger than the momentum gradient within the inertial sublayer. As such, it is more likely that the net downwards transport of momentum is predominantly produced by the upwards propagation of slower air parcels than by sweeps of overlaying air with higher momentum. During the night or under stable conditions, when the momentum gradient is generally weak, differences between ejections and sweeps become less important. The interplay of ejections and sweeps for the sensible heat flux can largely be explained by the diurnal cycle of sensible-heat production. While surface warming during the day favours the upwards transport of warmer air by ejections, the more stable stratification during the night enables a more frequent downwards transport of cooler air from the overlaying air. For the scalars CO_2 and H_2O, while we also expect the flux-generating sources at the ground, the differences between ejections and sweeps are not that apparent. Because the sources of CO_2 and H_2O are distributed less homogeneously compared with the sources of the sensible heat flux, the entrainment of air of lower CO_2 and H_2O concentration from above is seemingly equally important than the active upwards transportation of air parcels with a higher concentration. Accordingly, during the night, the CO_2 and H_2O fluxes are probably influenced by the entrainment of air from the rural surroundings with a lower concentration of CO_2 and H_2O. Especially for CO_2 and H_2O, vertical gradients are generally maintained by source activity at the ground during the day and by the overlaying airmass during the night, which is reflected in the interplay of ejections and sweeps under these conditions.

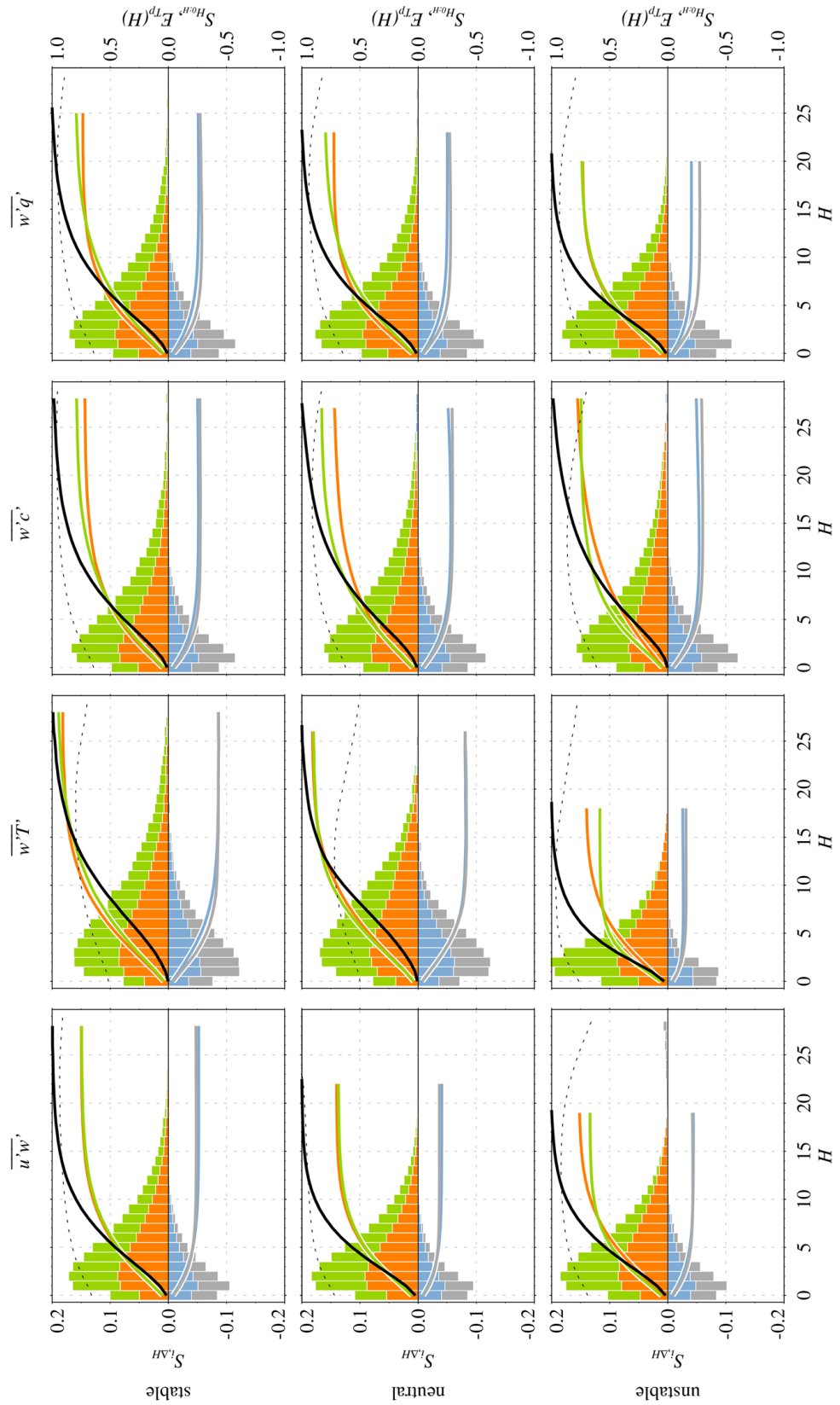
unstable
neutral
stable
$S_{i,\Delta H}$
$S_{H_{0.H}}, E_{Tp}(H)$
$\overline{u'w'}$
$\overline{w'T'}$
$\overline{w'c'}$
$\overline{w'q'}$
H

Finally, Fig. 8 presents the time fractions of all four quadrants for each stability class. The time fraction $\vartheta_{i,H}$ decreases quickly with increasing hole size, and structures larger than $H = 5$ mostly occupy less than 5% of the overall time for both sweeps and ejections. By combining this information with the findings from Fig. 7, we have evidence that efficient structures at scales from $H = 5$–15 contribute significantly (40–75%) to the net flux, but cover < 10% of the averaging period. This gives strong evidence for the existence and the importance of organized structures, which are analyzed in the next section.

3.3 Detecting Events

The detection of organized structures using a quadrant analysis requires the hyperbolic hole size to be adjusted to exclude small-scale motions in the near-isotropic range. From the analysis of the ejection–sweep interactions, we find that efficient ejection–sweep cycles

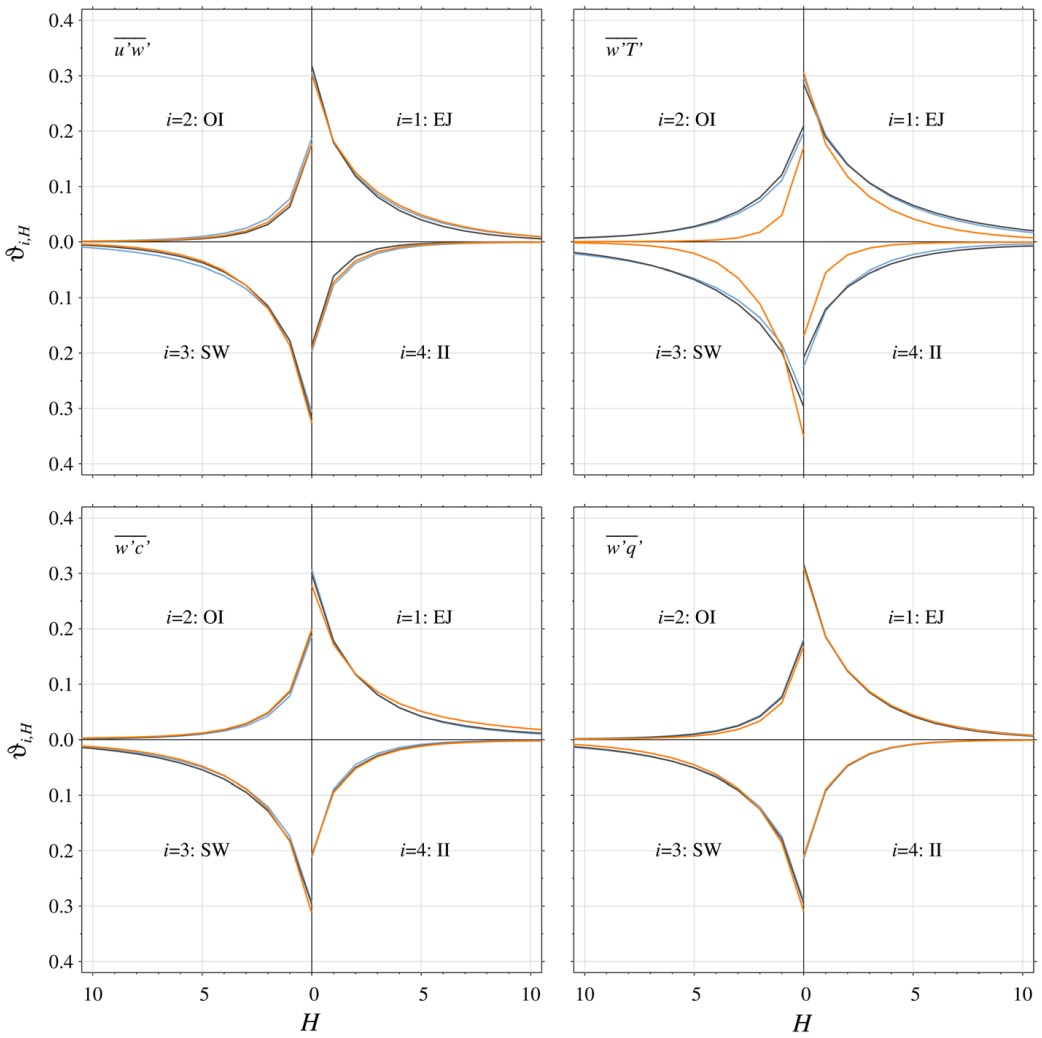

Fig. 8 Time fractions ϑ for momentum, heat, CO_2 and H_2O as a function of hole size H, separated by stability for each quadrant. Atmospheric stability is indicated by orange (unstable), black (near-neutral) and blue (stable) lines

only appear above a hole-size factor of $H \approx 5$, and have transferred this information into the event-detection algorithm as it has proven to deliver reasonable results. Other studies (Luchik and Tiederman 1987; Steiner et al. 2011) applied a hole-size factor of $H = 1$, which they multiply by the root mean square instead of the covariance, whereas the root mean square is usually somewhat larger than the actual covariance.

We analyze the events in terms of number, average and total duration, as well as their flux and time fraction per 30-min run (Fig. 9). The average event duration ranges between 1 s and 4 s for all cases, with a trend to slightly longer events under unstable conditions, and the shortest events are observed in near-neutral conditions. However, the sensible heat flux in stable cases is generally characterized by longer event durations. Apart from this exception, single events are generally shorter under neutral and stable conditions where the number of detected events and, thus, the total duration of all events, is larger compared with unstable conditions. Differences between stability regimes are most apparent for the sensible heat flux, but not that clear for the momentum, CO_2 and H_2O fluxes. However, there is a clear pattern of shorter, but more frequent, organized structures with increasing stability, which is also found when considering flux fractions covered by the events. Despite being shorter, the higher frequency of occurrence of organized structures under near-neutral and stable conditions implies they contribute more to the final flux than for unstable cases. In most cases, the flux fraction of events ranges from 50–75%, with significantly larger flux contributions under stable conditions. While differences between the momentum, CO_2 and H_2O fluxes are relatively small, the sensible heat flux is less influenced by organized structures under unstable conditions but clearly more dominant under stable conditions. While the larger frequency of occurrence of organized events under stable conditions compared with unstable cases is also reported by Barthlott et al. (2007) (30%) and Steiner et al. (2011) (20%), these data were collected from natural ecosystems. Nonetheless, our results are comparable, with 15% more events under stable conditions for momentum, 60% for sensible heat, 23% for CO_2, and 15% for H_2O here. Steiner et al. (2011) performed a similar analysis of organized structures but with a hole-size factor multiplied by the root mean square, and generally found a slightly higher number of coherent events of shorter duration, which may be explained by their use of a smaller hole-size factor. The time fraction covered by the events reveals the importance of organized structures. A large flux fraction of more than 50% is achieved in generally less than 10% of the averaging period, which means that large parts of the down-gradient transport take place within a few minutes. The buoyancy-driven turbulence under unstable conditions seemingly leads to less organized structures, and the influence of these events is less important. Under stable conditions, when mechanically-driven turbulence is apparent, more organized structures are generated, contributing more to the down-gradient transport.

4 Conclusions

We have conducted a quadrant analysis of more than 12 years of eddy-covariance data sampled at 39 m above street level in an urban environment in Basel, Switzerland to assess the characteristics of turbulent exchange, namely its dependence on atmospheric stability, scalar dissimilarity, ejection–sweep interaction, and the role of organized structures. The large dataset enabled the investigation of stable conditions, which are usually rare in cities.

In a first step, we analyzed the general characteristics of the vertical exchange of momentum, heat, CO_2 and H_2O fluxes as a function of atmospheric stability. Fluxes

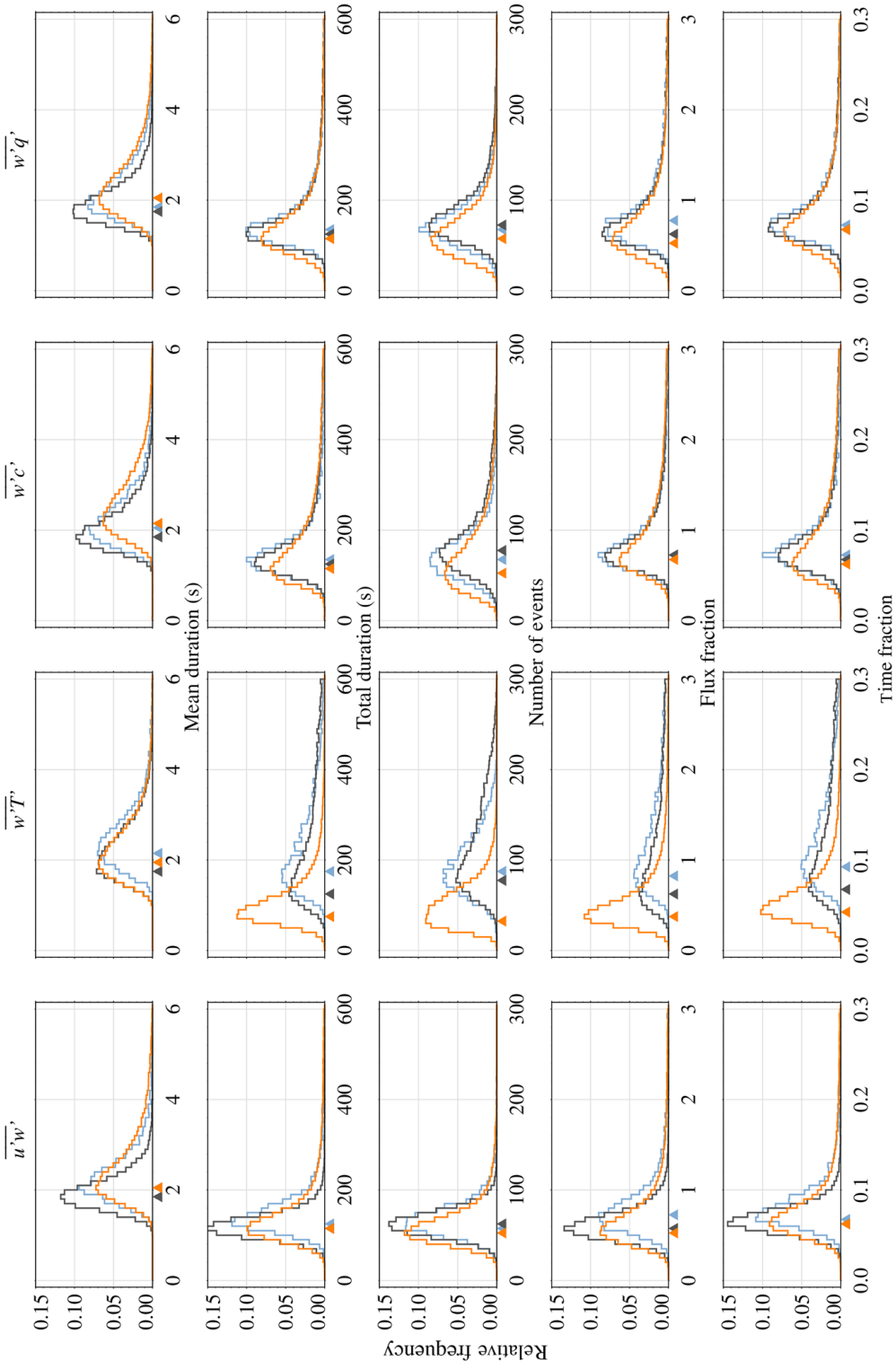

Fig. 9 Statistics of detected events for different stability classes. Triangles mark the mode of each histogram. Statistics refer to an averaging period of 30 min

derived from the eddy-covariance method show the typical behaviour of momentum and heat exchange as proposed in Monin–Obukhov similarity theory, and reported in recent studies. Both CO_2 and H_2O fluxes are heavily modulated by a change in the stability conditions, with unstable cases characterized by buoyancy-driven turbulence, while stable conditions are more dominated by mechanical turbulence. However, for H_2O fluxes, only a weak dependence on atmospheric stability is observed during stable conditions, whereas the net CO_2 flux shows no dependence on atmospheric stability throughout the entire stability range, indicating that CO_2 or H_2O fluxes are weakly controlled by the transporting mechanism, and more influenced by the individual source/sink configuration of each scalar.

The comparison of the transfer efficiency to the fitted functions proposed by Wood et al. (2010) (heterogeneous, urban) and De Bruin et al. (1993) (uniform, natural) confirms that the behaviour of momentum and sensible heat fluxes can also be explained as a function of atmospheric stability in the urban environment. However, passive scalars, which are assumed to be transported similarly to sensible heat, do not follow the proposed functions. In contrast to the transfer efficiency of H_2O, which is constant over all stability classes, the transfer efficiency of CO_2 is reduced in the unstable range as a possible result of photosynthesis. While the model is able to approximate the absolute value of the transfer efficiencies in the stable range, the direction (sign) of the CO_2 and H_2O fluxes cannot be predicted, because it depends on the source/sink configuration within the source area rather than on atmospheric stability. This being the case, scalar similarity between passive scalars is partially true, but the sensible heat flux clearly behaves differently and should be considered separately. Therefore, the congruence of the results for H_2O and CO_2 is largely controlled by the individual source/sink distribution and may change from site to site.

The important role of the heterogeneous source regime of the passive scalars is not only apparent from the missing stability dependence of the net flux density but also from the relationship between atmospheric stability and the quadrant statistics. For momentum and heat exchange, we find larger structures to be more important under stable conditions and towards unstable cases, with the relevant scales becoming clearly smaller. This tendency is less distinct for H_2O and not observable for CO_2.

As a general tendency, ejections are more important under unstable conditions as a direct result of the buoyancy-driven turbulence. Under near-neutral and stable conditions, sweeps are of equal importance or even dominate the exchange. When ejections dominate the overall exchange, sweeps are usually more important at smaller scales, with ejections contributing at larger scales to the net flux (large up, small down); the same is true for sweep-dominated regimes (small up, large down). Because the dominance of sweeps is most apparent for passive scalars, we assume the mixing conditions in the urban boundary layer to play an important role. Especially under near-neutral and stable conditions when sources of CO_2 and H_2O are less active, we suppose that the overlaying air (advected from the rural surroundings, with lower concentration) maintains an ambient gradient. As such, down-gradient transport by sweeps is enhanced.

Quadrant statistics enable us to identify those scales important for the turbulent exchange, and thus for large parts of the net flux within short periods. While for small hole sizes both down-gradient and counter-gradient motions transport large quantities of each property upwards and downwards, the transport efficiency is maximum for hole sizes $H = 10$–20. Since vertical exchange is almost solely characterized by ejections and sweeps at these scales, we adapted an event-detection algorithm to prove the suggested importance of such structures in the turbulent (urban) boundary layer. This method mostly leads to the detection of 50–100 events per averaging interval, with an average length of 1–4 s. While the results are similar for all variables, organized structures are least important for the

exchange of sensible heat under unstable conditions. As a general tendency, such structures are responsible for around 50–80% of the net flux density within usually less than 10% of the averaging period.

Current results concerning the turbulent exchange and its micrometeorological facets are still sparse compared with those in natural environments (e.g. forest sites). Since similarity between natural canopies and the urban "landscape" is mostly assumed, but not widely verified, and given the immense spatial and temporal heterogeneity of urban areas, further long-term time series are potentially needed to cover the entire range of relevant occurrences (e.g. stability classes). Hence, it would be worthwhile to have more results from urban long-term eddy-covariance time series as these would add valuable information to the current knowledge base.

Acknowledgements This research is funded from the project "Urban Climate Study of Bucharest" (IZERZ0_142160) made possible by the Romanian–Swiss Research Program. Special thanks go to E. Parlow and C. Feigenwinter from the MCR–Lab for supporting this research. The data used are listed in the references or available from the MCR–Lab on request (roland.vogt@unibas.ch).

References

Arnfield AJ (2003) Two decades of urban climate research: a review of turbulence, exchanges of energy and water, and the urban heat island. Int J Climatol 23:1–26

Barthlott C, Drobinski P, Fesquet C, Dubos T, Pietras C (2007) Long-term study of coherent structures in the atmospheric surface layer. Boundary-Layer Meteorol 125:1–24

Boppe RS, Neu WL, Shuai H (1999) Large-scale motions in the marine atmospheric aurface layer. Boundary-Layer Meteorol 92:165–183

Christen A, van Gorsel E, Vogt R (2007) Coherent structures in urban roughness sublayer turbulence. Int J Climatol 27:1955–1968

De Bruin HAR, Kohsiek W, Van Den Hurk BJJM (1993) A verification of some methods to determine the fluxes of momentum, sensible heat, and water vapour using standard deviation and structure parameter of scalar meteorological quantities. Boundary-Layer Meteorol 63:231–257

Dupont S, Patton EG (2012) Momentum and scalar transport within a vegetation canopy following atmospheric stability and seasonal canopy changes: the CHATS experiment. Atmos Chem Phys 12:5913–5935

Etling D, Brown RA (1993) Roll vortices in the planetary boundary layer: a review. Boundary-Layer Meteorol 65:215–248

Feigenwinter C, Vogt R, Parlow E (1999) Vertical structure of selected turbulence characteristics above an urban canopy. Theor Appl Climatol 62:51–63

Foken T (2017) Micrometeorology. Springer-Verlag, Berlin Heidelberg

Francone C, Katul GG, Cassardo C, Richiardone R (2012) Turbulent transport efficiency and the ejection-sweep motion for momentum and heat on sloping terrain covered with vineyards. Agric For Meteorol 162–163:98–107

Grimmond CSB, Oke TR (1999) Aerodynamic properties of urban areas derived from analysis of surface form. J Appl Meteorol 38:1262–1292

Hommema SE, Adrian RJ (2003) Packet structure of surface eddies in the atmospheric boundary layer. Boundary-Layer Meteorol 106:147–170

Hutchins N, Marusic I (2007) Evidence of very long meandering features in the logarithmic region of turbulent boundary layers. J Fluid Mech 579:1–28

Kaimal JC, Gaynor JE (1991) Another look at sonic thermometry. Boundary-Layer Meteorol 56:401–410

Katul G, Hsieh C-I, Kuhn G, Ellsworth D, Nie D (1997a) Turbulent eddy motion at the forest-atmosphere interface. J Geophys Res Atmos 102:13409–13421

Katul G, Kuhn G, Schieldge J, Hsieh C-I (1997b) The ejection-sweep character of scalar fluxes in the unstable surface layer. Boundary-Layer Meteorol 83:1–26

Kurppa M, Nordbo A, Haapanala S, Järvi L (2015) Effect of seasonal variability and land use on particle number and CO_2 exchange in Helsinki, Finland. Urban Clim 13:94–109

Lee X, Yu Q, Sun X, Liu J, Min Q, Liu Y, Zhang X (2004) Micrometeorological fluxes under the influence of regional and local advection: a revisit. Agric For Meteorol 122:111–124

Li D, Bou-Zeid E (2011) Coherent structures and the dissimilarity of turbulent transport of momentum and scalars in the unstable atmospheric surface layer. Boundary-Layer Meteorol 140:243–262

Lietzke B, Vogt R (2013) Variability of CO_2 concentrations and fluxes in and above an urban street canyon. Atmos Environ 74:60–72

Lu SS, Willmarth WW (1973) Measurements of the structure of the Reynolds stress in a turbulent boundary layer. J Fluid Mech 60:481

Luchik TS, Tiederman WG (1987) Timescale and structure of ejections and bursts in turbulent channel flows. J Fluid Mech 174:529

Maitani T, Ohtaki E (1987) Turbulent transport processes of momentum and sensible heat in the surface layer over a paddy field. Boundary-Layer Meteorol 40:283–293

Mason PJ, Sykes RI (1980) A two-dimensional numerical study of horizontal roll vortices in the neutral atmospheric boundary layer. Q J R Meteorol Soc 106:351–366

Mohr M, Schindler D (2016) Coherent momentum exchange above and within a scots pine forest. Atmosphere 7:61

Moriwaki R, Kanda M (2005) Local and global similarity in turbulent transfer of heat, water vapour, and CO_2 in the dynamic convective sublayer over a suburban area. Boundary-Layer Meteorol 120:163–179

Nordbo A, Järvi L, Haapanala S, Moilanen J, Vesala T (2012) Intra-city variation in urban morphology and turbulence structure in Helsinki, Finland. Boundary-Layer Meteorol 146:469–496

Raupach MR, Coppin PA, Legg BJ (1986) Experiments on scalar dispersion within a model plant canopy part I: the turbulence structure. Boundary-Layer Meteorol 35:21–52

Roth M (2000) Review of atmospheric turbulence over cities. Q J R Meteorol Soc 126:941–990

Roth M, Oke TR (1995) Relative efficiencies of turbulent transfer of heat, mass, and momentum over a patchy urban surface. J Atmos Sci 52:1863–1874

Schmutz M, Vogt R, Feigenwinter C, Parlow E (2016) Ten years of eddy covariance measurements in Basel, Switzerland: seasonal and interannual variabilities of urban CO_2 mole fraction and flux. J Geophys Res Atmos 121:8649–8667

Sempreviva AM, Højstrup J (1998) Transport of temperature and humidity variance and covariance in the marine surface layer. Boundary-Layer Meteorol 87:233–253

Shaw RH, Tavangar J, Ward DP (1983) Structure of the Reynolds stress in a canopy layer. J Climate Appl Meteor 22:1922–1931

Steiner AL, Pressley SN, Botros A, Jones E, Chung SH, Edburg SL (2011) Analysis of coherent structures and atmosphere-canopy coupling strength during the CABINEX field campaign. Atmos Chem Phys 11:11921–11936

Thomas C, Foken T (2007) Flux contribution of coherent structures and its implications for the exchange of energy and matter in a tall spruce canopy. Boundary-Layer Meteorol 123:317–337

Thomas C, Serafimovich A, Siebicke L, Gerken T, Foken T (2017) Coherent structures and flux coupling. In: Energy and matter fluxes of a spruce forest ecosystem. Springer, Berlin, pp 113–135

Tyagi B, Satyanarayana ANV (2014) Coherent structures contributions in fluxes of momentum and heat at two tropical sites during pre-monsoon thunderstorm season. Int J Climatol 34:1575–1584

Wang L, Li D, Gao Z, Sun T, Guo X, Bou-Zeid E (2013) Turbulent transport of momentum and scalars above an urban canopy. Boundary-Layer Meteorol 150:485–511

Webb EK, Pearman GI, Leuning R (1980) Correction of flux measurements for density effects due to heat and water vapour transfer. Q J R Meteorol Soc 106:85–100

Williams CA, Scanlon TM, Albertson JD (2006) Influence of surface heterogeneity on scalar dissimilarity in the roughness sublayer. Boundary-Layer Meteorol 122:149–165

Wood CR, Lacser A, Barlow JF, Padhra A, Belcher SE, Nemitz E, Helfter C, Famulari D, Grimmond CSB (2010) Turbulent flow at 190 m height above london during 2006–2008: a climatology and the applicability of similarity theory. Boundary-Layer Meteorol 137:77–96

Wyngaard JC, Moeng C-H (1992) Parameterizing turbulent diffusion through the joint probability density. Boundary-Layer Meteorol 60:1–13

CHAPTER 4

Fluxes of Carbon Dioxide

4.1 Urban Carbon Balance

Carbon (C) is one of the most abundant elements in our universe and bound into carbon-based molecules, it provides the main constituent of biological or mineral compounds. The global cycle of C embraces a sequence of essential biogeochemical processes, which - together with cycling of nitrogen and water - are of major importance for diverse and sustainable life on Earth. In 2013, 829 Pg C ($\pm$10) were attributed to the atmospheric pool with a postulated annual increase around 4 Pg C y^{-1} [Ciais et al., 2014]. While the pre-industrial atmospheric pool is estimated to be 589 Pg C, the accumulated anthropogenic carbon over the industrial period (1750-2011) sums up to 240 Pg C, which means, that the atmosphere gained around 29 % of carbon mostly due to human influence over the last 265 years. The most important compound in the atmospheric part of the C cycle is carbon dioxide (CO_2), despite its small mole fraction in the order of magnitude of 400 ppm. Besides being the main reservoir of C in the atmosphere, CO_2 is also the second most abundant greenhouse gas after water vapor. Together with other greenhouse gases, it retains habitable conditions on Earth by reducing the planet's radiative loss of energy in the longwave spectrum (>4 µm).

Exchange between the atmosphere and terrestrial pools takes place by ocean-atmosphere gas exchange, freshwater outgassing, burning of fossil fuels, photosynthesis, respiration, volcanism and rock weathering. Despite the fact, that e.g. ocean-atmosphere gas exchange ($\downarrow$80/$\uparrow$78.4/$\updownarrow$1.6 Pg C y^{-1}) or photosynthesis / respiration ($\downarrow$123/$\uparrow$118.7/$\updownarrow$4.3 Pg C y^{-1}) are responsible for large fluxes of C, their net fluxes are comparatively small and the major net flux into the atmosphere is due to burning of fossil fuels ($\Uparrow$7.8 Pg C y^{-1}). Out of all global CO_2 emissions, around 75 % originate from urban areas [Seto et al., 2014], which on the other hand cover only a minor fraction of less than 0.5 % of the Earth's surface [Schneider et al., 2009]. Today, urban areas are home to approximately 52–54 % of the human population [The World Bank, 2017; Food and Agriculture Organization of the United Nations, 2017], and with ongoing urbanization, this number is increasing permanently. This emphasizes the importance of urban areas within the global C cycle and its direct connections to the production of food, textiles or fuel [Churkina, 2016]. In spite of that, many approaches to global modeling of the C cycle do not

take into account cities as hot spots of C exchange between atmosphere and terrestrial pools, because (i) models are not yet able to resolve the small fractional cover of urban areas on a global scale or (ii) too little information about the complex pathways of C through the urban metabolism are available in order to base global models on. If horizontal transportation of C into and out of the city is accounted to the urban C balance too [e.g. Christen, 2014], the urban footprint hypothetically extends far beyond the city limits. The consideration of this indirect influence on the C cycle additionally hinders the determination of the overall impact of urban areas.

Because measurements of CO_2 in urban areas take place at some height above ground in order to sample a representative area, the urban C balance is addressed as a volume budget [Feigenwinter et al., 2012]. The main transformation processes between the surface and the atmosphere can be balanced as follows

$$F_{C(0)} = F_{C(z_m)} + F_{C(S)} + F_{C(A)} = F_{C(Cb)} + F_{C(R)} + F_{C(P)}, \tag{4.1}$$

where A stands for advection, S for storage, Cb for combustion, R for respiration and P for photosynthesis and F is usually in units of µmol m^{-2} s^{-1}. As described in the following section, combustion and respiration processes can be further separated into different sub processes.

4.1.1 Anthropogenic Activity

Cities are most notably hot spots of human activity and the city location, size and structure is directly coupled to the needs of the inhabitants. In an analogy to the cells of living organisms, the set of life sustaining flows of energy and materials through the city as well as the conversion of materials into goods or different forms of energy, the whole system is considered as an "urban metabolism" [Wolman, 1965]. While urban areas usually retain a distinct urban climate modulated by time, weather, city form, city size, city location as well as the urban metabolism itself, they also adapt the cycle of C in a distinct manner.

4.1.1.1 Combustion Processes $F_{C(Cb)}$

The major source of CO_2 in cities originates from combustion of fossil fuels such as oil and natural gas for heating as well as gasoline and diesel used by motorized vehicles. Both sources, traffic and heating, show a high variability in their spatial and temporal emission patterns. Even though emissions from combustion released through chimneys can be seen as point sources, the wide distribution of buildings across the city makes them behave more like a plane source. In contrast, emissions from traffic are concentrated on streets, which are typical line sources and often only cover minor fractions of the urban area. In Fig. 4.1 the main panel shows an isopleth diagram of diurnal and monthly traffic volume. As traffic is directly linked to the working activity of people, a typical dual peaked pattern with morning and evening rush hours as well as a small depression at noon is apparent. There is no clear seasonal cycle but a depression seems to be

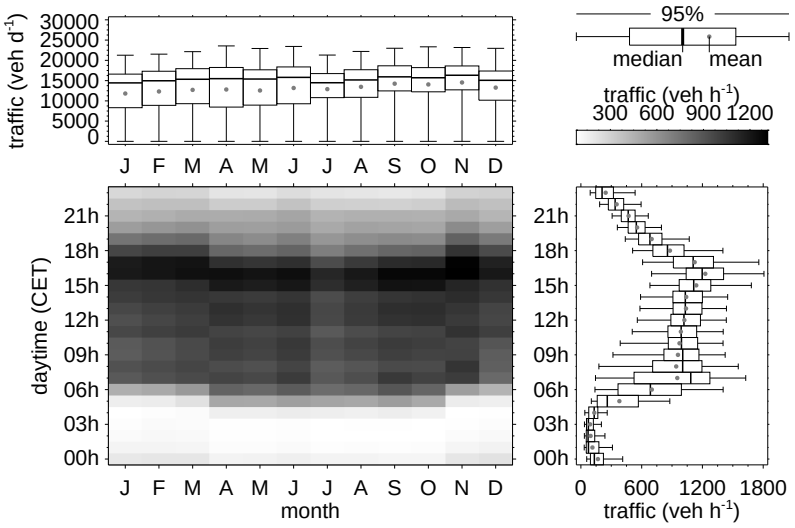

Figure 4.1 Isopleth diagram of traffic volume derived from traffic counts near BKLI. The top and right panel show average daily traffic volume per month and average amount of vehicles per hour.

present in July due to public summer holidays. Because of the shift to daylight-saving time in spring and back to standard time in fall, the diurnal dynamic of traffic is shifted by one hour CET. Figure 4.2 shows the daily and annual dynamic of air temperature. Converted into heating degree days (HDD) [1] air temperature can be taken as an indicator for heating activity, which is obviously largest in winter and zero during summer months. Diurnal dynamics of heating activity can hardly be related to environmental parameters as most heating system follow time-controlled programs. Usually heating systems are active in the morning and in the evening, which is when most people are at their homes. Some cities like Basel also have district heating systems, which leads to a concentration of CO_2 emissions from heating related combustion to few single point sources. Additionally, combustion processes from industrial areas need to be considered individually.

4.1.1.2 Human Respiration $F_{C(R_H)}$

Exhalation of CO_2 is part of the human metabolism and an average adult person respires around 250 g C d^{-1}. With a population density of 7380 pop km^{-2} in the city of Basel this results in an average CO_2 flux of roughly 1.8 µmol m^2 s^{-1}, which adds significantly to the urban CO_2 balance. However, this number might not apply directly in practice, because during the day many people commute into the city to their working places and vice versa. Furthermore, the population is not evenly distributed over the city with time and especially during day people concentrate in the busy parts of the town, whereas residential areas are less populated. This might lead to significantly higher or lower fluxes of CO_2 due to human respiration in the corresponding areas. In practice, the quantification of CO_2 emissions by human respiration is difficult to achieve by

[1] A HDD is a measure for heating activity which sets the strength of heating in relation to the indoor-outdoor temperature difference if the daily average temperature drops below a threshold value: HDD $= 20 - T_{daily} < 12$

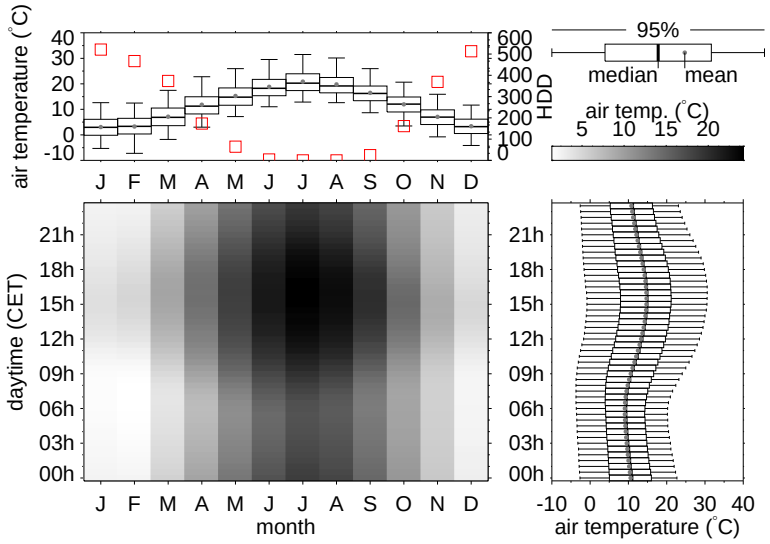

Figure 4.2 Isopleth diagram of air temperature at BKLI. Red squares in the top panel indicate the monthly sum of HDD.

direct flux measurements as many people stay indoors most of the time and the signal cannot be easily separated from other major sources of CO_2 like combustion.

4.1.1.3 Waste Decomposition $F_{C(R_w)}$

In many cities, the large amount of solid and liquid waste produced by the urban population is deposited in landfills. Decomposition processes in landfills lead to degassing of methane, volatile organic compounds, CO_2 and other gases. Dependent on the vicinity to the city this might add directly to the CO_2 exchange within the city or should be attributed to the general C balance as part of the larger urban footprint.

4.1.2 Ecosystem Activity

Urban areas are highly complex systems constructed by humans. In a first glance, they occur as an agglomeration of artificial structures like buildings, streets or industrial facilities and may appear to be hostile to life apart from human being, but seen from other perspectives they reveal an incredibly diverse mixture of habitats for many living entities. The manifold biotopes are not only an imitation of the natural counterpart, but they are also a creation of a completely new coexistence of flora and fauna, which deserves the term urban ecosystem. Besides the artificial modulation of the C cycle, natural processes are still influencing significantly the C balance, dependent on the presence and activity of plants and animals, the buildup density as well as the geographical latitude [Churkina, 2016].

4.1.2.1 Photosynthesis $F_{C(P)}$

Gross primary production (GPP) is the total amount of C uptake by photosynthetic activity within the ecosystem, e.g. by vegetation. Photosynthesis is the only true sink for CO_2 in cities, as other

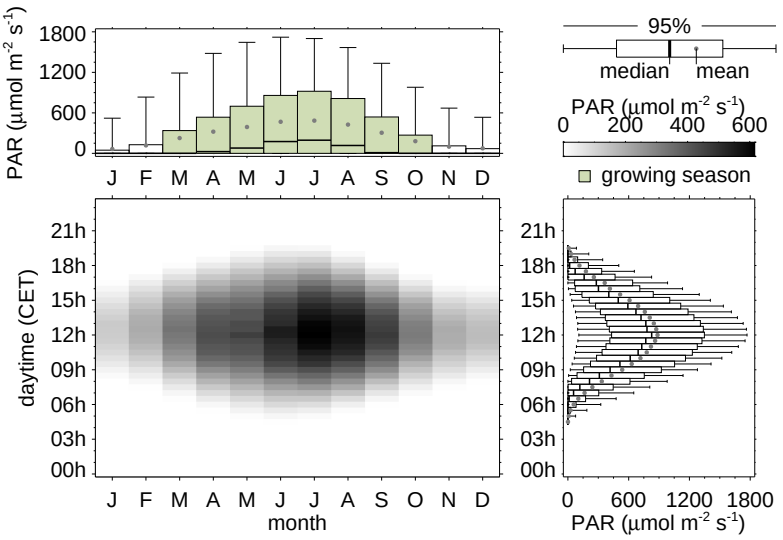

Figure 4.3 Isopleth diagram of modeled photosynthetically active radiation (PAR) at BKLI [Alados and Alados-Arboledas, 1999]. Green colored bars indicate growing season as defined in section 4.1.2.1.

processes like sequestration of CO_2 through the pores of concrete act at a negligibly small rate. The primary controlling factor of photosynthetic activity is the availability of photosynthetically active radiation (PAR) between 400–700 nm as depicted in Fig. 4.3. As PAR is nearly linearly correlated to the global radiation, it shows the same diurnal and seasonal variability, with highest values during the day and in summer. Despite the presence of light, vegetation needs certain environmental conditions in order to be able to be active. The growing season is defined as the period between the first occurrence of six consecutive days with a daily mean temperature >5 °C and the first occurrence of six consecutive with a daily mean temperature <5 °C after July (green bars in Fig. 4.3). Furthermore, air temperature, water availability or air pollution might influence the rate of photosynthesis and thus the effective photosynthetic uptake of CO_2. In most cities, photosynthesis is not able to offset the strong emissions by combustion but might have a small compensating effect [Lietzke and Vogt, 2013; Schmutz et al., 2016]. This, however, highly depends on the amount of vegetation and the climatological conditions.

Due to the small order of magnitude of $F_{C(P)}$, direct quantification of the CO_2 uptake by vegetation is difficult without chamber measurements. Usually the influence of CO_2 sources and sinks is analyzed by looking at the net flux density of CO_2 from different wind sectors at a specific time of the day. Within the heterogeneous urban landscape it is mostly impossible, to separate the data into meaningful bins, without drastically decreasing the amount of data points remaining for statistical analysis. Because the dynamics of the source activity of CO_2 like e.g. traffic is influencing the net flux density much more than the CO_2 uptake by plants, it is mostly impossible to interpret dips or peaks of F_C by the means of source/sink counter play. In such situations the correlation coefficient or transfer efficiency $R_{w'c'}$ supplies additional information. Due to the fact, that ground sources produce an upward flux and ground sinks a downward flux

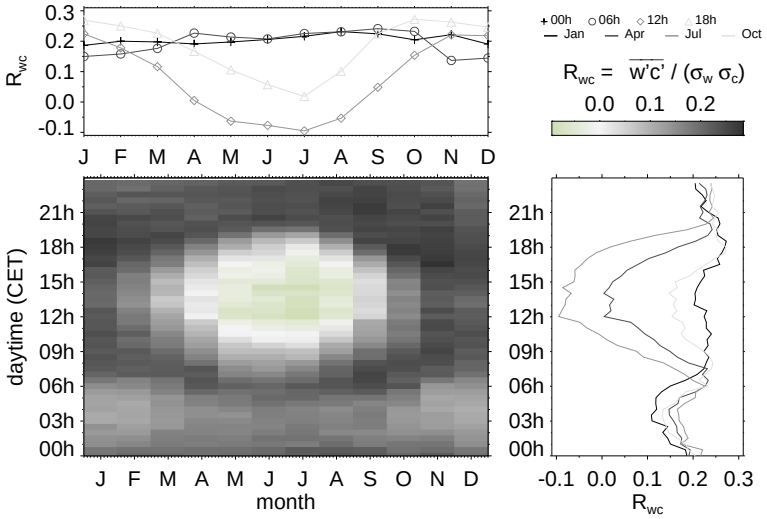

Figure 4.4 Isopleth diagram of the correlation coefficient (transfer efficiency) R_{wc} between vertical wind and CO_2 for BKLI.

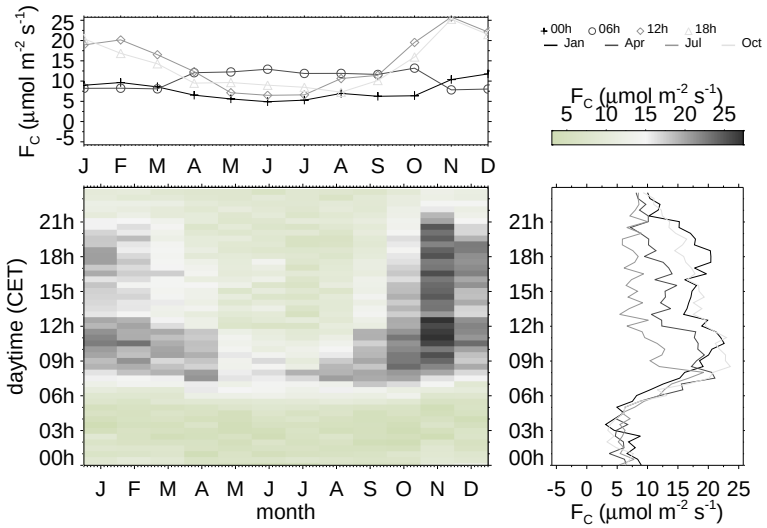

Figure 4.5 Isopleth diagram of CO_2 net flux density F_C for BKLI

of CO_2, the correlation between fluctuations of vertical wind and CO_2 changes, if the interplay of sources and sinks changes too. In Fig. 4.4 an isopleth diagram of $R_{w'c'}$ is depicted for BKLI and Fig. 4.5 shows the corresponding isopleth diagram for F_C. In contrast to the dual peaked diurnal course of F_C, the transfer efficiency shows a symmetric shape during daytime with a clear minimum in the early afternoon. While F_C is highly sensitive to the change in wind direction from east to west over the course of the day (comp. sec. 4.2.1.2), the correlation coefficient only responds to the change in solar input (comp. Fig. 4.3) over the course of a day and a year, respectively. During wintertime the diurnal course of $R_{w'c'}$ almost completely vanishes, due to the absence of plant uptake.

In Fig. 4.6 $R_{w'c'}$ is additionally depicted as a function of wind direction. Next to the temporal differentiation of the photosynthetic activity this depiction also allows to make out sectors

where the transfer efficiency is altered by a change in the source/sink scheme. The transfer efficiency is generally smaller during daytime in summer, which points at a generally less organized flux of CO_2 due to weaker sources and plant uptake within the source area. The northeastern sectors even show a negative transfer efficiency, which is an indicator, that the downward transport is more organized than the upward transport. This gives clear evidence, that photosynthesis is significantly influencing the turbulent transport of CO_2. However, on average there is no uptake from these sectors, because the less organized upward transport is still overcompensating the organized downward component. Summarizing, the transfer efficiency is a measure to qualitatively detect organized counter gradient transport like introduced by photosynthetic activity in urban areas, however, it does not allow to directly determine the quantitative uptake effect.

4.1.2.2 Plant and Soil Respiration $F_{C(R_{PS})}$

Respiration processes, which can be separated into plant and soil respiration, lead to a release of CO_2. These processes are especially relevant during nighttime, when photosynthesis and many other sources have their lowest activity. Like photosynthesis plant and soil respiration also depends on the amount of vegetation present.

4.1.2.3 Vertical and Horizontal Advection

Due to the complexity and heterogeneity of the source/sink distribution within the urban area, it is likely that air masses of different CO_2 concentration are transported horizontally. This leads to a change in ρ_C within the air volume at the measurement site. Because advected air can have either higher or lower concentration of CO_2, horizontal advection might act as a source as well as a sink. It is frequently observed, that e.g. air of lower CO_2 concentration is advected from the rural surrounding, which might lower the concentration within the city due to mixing of air masses. Additionally there is also a non-turbulent vertical transport, denoted as vertical advection.

4.1.2.4 Storage $F_{C(S)}$

The net exchange between the surface and the atmosphere is normally characterized by vertical fluxes. In practice measurement in urban areas take place at considerable height above ground z_m and due to non-constant fluxes within the air volume up to z_m a storage term needs to be accounted for. The storage term, which is the change in concentration with time and with height, is added like

$$F_{C(0)} = \overline{w'C'}_{z_m} + \int_0^{z_m} \frac{\partial C}{\partial t} \partial z, \tag{4.2}$$

in order to achieve the flux at surface $F_{C(0)}$. However, to gain information about the vertical flux divergence, profile measurements of F_C would be necessary, which is rarely the case.

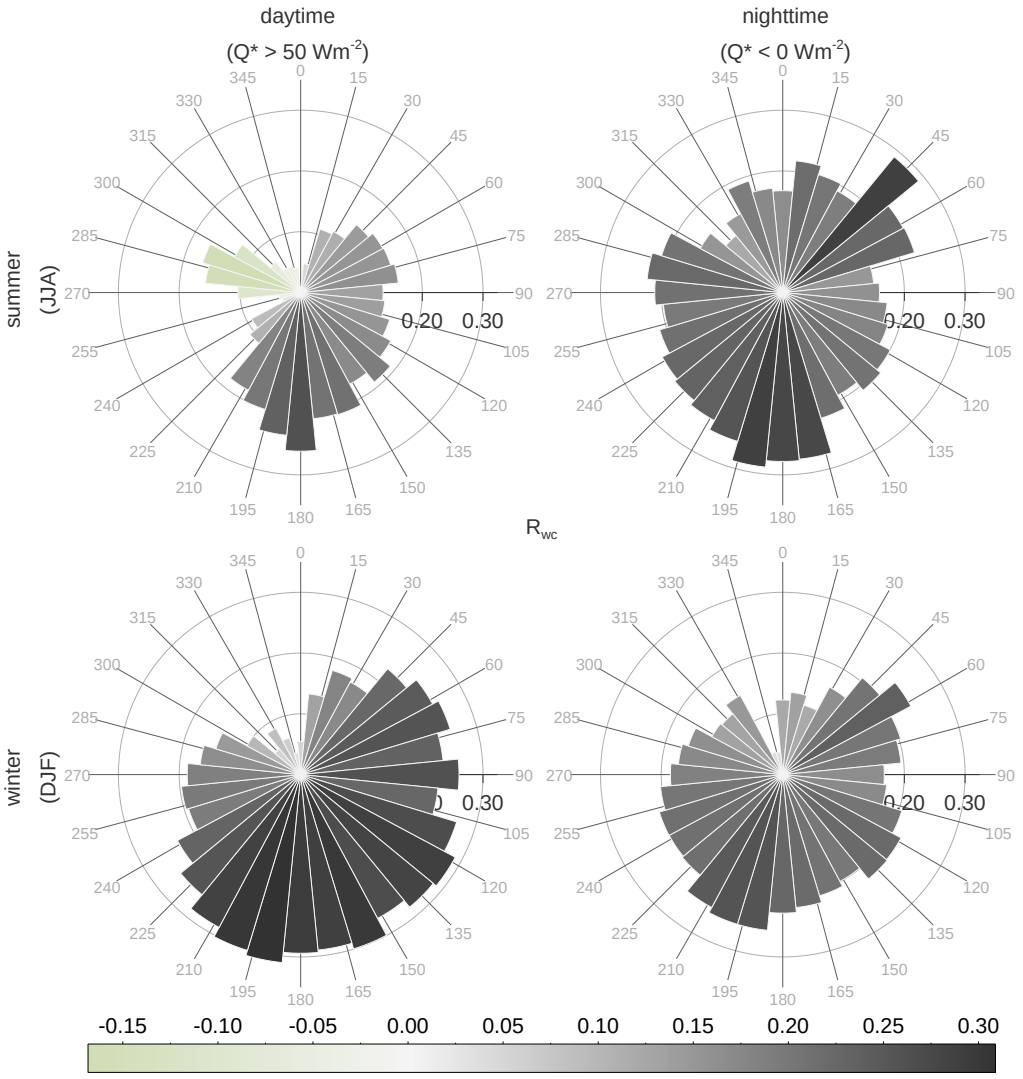

Figure 4.6. $R_{w'c'}$ at BKLI displayed per wind sector (32 bins) split by winter/summer and daytime/nighttime, respectively.

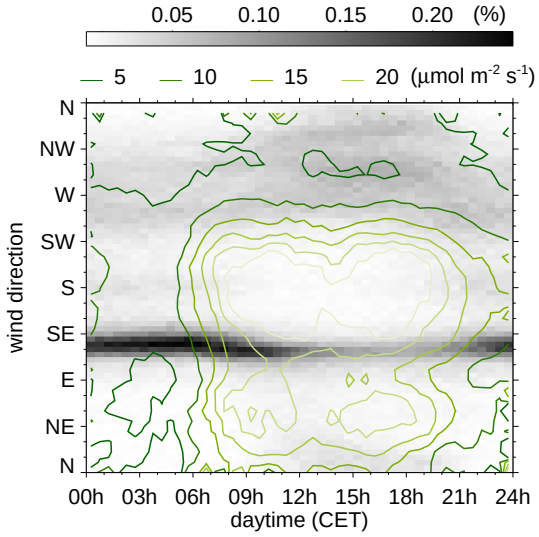

Figure 4.7 Histogram of the wind direction as a function of daytime at BKLI. Contour lines indicate strength of F_C.

4.2 Footprint Estimations of Urban CO_2

Within the research field of micro-meteorology the "footprint" of a near-surface measurement is defined as the ground area that is sensed by the observation [comp. Schuepp et al., 1990; Leclerc and Thurtell, 1990; Leclerc and Foken, 2014]. For some observations like e.g. measurements of solar radiation the source area is a function of static geometric parameters of the sensor (sensor height, field of view, surface morphology). In contrast, turbulent fluxes derived by the EC method are the integrative result of ongoing turbulent exchange processes within the averaging interval. Dependent on wind direction, wind speed, atmospheric stability and surface roughness properties, the footprint of such flux measurements represents an upwind source area of varying shape and extent which encompasses all relevant sources and sinks. While the extend of the footprint is not crucial over surfaces where the requirement of horizontal homogeneity is nearly fulfilled, measurements carried out over heterogeneous (urban) surfaces are very sensitive to the size of the footprint and especially to the source/sink composition within the area covered. For this reason footprint estimations are an important tool to gain knowledge about the "effective" investigation area of an observation and to evaluate the significance and importance of the derived results.

Estimations of the footprint can be achieved by modeling approaches, either by numerical [e.g. Kljun et al., 2015] or analytical [e.g. Hsieh et al., 2000; Kormann and Meixner, 2001] implementations. Analytical approaches like the Kormann and Meixner [2001] model used in this thesis are relatively easy to implement and only need little computational power. The Kormann and Meixner [2001] model takes into consideration average longitudinal wind speed, variance of lateral wind speed, wind direction, atmospheric stability as well as the effective measurement height and the roughness length. The model outputs a per-pixel (dependent on the defined spatial resolution) based relative flux-contribution, which is then usually converted

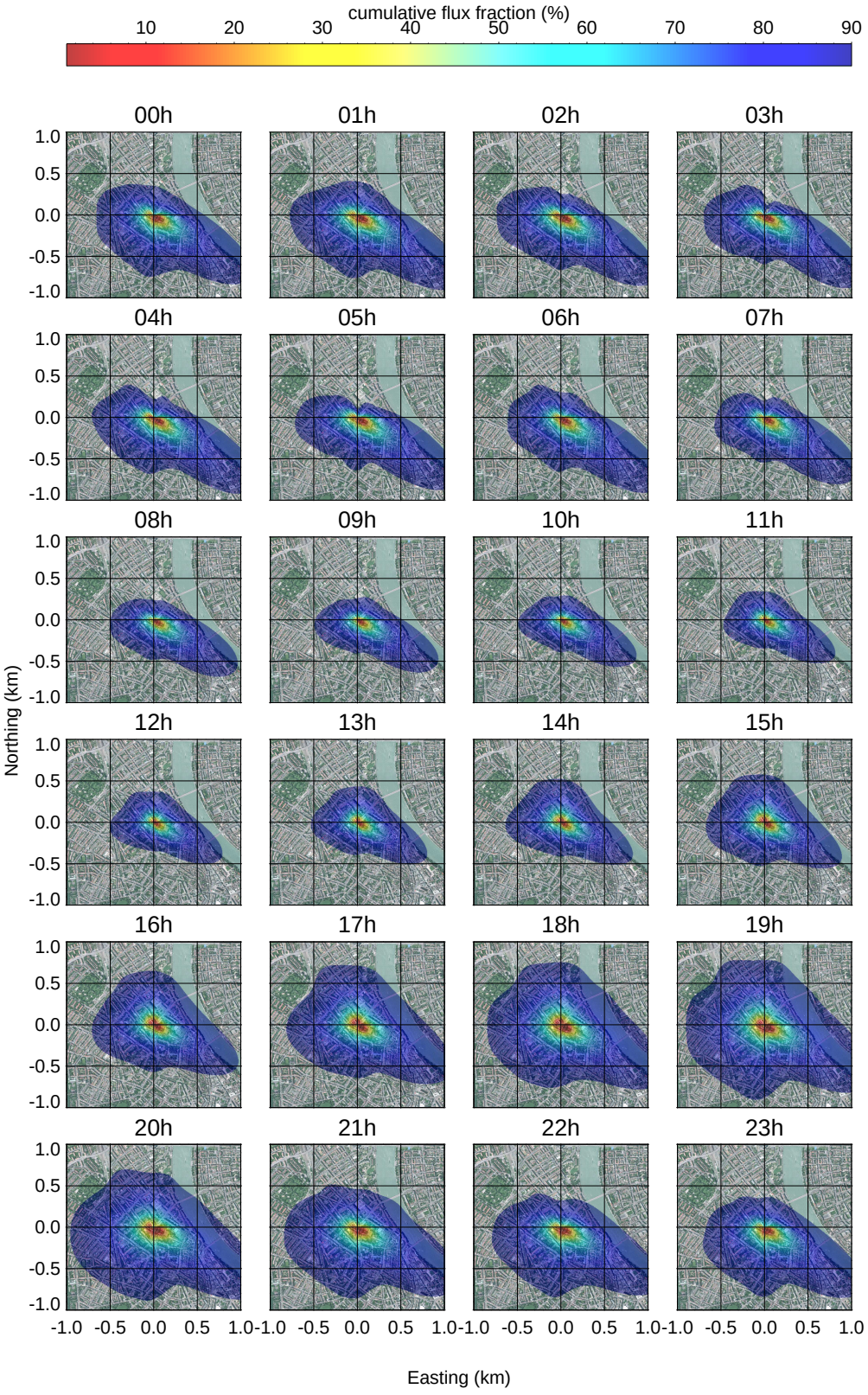

Figure 4.8. Average hourly footprint for CO_2 at BKLI calculated with the Kormann & Meixner model.

to a cumulative source area to achieve relative flux-contributions by area. While the model is valid for all atmospheric stability conditions and takes into account crosswind-dispersion, the resulting footprint is not an accurate representation of the real footprint over a very heterogeneous surface. Firstly, the usage of average information on wind speed and wind direction already introduces some uncertainty because the longitudinal and lateral variability might not be represented well enough. Secondly, it is difficult to feed the model with accurate information about the surface roughness for an urban environment with a spatially heterogeneous composition of three-dimensional structures. Thirdly, scalar fluxes rarely have plane source areas but rather line (e.g. streets, rivers) or point (e.g. chimneys, trees) sources and sinks are controlling the fluxes, which is why the per-pixel flux contribution of the model output is barely accurate. Thus, the urban footprint should more be considered as a source area estimation which helps to understand the extend and the variability of the area which is influencing the calculated flux. The complexity of the investigation area needs to be incorporated and interpreted individually. As an example, Fig. 4.8 presents average hourly footprint estimations for BKLI. While the general shape is similar throughout the day, the extend of the source area varies largely. Mostly due to the influence of atmospheric stability, the footprint shrinks to its minimal size in the afternoon and reaches its maximum extend during times of stable conditions in the evening.

4.2.1 Horizontal Averaging

4.2.1.1 Basic Concept

The size and the shape of the source area for a given measurement height is primarily determined by the atmospheric stability as well as the longitudinal wind speed and its lateral variance. The extend of the footprint certainly influences the strength of the measured fluxes. On average, the variation in size does only change the weighting of individual sources and sinks in upwind direction, but it does not necessarily alter the source/sink composition. In contrast, the wind direction changes the orientation of the upwind source area which often leads to a fundamental change in the footprint characteristics if the sources and sinks are distributed irregularly around the measurement station. Due to the immense complexity of urban areas, this is probably the case for many urban measurement sites. As a result, the prevailing wind regime determines by large parts, which sources and sinks are actively contributing to the measured flux and which are not. Often alternating wind regimes like mountain-valley or land-sea wind systems cause an unequal representation of source/sink activity over the course of a day or even a year. Strong sources (e.g. streets for CO_2) might be excluded during times of high activity during the day, but incorporated by the footprint during times of low activity e.g. during the night, and vice versa. To illustrate this issue, Fig. 4.7 shows F_C as a function of wind direction and daytime as well as the relative frequency of each bin. Apparently, the diurnal

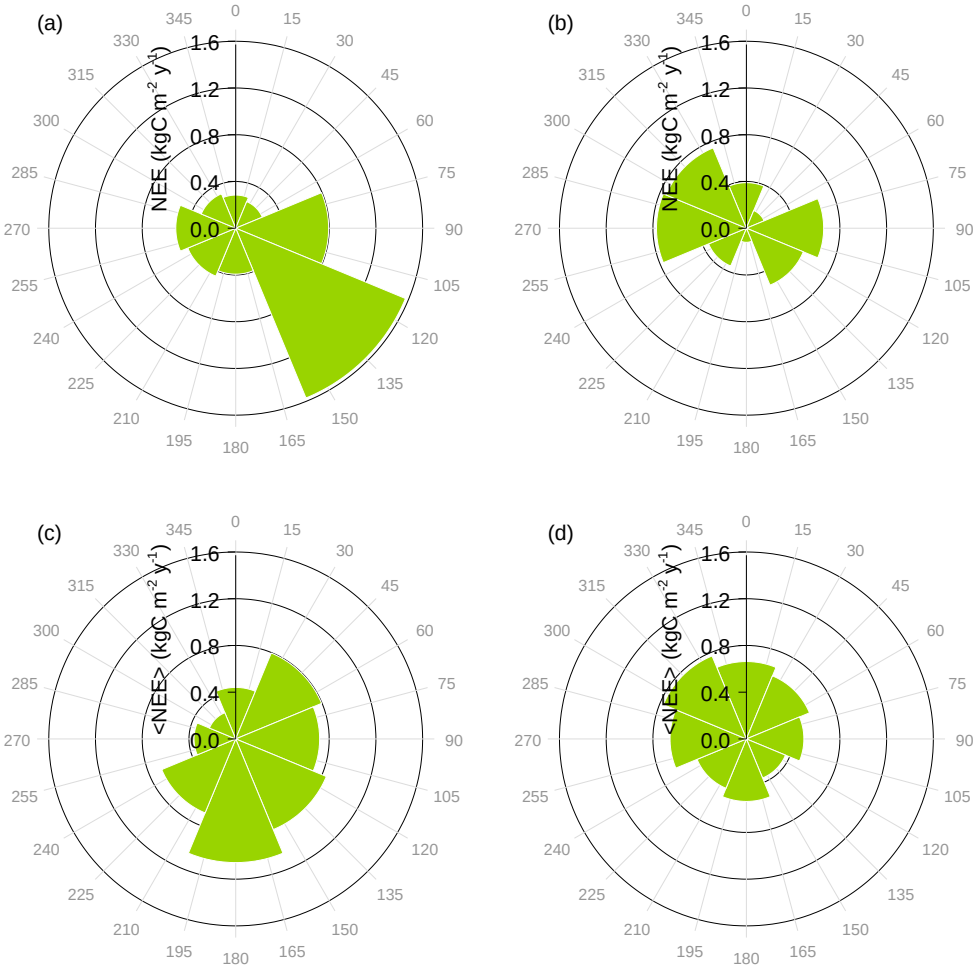

Figure 4.9. Average Sectorial net ecosystem exchange (NEE) and horizontally averaged net ecosystem exchange (<NEE>) for BKLI (a), (c) and BAES (b), (d).

course of F_C and the dynamics of the wind system do not coincide and the effectively measured flux does not lead to a complete picture. When calculating e.g. daily or monthly averages or total values like net ecosystem exchange (NEE), this circumstance is significantly influencing the results and can lead to an over- or underestimation of the effective flux. The measured or calculated values are representative for the single point in space, where the station is located, but might not be valid for a larger area around the measurement site, which is usually desired.

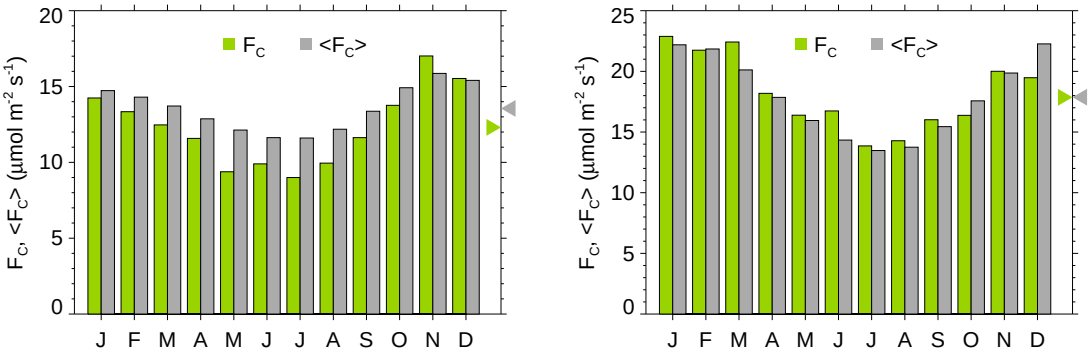

Figure 4.10. Average monthly F_C and $< F_C >$ for BKLI (left) and BAES (right). Marks on secondary y-axis indicate average fluxes.

To overcome this shortcoming, a horizontally averaged flux $< F_C >$ can be calculated. The refined method introduced in Schmutz et al. [2016] (sec. 5 - P2) simulates a situation where the wind is theoretically blowing from all direction with an equal frequency of occurrence. The resulting flux should therefore no longer be a function of wind direction but rather closely represents the expected turbulent exchange of the surrounding area. To be able to catch the heterogeneity of the surrounding, an adequate number of wind sectors are distinguished, e.g. eight for BKLI or BAES (comp. Fig. 4.9). Data from each wind sector are considered as an independent time series and a gap-filling algorithm (comp. sec. 2.1.2) is applied to each sector. Finally, all eight time series are arithmetically averaged which results in a horizontally averaged time series with equal influence of all wind sectors. It is important to mention, that the horizontally averaged fluxes should not be interpreted as time series of measurements due to the large amount of gap filled values. The $< F_C >$ values should only be taken as a base population to calculate average statistics, e.g. average diurnal courses or NEE. While horizontal averaging eliminates the influence of the unequal distribution of wind directions by large parts, there are still other factors like wind speed, atmospheric stability or surface roughness parameters which might differ between sectors and lead to some inequality in the sampled footprint scale.

4.2.1.2 Influence on CO_2 Balance Estimation in Basel

Basel is subject to a very distinct diurnal wind regime due to the Rhine Valley, which leads to a strong eastern component during the night into the morning and a northwest component during the day. The general synoptical situation adds an additional western component. The predominant east wind in the morning advects a strong CO_2 signal from emissions from the nearby Klingelbergstrasse whereas in the afternoon the west wind moves the source area to the western residential area with much lower CO_2 emissions. This leads to the situation, that the diurnal dynamic of the traffic is not caught completely by the measurements. The northern and southwestern sectors are clearly underrepresented and would probably lead to smaller average fluxes due to low activity of CO_2 sources. Figure 4.9 presents the average sectorial NEE for BKLI (left) and BAES (right) before horizontal averaging (top) and after (bottom). The sectorial distribution of NEE as derived from the measurements is largely superimposed by the wind rose and most of the CO_2 emissions are attributed to the southeastern and western sectors. In contrast, <NEE> is no longer a function of the wind regime and the differences between single sectors can be discussed in relation to the source/sink distribution. Thus, highest NEE can be expected from sectors 2-5 at BKLI due to the highly trafficked Klingelbergstrasse and at BAES from sectors 1, 2, 7 and 8 due to the high traffic activity on the Aeschenplatz to the northwest. The effect of horizontal averaging on monthly fluxes of CO_2 is demonstrated in Fig. 4.10 for both BKLI and BAES. At BKLI measured fluxes are underestimated for most months due to the rare occurrence of sectors 2 and 4 which are subject to high CO_2 emissions from the Klingelbergstrasse. The underestimation is largest in summertime with $< F_C >$ being up to 2.7 μmol m^2 s^{-1} larger than F_C. In contrast F_C is slightly overestimated in November and June due to a very strong east component in the wind system during these months. At BAES the frequent west winds lead to a slight overestimation of F_C due to the CO_2 emission from the Aeschenplatz. Only in October, December and February F_C is underestimated as a result of the east-wind dominance which more often moves the footprint to sectors of low CO_2 emissions. At BKLI $< F_C >$ takes an average value of 13.6 μmol m^2 s^{-1} and F_C of 12.3 μmol m^2 s^{-1}. Despite slight differences over the course of a year at BAES, both $< F_C >$ and F_C show an average value of 17.9 μmol m^2 s^{-1}. These results show that $< F_C >$ is a better representative of the ongoing CO_2 exchange processes within the surrounding area of the station. This not only enhances the representativeness of the derived statistics for the corresponding location, but it also improves the comparability between different sites. In Fig. 4.11 a correlation analysis between BKLI and BAES is shown for F_C and $< F_C >$ based on daily averages. Note, that the two relatively nearby stations do not necessarily have to show a high correlation, but due to the similar source/sink scheme (major sources are traffic and heating, [Lietzke et al., 2015]) they should be similar in the general dynamics of the CO_2 balance over the course of a day and a year, respectively. Between F_C at BKLI and BAES there is nearly no linear correlation with r^2 near zero. After applying

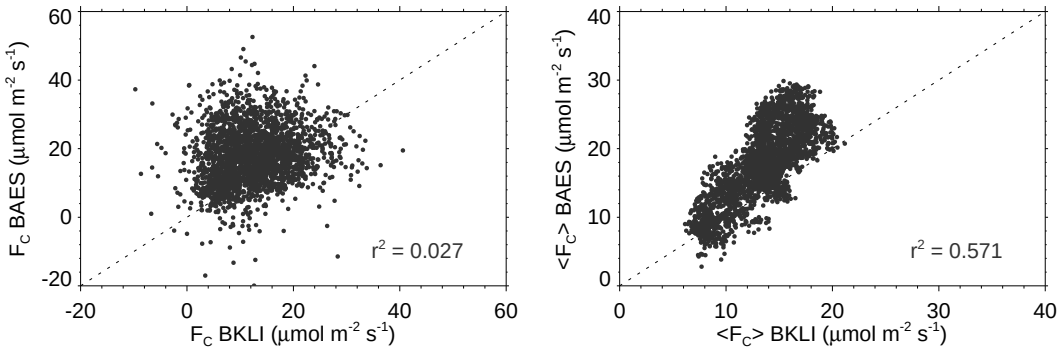

Figure 4.11. Correlation between BKLI and BAES for F_C (left) and $< F_C >$ (right). Displayed are daily average values.

horizontal averaging to both stations the correlation increases significantly with r^2=0.571. While the comparison of F_C would result in the conclusion, that the dynamics of the CO_2 balance at both stations are almost completely uncorrelated, the interpretation of $< F_C >$ reveals a significant amount of similarity.

4.3 Benefits of Long-term Measurements

Long-term investigations are essential to gain information about trends and to quantify the variability over time. Longer time series not only lead to a more solid population, but also increase the chance, that the dataset covers all occurrences of the investigated property. When it comes to environmental monitoring by the EC method, the term "long-term" is often used manifold for different periods. As such, the length of a time series always has to be put in relation to the investigated time scale and the time covered by the measurements should cover multiple periods in order to achieve a solid statistic. It has to be taken into account, that even if only a certain time scale is investigated, there is always a superposition of other, mostly longer, time scales, which might significantly influence the results. It is therefore particularly important to be aware of such influences when analyzing data snippets shorter than the longest time scale, because properties of larger time scales are usually inherited to smaller scales. From this perspective, "long-term" can be defined as the period, where all relevant time scales are represented and where any trend, if existent, is significant.

Whereas for CO_2 in most natural ecosystems a diurnal and a yearly time scale can be discerned due to varying photosynthetic activity over the course of a day and a year, respectively, urban ecosystems usually show a more complex pattern. Even though photosynthesis takes up CO_2 during the day and plant respiration releases CO_2 during the night, the diurnal course in cities is mostly superimposed by traffic activity, which leads to a typical dual shaped pattern with higher F_C during the day, a small depression at noon and lower F_C during the night. The yearly course

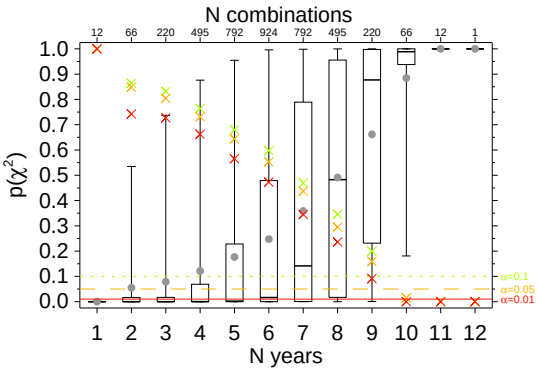

Figure 4.12 Composition of the statistics from the χ^2 goodness of fit test. Boxplots show the distribution of the results from the χ^2-test for each possible combination of N years out of 12, whereas the number of possible combinations is indicated on the top x-axis. The green, orange and red lines show the significance levels and the crosses mark the amount of results out of the number of combinations, that reject H_0 at the significance level with the corresponding color.

is additionally controlled by heating activity, which leads to more CO_2 emissions during the heating season in wintertime. While the diurnal cycle of anthropogenic CO_2 emissions is opposed to the natural photosynthetic activity, the yearly cycles coincide. In addition to natural ecosystems, urban areas also show a weekly dynamic due to the difference in traffic volume between working days and weekends. Furthermore, some irregularity is introduced by public holidays, which are mostly comparable to weekends. Dependent on the location, other sources like e.g. combustion can have significant influence on the dynamics of CO_2. On top of both, the natural and the anthropogenic influences, CO_2 concentration is likely to show a long-term increasing trend due to the steady increase of the global background concentration.

By looking at the different time scales of the urban C balance it can simply be concluded, that at least one year of measurements should be taken into account in order to gain information about all relevant time scales. However, it is necessary to cover more than one period of each time scale, to be able to distinguish any period-to-period variability or long-term trends. As such, "long-term" should only be referred to multi-year CO_2 time series, especially when investigating extremely heterogeneous urban environments. Within the following two section statistical tests are applied to the long-term dataset from BKLI to discuss the significance of statistics of F_C as well as the trend of ρ_C.

4.3.1 Goodness of Fit Test

In an approximation the 12 year long time series from BKLI is taken as a base population of F_C at this location. As such, it is assumed, that within this time, all relevant dynamics and variabilities are caught. A χ^2 goodness of fit test is applied to investigate how many years should be covered by the measurements in order to have no significant difference between the histograms of a subset of years (h_O) compared to that of the entire period of 12 years (h_E) calculated from half-hourly data. The χ^2 test probes the differences between an observed distribution h_O and an expected distribution h_E as follows

$$\chi^2 = \sum_{i=0}^{n-1} \frac{(h_{O,i} - h_{E,i})^2}{h_{E,i}}. \tag{4.3}$$

The result χ^2 is used to test the Null-Hypothesis

> *H_0: There are no significant differences between histograms of selected combinations of N years and the base population*

against the alternative Hypothesis

> *H_1: There are significant differences between histograms of selected combinations of N years and the base population*

at significance levels $\alpha = 0.1$, $\alpha = 0.05$ and $\alpha = 0.01$. The Null-Hypothesis is rejected, if $p(\chi^2) < \alpha$. Histograms are calculated for bins of 4 µmol m^2 s^{-1} and data are cut-off before at the 99 % percentile to prevent unnecessary stretching of the histogram towards outliers, which would lead to a large number of null-bins. The range of F_C used to calculate the statistics is thus -72 to 106 µmol m^2 s^{-1}. The Hypothesis are tested for all possible combinations of $N \in \{1, ..., 12\}$ to select N years out of 12 without repetitions. In Fig. 4.12 a composition of the results of the χ^2 test is given. Clearly, single years do not represent the base population well enough and there is high evidence, that the deviation from the long-term average histogram is significant. Starting from two years of measurements it becomes possible, that the base population can be represented without significant differences, but only for 15–25 % of all cases. It takes up to seven years until the chance of representing the base population is around 50 % and with 10 years or more the 12-year histogram is reproduced without any significant difference in all cases. Concerning the median value, differences between the base population and subsets of up to six years are significant and it is more likely due to chance, that the true distribution of F_C is caught within six years or less.

4.3.2 Long-term Trend Evaluation

Measurements of CO_2 concentration go back to 1958 when C. David Keeling started sampling at Mauna Loa [Keeling et al., 1976]. From this data and from many other background concentration measurements started later on, the dynamics of ρ_C can be traced with high precision on a global level and the evaluation of trends and tendencies is based on a solid population. While decadal mean annual growth rates of CO_2 at Mauna Loa started below 1 ppm y^{-1} during the sixties, a steady increase is observed since then. During the last full decade between 2000 and 2010 annual growth rates reached 1.97 ppm y^{-1} on average. A preliminary calculation of the average growth rate starting from 2011 until today results in a mean value of 2.44 ppm y^{-1}. In a rough approximation the increase in ρ_C can be taken as linear over the course of a decade, but the average increase in annual growth rates clearly states, that the trend follows an exponential curve. In Schmutz et al. [2016] it could be shown, that the local CO_2 concentration in Basel is coupled directly to the background concentration level with a hysteresis of several month and an average positive offset around 10 ppm. The trend calculated for Basel follows that of the

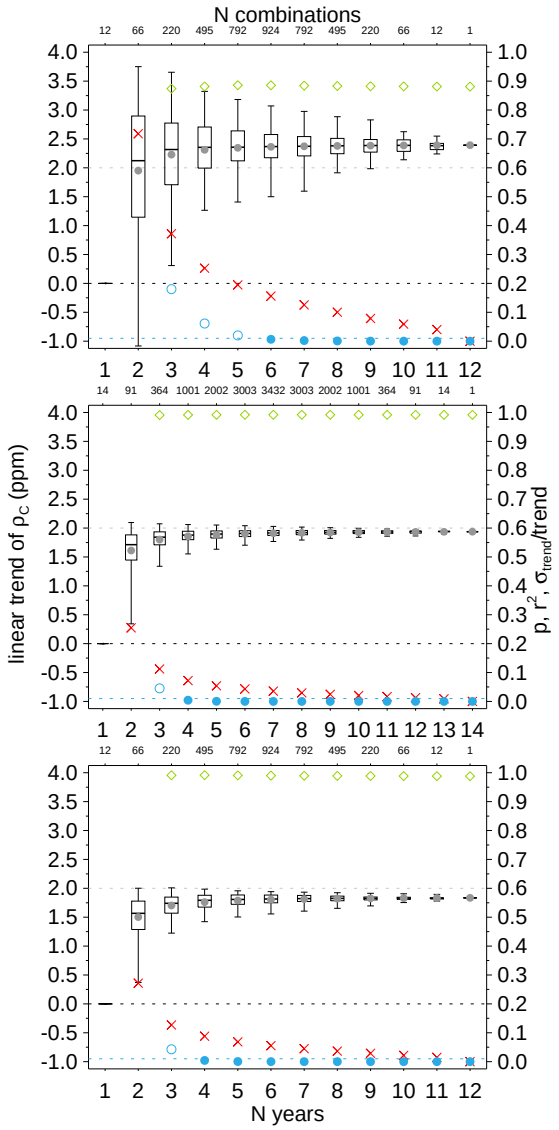

Figure 4.13 Linear trends of CO_2 concentration for each possible combination of years out of the investigation period at BKLI (top), Schauinsland (SAL) (middle) and Jungfraujoch (JFJ) (bottom). Green diamonds indicate the correlation coefficient r^2 between yearly averages and fitted values of the linear trend, red crosses the ratio between the standard deviation of the trend and the average trend and the blue circles represent the p-values of the trend. Circles are filled, when the p-value drops below the significance level $p = 0.01$. Dotted lines represent the zero crossing and the 2 ppm level.

background concentration very closely between 2005 and 2015. The performance of the long-term trend of ρ_C is tested by calculating linear trends based on half hourly data over all possible combinations of years within the investigation period. To assess the significance of the trend the correlation coefficient between yearly averages of ρ_C and the linear trend and the corresponding p-value are calculated. The evaluation of the p-value is done at the significance level $\alpha = 0.01$. The results of the analysis for BKLI, JFJ and SAL are displayed in Fig. 4.13.
Due to the larger variability in the local measurements at BKLI the calculated trends from different subsets of single years vary more compared to the background concentration measurements. At all three stations the long-term trend is approached from below and becomes significant after six years at BKLI and four years at SAL and JFJ, respectively. Even though it takes some years to significantly represent the long-term trend, the correlation coefficient between the linear fit and the measured yearly averages is already high.

CHAPTER 5 - P2

Ten Years of Eddy Covariance Measurements in Basel, Switzerland: Seasonal and Interannual Variabilities of Urban CO_2 Mole Fraction and Flux

The following chapter is published as a research article in the Journal of Geophysical Research: Atmospheres:

M. Schmutz[1], R. Vogt[1], C. Feigenwinter[1], E. Parlow[1] (2016): Ten years of eddy covariance measurements in Basel, Switzerland: Seasonal and interannual variabilities of urban CO_2 mole fraction and flux. *Journal of Geophysical Research: Atmospheres 121*(14), 8649-8667.

[1]Research Group Meteorology, Climatology, and Remote Sensing, University of Basel, Switzerland

AGU PUBLICATIONS

JGR

Journal of Geophysical Research: Atmospheres

RESEARCH ARTICLE
10.1002/2016JD025063

Key Points:
- Improved method of horizontal averaging for better comparability of flux data in heterogeneous environments presented
- Comparison of urban CO_2 mole fraction to regional background records
- Long-term (10 years) trends and variability of urban CO_2 flux and mole fraction reported

Correspondence to:
M. Schmutz,
mi.schmutz@unibas.ch

Citation:
Schmutz, M., R. Vogt, C. Feigenwinter, and E. Parlow (2016), Ten years of eddy covariance measurements in Basel, Switzerland: Seasonal and interannual variabilities of urban CO_2 mole fraction and flux, *J. Geophys. Res. Atmos.*, *121*, 8649–8667, doi:10.1002/2016JD025063.

Received 9 MAR 2016
Accepted 27 JUN 2016
Accepted article online 2 JUL 2016
Published online 19 JUL 2016

Ten years of eddy covariance measurements in Basel, Switzerland: Seasonal and interannual variabilities of urban CO_2 mole fraction and flux

M. Schmutz[1], R. Vogt[1], C. Feigenwinter[1], and E. Parlow[1]

[1]Research Group Meteorology, Climatology, and Remote Sensing, University of Basel, Basel, Switzerland

Abstract Eddy covariance (EC) measurements of carbon dioxide (CO_2) in urban environments are carried out widely since the late nineties. However, long-term time series are still rare and little is known about long-term tendencies, even though cities are major sources of CO_2 globally. Here a full decade of EC measurements from Basel, Switzerland, is presented. An approach for the calculation of horizontal averages is presented. It improves the significance and comparability of measured fluxes from heterogeneous environments and emphasizes the need of adequate weighting by horizontal averaging in such heterogeneous urban environments, especially for the derivation of cumulative quantities like the annual net ecosystem exchange. The urban CO_2 mole fraction (ρ_C) is compared with regional background measurements, and good agreement in terms of long-term trend and seasonal variability is found. Over the last decade an increase of 2 ppm y^{-1} is observed, both locally and globally. CO_2 flux (F_C) data are analyzed for diurnal and seasonal cycles as well as interannual variabilities. F_C shows a large interannual variability in times of high source activity (e.g., during the day and in winter). In contrast, a relatively constant background flux of 5 μmol m^{-2} s^{-1} is found during periods of low source activity. The long-term trend of F_C is mostly superimposed by the large temporal variability and is found to be −5% over the last 10 years.

1. Introduction

1.1. Importance of Long-Term CO_2 Records

Recently, many studies focused on approaches toward a better understanding of the linkage between carbon dioxide (CO_2) emissions in urban environments and their controlling factors [*Christen et al.*, 2011; *Contini et al.*, 2012; *Lietzke et al.*, 2015; *Velasco et al.*, 2014]. Modeling approaches are an important step forward to transform information from point measurement to larger spatial (e.g., city) scales, which is essential to achieve a comprehensive picture of the entire urban metabolism.

The significance and resilience of the results, however, depend strongly on whether the emission factors and theoretical assumptions can be validated by reliable measurement-based data sets. As the eddy covariance (EC) method for the determination of turbulent fluxes of mass and energy only became a widely applicable method in urban areas since the late nineties, multiyear studies able to catch long-term trends and interannual variabilities are still rare. A comprehensive overview of recent studies on urban CO_2 fluxes (F_C) is given in *Lietzke et al.* [2015], whereas the longest time series reported in literature cover at most 5–6 years [*Crawford et al.*, 2011, *Gioli et al.*, 2012]. In contrast, there are numerous long-term data sets of CO_2 mole fraction (ρ_C) and F_C from natural terrestrial ecosystems (e.g., FLUXNET, www.fluxdata.org) or remote background concentration measurements (e.g., Carbon Dioxide Information Analysis Center, http://cdiac.ornl.gov/) and a variety of corresponding studies [*Hofmann et al.*, 2009; *Liu et al.*, 2015]. Taking into account, that urban areas are responsible for large parts of the global greenhouse gas emissions (~50%, depends on methodology and boundary definition of urban areas [*Intergovernmental Panel on Climate Change* (*IPCC*), 2014; *Marcotullio et al.*, 2013]), still little is known about one of the major sources of atmospheric CO_2 [*Rosenzweig et al.*, 2010].

Compared to most natural ecosystems, urban areas are hot spots of changes and development, and thus, it is barely possible to characterize and understand the ongoing processes by looking at a "short-term" snapshot of the current state. Relationships between emissions and their drivers derived from single years are not implicitly valid for longer time periods, and the validity of reported correlations still needs to be proved. Because urban CO_2 is subject to cycles on daily, weekly, and yearly scales, it is inevitable that multiple years are needed in order to detect trends and periods on all relevant time scales.

Journal of Geophysical Research: Atmospheres 10.1002/2016JD025063

1.2. Measuring Urban Carbon Dioxide

Research on the complex pathways of CO_2 in the urban landscape is a substantial contribution to the rapid progress in urban climatology over recent years. Whereas tracking of, e.g., fuel consumption or use of other commodities linked to greenhouse gas emissions can be achieved on national or regional scales by inventory approaches, the task becomes increasingly more sophisticated for the densely populated urban environment. Major sources of CO_2 in cities are well known, most being linked to the massive energy demand of the urban metabolism (flows of material and energy caused by human activity). Large parts of urban CO_2 is caused by fuel combustion for heating, transportation, industry, and power generation and to a minor degree by processes like waste decomposition or human respiration [*Christen*, 2014]. Effective sinks of CO_2, e.g., vegetation are rare and cover only minor, patchy fractions of cities. Therefore, urban environments are normally net sources of CO_2 all over the year [*Christen et al.*, 2011; *Crawford et al.*, 2011; *Lietzke and Vogt*, 2013]. The need of adequate monitoring systems to quantify the impact of cities to the total CO_2 budget is obvious, and a large number of studies about measurement and modeling of urban air pollution have been released during the last decade. Current research on local-scale urban micrometeorology focuses on the link between direct measurements of CO_2 and its controlling factors derived from geographic information system (GIS) data (e.g., land use, traffic count, and local climate zones) [*Lietzke et al.*, 2015] or on bottom up modeling of emission processes tuned by experimental data [*Christen et al.*, 2011].

A comprehensive overview on measurement techniques to quantify greenhouse gas emissions from cities is given in *Christen* [2014], who discusses different approaches for mesoscale, local-scale, and microscale data acquisition. Regardless of theoretical and technical challenges, the EC technique provides probably the best way to determine local-scale urban CO_2 emissions from a point measurement. If the measurements take place within the urban inertial sublayer (ISL), the footprint extends several hundred meters upwind and the measured flux represents a well-mixed CO_2 signal from the corresponding area. The application of a sectorial analysis allows attributing the flux data to distinct sources or land use classes within the footprint area. Many studies have shown that, e.g., correlations can be found between F_C and traffic volume or heating activity indices [*Helfter et al.*, 2011; *Lietzke and Vogt*, 2013; *Lietzke et al.*, 2015; *Pataki et al.*, 2009; *Pawlak et al.*, 2011; *Velasco et al.*, 2005]. Despite the theoretical requirements [*Aubinet et al.*, 2012] of the EC-method (e.g., horizontal homogeneity and stationarity) are barely satisfied, EC measurements turned out to deliver reliable results even for the heterogeneous urban environment if an appropriate station setup is chosen as suggested by *Feigenwinter et al.* [2012].

The aim of this study is to contribute to an enhanced understanding of the seasonal and interannual variabilities of ρ_C and F_C by analysis of 10 years of EC data from an urban area in Basel, Switzerland, between 2005 and 2014.

2. Material and Methods

2.1. Study Site

Long-term urban meteorological measurements are carried out by the University of Basel, MCR-Lab (Meteorology, Climatology, and Remote Sensing) in the city of Basel. An 18 m tall tower is mounted on the flat roof top of the 20 m high MCR building (BKLI, 47.56173°N, 7.58049°E) since 2003. The neighborhood of the site is mainly characterized by the inner ring street Klingelbergstrasse to the east with heavy traffic, oriented along the 200°/20° axis, as well as by residential buildings enclosing green backyards, to the west. Furthermore, some tall university buildings are located approximately 250 m to the north and the northeast of the site. An aerial image of the surrounding is given in Figure 1, specific land use characteristics are depicted in Figure 2, and a summary of land use classes per sector can be found in Table 1. The site characteristics are described in more detail in *Lietzke and Vogt* [2013], where a second tower has been operated in an adjacent street canyon from mid-October 2009 until end of March 2011.

2.2. Measurements and Data Processing

The EC system of the BKLI site is operative since May 2004, and thus covering now more than a decade of measurements. The instruments are mounted to a vertical extension at the tower top at a total height of 39 m above street level (Figure 3). According to *Lietzke and Vogt* [2013] and *Feigenwinter et al.* [2012], the measurements take place above the roughness sublayer, but inside the ISL. The EC system consists of an

AGU Journal of Geophysical Research: Atmospheres 10.1002/2016JD025063

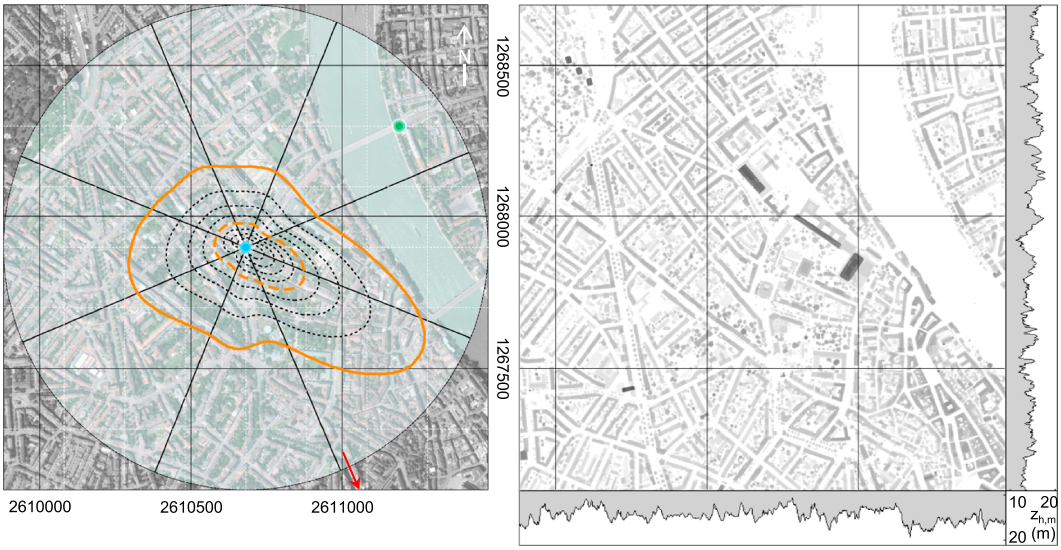

Figure 1. On the left site an aerial image (1.6 km × 1.6 km) [*Geodaten Kanton Basel-Stadt*, 2015] centered around the BKLI site (2610678/1267902, blue dot) is shown. Traffic counts at Johanniterbrücke (BJH, green dot) and Heuwaage (BHA, not on map, red arrow) are marked. The white dashed grid lines indicate steps of 200 m from the measurement site, whereas the black grid represents the Swiss coordinate system (LV03, EPSG:21781). Additionally, the average footprint estimation is shown. The thick solid and dashed orange lines indicate the 90% and 50% contour, respectively. The thin dashed black lines give additional information on the contour shape in steps of 10%. The radial black lines indicate sectors of 45° used during this study. On the right site the corresponding digital elevation data of the surrounding is shown. Building height is scaled white (0 m) to black (62.4 m). Profiles on the right and at the bottom of the graph present the median building height.

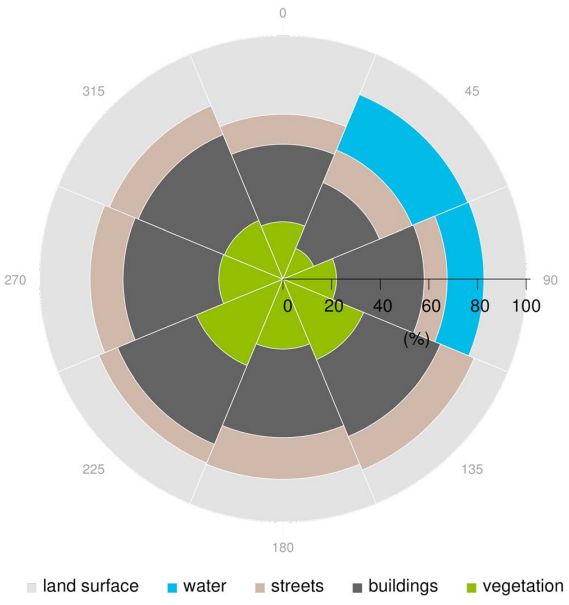

Figure 2. Fractions of land surface, water, roads, buildings, and vegetation per sector within a radius of 500 m around the BKLI site. Sectors are as defined in Figure 1, and details are listed in Table 1.

ultrasonic anemometer (=sonic, HS-50, Gill Instruments Ltd.) and an open path CO_2/H_2O infrared gas analyzer (=IRGA, LI-7500, LI-COR Inc.), both facing northward, allowing the predominant winds from east and west to pass the measuring volume mostly undisturbed. Sensor separation is 0.4 m, and the gas analyzer is tilted 35° in order to reduce the influence of water droplets on the windows. Both, the sonic and the IRGA are sampled at 20.83 Hz, whereas the IRGA is connected to the analogue input of the sonic. Thus, the internal quality control value (Automatic Gain Control) of the IRGA is not available. To calibrate the IRGA N_2 (dry) is used as zero gas and N_2/CO_2 (500 ppm) for the span.

Raw data are stored as 30 min files of orthogonal wind components u, v, and w; acoustic temperature T_s; as well as the voltage signals of the IRGA, which were converted into concentrations and later into mole fractions of CO_2 and H_2O during postprocessing

Journal of Geophysical Research: Atmospheres 10.1002/2016JD025063

Table 1. Sectorial and Average Characteristics of the BKLI Site[a]

	z_0 (m)	z_h (m)	λ_i(%)	λ_w(%)	λ_s(%)	λ_b(%)	λ_v(%)
337.5°–22.5°	5.7	18.8	32.2	0.0	12.4	32.0	23.5
22.5°–67.5°	8.5	18.1	17.8	24.8	14.5	29.3	13.7
67.5°–112.5°	4.0	19.0	17.4	15.1	9.5	36.0	22.0
112.5°–157.5°	3.2	15.3	14.9	0.0	15.0	34.2	35.9
157.5°–202.5°	4.7	14.7	17.6	0.0	17.2	36.4	28.8
202.5°–247.5°	5.4	16.1	18.1	0.0	8.4	35.0	38.5
247.5°–292.5°	3.5	15.4	20.7	0.0	13.6	39.3	26.4
292.5°–337.5°	2.5	16.0	22.8	0.0	12.9	38.3	26.0
Mean	3.8	16.7	20.2	5.0	12.9	35.1	26.9

[a]Land use fractions λ_i (land surface), λ_w (water), λ_s (streets), λ_b (buildings), and λ_v (vegetation) are calculated for 500 m radius around the measurement site. Roughness length z_0 is derived from logarithmic wind profile during neutral conditions, and z_h is calculated from a 3-D city model.

(0–5 V = 10–30 mmol m^{-3}). The sonic is operated in uncalibrated mode, and a matrix correction [*Vogt*, 1995] was applied afterward. Average 30 min statistics were calculated using EddyPro® v5.2.1 (LI-COR Inc.). During processing, axis rotation for tilt correction, linear detrending, covariance maximization, as well as the Webb-Pearman-Leuning terms for compensation of density fluctuations [*Webb et al.*, 1980] were applied. Furthermore, data were corrected for high-pass and low-pass filtering effects [*Moncrieff et al.*, 1997, 2005], and statistical tests for raw data screening following *Vickers and Mahrt* [1997] were used. For quality check flags were calculated from steady state and developed turbulent conditions tests [*Foken et al.*, 2005; *Foken and Wichura*, 1996; *Göckede et al.*, 2007].

To avoid streamline distortion from the sonic spars and the IRGA, the wind sector 180° ± 15° was generally rejected and treated with special care during gap-filling later on. In addition to the above data removal criteria, data are rejected during rain events ±2 h and during maintenance activities. Overall data availability after completion of postprocessing is approximately 70% for flux data and up to 98% for other meteorological quantities.

2.3. Gap-Filling Algorithm

Data loss due to postprocessing, maintenance, and system failures is up to 30% for flux data. Among the different approaches for gap-filling discussed in literature [*Falge et al.*, 2001; *Moffat et al.*, 2007; *Schmidt et al.*,

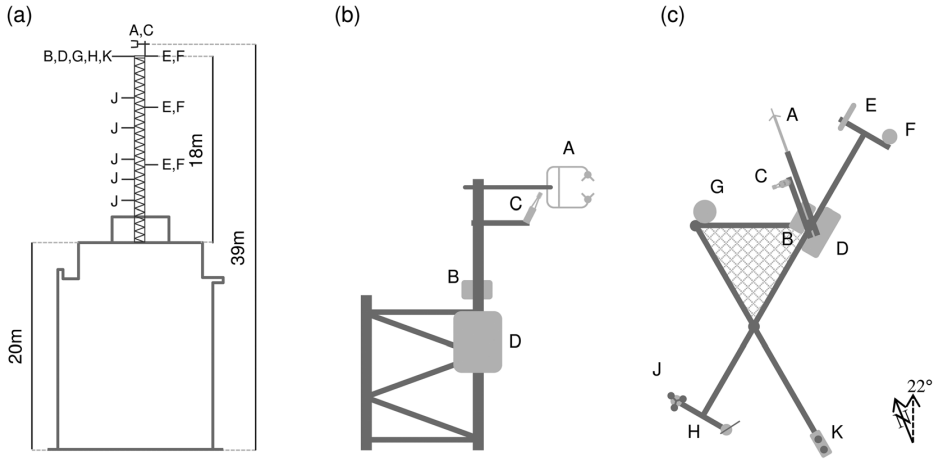

A: Gill HS-50 Ultrasonic Anemometer, **B:** Sonic Electronics Box, **C:** LI-7500 CO_2/H_2O Analyzer Sensor Head, **D:** LI-7500 Control Box, **E:** Aspirated Thermocouple, **F:** HMP155 Humidity and Temperature Probe, **G:** THYGAN Thermohygrometer, **H:** WA15 Crossarm, **J:** WAA151 Cup Anemometer, **K:** CNR1 Net Radiometer

Figure 3. (a) Side view of institute building and flux tower, (b) close-up view of EC setup at tower top, and (c) layout of complete instrumentation at tower-top level. Drawings are not to scale and aligned along the buildings orientation toward 22°.

AGU Journal of Geophysical Research: Atmospheres 10.1002/2016JD025063

2008], the most common methods are artificial neural networks, nonlinear regression analysis, or look-up tables (LUTs). For this study an improved moving LUT (mLUT) technique [*Reichstein et al.*, 2005] is implemented. Instead of LUTs based on static bins for specific temporal and meteorological conditions, the gap-filling values are derived from a temporal moving frame. These moving frames for a gap at a certain day, time, and wind direction (d_G, t_G, and α_G) are defined as $d_G \pm 45$ days, $t_G \pm 1.5$ h, and $\alpha_G \pm 22.5°$. Compared to the static LUT technique, the mLUT algorithm has the disadvantage of a much smaller sample size, because only few neighboring values meet the criteria. At the same time, the mLUT technique benefits from a better representativeness of the gap-filled values for a specific point in time because only temporally adjacent data are considered. This is not the case, if, e.g., data from multiple years are used for the calculation of static LUT. Due to the usage of static LUT, statistics of the time series tend to converge toward the LUT, whereas mLUTs preserve the temporal variability on a much smaller temporal scale. This is crucial, if interannual variability or long-term trends are investigated. Data availability after application of the gap-filling algorithm is at least 98%.

2.4. Horizontal Averaging

CO_2 fluxes measured by the EC method always represent an integrated signal from all sources and sinks within the footprint area. At BKLI, the sources and sinks are not evenly distributed around the station, and thus, the footprint composition and the resulting flux clearly vary with wind direction. In addition, the frequency of occurrence of wind directions changes with daytime and season; thus, there is no equilibrium between data sampled during, e.g., daytime and nighttime or in different seasons. The values measured at the tower are thus only valid for this specific point in space with the corresponding wind system and do not represent the general properties of the surrounding area. Therefore, it is necessary to consider horizontal averages in order to achieve fluxes representative for a certain spatial scale (e.g., neighborhood scale).

The basic concept of horizontal averaging goes back to *Raupach and Shaw* [1982], and different applications of horizontal averages are described by *Rotach* [1993], *Rotach* [1995], or *Christen* [2005], who showed the benefit for comparison of simultaneous measurements at different locations. In order to consider the uneven sampling of different scenarios (daytime/nighttime, weekday/weekend, seasons, and wind sectors) an adapted concept of horizontal averaging has been implemented following *Lietzke et al.* [2015], who introduced a method for the calculation of so-called "expected fluxes." Instead of weighting sectorial fluxes by the relative frequency of occurrence of the corresponding wind direction, for each sector (s) a gap-filled (X, only values from this sector) time series $F_{CX}(s)$ is generated. Subsequently, the arithmetic average is calculated out of the sectorial values for each point in time (t) which leads to the horizontal average

$$< F_C >= \frac{1}{8} \sum_{s=1}^{8} F_{CX}(s,t).$$

All terms in angle brackets in the current study are calculated following the above method.

2.5. Long-Term Development of the Urban Neighborhood

Long-term measurements of F_C are not only affected by the diurnal and seasonal variations of the local sources and sinks but also by changes in footprint composition which are caused by modifications of the city structure or variations of the urban metabolism. Modification of the land use structure like new buildings/streets, political decisions (e.g., new traffic concepts), or generally population growth is influencing the local source/sink regime and has to be taken into account when interpreting the results.

From analysis of GIS data [*Geodaten Kanton Basel-Stadt*, 2015], information about the development of the surrounding building structure could be derived. In general, there was only little construction activity during the last 10 years. An exception is the newly built (2007–2010) "Universitäts-Kinderspital" (Children's Hospital) 200 m north-northeast, which replaces a former hospital building of similar shape. Furthermore, demolition work has begun in summer 2014 in the backyard to the west of the institute, and there is ongoing construction work for the new "Biozentrum" (Center for Molecular Life Sciences) 300 m to the north since 2013.

For the Klingelbergstrasse information about traffic volume is available from a permanent traffic count 500 m northeast, at the Johanniterbrücke (BJH) and approximately 1.3 km to the other direction at the Heuwaage (BHA) for the entire measurement period, both on an hourly resolution [*Geodaten Kanton Basel-Stadt*, 2015]. Between 2004 and 2007 the average daily traffic volume at BJH was approximately 20,000 veh day^{-1}.

AGU Journal of Geophysical Research: Atmospheres 10.1002/2016JD025063

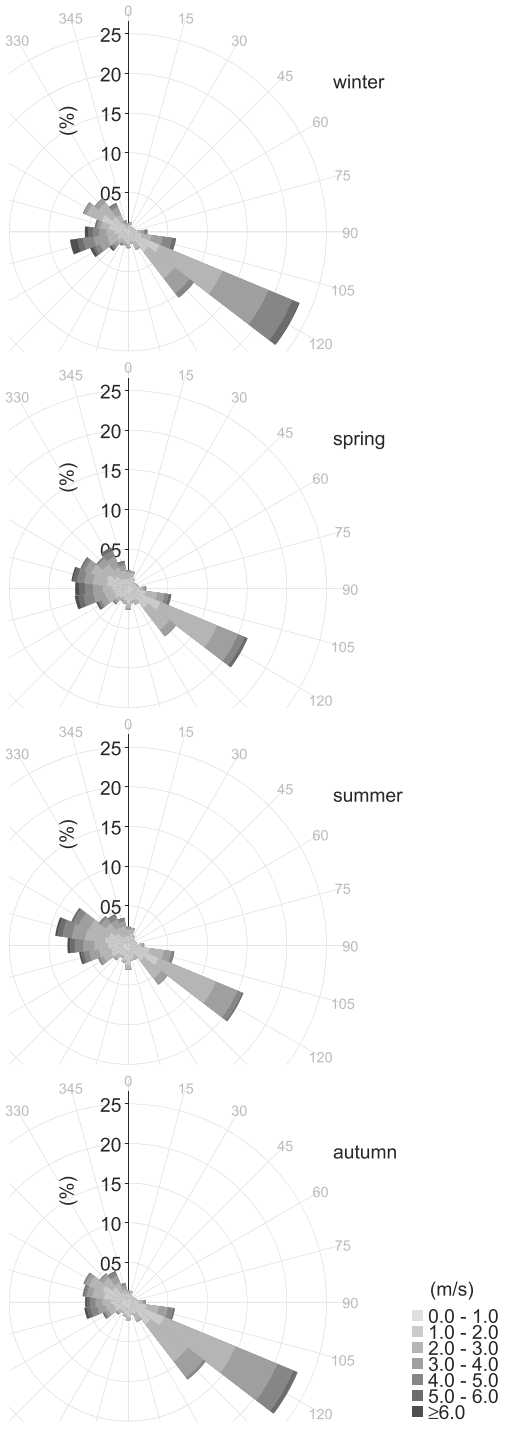

Figure 4. Seasonal relative frequencies of wind direction and velocity at BKLI (24 bins based on 30 min averages).

With the opening of the traffic bypass "Nordtangente" in 2007/2008 the average daily number of vehicles has steadily diminished to roughly 15,000 veh day^{-1} until 2011 and then stayed more or less constant.

In 2013 the local authorities reported a total population of 173,330 inhabitants for the city of Basel (without agglomeration). The total population growth since 2004 is 3.9%, whereas the yearly growth rate is 0.43% for the whole city and varies between 0.24 and 0.65% for the residential districts around BKLI [*Statistisches Amt Basel-Stadt*, 2015].

2.6. Definition of Wind Sectors and Seasons

For the application of sectorial analysis, data were separated into eight wind sectors of equal width (45°) (Figure 1 and Table 1). Sectors are numbered clockwise from 1 to 8 starting at north. For the analysis of seasonality the four seasons winter (December-January-February), spring (March-April-May), summer (June-July-August), and autumn (September-October-November) are distinguished following the meteorological convention. Thus, if yearly values are indicated, December is always attributed to the following year.

3. Results and Discussion

3.1. Meteorology at the BKLI Site

The climate of Basel is characterized by mild winters and warm summers (Cfb-climate according to Köppen classification). The yearly temperature amplitude calculated from monthly averages is 18 K, whereas minima and maxima can be around 0°C and 25°C, respectively. Average rainfall is 804 mm and is distributed all over the year with a maximum during summer. In Figure 4 the average seasonal wind roses for the 10 years show the dominant wind directions ESE and W/NW. The local wind system has a distinct diurnal cycle, where ESE and

AGU Journal of Geophysical Research: Atmospheres 10.1002/2016JD025063

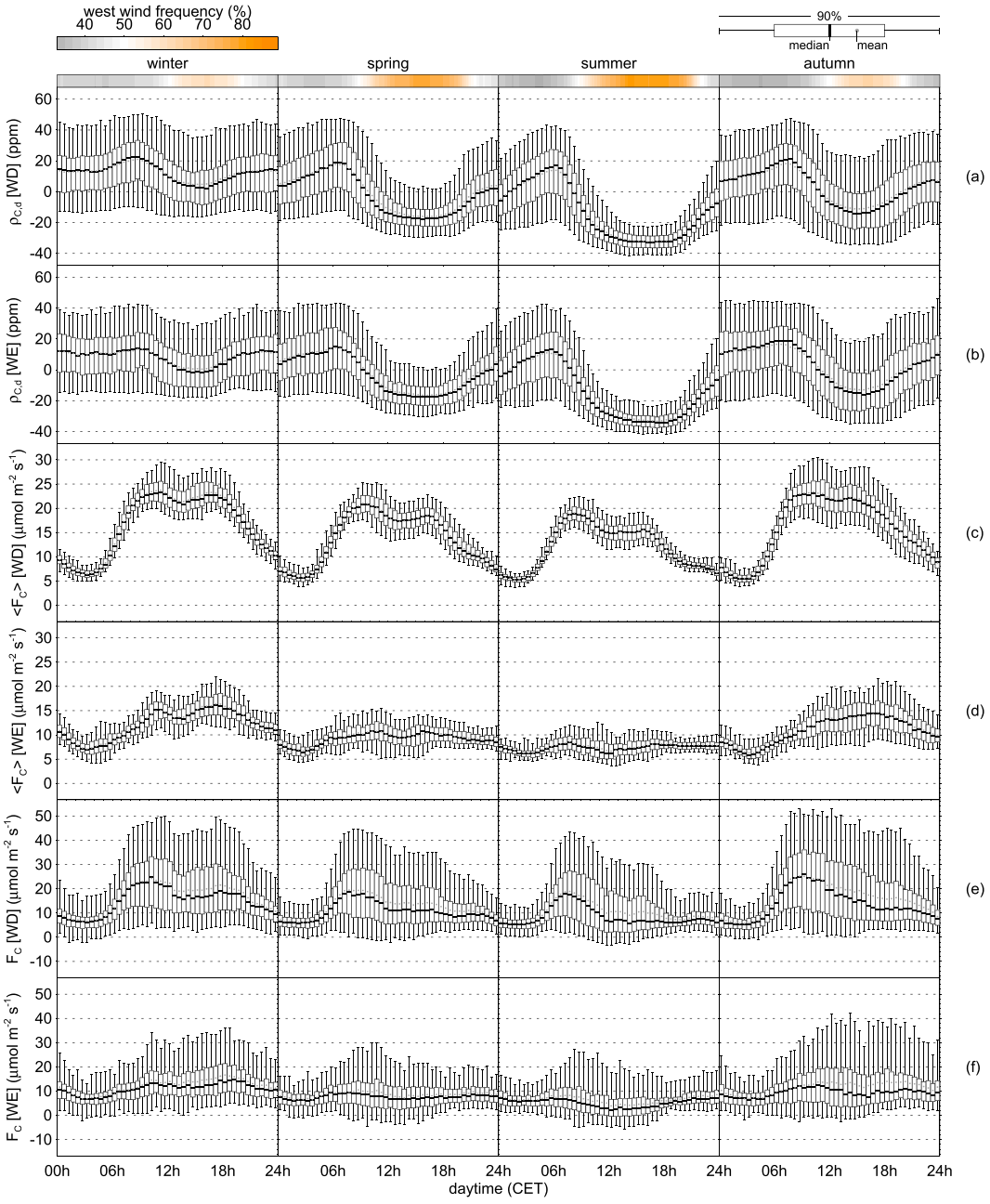

Figure 5. Mean seasonal diurnal courses of (a and b) ρ_C, (c and d) $<F_C>$, and (e and f) F_C from 2005 to 2014. Columns represent different seasons. Variables are presented for weekdays (WD) as well as weekends (WE). The bar on top of plot indicates frequency of west wind. The boxplots show the 5th, 25th, 75th, and 95th percentiles as well as the mean and the median of the data. Note the difference in *y* axis scale between Figures 5c and 5d and Figures 5e and 5f.

NW winds are subject to the nighttime and daytime parts of the mountain-valley system of the Rhine valley, respectively. While the general wind regime is very persistent, the ESE component occurs more often during day in autumn and winter and the W/NW component is typically more frequent in spring and summer. Average wind speed is 2.4 m s^{-1} ± 1.2, whereas stronger wind speeds are normally related to the western sector.

Journal of Geophysical Research: Atmospheres 10.1002/2016JD025063

The local wind system with its diurnal behavior is crucial to the measurement of F_C as the wind direction determines, which sources actively contribute to the measured signal. In the morning, high CO_2 emissions are advected from the Klingelbergstrasse in the east, resulting in high F_C, whereas in the afternoon, when the west winds advect emission from the residential sector, measured F_C is relatively low. Only between October and February, when the ESE component is more persistent during the day, afternoon traffic or the evening rush hour is clearly represented by the measurements (Figures 5e and 5f). The calculation of horizontal averages compensates for this effect.

3.2. Carbon Dioxide Footprint Estimation

Footprints for F_C were calculated from 30 min data according to *Kormann and Meixner* [2001], which is an analytical footprint model for nonneutral stratification. To run the model the displacement height z_d and the roughness height z_0 were derived by the rule of thumb $z_d = 2/3\ z_h$ and $z_0 = 0.1\ z_h$, respectively, where z_h is the mean building height (16.6 m) derived from the 3-D city model. For an estimation of source area seasonality, average source areas were calculated for single seasons and years from the 30 min footprints. The overall average footprint is shown in Figure 1 for a domain of 1.6×1.6 km. The general shape of the footprint contour lines compares well with the characteristic east-west distribution of the wind rose (Figure 4). A strong SE component and a rather diffuse west branch are characteristic for the source area. The footprint extends at its maximum 500 m (east), but typically ranges within 300–400 m (90% contours). The general shape of the footprint is preserved over the year, because of the persistent daily wind regime. Nevertheless, between single years and especially between seasons characteristic differences can be distinguished. The area within the 90% contours is largest during winter with 0.74 km^2 and smallest in autumn with 0.57 km^2 (−23.3%), whereas during spring and summer the footprint covers 0.70 km^2 (−5.3%) and 0.60 km^2 (−19.1%), respectively. The differences in footprint size are primarily subject to the varying strength of the eastern branch of the footprint area, which extends the most in winter, followed by autumn, spring, and summer. The variation of the western part is smaller, except for the autumn situation, where less of the residential area to the northwest is covered. From a larger footprint area a well-mixed signal with fewer contributions of single nearby sources can be assumed. The footprint defines which sources and sinks actively contribute to the measured, and thus, a variation in the source area can directly affect the measured pattern, especially in a heterogeneous urban environment.

3.3. The Impact of Horizontal Averaging on Sectorial CO_2

To quantify the impact of horizontal averaging on the total carbon (C) balance, average yearly cumulative fluxes nC and $<nC>$ were calculated from the EC data. Due to the inaccuracy of C storage estimations from single point measurements, the storage term ΔC_S was not calculated for the derivation of net ecosystem exchange values. From street canyon profile measurements in London, UK, *Bjorkegren et al.* [2015] have shown that the impact of ΔC_S on F_C is typically less than 1% of the magnitude of the vertical flux during well-mixed conditions and diurnal and seasonal patterns are not altered significantly. nC is a good indicator to reveal the heterogeneity of the source/sink distribution within the surrounding of the BKLI site as well as the unequally distributed occurrence of different wind directions. Both F_C and nC are affected significantly by the horizontal averaging procedure, but the effect on nC is much larger. While the frequency of occurrence of a sector does not directly affect the magnitude of F_C, nC is very sensitive to the distribution of wind directions. Changes in F_C are thus more related to the unequal frequency distribution of daytime and nighttime values and different seasons recorded for each sector. Sectorial values of F_C and nC as well as $<F_C>$ and $<nC>$ are shown in Figure 6. Horizontal averaging leads to increased F_C for sectors 4 through 7 and clearly smaller fluxes for sectors 1 through 3 and sector 8. Largest changes are observed for sector 2 (−12.8%) and sector 5 (+12.8%). Changes for nC are much larger, especially for the frequent sector 4, where nC is reduced by −116%. Compared to nC, $<nC>$ clearly better reflects the sectorial CO_2 balance represented by $<F_C>$ in Figure 6b. The different weighting of individual sectors by horizontal averaging leads to an average $<F_C>$ of 13.3 $\mu mol\ m^{-2}\ s^{-1}$ (+7.6%) compared to the directly measured F_C of 12.3 $\mu mol\ m^{-2}\ s^{-1}$. The increase in nC is of the same order of magnitude from 4.6 to 4.9 $kg\ C\ m^{-2}\ yr^{-1}$ (+6.5%).

3.4. Long-Term Time Series of CO_2 Mixing Ratio

3.4.1. Diurnal Cycles and Yearly Variability

Mean diurnal cycles of ρ_C were calculated from 30 min averages. Influences of long-term trends have been removed from the time series by subtracting the linear trend calculated over the past 10 years from each

AGU Journal of Geophysical Research: Atmospheres 10.1002/2016JD025063

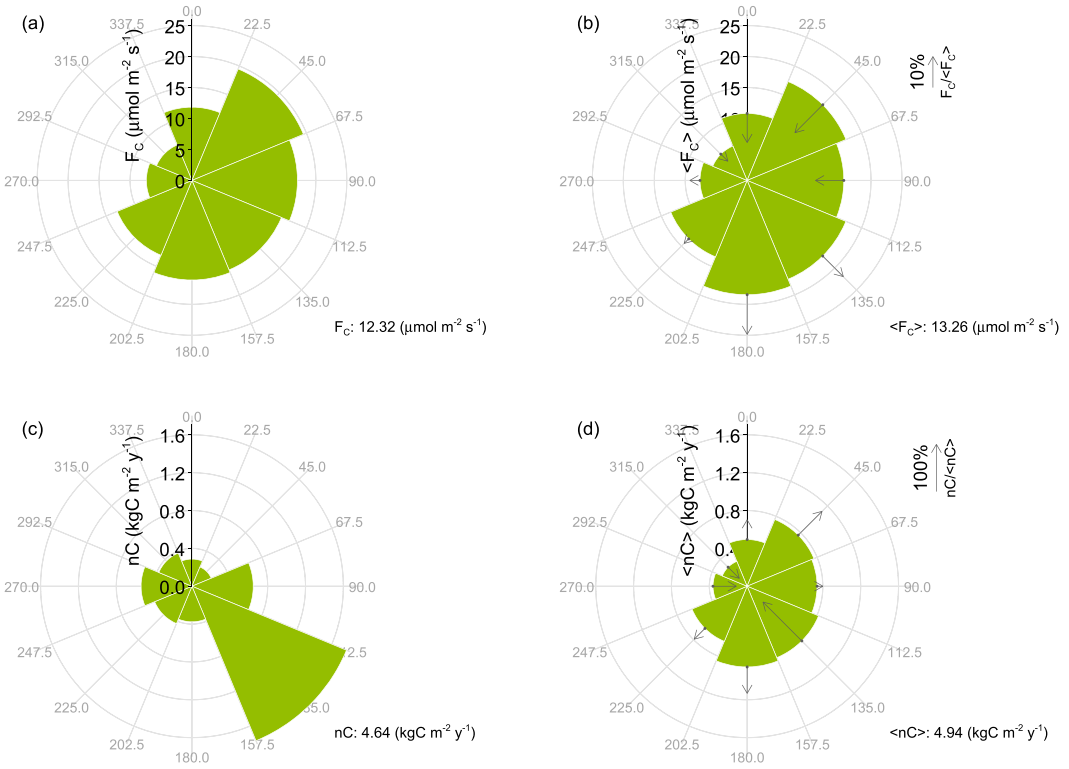

Figure 6. Average annual (a) F_C, (b) $<F_C>$, (c) nC, and (d) $<nC>$ per sector between 2005 and 2014. The arrows in Figures 6b and 6d indicate relative effect of horizontal averaging on F_C and nC, respectively.

value ($\rho_{C,d}$). Diurnal courses split by seasons are plotted in Figure 5a for weekdays and Figure 5b for weekends. Besides the impacts of surface sources and sinks, the diurnal variability of $\rho_{C,d}$ is by large parts controlled by the dynamics of the convective mixed layer [*Reid and Steyn*, 1997]. Because the mole fraction of CO_2 is inversely correlated to the air volume in the boundary layer (BL) top, highest values are measured in the shallow early morning BL between 05:00 and 07:00. With increasing turbulence after sunrise $\rho_{C,d}$ continuously decreases until minima values are reached around 15:00 at the BKLI site. After sunset, when the BL height decreases, $\rho_{C,d}$ increases steadily during the night. The daily amplitude (A_D), calculated as the average peak to trough difference, ranges from 16.4 ppm in winter to 46.2 ppm in summer. The average A_D is 31.5 ppm, although on individual diurnal cycles the variability around the mean can be large as indicated by the boxplots in Figures 5a and 5b. Results from similar measurements are reported by *Grimmond et al.* [2002] for Chicago (35 ppm (summer), 13 days), by *Reid and Steyn* [1997] for Vancouver (27 ppm (June), 11 days), by *Vogt et al.* [2005] for Basel (61 ppm (June/July), 28 days), and by *Moriwaki and Kanda* [2004] for Kugahara, Tokyo (10 ppm (July), 20 ppm (December), 1 year). Nevertheless, these studies are all very short ranging and thus hardly comparable to the present data set. For the EGH site nearby London a representative average daily amplitude of 17 ppm was calculated by *Hernández-Paniagua et al.* [2015] from data between 2000 and 2012, which is clearly below BKLI because the EGH site located 32 km outside the dense urban center of London. The general diurnal behavior of ρ_C is also reported in several other studies from (sub)urban environments [*Coutts et al.*, 2007; *Crawford and Christen*, 2014; *Lietzke and Vogt*, 2013; *Velasco et al.*, 2005], but comparable results from multiyear studies are rare.

The average diurnal courses clearly indicate that during winter the morning maxima occur later and the increase in the late afternoon starts earlier as a direct result of the shorter period of daylight. The wintertime daily average mole fraction is roughly 25 ppm higher compared to summer because (i) during winter the UBL

AGU Journal of Geophysical Research: Atmospheres 10.1002/2016JD025063

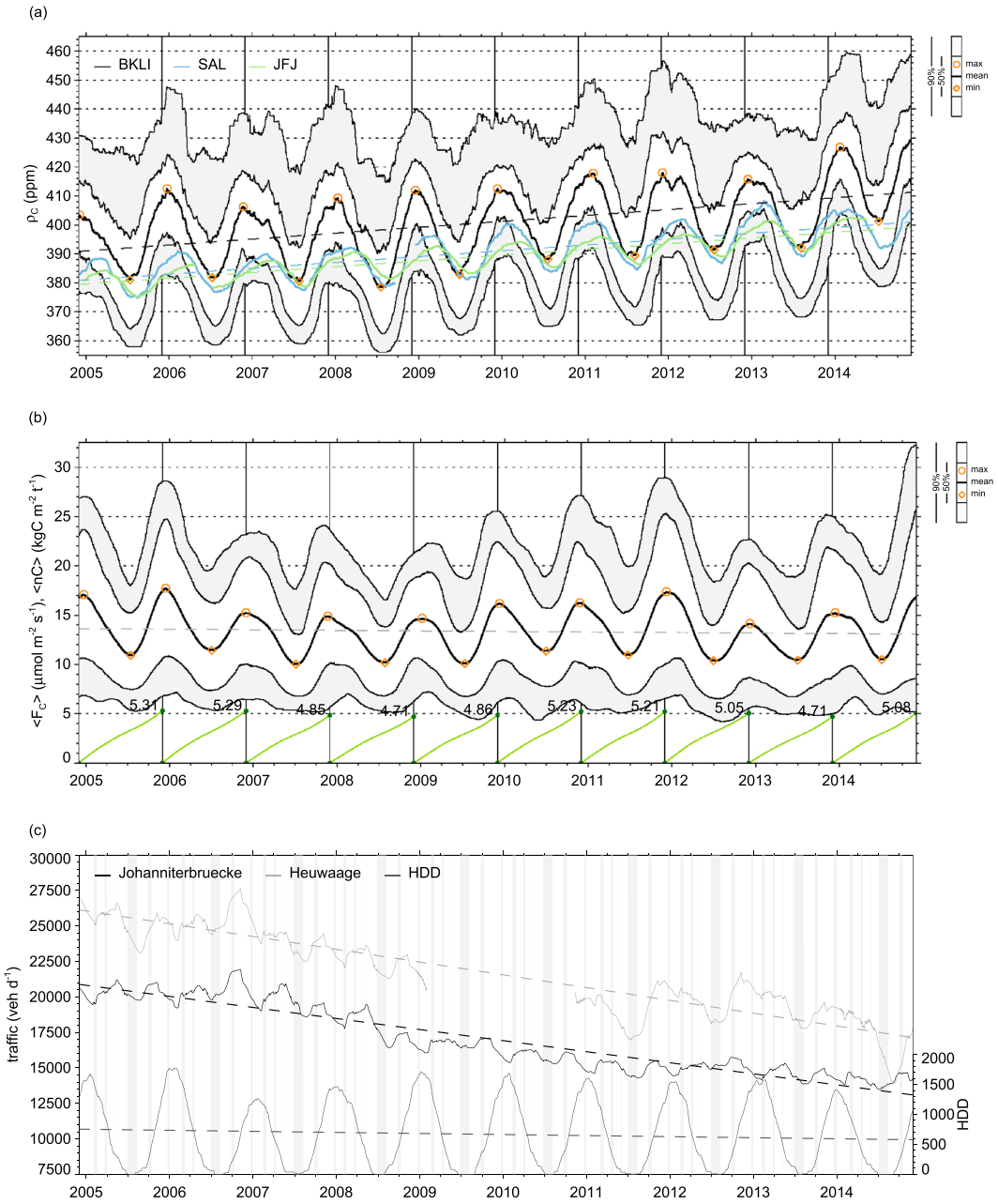

Figure 7. (a) Time series of ρ_C at BKLI, Schauinsland (SAL), and Jungfraujoch (JFJ) and (b) time series of $<F_C>$ and yearly cumulative $<nC>$ (green lines) and (c) traffic count as well as HDD from 2005 until 2014. The solid lines are 90 days running means of half hourly data. Statistics for BKLI are indicated by grey shaded areas. The dashed lines show the linear regression for each time series. Additionally, winter maxima (circles) and summer minima (diamonds) are drawn. The grey shaded areas in Figure 7c indicate public and school holidays.

is generally stratified less unstable, (ii) additional CO_2 is emitted from anthropogenic sources, and (iii) uptake by photosynthesis is mostly inactive. This difference can be as high as 40 ppm during the day, but almost vanishes in the early morning. If weekdays are compared to weekends, $\rho_{C,d}$ is reduced by 3.4 ppm (winter), 1.8 ppm (spring), 0.8 ppm (summer), and 0.4 ppm (autumn) during weekends. Thus, the variation in direct

Journal of Geophysical Research: Atmospheres 10.1002/2016JD025063

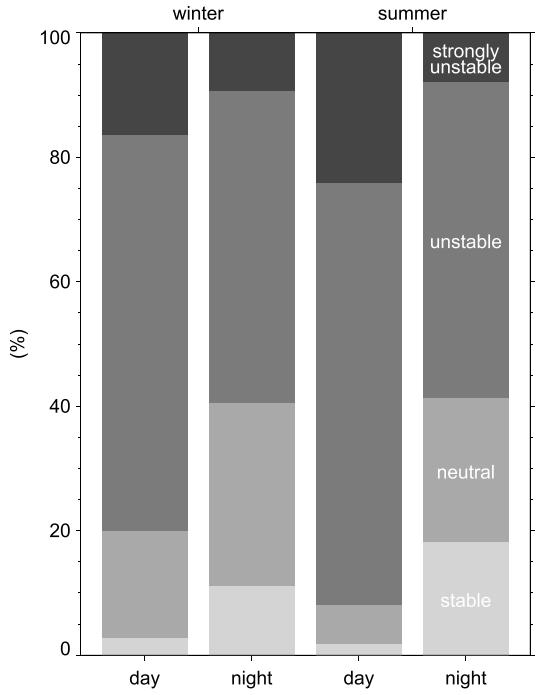

Figure 8. Relative frequency of stability classes split by winter and summer as well as day and night (separated by shortwave radiation data). Stable $\zeta > 0.05$, neutral $0.05 > \zeta >$ -0.05, weakly unstable $-0.05 > \zeta > -1.0$, and unstable $\zeta < -1.0$. The stability index represents $(z - z_d)/L$, where L is the Obukhov length.

CO_2 emissions from, e.g., traffic only contributes little to the absolute mole fraction of CO_2, and the impact of the BL dynamics and uptake by vegetation is of much higher importance for the variability of $\rho_{C,d}$ on daily and seasonal scales. The statistics in Figures 5a and 5b also indicate that the variability within the 10 years is smallest during the day in spring and in summer but nearly the same during nighttime for all seasons. The larger mixing volume during summer and spring days seems to prevent large variations in ρ_C, whereas in the shallow nocturnal BL changes in ρ_C occur more rapidly.

3.4.2. Long-Term Trend and Seasonal Patterns

For the analysis of long-term trends in ρ_C the time series was smoothed by applying a 90 day running mean filter to the 30 min data (Figure 7a). For comparison, high-accuracy CO_2 samples from Global Atmosphere Watch (GAW) stations at Schauinsland (SAL, 40 km northward, 1205 m above sea level (asl) [*Luftmessnetz des Umweltbundesamtes*, 2015]) and Jungfraujoch (JFJ, 120 km southward, 3580 m asl [*University of Bern*, 2015]) are considered. While BKLI represents the local urban BL, SAL acts as a regional background only partially influenced by local sources depending on the vertical BL extension and JFJ gives information about the free atmosphere. Like this these three stations are considered as a quasi-vertical transect through the lower troposphere. The residual after filtering the data reveals the typical seasonal patterns with highest values during winter and lowest values during summer, which has also been reported by several studies for different urban environments [*Hernández-Paniagua et al.*, 2015; *Lietzke et al.*, 2015; *Park et al.*, 2014; *Strong et al.*, 2011; *Valentino et al.*, 2008]. The driving mechanisms of the seasonal course of ρ_C are basically the same as those responsible for the daily cycle. During the day in winter time the mixed BL at BKLI is generally less developed indicated by the shift of stability toward less unstable conditions (Figure 8). Thus, higher ρ_C values partly result from the smaller mixing volume. On the other hand, during the night, differences in the stability regime between summer and winter are negligible and the frequency of stable conditions during summer is even higher at the expense of less neutral stratification. This explains, why the early morning maximum peak of ρ_C does not vary that much between season compared to the differences in the afternoon minimum (Figures 5a and 5b). Additionally, the seasonal differences are enforced due to the varying CO_2 uptake by vegetation in summer and winter, but the influence of photosynthetic CO_2 uptake cannot be determined quantitatively for the BKLI site.

The seasonal behavior of the BKLI data coincides well with the patterns observed at the regional background. The course of the BKLI measurements shows more short-term variability, and the seasonal shape is less marked, especially during the winter, which highlights that the urban BL encounters more variation in source/sink distribution and atmospheric conditions than the overlying lower troposphere. The long-term trend, calculated as the linear regression from 30 min data, emphasizes the long-term increase in ρ_C observed on a global scale [*Tans and Keeling*, 2015]. Over the last 10 years the slope is 1.98 ppm yr^{-1} at BKLI, which compares well to the values calculated for SAL (1.97 ppm yr^{-1}) and JFJ (1.98 ppm yr^{-1}). For the EGH site near

AGU Journal of Geophysical Research: Atmospheres 10.1002/2016JD025063

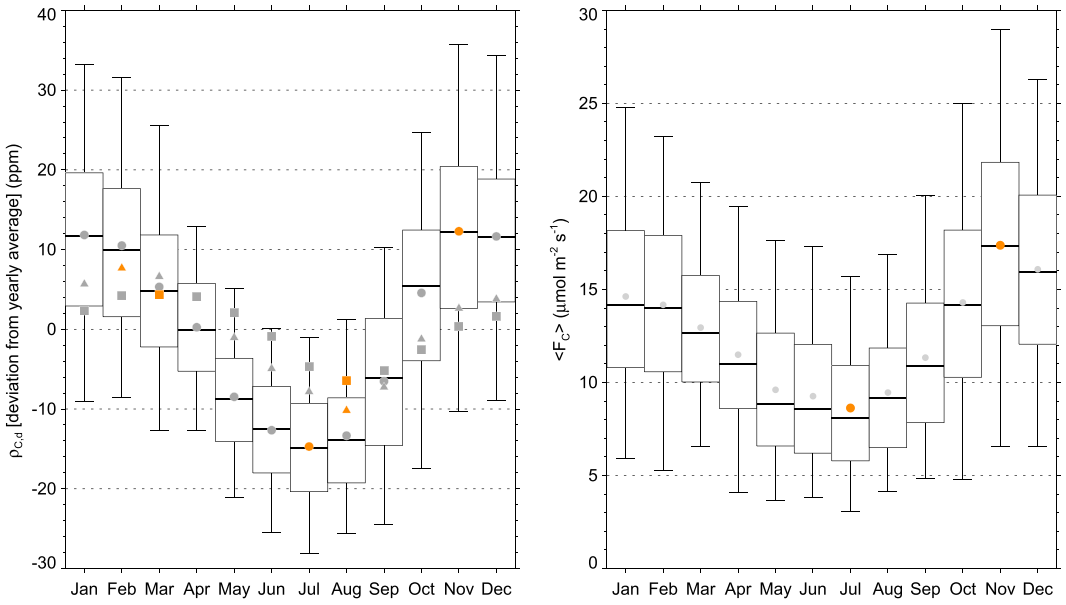

Figure 9. (left) Average seasonal amplitude (deviation from yearly mean) of ρ_C for BKLI (circle), SAL (triangles), and JFJ (squares) and (right) average seasonal amplitude of $<F_C>$ at BKLI. Depicted are average monthly values of $\rho_{C,d}$ calculated from daily averages corrected for long-term trend of each station. Winter and summer peak values are marked orange. Boxplots as in Figure 5.

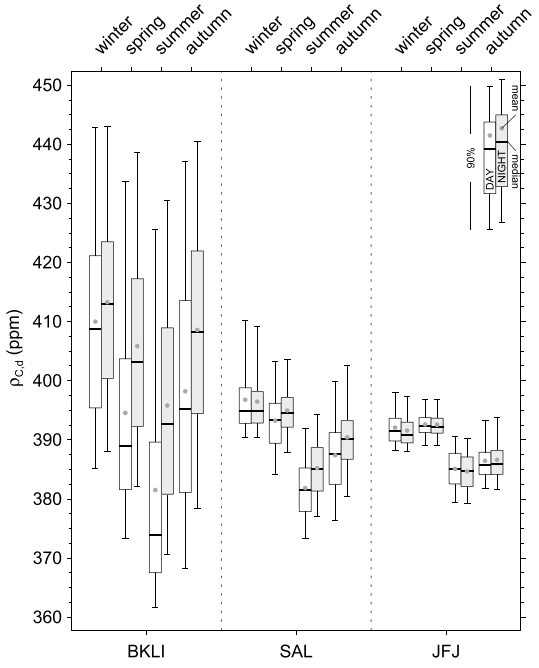

Figure 10. Average seasonal daytime and nighttime $\rho_{C,d}$ for BKLI, SAL, and JFJ. Values are corrected for long-term trend, and the long-term mean is added afterward.

London *Hernández-Paniagua et al.* [2015] report 2.5 ppm yr^{-1} for the period between 2000 and 2012, and the most recent IPPC report [*IPCC*, 2013] specifies a global trend of 2.0 ppm yr^{-1} between 2001 and 2013 calculated from Mauna Loa and South Pole data.

Even though the secular trend reveals that regional and local ρ_C is interconnected concerning long-term trends, the variation in local ρ_C can be large. The year-to-year growth rate at BKLI, for example, varies from -1.7 ppm yr^{-1} (2006 to 2007) to 4.6 ppm yr^{-1} (2010 to 2011) and was unexceptionally high from 2013 to 2014 with 13.4 ppm yr^{-1}. Nevertheless, the average yearly growth rate is 2.6 ppm yr^{-1} and thus of the same order of magnitude than the calculated linear trend which led to an increase in ρ_C from 393.8 ppm in 2005 up to 417.0 ppm in 2014. Since 2010, the average yearly ρ_C never dropped below the 400 ppm margin again.

The average seasonal drop of ρ_C from winter mean to summer mean is 22.0 ppm, and the average raise from summer mean

AGU Journal of Geophysical Research: Atmospheres 10.1002/2016JD025063

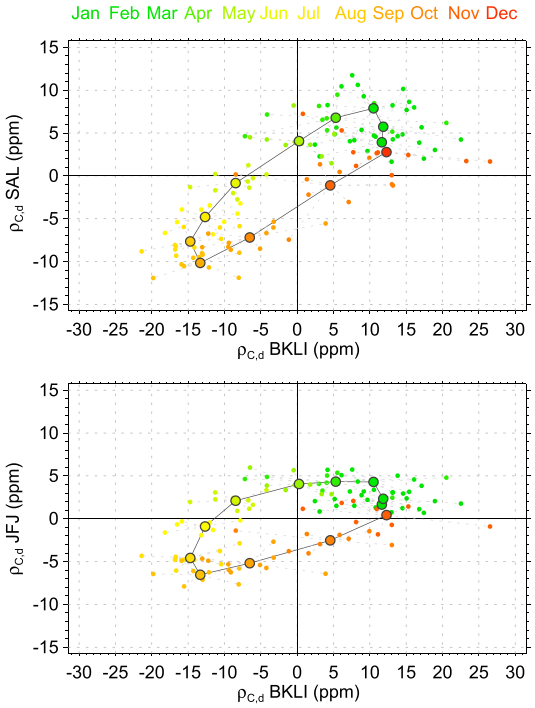

Figure 11. Hysteresis between detrended $\rho_{C,d}$ of (top) BKLI and SAL as well as (bottom) BKLI and JFJ. Depicted are monthly mean values (small dots) and average monthly values (large dots).

to winter mean is 24.9 ppm. The average peak to trough (Figure 7a) drop (max to min) and raise (min/max.) values are slightly higher with 26.8 ppm and 29.5 ppm, respectively. For single years the seasonal drop and raise of ρ_C in spring can be as large as 25.7 ppm (2006) and 30.8 ppm (2013) or as low as 17.0 ppm (2005) and 19.1 ppm (2006). The average yearly course of ρ_C is visualized in Figure 9a by monthly mean values based on daily averages corrected for long-term trend. The seasonal amplitude is skewed, and the raise of ρ_C in autumn occurs faster than the drop in spring. During winter month the variability is slightly larger, which reflects the fact that ρ_C varies more in the shallow wintertime boundary layer due to the smaller mixing volume compared to the better mixed and more evolved boundary layer during summer month. The winter maxima at BKLI occur relatively regularly in late November or early December, whereas the summer minima appear between June and August. The variability in summertime peaks is generally larger ($\sigma = 2.1$ ppm, where σ is the standard deviation) compared to wintertime maximum values ($\sigma = 1.9$ ppm).

3.4.3. Coupling to Background CO_2 Mole Fraction

In Figure 10 average seasonal ρ_C split by season and day/night are shown for BKLI and JFJ. Compared to the regional and tropospheric background mole fraction BKLI shows on average an increased ρ_C of about 10 ppm (SAL) to 11.4 ppm (JFJ) as a result of the nearby strong surface sources of CO_2. While ρ_C always stays above background mole fraction during winter and autumn all the day and also in spring and summer during the night, daytime ρ_C during spring and summer is on average mixed down to the background mole fraction level. Indicated by the statistics in Figure 10, local ρ_C also very frequently drops below the background record. Even though plant uptake of CO_2 at BKLI might not be able to reduce ρ_C that much, the vertical stretching of the BL during the day and large-scale horizontal advection of air masses from the rural surrounding keep the mole fraction below the tropospheric level [*Helfter et al.*, 2011; *Strong et al.*, 2011].

Concerning summer and winter peak, local ρ_C clearly differs from the background record not only in absolute values but also in time when the maxima and minima values are measured during the year. On average ρ_C at BKLI peaks in late November or early December and summertime minima occur in June and July (Figure 7). In contrast ρ_C at SAL and JFJ peaks in February and March, respectively, and both have their minima sometime during August. Whereas the decadal trend and the similarity of seasonal patterns between BKLI, SAL, and JFJ already point toward a direct coupling between local and background ρ_C, the shift in peak refines this relationship. The average exchange between the local BL and the troposphere follows a hysteresis with a delay of up to 3 months in winter and at least 1 month in summer. The hysteresis (Figures 11a and 11b) becomes more distinct with increasing distance to surface sources horizontally and vertically.

Journal of Geophysical Research: Atmospheres 10.1002/2016JD025063

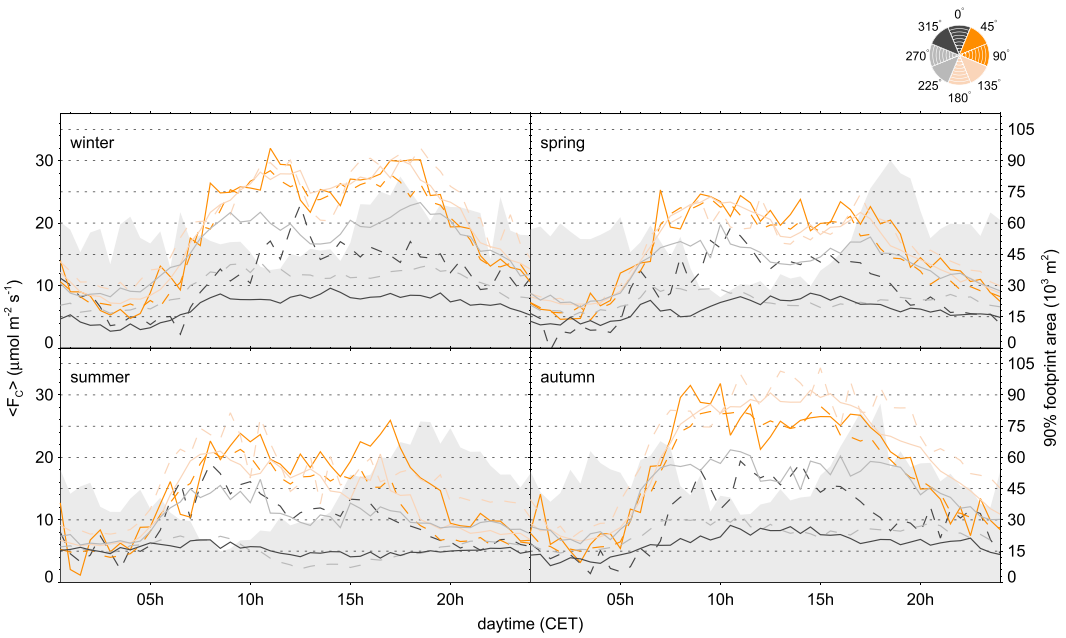

Figure 12. Average sectoral diurnal course of $<F_C>$ for each season. Additionally, the area covered by the 90% footprint contour line is indicated on the secondary *y* axis (grey shaded area).

3.5. Long-Term Time Series of CO_2 Flux

3.5.1. Diurnal Course and Yearly Variability of $<F_C>$

Average diurnal courses of $<F_C>$ were derived from 30 min data separated by season and weekday/weekend (Figures 5c and 5d). Generally, the diurnal course of $<F_C>$ follows the daily dynamic of the traffic. The direct relationship between $<F_C>$ and the diel cycle of traffic has already been reported by a number of studies qualitatively [*Coutts et al.*, 2007; *Moriwaki and Kanda*, 2004; *Song and Wang*, 2012; *Vogt et al.*, 2005] and quantitatively [*Lietzke and Vogt*, 2013; *Velasco et al.*, 2005]. Both traffic and $<F_C>$ follow a dual peaked pattern with minimum values in the early morning and two maxima corresponding to the morning and evening rush hour. Between the rush hours there is a depression at noon. The two peaks of $<F_C>$ relating to the two rush hours around 08:00–09:00 in the morning and 16:00–17:00 in the afternoon are apparent during all seasons. Nevertheless, the afternoon peak in $<F_C>$ is slightly reduced in spring and summer. If sectorial diurnal courses of $<F_C>$ are considered for different seasons (Figure 12) it becomes clear that the smaller afternoon peak is persistent for all wind directions in spring and summer and is thus not a direct function of wind direction. Figure 12 additionally shows the average diurnal course of the calculated footprint area (90% contour line) for each season. Generally, the footprint extends the most in afternoon and shows a minimum between 06:00 and 12:00 in the morning. The diurnal course is less developed in autumn and winter but shows a very distinct shape during spring and summer. The larger footprint in the afternoon, mainly caused by higher wind speed, results in smaller CO_2 fluxes because the additional extent of the footprint area damps the impact of the strong nearby traffic source and leads to a better mixed CO_2 input. During autumn and winter additional sources are active due to heating activity; thus, the footprint size does not affect the CO_2 signal the same. Still, also during the winter months a damping effect on the afternoon peak is observable, if the fact is taken into account that the evening traffic rush hour is more intensive compared to the morning traffic peak.

All over the year, lowest fluxes are measured in the early morning (03:00–04:00) with 5–6 $\mu mol\,m^{-2}\,s^{-1}$. This is when traffic volume, heating activity, and human activity, in general, are lowest. The daily minimum is also consistent for weekdays and weekends. Thus, the base load of the CO_2 emissions of the urban metabolism at BKLI seems to prohibit $<F_C>$ dropping below the threshold of approximately 5 $\mu mol\,m^{-2}\,s^{-1}$ on average.

AGU Journal of Geophysical Research: Atmospheres 10.1002/2016JD025063

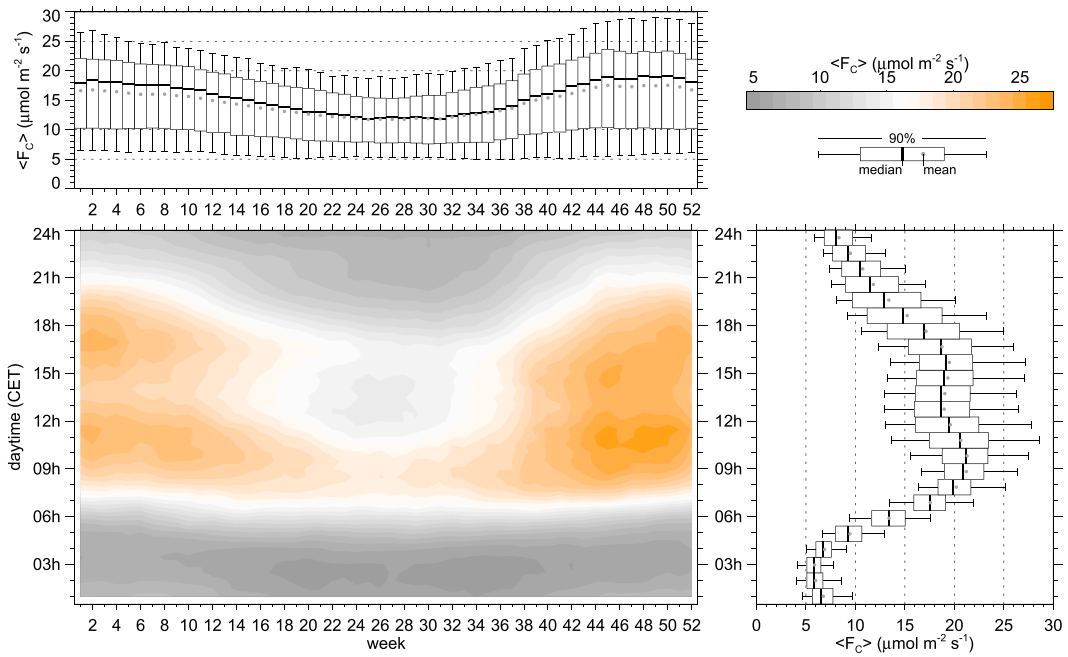

Figure 13. Isopleth diagram for 7 day bins of $<F_C>$ with (top) average seasonal and (right) average diurnal courses. Color levels indicate steps of 1 µmol m^{-2} s^{-1}.

Highest values usually occur during the morning rush hour ranging between 20–25 µmol m^2 s^{-1} in winter/autumn and 15–20 µmol m^{-2} s^{-1} in summer. Average daily values reach from 11.2 µmol m^{-2} s^{-1} in summertime to 16.6 µmol m^{-2} s^{-1} during the winter month, and the variability during winter and autumn is larger ($\sigma = 1.42$ and $\sigma = 1.29$) compared to spring and summer ($\sigma = 0.6$ and $\sigma = 0.64$). Generally, the interannual variability is lower during periods with lower activity of CO_2 sources (summer, nighttime). On average, positive values are recorded for all seasons and all years, which accentuates that CO_2 uptake by photosynthesis is too weak to completely offset the CO_2 emissions. Minor effects of photosynthetic activity can be observed for sectors 6 and 7, where the daytime $<F_C>$ slightly drops below the nocturnal values during summer (Figure 12). The seasonal pattern of the diurnal course of $<F_C>$ is depicted in Figure 13 also by an isopleth diagram. Especially, in the morning, one can recognize that $<F_C>$ starts to increase earlier between weeks 13 and 43 as a result of the shift between daylight saving time and standard time. This highlights the direct influence of human activity on the diurnal course of CO_2.

3.5.2. Interannual Anomaly of CO_2

In Figure 7b a 90 day running mean filter was applied to $<F_C>$. Generally, $<F_C>$ follows a sinusoidal pattern with maximum values between 14.2 and 17.7 µmol m^{-2} s^{-1} during winter and minimum values between 10.0 and 11.4 µmol m^{-2} s^{-1} during summer. The variability of the winter time peak ($\sigma = 1.19$) is larger than the summer minima ($\sigma = 0.52$), and the interquartile range (IQR) also points out that variation in $<F_C>$ is generally larger during winter months (IQR ≈ 10–15 µmol m^{-2} s^{-1}) compared to summer month (IQR ≈ 5–8 µmol m^{-2} s^{-1}). The variability is only weakly represented by the lower quartile, whereas the upper quartile follows well the interannual differences both during winter and summer. The seasonal statistics reveal again that $<F_C>$ minima values occur around 5 µmol m^{-2} s^{-1}. This value is slightly higher during winter, when the base load of the city is on a higher level due to additional CO_2 emissions from heating activity and possibly plant respiration. Additionally, the seasonal course of $<F_C>$ shows again that photosynthetic activity is far from offsetting the CO_2 emissions. This is also observed in most other comparable urban environments, and only studies from vegetated suburban neighborhoods report clear offsetting effects by vegetation [*Bergeron and Strachan*, 2011; *Crawford et al.*, 2011; *Ramamurthy and Pardyjak*, 2011; *Velasco et al.*, 2013].

The seasonal amplitude of $<F_C>$ is on average 4.2 µmol m^{-2} s^{-1} ($\sigma = 0.95$) for the drop in spring and 4.1 µmol m^{-2} s^{-1} ($\sigma = 0.94$) for the raise in autumn. Large raise of $<F_C>$ in autumn is usually followed by large

Journal of Geophysical Research: Atmospheres 10.1002/2016JD025063

drop in spring, because variability in winter maxima is much larger and $<F_C>$ always drops to similar values in summer. Peak dates of $<F_C>$ are comparable to those of ρ_C; thus, winter maxima are generally reached in early December, whereas the summertime minimum occurs around July. Winter peak dates are very consistent and vary only little. Summertime minima peak dates in contrast are scattered from late June until early August.

If temperature as a measure for heating activity is considered as the main driver for seasonal variation of $<F_C>$, the winter peaks occur unexpectedly early. If the yearly course of temperature is considered, minimum values are usually recorded in early January, which is approximately 1 month after the peak in $<F_C>$. Despite the fact that $<F_C>$ follows the seasonal course of air temperature, the relationship between $<F_C>$ and heating activity controlled by air temperature is not straightforward and has to be validated furthermore with, e.g., current energy consumption data. To demonstrate this issue, heating degree days (HDD) as a measure for heating activity are plotted in Figure 7c. Clearly, the maximum values are reached after New Year's Day in most occasions. From these values, peak date of $<F_C>$ is rather expected to occur in mid-January. The small footprints in autumn compared to the larger ones in winter possibly explain the relatively early peak of $<F_C>$. Accordingly, in autumn strong nearby CO_2 sources (e.g., Klingelbergstrasse) contribute more to $<F_C>$, whereas the larger footprint in winter leads to a generally better mixed CO_2 signal, because the relative contribution of point or linear sources decreases.

3.5.3. Secular Trends and Long-Term Behavior of $<F_C>$

Between 2005 and 2009 $<F_C>$ clearly shows a decrease, but this period is followed by 3 years of slightly higher fluxes. Following the linear trend calculated over the last 10 years $<F_C>$ is reduced by $-0.65\ \mu mol\ m^{-2}\ s^{-1}$. Even though the trend points toward the expected direction, it is surprisingly low. The analysis of the nearby traffic count data shows that due to the opening of the northern traffic bypass in 2007/2008, total traffic volume at BKLI was reduced by approximately 25% between 2005 and 2014 (Figure 7c). By comparison, $<F_C>$ was reduced by 4.7% within the same period. Even though the reduction in traffic volume seems to have a reducing effect on $<F_C>$, the correlation is relatively weak (not shown). This is in contrast to the very strong relations achieved by regression analysis of diurnal cycles of $<F_C>$ and traffic. The question then arises as to how far a single nearby traffic count is representative for the investigation area. From the current data, it seems as the shape of the diurnal cycle of $<F_C>$ is given by the increase and decrease of the traffic volume, but the absolute $<F_C>$ values are not solely controlled by direct traffic emissions.

First, the measured F_C is possibly composed of emissions not only from the nearby Klingelbergstrasse. Thus, the reduction of 25% in traffic volume is not necessarily valid for the whole road network within the footprint area. On a city scale traffic is actually not reduced but translocated. Additionally, changes in vehicle fleet composition and vehicle emission efficiency due to recent technologies are also influencing the CO_2 emissions but are difficult to account for and remain an uncertainty factor.

Second, the turbulent transport mechanisms from the source within the street canyon up to the measurement device are still not completely understood. For example, *Lietzke and Vogt* [2013] showed that at BKLI for east winds, in-canyon vortex structures work against the vertical transport, in contrast to west wind flows, where the vertical transport of air masses inside the canyon is enhanced. Due to these complex transport mechanisms, a linear relationship between emitted CO_2 or traffic volume and measured $<F_C>$ for all situations might be too simple. In addition, it is worth mentioning that while values of $<F_C>$ reported in literature (overview in *Lietzke et al.* [2015]) compare well between different sites, the corresponding traffic amounts do not reflect any simple correlation. There are many sites with measured $<F_C>$ far below the one at BKLI, but with 2 or 3 times the daily amount of traffic and vice versa.

Lastly, besides traffic volume other controlling factors (heating, vegetation, human activity, footprint variability etc.) are influencing the magnitude of $<F_C>$. Because these controlling factors do not implicitly show the same long-term trends, linear regressions from short investigation periods are not transferable to long-term time series.

4. Conclusions

This is the first study to present a full decade of urban CO_2 flux (F_C) measurements. The general long-term behaviors of CO_2 mole fraction (ρ_C) and F_C were analyzed from 10 years of open-path eddy covariance (EC)

AGU Journal of Geophysical Research: Atmospheres 10.1002/2016JD025063

measurements at the BKLI site between 2005 and 2014. So far, only little is known about the long-term trends of F_C in urban environments. Multiyear records of ρ_C and F_C are available for natural ecosystems, but rare for heterogeneous urban environments. Longest time series reported in literature cover at most 5–6 years, and thus, the analysis of the BKLI long-term data contributes substantially to the better understanding of seasonality and long-term variability of CO_2 in cities.

In contrast to relatively homogeneous footprints of natural ecosystems, the highly heterogeneous urban area increases the requirements for data post processing in order to achieve reliable and comparable results. Besides well-known processing steps for big data like gap-filling, our study proved the necessity of horizontal averaging for F_C to minimize effects of heterogeneous distribution in time and space of sources and sinks around the measurement site as well as the impact of changing diurnal and seasonal wind system. Another main advantage of horizontal averaging is that the comparability of data sets from different measurement sites can be improved considerably, because site-specific properties like wind system and source distribution are properly weighted and thus less influencing the variability factors of F_C.

The analysis of long-term ρ_C in the urban environment of Basel reveals good consistency with background concentration measurements at GAW stations (Schauinsland and Jungfraujoch), both in terms of seasonality and long-term trend (+2 ppm yr^{-1}). Between local and background ρ_C a phase shift of up to 3 months in winter and around 1 month in summer is observable. This can be explained by the time needed to mix the CO_2 from local near-surface air masses to the lower troposphere. The different time scales of this mixing process in winter and summer result from the varying mixing conditions in the boundary layer over the year. Being aware that it is not the intended purpose of open-path gas analyzers to deliver high-accuracy absolute CO_2 concentration measurements, the results of this study clearly prove a sufficiently high data quality to perform general trend analysis and detailed investigations on daily, seasonal, and even annual scales in urban environments.

Apart from typical diurnal, weekly, and seasonal features the current data give new insights into the temporal patterns and the variability of F_C also on interannual time scales. The relationship between F_C and human activity in urban areas is apparent due to distinct differences between weekday and weekend fluxes, the characteristic dual-peak diurnal course as a result of daily traffic volume, as well as the seasonality which is primarily caused by additional heating activity in winter. The variability of F_C is largest in times of high source activity during the day and especially in winter, but nearly vanishes e.g., in early morning, when most CO_2 sources show the lowest activity. Even though traffic volume was declining during the last decade, F_C was only reduced by roughly 5%. Clearly, the short-term variabilities in time and space caused by the highly heterogeneous environment and the local meteorology are superimposing any long-term tendency happening on much smaller scales.

Generally, the applicability of the EC method in heterogeneous urban environments is supported, even though basic theoretical requirements like stationarity or horizontal homogeneity are rarely fulfilled. But still, too few time series are available yet, which would be absolutely necessary as a solid data base for the increasing number of modeling approaches reported in literature as well as for intercomparisons of observed long-term pattern using horizontal averaging.

Acknowledgments
Research leading to this paper received funding from the project "Urban Climate Study of Bucharest" (IZERZ0_142160) made possible by the Romanian-Swiss Research Program. Special thanks go to the local authorities of Basel for open access to geospatial statistics and GIS data; the Luftmessnetz des Umweltbundesamtes, Germany, and the University of Bern, Switzerland, for providing the GAW data; as well as to Björn Lietzke for proofreading. The data used are listed in the references or available from the MCR-Lab on request (mi.schmutz@unibas.ch).

References

Aubinet, M., T. Vesala, and D. Papale (2012), *Eddy Covariance a Practical Guide to Measurement and Data Analysis*, Springer, New York, doi:10.1007/978-94-007-2351-1.

Bergeron, O., and I. B. Strachan (2011), CO_2 sources and sinks in urban and suburban areas of a northern mid-latitude city, *Atmos. Environ.*, *45*(8), 1564–1573, doi:10.1016/j.atmosenv.2010.12.043.

Bjorkegren, A. B., C. S. B. Grimmond, S. Kotthaus, and B. D. Malamud (2015), CO_2 emission estimation in the urban environment: Measurement of the CO_2 storage term, *Atmos. Environ.*, *122*, 775–790, doi:10.1016/j.atmosenv.2015.10.012.

Christen, A. (2005), Atmospheric turbulence and surface energy exchange in urban environments: Results from the Basel Urban Boundary Layer Experiment (BUBBLE), in *Stratus*, edited by E. Parlow, 142 pp., Univ. of Basel, Basel, Switzerland, doi:10.5451/unibas-003631734.

Christen, A. (2014), Atmospheric measurement techniques to quantify greenhouse gas emissions from cities, *Urban Clim.*, *10*, 241–260, doi:10.1016/j.uclim.2014.04.006.

Christen, A., N. C. Coops, B. R. Crawford, R. Kellett, K. N. Liss, I. Olchovski, T. R. Tooke, M. van der Laan, and J. A. Voogt (2011), Validation of modeled carbon-dioxide emissions from an urban neighborhood with direct eddy-covariance measurements, *Atmos. Environ.*, *45*(33), 6057–6069, doi:10.1016/j.atmosenv.2011.07.040.

Contini, D., A. Donateo, C. Elefante, and F. M. Grasso (2012), Analysis of particles and carbon dioxide concentrations and fluxes in an urban area: Correlation with traffic rate and local micrometeorology, *Atmos. Environ.*, *46*, 25–35, doi:10.1016/j.atmosenv.2011.10.039.

AGU Journal of Geophysical Research: Atmospheres 10.1002/2016JD025063

Coutts, A. M., J. Beringer, and N. J. Tapper (2007), Characteristics influencing the variability of urban CO_2 fluxes in Melbourne, Australia, *Atmos. Environ.*, *41*(1), 51–62, doi:10.1016/j.atmosenv.2006.08.030.
Crawford, B., and A. Christen (2014), Spatial variability of carbon dioxide in the urban canopy layer and implications for flux measurements, *Atmos. Environ.*, *98*, 308–322, doi:10.1016/j.atmosenv.2014.08.052.
Crawford, B., C. S. B. Grimmond, and A. Christen (2011), Five years of carbon dioxide fluxes measurements in a highly vegetated suburban area, *Atmos. Environ.*, *45*(4), 896–905, doi:10.1016/j.atmosenv.2010.11.017.
Falge, E., et al. (2001), Gap filling strategies for defensible annual sums of net ecosystem exchange, *Agric. For. Meteorol.*, *107*(1), 43–69, doi:10.1016/S0168-1923(00)00225-2.
Feigenwinter, C., R. Vogt, and A. Christen (2012), Eddy covariance measurements over urban areas, in *Eddy Covariance a Practical Guide to Measurement and Data Analysis*, edited by M. Aubinet, T. Vesala, and D. Papale, pp. 377–397, Springer, New York, doi:10.1007/978-94-007-2351-1_16.
Foken, T., and B. Wichura (1996), Tools for quality assessment of surface-based flux measurements, *Agric. For. Meteorol.*, *78*(1–2), 83–105, doi:10.1016/0168-1923(95)02248-1.
Foken, T., M. Göckede, M. Mauder, L. Mahrt, B. Amiro, and W. Munger (2005), Post-field data quality control, in *Handbook of Micrometeorology*, vol. 29, pp. 181–208, Kluwer Acad., New York, doi:10.1007/1-4020-2265-4_9.
Geodaten Kanton Basel-Stadt (2015), Grundbuch- und Vermessungsamt, Fachstelle für Geoinformation, Switzerland. [Available at http://www.geo.bs.ch/.]
Gioli, B., P. Toscano, E. Lugato, A. Matese, F. Miglietta, A. Zaldei, and F. P. Vaccari (2012), Methane and carbon dioxide fluxes and source partitioning in urban areas: The case study of Florence, Italy, *Environ. Pollut.*, *164*, 125–131, doi:10.1016/j.envpol.2012.01.019.
Göckede, M., et al. (2007), Quality control of CarboEurope flux data Part I: Footprint analyses to evaluate sites in forest ecosystems, *Biogeosci. Discuss.*, *4*(6), 4025–4066, doi:10.5194/bgd-4-4025-2007.
Grimmond, C. S. B., T. S. King, F. D. Cropley, D. J. Nowak, and C. Souch (2002), Local-scale fluxes of carbon dioxide in urban environments: Methodological challenges and results from Chicago, *Environ. Pollut.*, *116*(Suppl.1), S243–S254, doi:10.1016/S0269-7491(01)00256-1.
Helfter, C., D. Famulari, G. J. Phillips, J. F. Barlow, C. R. Wood, C. S. B. Grimmond, and E. Nemitz (2011), Controls of carbon dioxide concentrations and fluxes above central London, *Atmos. Chem. Phys.*, *11*(5), 1913–1928, doi:10.5194/acp-11-1913-2011.
Hernández-Paniagua, I. Y., D. Lowry, K. C. Clemitshaw, R. E. Fisher, J. L. France, M. Lanoisellé, M. Ramonet, and E. G. Nisbet (2015), Diurnal, seasonal, and annual trends in atmospheric CO_2 at southwest London during 2000–2012: Wind sector analysis and comparison with Mace Head, Ireland, *Atmos. Environ.*, *105*, 138–147, doi:10.1016/j.atmosenv.2015.01.021.
Hofmann, D. J., J. H. Butler, and P. P. Tans (2009), A new look at atmospheric carbon dioxide, *Atmos. Environ.*, *43*(12), 2084–2086, doi:10.1016/j.atmosenv.2008.12.028.
Intergovernmental Panel on Climate Change (IPCC) (2013), *Climate Change 2013: The Physical Science Basis. Contribution of Working Group I to the Fifth Assessment Report of the Intergovernmental Panel on Climate Change*, 1535 pp., Cambridge Univ. Press, Cambridge, U. K., doi:10.1017/CBO9781107415324.
Intergovernmental Panel on Climate Change (IPCC) (2014), *Climate Change 2014: Mitigation of Climate Change. Contribution of Working Group III to the Fifth Assessment Report of the Intergovernmental Panel on Climate Change*, Cambridge Univ. Press, Cambridge, U. K.
Kormann, R., and F. X. Meixner (2001), An analytical footprint model for non-neutral stratification, *Boundary Layer Meteorol.*, *99*(2), 207–224, doi:10.1023/a:1018991015119.
Lietzke, B., and R. Vogt (2013), Variability of CO_2 concentrations and fluxes in and above an urban street canyon, *Atmos. Environ.*, *74*, 60–72, doi:10.1016/j.atmosenv.2013.03.030.
Lietzke, B., R. Vogt, C. Feigenwinter, and E. Parlow (2015), On the controlling factors for the variability of carbon dioxide flux in a heterogeneous urban environment, *Int. J. Climatol.*, doi:10.1002/joc.4255.
Liu, M., J. Wu, X. Zhu, H. He, W. Jia, and W. Xiang (2015), Evolution and variation of atmospheric carbon dioxide concentration over terrestrial ecosystems as derived from eddy covariance measurements, *Atmos. Environ.*, *114*, 75–82, doi:10.1016/j.atmosenv.2015.05.026.
Luftmessnetz des Umweltbundesamtes (2015), WMO World Data Centre for Greenhouse Gases, Germany. [Available at http://ds.data.jma.go.jp/gmd/wdcgg/cgi-bin/wdcgg/download.cgi?index=SSL647N00-UBAG&param=200612120147&select=parameter&parac=observation.]
Marcotullio, P. J., A. Sarzynski, J. Albrecht, N. Schulz, and J. Garcia (2013), The geography of global urban greenhouse gas emissions: An exploratory analysis, *Clim. Change*, *121*(4), 621–634, doi:10.1007/s10584-013-0977-z.
Moffat, A. M., et al. (2007), Comprehensive comparison of gap-filling techniques for eddy covariance net carbon fluxes, *Agric. For. Meteorol.*, *147*(3–4), 209–232, doi:10.1016/j.agrformet.2007.08.011.
Moncrieff, J., R. Clement, J. Finnigan, and T. Meyers (2005), Averaging, detrending, and filtering of Eddy covariance time series, in *Handbook of Micrometeorology*, vol. 29, pp. 7–31, Kluwer Acad., New York, doi:10.1007/1-4020-2265-4_2.
Moncrieff, J. B., J. M. Massheder, H. de Bruin, J. Elbers, T. Friborg, B. Heusinkveld, P. Kabat, S. Scott, H. Soegaard, and A. Verhoef (1997), A system to measure surface fluxes of momentum, sensible heat, water vapour and carbon dioxide, *J. Hydrol.*, *188–189*, 589–611, doi:10.1016/s0022-1694(96)03194-0.
Moriwaki, R., and M. Kanda (2004), Seasonal and diurnal fluxes of radiation, heat, water vapor, and carbon dioxide over a suburban area, *J. Appl. Meteorol.*, *43*(11), 1700–1710, doi:10.1175/jam2153.1.
Park, M.-S., S. J. Joo, and S.-U. Park (2014), Carbon dioxide concentration and flux in an urban residential area in Seoul, Korea, *Adv. Atmos. Sci.*, *31*(5), 1101–1112, doi:10.1007/s00376-013-3168-y.
Pataki, D. E., P. C. Emmi, C. B. Forster, J. I. Mills, E. R. Pardyjak, T. R. Peterson, J. D. Thompson, and E. Dudley-Murphy (2009), An integrated approach to improving fossil fuel emissions scenarios with urban ecosystem studies, *Ecol. Complexity*, *6*(1), 1–14, doi:10.1016/j.ecocom.2008.09.003.
Pawlak, W., K. Fortuniak, and M. Siedlecki (2011), Carbon dioxide flux in the centre of Łódź, Poland-analysis of a 2-year eddy covariance measurement data set, *Int. J. Climatol.*, *31*(2), 232–243, doi:10.1002/joc.2247.
Ramamurthy, P., and E. R. Pardyjak (2011), Toward understanding the behavior of carbon dioxide and surface energy fluxes in the urbanized semi-arid Salt Lake Valley, Utah, USA, *Atmos. Environ.*, *45*(1), 73–84, doi:10.1016/j.atmosenv.2010.09.049.
Raupach, M. R., and R. H. Shaw (1982), Averaging procedures for flow within vegetation canopies, *Boundary Layer Meteorol.*, *22*(1), 79–90, doi:10.1007/bf00128057.
Reichstein, M., et al. (2005), On the separation of net ecosystem exchange into assimilation and ecosystem respiration: Review and improved algorithm, *Global Change Biol.*, *11*(9), 1424–1439, doi:10.1111/j.1365-2486.2005.001002.x.
Reid, K. H., and D. G. Steyn (1997), Diurnal variations of boundary-layer carbon dioxide in a coastal city—Observations and comparison with model results, *Atmos. Environ.*, *31*(18), 3101–3114, doi:10.1016/s1352-2310(97)00050-2.

Journal of Geophysical Research: Atmospheres 10.1002/2016JD025063

Rosenzweig, C., W. Solecki, S. A. Hammer, and S. Mehrotra (2010), Cities lead the way in climate-change action, *Nature*, *467*(7318), 909–911, doi:10.1038/467909a.

Rotach, M. (1995), Profiles of turbulence statistics in and above an urban street canyon, *Atmos. Environ.*, *29*(13), 1473–1486, doi:10.1016/1352-2310(95)00084-c.

Rotach, M. W. (1993), Turbulence close to a rough urban surface part I: Reynolds stress, *Boundary Layer Meteorol.*, *65*(1–2), 1–28, doi:10.1007/bf00708816.

Schmidt, A., T. Wrzesinsky, and O. Klemm (2008), Gap filling and quality assessment of CO_2 and water vapour fluxes above an urban area with radial basis function neural networks, *Boundary Layer Meteorol.*, *126*(3), 389–413, doi:10.1007/s10546-007-9249-7.

Song, T., and Y. Wang (2012), Carbon dioxide fluxes from an urban area in Beijing, *Atmos. Res.*, *106*, 139–149, doi:10.1016/j.atmosres.2011.12.001.

Statistisches Amt Basel-Stadt (2015), Präsidialdepartement, Switzerland. [Available at http://www.statistik-bs.ch/tabellen.]

Strong, C., C. Stwertka, D. R. Bowling, B. B. Stephens, and J. R. Ehleringer (2011), Urban carbon dioxide cycles within the Salt Lake Valley: A multiple-box model validated by observations, *J. Geophys. Res.*, *116*, D15307, doi:10.1029/2011JD015693.

Tans, P., and R. Keeling (2015), NOAA/ESRL, Scripps Inst. of Oceanogr. [Available at scrippsco2.ucsd.edu/.]

University of Bern (2015), WMO World Data Centre for Greenhouse Gases, Switzerland. [Availalbe at http://ds.data.jma.go.jp/gmd/wdcgg/cgi-bin/wdcgg/download.cgi?index=JFJ646N00-KUP&param=201106030001&select=inventory.]

Valentino, F. L., M. Leuenberger, C. Uglietti, and P. Sturm (2008), Measurements and trend analysis of O_2, CO_2 and delta13C of CO_2 from the high altitude research station Junfgraujoch, Switzerland--A comparison with the observations from the remote site Puy de Dome, France, *Sci. Total Environ.*, *391*(2–3), 203–210, doi:10.1016/j.scitotenv.2007.10.009.

Velasco, E., S. Pressley, E. Allwine, H. Westberg, and B. Lamb (2005), Measurements of CO_2 fluxes from the Mexico City urban landscape, *Atmos. Environ.*, *39*(38), 7433–7446, doi:10.1016/j.atmosenv.2005.08.038.

Velasco, E., M. Roth, S. H. Tan, M. Quak, S. D. A. Nabarro, and L. Norford (2013), The role of vegetation in the CO_2 flux from a tropical urban neighbourhood, *Atmos. Chem. Phys.*, *13*(20), 10,185–10,202, doi:10.5194/acp-13-10185-2013.

Velasco, E., R. Perrusquia, E. Jiménez, F. Hernández, P. Camacho, S. Rodríguez, A. Retama, and L. T. Molina (2014), Sources and sinks of carbon dioxide in a neighborhood of Mexico City, *Atmos. Environ.*, *97*, 226–238, doi:10.1016/j.atmosenv.2014.08.018.

Vickers, D., and L. Mahrt (1997), Quality control and flux sampling problems for tower and aircraft data, *J. Atmos. Oceanic Technol.*, *14*(3), 512–526, doi:10.1175/1520-0426(1997)014<0512:qcafsp>2.0.co;2.

Vogt, R. (1995), Theorie, Technik und Analyse der experimentellen Flussbestimmung am Beispiel des Hartheimer Kieferwaldes: Ein Beitrag zu den Energiebilanzuntersuchungen im Reklip, *Stratus*, *3*, 1–101.

Vogt, R., A. Christen, M. W. Rotach, M. Roth, and A. N. V. Satyanarayana (2005), Temporal dynamics of CO_2 fluxes and profiles over a Central European city, *Theor. Appl. Climatol.*, *84*(1–3), 117–126, doi:10.1007/s00704-005-0149-9.

Webb, E. K., G. I. Pearman, and R. Leuning (1980), Correction of flux measurements for density effects due to heat and water vapour transfer, *Q. J. R. Meteorol. Soc.*, *106*(447), 85–100, doi:10.1002/qj.49710644707.

CHAPTER 6

Conclusions

Within this thesis results from more than ten years of EC measurements at a central urban site are presented. Among EC sites covering multiple years of CO_2 observations in other cities, the current dataset is the longest time series available in literature reporting results about urban CO_2 fluxes. The main objective of this thesis was to gain information about the long term behavior of urban CO_2 and to add to the current state of understanding about the transport mechanisms in the UBL.
Specific conclusions of these two topics are found within the corresponding publications in sections 3 - P1 and 5 - P2. Concluding, the results of both studies showed the importance of long-term EC time series on different temporal scales:

- The investigation of turbulent exchange mechanisms on small spatial scales benefit from the solid data base throughout the entire stability range. Thus, the dependence of transport processes in the UBL on atmospheric stability can be analyzed with a much higher resolution and certainty.
- The study of seasonal pattern as well as long-term tendencies can be done with an enhanced significance. The length of the time series helps to better understand the spatial heterogeneity and spatial variability.

Together the large amount of collected data ensures, that the derived results are not only valid for the specific time period of the investigation, but most likely apply in general for investigation areas with similar characteristics. Even if longer time series do not necessarily yield in advanced findings, they help to point at weaknesses from results derived with shorter datasets and they may give other researchers a guideline for the validity of the outcomes of their studies. The findings of this thesis result in the following set of general conclusions towards the benefit of long-term EC time series in urban areas:

Scalar dissimilarity for CO_2 and H_2O needs to be considered in the urban environment. By definition the transport of momentum and sensible heat are (auto-)correlated to the atmospheric stability. The exchange of passive scalars like CO_2 or H_2O on the other hand is by

large parts controlled by the individual source/sink configuration and the prevailing transport processes are of secondary importance. Generally, the transfer efficiency of these two variables is not altered directly by the atmospheric stability conditions. However, the transfer efficiency of CO_2 is weaker under unstable conditions as a result of a counter gradient transport induced by photosynthesis. The interplay between transfer efficiency of CO_2 and uptake by vegetation is most evident by looking at the seasonal and sectorial variation of the transfer efficiency in combination with the dynamics of the solar input and the vegetation fraction of the footprint, respectively. Because CO_2 and H_2O are predominately controlled by their sources, scalar-similarity cannot be assumed and the transport processes of the passive scalars need to be modelled individually.

Seasonal variability of local urban CO_2 concentration is coupled by a hysteresis to the atmospheric background concentration. Remote high accuracy measurements of atmospheric CO_2 concentration are carried out globally to determine the global and regional atmospheric background concentration of CO_2. On average the atmospheric background concentration reflects the seasonal cycle of the sources and sinks on a meso- or macro-scale and long-term trends on a global scale. While these measurements are a useful tool to monitor the CO_2 concentration on large spatial scales, the distance to the effective sources and sinks leads to a considerable delay in the observed seasonal patterns. Whereas local scale measurements in close vicinity to the sources and sinks within an urban environment directly reflect the ongoing changes in the CO_2 concentration, the background concentration measurements are lagged by 2–$3\,\mathrm{month}$ in terms of average CO_2 concentration. This is the case, because some time is needed until CO_2 is mixed throughout the atmosphere and particularly because the atmospheric background concentration of CO_2 is mainly influenced by the much larger seasonal variation of respiration and uptake by the biosphere. This circumstance should be considered when background concentration values are consulted for comparison reasons on scales of less than one year.

Long term trend of urban CO_2 concentration follows the global trend. Cities are hotspots of fossil fuel burning and thus a lot of CO_2 is pumped into the atmospheric pool. As a result the local urban CO_2 concentration stays around $10\,\mathrm{ppm}$ above the background concentration on average. Being a well mixed trace gas, CO_2 is however relatively efficiently mixed across the atmospheric pool even taking into account the delay of several months. As a result, the general global trend around $2\,\mathrm{ppm}$ is also observed locally, even though year to year fluctuations are significantly larger in the local UBL. If the influence of single outlying years is eliminated by statistical analysis, the local urban trend is 0.2–$0.4\,\mathrm{ppm\,y^{-1}}$ larger compared to the background concentration.

The variability of CO_2 fluxes is larger than any observable trend in Basel. The EC method is very sensitive to the ongoing turbulent processes and thus, the variance of the measurements is

usually large. While the exchange of momentum and sensible heat is normally well correlated to the transport processes, the interplay between vertical wind and passive scalars like CO_2 or H_2O is less organized and hence, the calculated EC flux is subject to a much larger variability. Over the course of ten years, a linear trend of $0.65\,\mu mol\,m^{-2}\,s^{-1}$ was found. However, compared to the seasonal and diurnal amplitude of F_C this trend is negligibly small.

Horizontal averages turn results from complex and heterogeneous urban environments into transferable information. The footprint of a single point measurement is by large parts determined by the wind direction and persistent wind regimes may thus bias the average observations towards certain wind sectors. To account for this circumstance the frequency of wind sectors should be considered and a appropriate weighting of the data needs to be applied. The presented approach for the calculation of horizontal averages eliminates the influence of unequal distribution of wind directions on diurnal and seasonal cycles substantially. Applied to fluxes of CO_2 the interpretability of the results in combination with the average characteristics of the investigation area as well as the comparability of the results between different sites is significantly improved. The usage of moving look-up tables better reflects the short term variability and furthermore, the statistics of the look-up tables do not change if new data is added at the end of the time series. At the same time, long-term statistics e.g. trends, can be calculated from these horizontal averages as there is no convergence of the averages towards the mean of the total data population.

How long is long enough? The long-term record increases the probability that all occurrences, which are characterizing the investigation area, are caught and that the observed results are not due to chance. In the urban environment the year to year variability in CO_2 concentration and especially in F_C is considerably large and as such single years might not be a solid representative of the ongoing processes. In turn, it needs to be mentioned, that cities are ever-changing places and that there is mostly no basic state that lasts over years. Adding new data into the time series will always introduce new information to the data and it is unlikely to achieve a state where the investigation area is completely characterized. If the entire dataset of the current study is taken as a base population of F_C, up to ten years of measurements would be needed, to represent the base population without significant differences. In the case of CO_2 concentration, a six-year long dataset is needed, until the calculated linear trend becomes significant in comparison to the individual yearly averages. The fact, that many years are needed to characterize an urban area to greatest possible extend reveals the extremely heterogeneous and ever changing nature of the urban metabolism and the need for more reliable and continuous long-term EC time series..

References

Alados, I. and L. Alados-Arboledas (1999). Validation of an empirical model for photosynthetically active radiation. *International Journal of Climatology 19*(10), 1145–1152.

Aubinet, M., T. Vesala, and D. Papale (Eds.) (2012). *Eddy Covariance*. Springer Netherlands.

Barrett, E. W. and V. E. Suomi (1949). Preliminary report on temperature measurement by sonic means. *Journal of Meteorology 6*(4), 273–276.

Britter, R. E. and S. R. Hanna (2003). Flow and dispersion in urban areas. *Annual Review of Fluid Mechanics 35*(1), 469–496.

Businger, J. A., J. C. Wyngaard, Y. Izumi, and E. F. Bradley (1971). Flux-profile relationships in the atmospheric surface layer. *Journal of the Atmospheric Sciences 28*(2), 181–189.

Christen, A. (2014). Atmospheric measurement techniques to quantify greenhouse gas emissions from cities. *Urban Climate 10*(Part 2), 241 – 260. ICUC8: The 8th International Conference on Urban Climate and the 10th Symposium on the Urban Environment.

Churkina, G. (2016). The role of urbanization in the global carbon cycle. *Frontiers in Ecology and Evolution 3*, 144.

Ciais, P., C. Sabine, G. Bala, L. Bopp, V. Brovkin, J. Canadell, A. Chhabra, R. DeFries, J. Galloway, M. Heimann, C. Jones, C. Le Quéré, R. Myneni, S. Piao, and P. Thornton (2014). Carbon and other biogeochemical cycles. In T. Stocker, D. Qin, G.-K. Plattner, M. Tignor, S. Allen, J. Boschung, A. Nauels, Y. Xia, V. Bex, and P. Midgley (Eds.), *Climate Change 2013: The Physical Science Basis. Contribution of Working Group I to the Fifth Assessment Report of the Intergovernmental Panel on Climate Change*, pp. 465–570. Cambridge, United Kingdom and New York, NY, USA: Cambridge University Press.

Feigenwinter, C., R. Vogt, and A. Christen (2012). Eddy covariance measurements over urban areas. In M. Aubinet, T. Vesala, and D. Papale (Eds.), *Eddy Covariance: A Practical Guide to Measurement and Data Analysis*, pp. 377–397. Dordrecht: Springer Netherlands.

Finkelstein, P. L. and P. F. Sims (2001). Sampling error in eddy correlation flux measurements. *Journal of Geophysical Research: Atmospheres 106*(D4), 3503–3509.

Food and Agriculture Organization of the United Nations (2017). Annual population 2017. http://www.fao.org/faostat/en/#data/OA. Accessed 29/10/2017.

Geodaten Kanton Basel-Stadt (2017). Grundbuch- und Vermessungsamt, Fachstelle für Geoinformation, Switzerland. http://www.geo.bs.ch. Accessed 29/10/2017.

Howard, L. (1818). *The Climate of London*, Volume 1 of *The Climate of London*. W. Phillips, London.

Howard, L. (1820). *The Climate of London*, Volume 2 of *The Climate of London*. W. Phillips, London.

Howard, L. (1833). *The Climate of London*, Volume 1-3 of *The Climate of London*. Harvey and Darton, London.

Hsieh, C.-I., G. Katul, and T. wen Chi (2000). An approximate analytical model for footprint estimation of scalar fluxes in thermally stratified atmospheric flows. *Advances in Water Resources 23*(7), 765 – 772.

Keeling, C. D., R. B. Bacastow, A. E. Bainbridge, C. A. Ekdahl, P. R. Guenther, L. S. Waterman, and J. F. S. Chin (1976). Atmospheric carbon dioxide variations at mauna loa observatory, hawaii. *Tellus 28*(6), 538–551.

Kljun, N., P. Calanca, M. W. Rotach, and H. P. Schmid (2015). A simple two-dimensional parameterisation for flux footprint prediction (ffp). *Geoscientific Model Development 8*(11), 3695–3713.

Kormann, R. and F. X. Meixner (2001). An analytical footprint model for non-neutral stratification. *Boundary-Layer Meteorology 99*(2), 207–224.

Leclerc, M. Y. and T. Foken (2014). *Footprints in Micrometeorology and Ecology*. Springer Berlin Heidelberg.

Leclerc, M. Y. and G. W. Thurtell (1990). Footprint prediction of scalar fluxes using a markovian analysis. *Boundary-Layer Meteorology 52*(3), 247–258.

Lettau, Heinz H. Davidson, B. (1957). *Exploring the Atmosphere's First Mile: Proceedings of the Great Plains Turbulence Field Program, 1 August to 8 September 1953, O'Neill, Nebraska*. Number Bd. 2 in Exploring the Atmosphere's First Mile. Symposium Publications Division, Pergamon Press.

Lietzke, B. and R. Vogt (2013). Variability of CO2 concentrations and fluxes in and above an urban street canyon. *Atmospheric Environment 74*(Supplement C), 60 – 72.

Lietzke, B., R. Vogt, C. Feigenwinter, and E. Parlow (2015). On the controlling factors for the variability of carbon dioxide flux in a heterogeneous urban environment. *International Journal of Climatology 35*(13), 3921–3941.

Lumley, J. L. (1992). Some comments on turbulence. *Physics of Fluids A: Fluid Dynamics 4*(2), 203–211.

Mauder, M. and T. Foken (2004). Documentation and instruction manual of the eddy covariance software package tk2. *Arbeitsergebn, Univ Bayreuth, Abt Mikrometeorol 26*, 42.

Moncrieff, J., R. Clement, J. Finnigan, and T. Meyers (2004). Averaging, detrending, and filtering of eddy covariance time series. In L. B. Lee X., Massman W. (Ed.), *Handbook of Micrometeorology*, Volume 29. Springer, Dordrecht.

Moncrieff, J., J. Massheder, H. de Bruin, J. Elbers, T. Friborg, B. Heusinkveld, P. Kabat, S. Scott, H. Soegaard, and A. Verhoef (1997). A system to measure surface fluxes of momentum, sensible heat, water vapour and carbon dioxide. *Journal of Hydrology 188-189*, 589–611.

Montgomery, R. B. (1948). Vertical eddy flux of heat in the atmosphere. *Journal of Meteorology 5*(6), 265–274.

Munger, J. W., H. W. Loescher, and H. Luo (2012). Measurement, tower, and site design considerations. In M. Aubinet, T. Vesala, and D. Papale (Eds.), *Eddy Covariance: A Practical Guide to Measurement and Data Analysis*, pp. 21–58. Dordrecht: Springer Netherlands.

Obukhov, A. (1951). Charakteristiki mikrostruktury vetra v prizemnom sloje atmosfery (characteristics of the microstructure of the wind in the surface layer of the atmosphere). *Izv AN SSSR, ser Geofiz 3*, 49–68.

Oke, T. (1987). *Boundary Layer Climates*. Vie juridique des peuples [par la] Bibliothèque de droit contemporain. Routledge.

Oke, T. R. (2006). Towards better scientific communication in urban climate. *Theoretical and Applied Climatology 84*(1), 179–190.

Oke, T. R., G. Mills, A. Christen, and J. A. Voogt (2017). *Urban Climates*. Cambridge University Press.

Rotach, M. W., R. Vogt, C. Bernhofer, E. Batchvarova, A. Christen, A. Clappier, B. Feddersen, S.-E. Gryning, G. Martucci, H. Mayer, V. Mitev, T. R. Oke, E. Parlow, H. Richner, M. Roth, Y.-A. Roulet, D. Ruffieux, J. A. Salmond, M. Schatzmann, and J. A. Voogt (2005). Bubble – an urban boundary layer meteorology project. *Theoretical and Applied Climatology 81*(3), 231–261.

Roth, M. (1993). Turbulent transfer relationships over an urban surface. II: Integral statistics. *Quarterly Journal of the Royal Meteorological Society 119*(513), 1105–1120.

Roth, M. and T. R. Oke (1993). Turbulent transfer relationships over an urban surface. i. spectral characteristics. *Quarterly Journal of the Royal Meteorological Society 119*(513), 1071–1104.

Schmid, H. P. (1994). Source areas for scalars and scalar fluxes. *Boundary-Layer Meteorology 67*(3), 293–318.

Schmidt, W. (1928). Über die temperatur- und stabilitätsverhältnisse von seen. *Geografiska Annaler 10*, 145–177.

Schmutz, M., R. Vogt, C. Feigenwinter, and E. Parlow (2016). Ten years of eddy covariance measurements in basel, switzerland: Seasonal and interannual variabilities of urban co2 mole fraction and flux. *Journal of Geophysical Research: Atmospheres 121*(14), 8649–8667. 2016JD025063.

Schneider, A., M. A. Friedl, and D. Potere (2009). A new map of global urban extent from modis satellite data. *Environmental Research Letters 4*(4), 044003.

Schotland, R. M. (1955). The measurement of wind velocity by sonic means. *Journal of Meteorology 12*(4), 386–390.

Schuepp, P. H., M. Y. Leclerc, J. I. MacPherson, and R. L. Desjardins (1990). Footprint prediction of scalar fluxes from analytical solutions of the diffusion equation. *Boundary-Layer Meteorology 50*(1), 355–373.

Scrase, F. (1930). *Some characteristics of eddy motion in the atmosphere*. Geophysical memoirs. H. M. Stationery off.

Seto, K. C., S. Dhakal, A. Bigio, H. Blanco, G. C. Delgado, D. Dewar, L. Huang, A. Inaba, A. Kansal, S. Lwasa, J. E. McMahon, D. B. Müller, J. Murakami, H. Nagendra, and A. Ramaswami (2014). Human settlements, infrastructure and spatial planning. In O. Edenhofer, R. Pichs-Madruga, Y. Sokona, E. Farahani, S. Kadner, K. Seyboth, A. Adler, I. Baum, S. Brunner, P. Eickemeier, B. Kriemann, J. Savolainen, S. Schlömer, C. von Stechow, T. Zwickel, and J. Minx (Eds.), *Climate Change 2014: Mitigation of Climate Change. Contribution of Working Group III to the Fifth Assessment Report of the Intergovernmental Panel on Climate Change*, pp. 923–1000. Cambridge, United Kingdom and New York, NY, USA: Cambridge University Press.

Swinbank, W. C. (1951). The measurement of vertical transfer of heat and water vapor by eddies in the lower atmosphere. *Journal of Meteorology 8*(3), 135–145.

The World Bank (2017). Urban population and population, total, 2016. https://data.worldbank.org/indicator/SP.URB.TOTL. Accessed 29/10/2017.

U.S. Geological Survey (2017). EarthExplorer. https://earthexplorer.usgs.gov. Accessed 29/10/2017.

Wolman, A. (1965). The metabolism of cities. *Scientific American 213*(3), 178–190.

APPENDIX A

Additional Contribution to Research Articles

Micrometeorological long-term measurements conducted in Basel are an important data basis for investigations on various research questions. The data preparation during the course of this thesis made it possible, to contribute to other peoples research, which led to the research articles P3, P4 and P5. This chapter gives an overview of additional contributions to research articles published in scientific journals. Co-authorship for each article is earned by substantial contribution to the data analysis and presentation of the results.

A.1 P3: A dual-inlet, single detector relaxed eddy accumulation system for long-term measurements of mercury flux

Within the PhD Thesis "Land-atmosphere exchange of elemental mercury: new insights using a novel relaxed eddy accumulation and enclosure techniques" (Osterwalder 2016) a new relaxed eddy accumulation (REA) system was developed and tested in the field in order to better quantify fluxes of gaseous elementary mercury (GEM) in different ecosystems. The research article P3 presents results from measurements conducted in Degerö (Sweden) and in Basel at BKLI.

The following chapter is published as a research article in Atmospheric Measurement Techniques:

Osterwalder, S., J. Fritsche, C. Alewell, **M. Schmutz**, M. B. Nilsson, G. Jocher, J. Sommar, J. Rinne, and K. Bishop (2016). Adual-inlet, single detector relaxed eddy accumulation system for long-term measurement of mercury flux. *Atmospheric Measurement Techniques 9*(2), 509-524.

Atmos. Meas. Tech., 9, 509–524, 2016
www.atmos-meas-tech.net/9/509/2016/
doi:10.5194/amt-9-509-2016

Atmospheric Measurement Techniques Open Access EGU

A dual-inlet, single detector relaxed eddy accumulation system for long-term measurement of mercury flux

S. Osterwalder[1], J. Fritsche[1], C. Alewell[1], M. Schmutz[1], M. B. Nilsson[2], G. Jocher[2], J. Sommar[3], J. Rinne[4,5], and K. Bishop[6,7]

[1]Department of Environmental Sciences, University of Basel, Basel, Switzerland
[2]Department of Forest Ecology and Management, Swedish University of Agricultural Sciences, Umeå, Sweden
[3]State Key Laboratory of Environmental Geochemistry, Chinese Academy of Sciences, Guiyang, China
[4]Department of Geosciences and Geography, University of Helsinki, Helsinki, Finland
[5]Finnish Meteorological Institute, Helsinki, Finland
[6]Department of Aquatic Sciences and Assessment, Swedish University of Agricultural Sciences, Uppsala, Sweden
[7]Department of Earth Sciences, University of Uppsala, Uppsala, Sweden

Correspondence to: S. Osterwalder (stefan.osterwalder@unibas.ch)

Received: 5 June 2015 – Published in Atmos. Meas. Tech. Discuss.: 5 August 2015
Revised: 31 December 2015 – Accepted: 18 January 2016 – Published: 15 February 2016

Abstract. The fate of anthropogenic emissions of mercury (Hg) to the atmosphere is influenced by the exchange of elemental Hg with the earth surface. This exchange holds the key to a better understanding of Hg cycling from local to global scales, which has been difficult to quantify. To advance research about land–atmosphere Hg interactions, we developed a dual-inlet, single detector relaxed eddy accumulation (REA) system. REA is an established technique for measuring turbulent fluxes of trace gases and aerosol particles in the atmospheric surface layer. Accurate determination of gaseous elemental mercury (GEM) fluxes has proven difficult due to technical challenges presented by extremely small concentration differences (typically $< 0.5\,\mathrm{ng\,m^{-3}}$) between updrafts and downdrafts. We present an advanced REA design that uses two inlets and two pairs of gold cartridges for continuous monitoring of GEM fluxes. This setup reduces the major uncertainty created by the sequential sampling in many previous designs. Additionally, the instrument is equipped with a GEM reference gas generator that monitors drift and recovery rates. These innovations facilitate continuous, autonomous measurement of GEM flux. To demonstrate the system performance, we present results from field campaigns in two contrasting environments: an urban setting with a heterogeneous fetch and a boreal peatland during snowmelt. The observed average emission rates were 15 and $3\,\mathrm{ng\,m^{-2}\,h^{-1}}$, respectively. We believe that this dual-inlet, single detector approach is a significant improvement of the REA system for ultra-trace gases and can help to advance our understanding of long-term land–atmosphere GEM exchange.

1 Introduction

The UN's legally binding Minimata Convention has been signed by 128 countries since October 2013 and aims to protect human health and welfare by reducing anthropogenic release of mercury (Hg) into the environment (UNEP, 2013a). Current anthropogenic sources, mainly from fossil fuel combustion, mining, waste incineration and industrial processes, are responsible for about 30 % of annual Hg emissions to the atmosphere. Additional 10 % comes from natural geological sources and the remaining 60 % from re-emission of previously deposited Hg (UNEP, 2013b). As a result, long-range atmospheric transport of gaseous elemental mercury (GEM or Hg^0) has led to Hg deposition and accumulation in soils and water bodies well in excess of natural levels even in remote areas, far away from anthropogenic pollution sources (Grigal, 2002; Slemr et al., 2003).

Quantification of Hg emission and deposition is needed to reduce the large gaps that exist in the global Hg mass balance estimates (Mason and Sheu, 2002) and as a basis of legisla-

Published by Copernicus Publications on behalf of the European Geosciences Union.

tion targeting the control of Hg emissions (Lindberg et al., 2007). Gustin et al. (2008) suggest that today a substantial amount of Hg deposited on soils with natural background concentrations of Hg ($< 0.1\ \mu g\ g^{-1}$) is re-emitted back to the atmosphere and that over the course of a year deposition is largely compensated for by re-emission, resulting in a net flux close to 0.

The state of the art in field techniques to quantify Hg flux from terrestrial surfaces has been summarized in review papers (Gustin, 2011; Gustin and Lindberg, 2005; Gustin et al., 2008; Sommar et al., 2013b; Agnan et al., 2016). They conclude that environmental, physicochemical and meteorological factors as well as surface characteristics determine the accuracy and precision of GEM flux measurements. Fluxes are commonly determined using dynamic flux chambers (DFCs) or micrometeorological techniques (relaxed eddy accumulation (REA), modified Bowen ratio (MBR) or the aerodynamic gradient (AGM) method). DFCs are the most widely used technique to measure in situ GEM fluxes since they are easy to handle and inexpensive. However, DFCs alter the enclosed environment of the volume and surface area being studied by affecting atmospheric turbulence, temperature and humidity (Wallschläger et al., 1999; Gillis and Miller, 2000; Eckley et al., 2010). Also the concern about influencing plant physiology means that DFCs are restricted to short-term measurements and studies comparing the relative differences between sites only, e.g., control and treatment experiments (Fritsche et al., 2014).

A major advantage of micrometeorological techniques is that they are conducted under conditions with minimal disturbance. As they can be applied continuously, they provide flux data valuable to characterize ecosystems as sinks or sources of atmospheric Hg and to interpret seasonal flux patterns. Micrometeorological techniques are also able to cover a much larger area than DFC techniques, although this larger "footprint" should be relatively flat and homogeneous. Several studies report results from GEM land–atmosphere exchange measurements over a variety of landscapes using MBR and AGM techniques (e.g., Kim et al., 1995; Meyers et al., 1996; Gustin et al., 2000; Lindberg and Meyers, 2001; Fritsche et al., 2008b; Converse et al., 2010). Fritsche et al. (2008a) concluded that micrometeorological techniques are appropriate to estimate Hg exchange rates but often suffered from large uncertainties due to extremely low concentration gradients over background soils. Eddy covariance (EC) has the potential to detect high-frequency atmospheric GEM concentration fluctuations and might improve flux estimates considerably (Bauer et al., 2002; Faïn et al., 2010). Pierce et al. (2015) conducted the first successful EC flux measurements of GEM over Hg-enriched soils measuring atmospheric GEM concentrations at high frequency (25 Hz). However, on background soils measured fluxes were below the detection limit.

To overcome the need for fast-response sensors, Desjardins (1977) has introduced the eddy accumulation method where fast-response sampling valves are combined with slow analysis techniques on the assumption that the turbulent covariance flux can be averaged separately for positive and negative vertical wind velocities. The technical breakthrough for REA was achieved by Businger and Oncley (1990), simulating the method with vertical wind, temperature and humidity time series in the surface layer. The main advantage of REA over other micrometeorological methods is that REA requires sampling at only one height and therefore flux divergence may be measured directly (Sutton et al., 2001). Reactive substances can be lost by chemical reaction between two sampling heights (Olofsson et al., 2005a; Foken, 2006; Fritsche et al., 2008a), and sensors at two heights also have different footprints. REA eliminates these drawbacks (Bash and Miller, 2008). There are disadvantages to be considered as well though. The technical requirements for REA are very stringent, increasing the demand on the precision of the sampling and chemical analysis. Irregularities in offset measurements and timing of the sampling valves can also not be corrected for later (Sutton et al., 2001).

The REA method has been widely used since 1990 to investigate fluxes of different trace gases and aerosols (e.g., Brut et al., 2004; Gaman et al., 2004; Olofsson et al., 2005a; Haapanala et al., 2006; Arnts et al., 2013). This includes a few applications on land–atmosphere GEM exchange over soils (Cobos et al., 2002; Olofsson et al., 2005b; Sommar et al., 2013a; Zhu et al., 2015a) and forest canopies (Bash and Miller, 2007, 2008, 2009). Additionally, reactive gaseous Hg fluxes have been measured over snow surfaces in the Arctic (Skov et al., 2006). Besides valuable data of net exchange rates of GEM over different environments, the studies have also identified potential for refinement in the technical implementation of REA. The dual detector system presented by Olofsson et al. (2005b) was criticized since it suffered from inherent variability and drift of sensitivity between the two Hg detectors (Sommar et al., 2013a). Sommar et al. (2013a) modified the systems employed by Cobos et al. (2002) and Bash and Miller (2008) to create a single-inlet REA system. However, their system lacks the capability to accumulate samples from the up- and downdraft channels synchronously. The application of sequential measurement of the channels impairs the accuracy with which fluxes can be gauged when the concentration of atmospheric GEM varies on the scale of the sampling period (Zhu et al., 2015b).

Even though there has been steady improvement in REA systems for measuring GEM fluxes, the financial and technical challenges to accurately measure the extremely low concentration differences (sub-ppt range) in up- and downdrafts have limited the number of studies (Foken, 2006). Thus, there remains a demand for a system especially designed to continuously monitor background GEM fluxes with minimum maintenance requirements.

To address these needs we designed a fully automated REA system with two inlet lines for continuous air sampling. The GEM contained in these samples is collected on a pair of

gold cartridges: with one for updraft and the other for downdraft. Two such pairs of gold cartridges are used, with one pair collecting GEM while the other pair is analyzed on a single Hg detector, one cartridge after the other. To detect any instrument drift, contamination and changes in GEM recovery, the system is equipped with a GEM reference gas generator and a Hg zero-air generator.

Our objective was to develop an advanced REA system that reduces the major measurement uncertainty of earlier systems created by sequential sampling procedures. We achieved this goal by

1. continuous, simultaneous sampling of GEM in up- and downdrafts using two pairs of gold cartridges;
2. regular analysis of a GEM reference gas as well as dry, Hg-free air to monitor accurate GEM quantification;
3. fully automated air sampling and GEM analysis with an online user interface that provides comprehensive information about system performance.

To test the system's performance under field conditions, we deployed it in two contrasting environments during campaigns of 2 to 3 weeks each. At the first site in the center of Basel, Switzerland, GEM fluxes were measured 20 m above the roof of a building, 39 m above ground level. Later on the system was installed 1.8 m above a boreal peatland called Degerö in northern Sweden during snowmelt.

This paper includes a description of the novelties in the REA design and presents a time series of GEM flux measurements from each of the deployments with contrasting atmospheric conditions and site characteristics. To analyze the system performance we compared source–sink characteristics using footprint models and analyzed turbulence regimes to determine possible flux attenuation. We briefly discuss several instrumental factors which might affect the accuracy of the flux measurements: bias in vertical wind measurements, control and response time of the REA sampling valves, measurement precision of the sample volumes as well as the performance of analytical schemes and calibration procedures. Furthermore, we describe the evaluation of the β constant, the method detection limit and rejection criteria for flux measurements based on the REA validation procedure.

2 Materials and methods

2.1 GEM-REA sampling system

The concept of our advanced REA design is based on a GEM sampling unit with two pairs of gold cartridges, a single Hg detector as well as a GEM reference gas generator and a zero-air generator. Figure 1 illustrates the setup of the sampling and analysis system. Table S1 in the Supplement lists the major components. Both study sites are equipped with continuously operating EC systems that have been measuring sensible and latent heat flux and CO_2 exchange at 30 min intervals

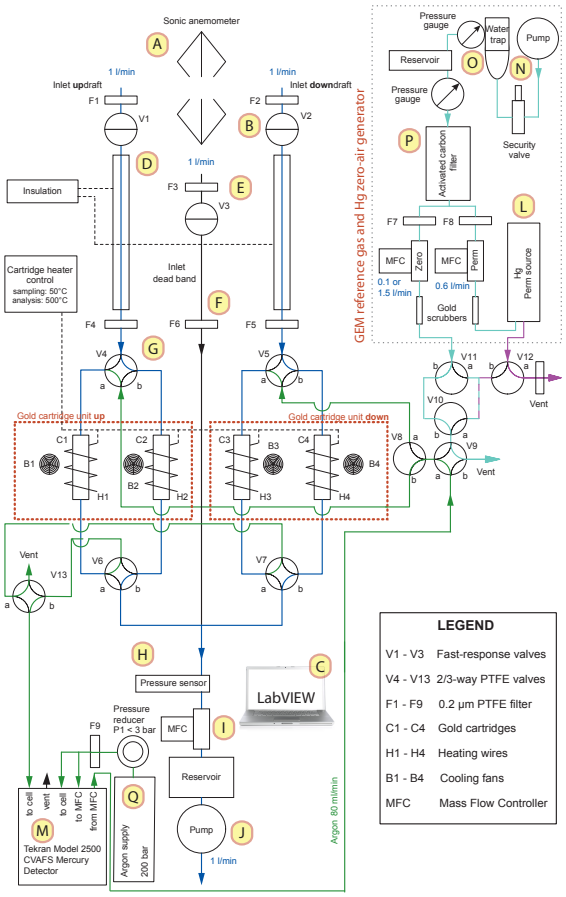

Figure 1. Schematic of the REA system hardware. It consists of a GEM sampling unit, a GEM reference gas generator and a Hg zero-air generator (upper right). Capital letters refer to REA components mentioned in the text and described in Table S1. The air volume drawn over the gold cartridges equaled 1 L min^{-1} in Basel and 1.5 L min^{-1} at Degerö.

(Sagerfors et al., 2008; Lietzke and Vogt, 2013) for many years. A suite of meteorological parameters were recorded as well: solar radiation, air and soil temperature, relative humidity, precipitation, snow depth, wind speed and direction, friction velocity and surface layer stability parameters.

Vertical wind velocity GEM flux quantification was measured with a 3-D sonic anemometer (10 Hz) (A1, A2). The wind signal was transferred to three fast-response switching solenoid valves (B) via LabVIEW (C) enabling sampling and separation of air into updraft, downdraft and deadband channels. The fast-response valves were installed 0.2 m downstream of the sampling inlets. The inlets of the 1/4″ PTFE sampling lines (D) were mounted near the anemometer head about 15 cm below the midpoint of the ultrasonic paths.

GEM carried in the "updrafts" and "downdrafts" was then collected on two pairs of gold cartridges. The flux (ng m^{-2} h^{-1}) was calculated from the GEM concentration difference (ng m^{-3}) in updraft ($\overline{C_u}$) and downdraft ($\overline{C_d}$) air, multiplied by σ_w (m s^{-1}), the standard deviation of vertical wind velocity.

$$F_{GEM} = \beta\sigma_w(\overline{C_u} - \overline{C_d}) \quad (1)$$

β is the unitless flux proportionality coefficient and depends on the wind velocity deadband (see Sect. 3.1.2) that is implemented to increase the concentration difference. β values typically range between 0.4 and 0.6. Deadband widths (m s^{-1}) used in recent REA measurement studies ranged from 0.33 to 0.6 times σ_w (Grönholm et al., 2008).

During the campaign in Basel larger eddies resulted in lower valve switching frequencies relative to the situation at Degerö. The atmospheric GEM concentration differences between updraft and downdraft were also larger in Basel. This made the fixed deadband appropriate for Basel, while a dynamic deadband was more favorable for Degerö. A fixed deadband makes β dependent on atmospheric conditions (Milne et al., 1999, 2001), with increased deadband widths leading to lower β values (Ammann, 1999). The application of a dynamic deadband at Degerö, with its smaller eddies, aimed to reduce the switching frequency of the fast-response valves. Using a dynamic deadband also ensured that large enough air volumes for the GEM analysis were measured that would not have been guaranteed by measuring with a fixed deadband. A dynamic deadband is applied more often (cf. Gaman et al., 2004; Olofsson et al., 2005b; Haapanala et al., 2006; Ren et al., 2011) and enables the use of a constant β (Grönholm et al., 2008).

β was calculated from the sonic temperature for each 30 min period at the same intervals used for the "up" and "down" GEM sampling system:

$$\beta = \frac{(\overline{w'T'})}{\sigma_w(\overline{T_u} - \overline{T_d})}, \quad (2)$$

where $\overline{T_u}$ and $\overline{T_d}$ are the "up" and "down" averages of temperature and $\overline{w'T'}$ is the average EC sensible heat flux. In our application a recursive high-pass filter was implemented to reduce low-frequency bias in turbulent time series of the vertical wind velocity (McMillen, 1988; Richardson et al., 2012):

$$\chi_i = \alpha\chi_{i-1} + (1-\alpha)\chi, \quad (3)$$

where χ_i is the filtered value, χ_{i-1} is the running mean from the previous time step and χ is the current, instantaneous value (Meyers et al., 2006).

$$\alpha = e^{-\frac{\Delta t}{\tau}} \quad (4)$$

The constant α results from the sampling interval of 10 Hz (Δt) and the time constant (τ), which was set to 1000 s.

The sampling lines were 20 m long and insulated to avoid condensation. PTFE filters (E, F) of 0.2 µm were installed after the inlets and before the PTFE valves, V4 and V5 (G). The resistance through the sampling lines was checked to be equal using thermal mass flow meters (Vögtlin Instruments AG, Switzerland). Conditionally sampled GEM is subsequently accumulated on two matched pairs of gold cartridges (Tekran Inc., Canada; difference between cartridge sensitivity < 5 % according to manufacturing tests by the supplier). Heating wires around the cartridges were kept at 50 °C during the sampling phase and heated to 500 °C during the desorption process (see Sect. 2.2). Downstream, a pressure sensor (H) operating at 10 Hz was installed to monitor pressure fluctuations. A high-precision thermal mass flow controller (MFC) (I) with a response time of 50 ms was used to regulate the air volume drawn over the gold cartridges. To dampen sampling flow disturbances a reservoir of 200 mL was installed between the pump and the MFC. Air was drawn through the three lines by a rotary vane pump (J) at a rate of 1 L min^{-1} (Basel) and 1.5 L min^{-1} (Degerö), respectively. Three temperature-controlled, weatherproof boxes (K) contained the GEM reference gas generator (L) and Hg detector (M), the gold cartridge unit and the control system as well as the Hg zero-air generator to produce dry, Hg-free air. Remote control of the system allowed online checks of the data and detection of instrumental failures.

2.2 GEM analysis

Air sampling and GEM analysis was performed in parallel in 30 min intervals (Fig. 2). GEM in air samples and injections from the GEM reference gas and Hg zero-air generator were quantified using cold vapor atomic fluorescence spectrophotometry (M). The temperature-controlled GEM reference gas generator provided precise GEM concentrations in a constant stream of dry, Hg-free air. The average recovery of the GEM standard was determined by back calculation from the manual calibration of the Hg detector. The average ± SD loading on cartridge pair 2–4 corresponded to 27.2 ± 1.1 and 22.2 ± 1.3 pg in Basel and 32.1 ± 2.1 and 32.1 ± 2.3 pg at Degerö. Dry, Hg-free air was generated using an air compressor (N) with air dryer (O) and an activated carbon filter (P). Additional gold mercury scrubbers were installed at the outlet of the Hg zero-air generator.

Figure 2 illustrates the sampling and analysis sequence. Upon startup cartridges C2 and C4 are in the air sampling mode, while GEM previously collected on C1 and C3 is analyzed. During the first 5 min GEM of the idle cartridges is desorbed by heating the cartridges to 500 °C in a stream (80 mL min^{-1}) of high-purity Argon (Ar) carrier gas (Q). The cartridge analysis procedure for individual samples included five steps: Ar flushing (20 s), recording baseline (10 s), cartridge heating (28 s), peak delay (30 s) and cooling of the cartridges (60 s). After up- and downdraft air samples had been analyzed (Aa), the cartridges were loaded for 5 min

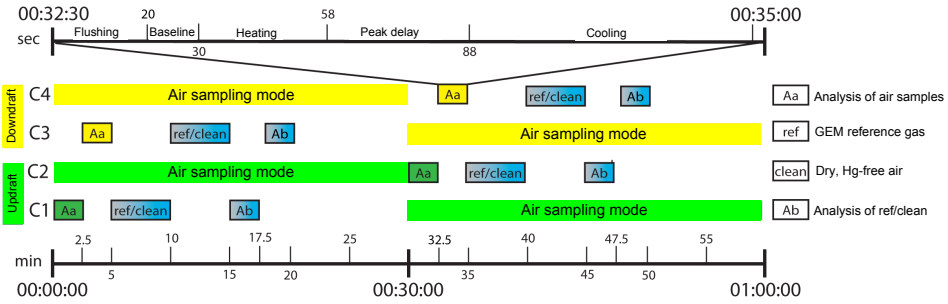

Figure 2. The hourly measuring cycle of the REA system subdivided into the air sampling and GEM analysis procedures (Aa, ref/clean, Ab). At the start of a sequence, cartridge pair C2 and C4 adsorb GEM in the up- and downdraft simultaneously while previously adsorbed GEM from cartridges C1 and C3 is analyzed. During each cycle, eight analysis procedures which last for 2.5 min were conducted.

each with either GEM reference gas (ref) or dry, Hg-free air (clean). The flow rate of dry, Hg-free air (carrier gas) through the GEM reference gas generator was set to 600 mL min^{-1} using a MFC. The GEM reference gas was pre-mixed with 100 mL min^{-1} dry, Hg-free air before being supplied to the cartridges. Dry, Hg-free air was delivered at a flow rate of 1500 mL min^{-1} regulated by another MFC. The cartridges loaded with ref/clean air were analyzed (Ab phase in Fig. 2) following the same procedure as the air samples.

The average and standard deviation of the Hg detector baseline were calculated for periods of three seconds before and after the Hg peak. The baseline below the peak was interpolated and subtracted from the peak. The peak areas were logged together with 30 min averages of the sampled air volume, opening times and number of switching operations of the fast-response valves. Air temperatures within the weatherproof boxes, Hg detector lamp- and UV sensor voltages as well as pressure sensor data were also recorded.

2.3 QA/QC

2.3.1 Calibration of Hg detector

The REA system was calibrated after the field campaigns using a temperature-controlled Hg vapor calibration unit (R) together with a digital syringe (S). Different concentrations of saturated GEM vapor were injected into the Hg-free air stream provided by a Hg zero-air generator (T). During calibration a simulated wind signal was used to supply both lines with an equal amount of air. Calibration factors were gained by linear regression between the injected quantity of GEM and observed peak areas (Fig. S1).

2.3.2 Monitoring of GEM recovery

Repeated injections from the GEM reference gas and Hg zero-air generator (Fig. 2) were performed to observe possible contamination, passivation or drift of the cartridges, as well as to check for temperature sensitivity in the Hg detector. Before and after a measurement campaign the system was checked for leaks by measuring dry, Hg-free air from the Hg zero-air generator and by constricting the sampling lines temporarily to check for pressure decrease within the lines. PTFE parts and tubing were cleaned with 5 % nitric acid according to a standard operating procedure (adapted from Keeler and Landis, 1994).

2.3.3 Bias of sampling lines

To assess potential systematic bias between up- and downdraft sampling lines, GEM reference gas was supplied to both lines. During 5 days in Basel and 28 h at Degerö, the REA system dynamically sampled reference gas using 2 s simulated wind signal to acquire identical up- and downdraft samples with respect to volume and GEM concentration. Accordingly, concentration bias between the REA sampling lines was corrected for in the GEM flux calculation.

2.4 Data processing

The analyzed air samples (Aa) for each cartridge were corrected for temperature sensitivity of the Hg detector by dividing the average GEM reference gas concentration over the entire campaign ($\overline{\mathrm{Ab_r}}$) through single GEM reference gas measurements ($\mathrm{Ab_r}$) according to

$$A_{\mathrm{corr}} = \mathrm{Aa} \cdot \frac{\overline{\mathrm{Ab_r}}}{\mathrm{Ab_r}}. \quad (5)$$

GEM concentrations ($\overline{C_{\mathrm{GEM}}}$) in up- and downdraft were computed by applying intercept (b) and slopes (s) calculated from the manual calibration procedure (Sect. 2.3.1) and the air volumes (V) drawn over the cartridges:

$$\overline{C_{\mathrm{GEM}}} = \frac{A_{\mathrm{corr}} - b}{s} \cdot \frac{1}{V}. \quad (6)$$

GEM concentration differences were corrected for the bias between the two sampling lines (Sect. 2.3.3). Finally, the

GEM flux was derived following Eq. (1). As the sampled air was not dried before being measured with a MFC calibrated for dry air, GEM fluxes were corrected for variations in the water vapor content of the air following Lee (2000):

$$F_{\mathrm{GEMcorr}} = (1 + 1.85\zeta)\,F_{\mathrm{GEM}} + 1.85\frac{\overline{\rho}_{\mathrm{GEM}}}{\overline{\rho}_{\mathrm{a}}}\mathrm{LE}_m, \quad (7)$$

where F_{GEMcorr} is the corrected and F_{GEM} the uncorrected GEM flux (ng m^{-2} h^{-1}). ζ is the water vapor mixing ratio (kg kg^{-1}). LE$_m$ is the water vapor flux (ng m^{-2} h^{-1}), and the ratio of mean GEM density ($\overline{\rho}_{\mathrm{GEM}}$) to mean air density ($\overline{\rho}_{\mathrm{a}}$) were determined from the data for each measurement interval.

Criteria to identify conditions under which REA is not valid will be presented in Sect. 3.1.4. Among them an integral turbulent characteristics test was applied to identify the development of turbulent conditions:

$$\frac{\sigma_{\mathrm{w}}}{u_*} = 1.3 \cdot (1 - 2 \cdot \frac{z}{L})^{\frac{1}{3}}, \quad (8)$$

including σ_{w}, friction velocity (u_*), measuring height (z) and Obukhov length (L). Therein, the dependent integral turbulence characteristic for vertical wind velocity (σ_{w}/u_*) equates with a model dependent on stability (z/L) (Panofsky and Dutton, 1984; Foken and Wichura, 1996; Foken, 2006). A deviation by more than a factor of 2 from the model was used as the threshold to reject periods of insufficient turbulence as well as periods of larger than expected turbulence (Fig. S2).

The effect of a potentially dampened GEM flux due to high- and low-frequency losses of the turbulent eddies has been derived by interpretation of turbulence spectra for both sites dependent on instrumental properties (lateral sensor separation), measuring height, wind speed and stability conditions (Sect. 3.3). The applied high-pass filter (Eqs. 3, 4) amplifies the attenuation by reducing random or systematic noise in the flux estimates caused by low-frequency bias in the turbulent time series. High-frequency attenuation might be caused by an electronic delay of the valve switching and sensor separation (Foken et al., 2012).

To predict the size of REA flux source areas during the campaigns the footprint model of Kormann and Meixner (2001) was applied in Basel and a Lagrangian stochastic forward model following Rannik et al. (2000) at Degerö. The footprint models were chosen in order to fit the specific requirements as defined by the source areas at each site. The actual source area was estimated for each half-hour period based on wind direction, wind speed, stability, surface roughness and sensor height.

2.5 Site descriptions

The climate in the city of Basel, Switzerland (47.56° N, 7.58° E; 264 m a.s.l.), is temperate with a mean annual temperature of +9.8 °C and 776 mm precipitation (MeteoSchweiz, 2016). The REA system was deployed on the flat roof of the University of Basel's Meteorology, Climatology and Remote Sensing Laboratory (MCR) 20 m above the ground. The REA sampling inlets were mounted on the top of the permanently installed tower at 39 m above ground level. The average building height around the tower is 17 m and the 90 % cumulative footprint mirrors dominant wind directions, which are W to NW (240–340°) and ESE (100–140°). Results from this site reflect the situation within the urban inertial sublayer (Lietzke and Vogt, 2013).

The second campaign was conducted at an Integrated Carbon Observatory System (ICOS) site in the center of a boreal peatland in Sweden (64.18° N, 19.55° E; 270 m a.s.l.) during snowmelt. The mixed acid mire system covers 6.5 km^2 and is located in the Kulbäcksliden Research Park of the Svartberget Long-Term Experimental Research (LTER) facility near the town of Vindeln, county of Västerbotten, Sweden. The site is part of the Swedish research infrastructure (funded by the Swedish Research Council). The snow cover normally reaches a depth up to 0.6 m and lasts for 6 months on average (Sagerfors et al., 2008). The average total Hg concentrations in the upper 40 cm of the peatland soil are 57.3± 6.0 ng g^{-1} (± SD) dry matter, which is a typical value for soils in northern Sweden (Shanley and Bishop, 2012; Åkerblom et al., 2013). The climate of the site is defined as humid cold temperate with mean annual precipitation and temperature of 523 mm and +1.2 °C, respectively (Alexandersson et al., 1991). A measurement height of 1.8 m above the surface was maintained by gradually decreasing of the instrumentation boom to account for snowmelt. Dominant wind direction during summer is NE and SE during winter. For a more detailed site description see Granberg et al. (2001) or Peichl et al. (2013).

3 Results and discussion

3.1 REA performance

3.1.1 Sampling accuracy

Compared to single-inlet REA designs, systems with separate inlets for up- and downdraft are less prone to measurement uncertainty due to unsynchronized conditional sampling (Baker et al., 1992) and high-frequency concentration fluctuations in the tube flow (Moravek et al., 2013). Zhu et al. (2015b) found that the calculation of concentration differences based on temporally intermittent GEM measurements (non-stationarity of atmospheric GEM concentrations) introduced the largest source of uncertainty in their single-inlet Hg^0-REA system. Accurate simultaneous sampling of GEM concentration using a two-inlet design is thus the major technical improvement of our system compared to most Hg-REA systems used to date, as summarized in Sommar

et al. (2013a). However, even though the dual-inlet avoids a major source of error, there are a number of other aspects of a Hg-REA system that need to work as well as possible to measure land–atmosphere GEM fluxes. One of these is the determination of the β value, which includes sonic temperature and sensible heat flux measurements (Sect. 3.1.2). It is estimated to introduce an uncertainty similar to Zhu et al. (2015b) of approximately 10 %. Uncertainty due to flux dampening of sampled low- and high-frequency concentration fluctuations is small and just relevant during specific stability and wind speed conditions depending on measurement height and quality of turbulence (Sect. 3.3). There are several other sources of error in the measurements such as (i) the possible bias in vertical wind velocity measurements, (ii) the precision of the switching of the fast-response valves, (iii) the sampled air volume, (iv) the peak integration and (v) the field calibration procedure (cf. Zhu et al., 2015b).

i. Vertical wind velocity is used for instantaneous valve control. Ammann (1999) ascribed the main error here to be the possibility for misalignment between the wind field and the sensor head due to a tilted sensor setup or wind distortion around the sensor. However, the application of a high-pass filter combined with a deadband was able to alleviate averaged vertical wind velocity bias from the wind signal.

ii. It is important to limit the electronic delay to switch the fast-response valves caused by the digital measurements system and signal processing. The effective response time to actuate the fast-response valves was determined to be 18 ms for the opening and 8 ms for the closing. The switching of the fast-response valves allowed a maximal resolution between updraft and downdraft samples of 5.2 Hz.

iii. A major challenge in applying a system with two inlet tubes and no dry Hg-free air addition at the inlets (as applied by Sommar et al., 2013a) is to control flow pressure that builds up within the sampling lines. Flow surges are dependent on the time the fast-response valves remain closed. Pressure variations were dampened by a reservoir of 200 mL volume between the pump and mass flow controller (Fig. 1). The resistance within the lines was initially checked to be equal to minimize pressure anomalies between the three flow paths. A simulated wind signal with fast-response valve opening times of 2 s for the up- and downdraft and 1 s for the deadband was applied and revealed maximal pressure fluctuations of 35 mbar. The vast majority of the 30 min measurements in Basel and Degerö showed higher switching rates which are generally associated with lower pressure fluctuations. The total volumes drawn over updraft, downdraft and deadband lines averaged 30 ± 0.09 in Basel and 45 ± 0.01 L ($\pm$ SD) at Degerö. The proportion of the air not analyzed accounted for 10.5 L in Basel and 20.3 L at Degerö. Measurements were discarded if the volume deviated more than 2.5 % from the flow setting value of the mass flow controller (cf. Sect. 3.1.4).

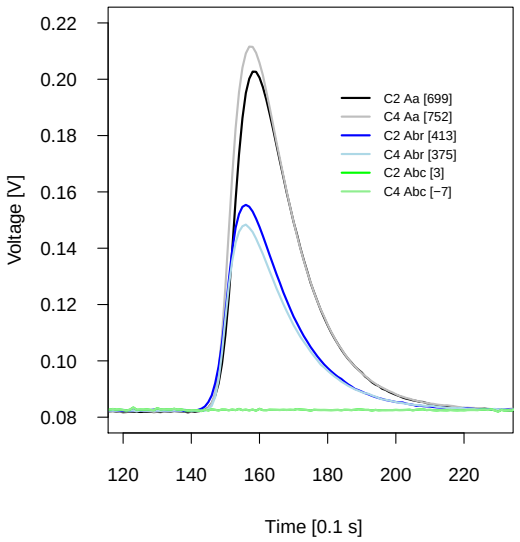

Figure 3. Representative peak recovery for gold cartridge pair C2–C4 during ambient air (Aa), GEM reference gas (Abr) and dry, Hg-free air measurements (Abc) on 11 February 2012, between 14:00 and 15:30 in Basel. The values in squared brackets equal the areas between the curves and the baseline. The plots show an extract of 10 s from the peak delay sequence which takes 30 seconds in total. *Y* axis indicates the Hg detector baseline voltage (V).

iv. An analysis of the detector peaks indicated that the signal for atmospheric and GEM reference gas samples were statistically different from blank measurements (99 % confidence) (Fig. 3).

v. The manual calibration procedure revealed a strong linear relationship between peak areas and syringe-injected GEM reference gas for the cartridge pairs (Fig. S1). The automated injection of GEM reference gas provided a 2-hourly quality control measure to monitor any bias caused by the temperature sensitivity of the Hg detector. The air temperature surrounding the Hg detector showed a strong linear relationship with the GEM reference gas measurements for up- and downdraft in Basel and a less pronounced dependence at Degerö (Fig. 4). The uncertainty of concentration measurements for our REA system is basically introduced by sampling-line bias, wherefrom the method detection limit is derived (Sects. 2.3.3 and 3.1.3).

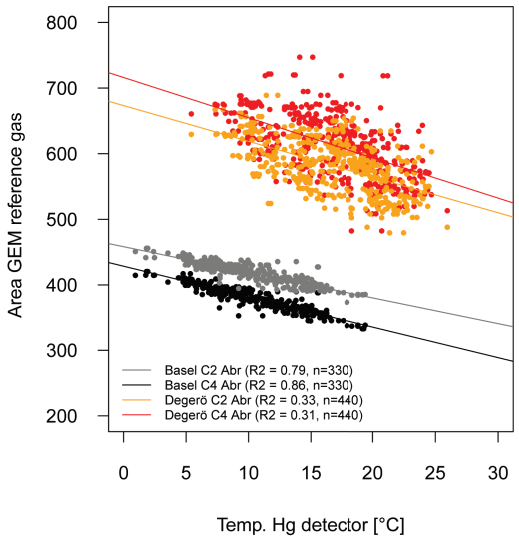

Figure 4. Linear relationship between GEM reference gas (Abr) measured with gold cartridge pair C2–C4 in Basel (grey, black) and Degerö (orange, red) and air temperatures within the Hg detector box.

3.1.2 β-factor evaluation

In this study, β is derived from EC time series of temperature and vertical wind speed at both sites (Eq. 2) during methodologically favorable conditions (cf. Sect. 3.1.4) with respect to turbulence for every 30 min GEM flux measurement averaging period. Due to considerable scatter in β especially during periods when sensible heat flux diminished to near zero, data were omitted for kinematic heat flux within the range of $\pm 0.01\,\mathrm{K\,m\,s^{-1}}$ (Ammann and Meixner, 2002; Sommar et al., 2013a). In accordance with Hensen et al. (2009) only β factors in the range of 0.1–1 were used. During the first study in Basel a fixed deadband of $|w| < 0.2\,\mathrm{m\,s^{-1}}$ was applied. This was done to restrict the analysis to periods when the discrimination between updraft and downdraft was large enough to allow for accurate estimation and to prolong the opening times of the fast-response valves. At Degerö a dynamic deadband approach with a sampling threshold $\pm 0.5\sigma_w$ was used. Data analysis revealed that the effect of surface layer stability or u_* on β calculation was negligible. The median $\pm$ mad (median absolute deviation) of observed β values in Basel and Degerö was 0.49 ± 0.21 ($n = 391$) and 0.45 ± 0.20 ($n = 342$), respectively. Median β values observed at Basel and Degerö concurred with literature in the range of 0.4–0.6 (Grönholm et al., 2008; Bash and Miller, 2009; Arnts et al., 2013; Sommar et al., 2013a).

The Basel measurements resulted in broad non-Gaussian frequency distributions for the fraction of time when air was sampled into up- and down reservoirs. The average cumulated opening times for the 30 min sampling periods for the up- and downdrafts were 9.6 and 9.8 min, respectively, which results in maxima in up/down/deadband sampling fractions of about 32/33/35 %. Periods of less developed turbulence caused the fast-response valves to switch less often and increased the opening times of the deadband. The corresponding confined frequency distributions observed at Degerö were 28/27/45 % and showed significantly lower variation than for the Basel measurements.

3.1.3 Detection limit

The instrument detection limit of the Hg detector was $< 0.1\,\mathrm{ng\,m^{-3}}$ and allowed discernment of GEM peaks from the baseline noise for all measurements. The gold cartridge pair offset criteria and the method detection limit were derived in the field from sampling the same air through updraft and downdraft lines. For this study we defined two strict rejection criteria for (1) maximum standard deviation of the offset of 0.05 and (2) maximum difference in gold cartridge response of 10 %. The assessment of the offset between the sampling lines during the Basel measurements was 0.009 ± 0.06 ($\pm$ SD) and $0.016 \pm 0.01\,\mathrm{ng\,m^{-3}}$ for gold cartridge pairs 1–3 and 2–4, respectively. At Degerö the offset was 0.17 ± 0.06 and $-0.004 \pm 0.02\,\mathrm{ng\,m^{-3}}$ for 1–3 and 2–4. If up- and downdraft lines sample the same air, the offset between these should be constant, independent of air Hg content. Scaling the GEM area difference detected in the up- and downdraft air by GEM area of the updraft air revealed an erroneous behavior of cartridge pair 1–3. Further inspection showed that the PTFE valves (V4–V7) seemed to restrict the air flow when energized, thus leading to erroneous air volume readings. In contrast, when air flows through cartridge pair 2–4, the valves are in the idle mode with free flow. Therefore, measurements with cartridge pair 1–3 were discarded for both campaigns due to the above threshold variability in Basel and the large gold cartridge pair offset at Degerö. Although data availability was reduced by 50 % this technical shortcoming may be solved by use of different valves, e.g., three-way flipper valves. Detailed results from the sampling line bias tests are presented in Figs. S3 and S4.

From these individual sampling lines bias measurements for Basel and Degerö a minimum detectable GEM concentration difference based on 1σ was derived. Thus, 98 % of the available 30 min data in Basel and 83 % at Degerö were above that limit. Zhu et al. (2015b) reported that 55 % of their Hg-REA flux data were significantly different from zero. Data from bias determination for cartridge pair 2–4 did not reveal any significant diurnal pattern or trend over time for both sites.

3.1.4 Data coverage

Based on the systematic bias when using cartridge pair 1–3, 50 % of the data from both sites, Basel and Degerö were discarded (Table 1). Some of the remaining flux measure-

Table 1. Overview of rejection criteria for the evaluation of REA field measurements. Rejected amount of data (%) and remaining numbers of observations (n) are given.

Criterion	Rejection percentage	
	Basel	Degerö
Gold cartridge pair offset	50 %	50 %
Logging failure	4 %	7 %
Insufficient turbulence (σ_w/u_*)	6 %	4 %
Extreme stability ($\lvert z/L\rvert>2$)	0 %	0 %
Sampling air flow and blank irregularities	1 %	4 %
Total rejection (excl. cartridge pair offset)	12 %	16 %
Remaining observations	$n = 292$	$n = 380$

ments were rejected due to logging failures including power breakdowns. Additionally, 6 % of the data at Basel and 4 % at Degerö were rejected due to poorly developed turbulence, determined by applying an integral turbulent characteristics test (Eq. 8). GEM flux measurements during extremely stable conditions were omitted ($z/L>2$). The data were also screened for irregularities in the measured sampling air flow (deviation from the flow setting value > 2.5 %). Dry Hg-free air was used to determine possible cartridge or sampling line contamination and to discard periods of a noisy Hg detector baseline, due to rapid temperature changes within the detector box. GEM flux measurements were discarded when the signal of the blank measurements exceeded 10 % of the integration peak area that was detected for atmospheric GEM. In other Hg-REA studies, 44 % (Sommar et al., 2013a) and 28 % (Zhu et al., 2015b) of the data were flagged as moderate and low data quality due to turbulence characteristics (cf. Mauder and Foken, 2004). In our study the overall half-hourly data loss was 62 % at Basel and 66 % at Degerö.

3.2 Meteorological conditions

During the measurements in Basel air temperatures averaged $-7.9 \pm 3.3\,^{\circ}\mathrm{C}$ ($\pm$ SD). Precipitation occurred in the first 2 days and caused substantial loss of EC data, while GEM flux determination was not affected. From 3 to 12 February 2012, measurements were done during predominantly cloudless conditions with daily solar radiation (Rg) peaks between 300 and 500 $\mathrm{W\,m^{-2}}$. Relative humidity ranged between 20 and 91 % and was on average significantly lower in Basel than at Degerö. Wind speed in Basel averaged 2.6 $\mathrm{m\,s^{-1}}$ and did not differ significantly between day ($\mathrm{Rg} > 5\,\mathrm{W\,m^{-2}}$) and night ($\mathrm{Rg} < 5\,\mathrm{W\,m^{-2}}$). Wind direction was predominantly from the northwest during the day and the southeast during the night. Polar histograms of 30 min averaged wind speed and atmospheric GEM concentration measurements at both sites are presented in Fig. S5. Unstable atmospheric stratification ($z/L<-0.05$) was predominant (92 % of time) during the Basel campaign while less than 3 % of the measurements were conducted during stable conditions ($z/L>0.05$).

The campaign on the boreal peatland commenced on 5 May 2012. The surface was covered by maximum of 33 cm snow which melted away towards the end of the campaign on 24 May 2012. A total precipitation amount of 19.6 mm was recorded during the campaign including a heavy snowfall during the morning of 6 May. Air temperatures averaged $5.4 \pm 3.5\,^{\circ}\mathrm{C}$, whereas daily averages increased from 0.0 to 9.1 °C over the period. Soil temperatures at 2 cm depth likewise increased from 3.2 to 8.0 °C (daily averages). The prevailing wind direction at Degerö was from the northeast to south with an average wind speed at 2.9 $\mathrm{m\,s^{-1}}$ (daytime mean: 3.1 $\mathrm{m\,s^{-1}}$, nighttime mean: 2.1 $\mathrm{m\,s^{-1}}$). Conditions were stable ($z/L>0.02$) 22 % of the time (daytime: 15 %, nighttime: 43 %), unstable for another 38 % (daytime: 42 %, nighttime: 22 %) ($z/L<-0.02$) and neutral during the remaining 40 % (daytime: 43 %, nighttime: 35 %).

3.3 Footprint and turbulence regime

In Basel the GEM flux measurements were conducted over a rough surface showing strongly modified vertical turbulent exchange processes. Measurements were conducted within the inertial sublayer 39 m above ground, which overlays the urban roughness sublayer assuming that the upper level of the roughness sublayer is about 2 times the average building height of 17 m (Feigenwinter et al., 2012). Of the GEM fluxes measured in Basel, 90 % originated from a source area that covered 78 ha and reflected a blended, spatially averaged signal (Fig. 5a). Within that footprint the water fraction accounts for 7 %, the vegetation fraction for 19 %, the building fraction for 36 % and impervious ground surface for 38 %. Main wind directions during the campaign mimicked the dominant seasonal wind direction from NNW and ESE.

An inspection of the normalized co-spectra for sensible heat, latent heat and CO_2 flux revealed the occurrence of large eddies leading to comparably low switching intervals of 1.4 ± 0.3 Hz (mean $\pm$ SD). The co-spectral estimates were derived from 20 Hz data over the entire campaign during unstable conditions and demonstrate that high-frequency losses for sensible heat, latent heat and CO_2 fluxes were minimal. Low-frequency losses resulted due to the applied high-pass filter which attenuated fluctuations at periods larger than the time constant of 16.6 min (RF in Fig. 6). Ogives were calculated after Foken et al. (2012) and converged at approximately 90 % of all cases within the 30 min averaging period (Fig. 6a). Simulated damping factors for REA fluxes revealed that at a mean wind speed of 2.6 $\mathrm{m\,s^{-1}}$ less than 10 % of the flux was dampened. We conclude that applying a 30 min averaging interval, a high-pass filter and valve switching at 10 Hz was adequate for REA flux calculations since considerable flux damping occurred just at low-frequency ranges, unstable conditions and low wind velocities.

At Degerö, 90 % of the footprint comprised 0.6 ha (Fig. 5b). For all contour lines calculated, the surface was physically homogenous. The roughness length z_0 present

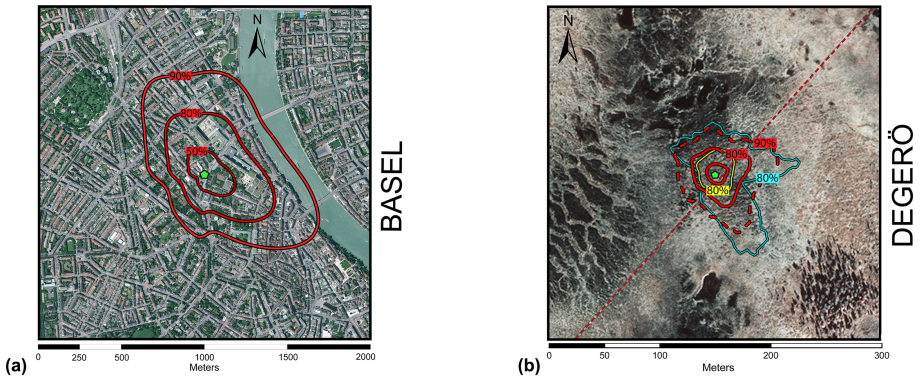

Figure 5. Aerial RGB and IR photographs with red contours containing 50, 80 and 90 % of the flux during the campaign in Basel **(a)** and Degerö **(b)**. The yellow and blue 80 % contours at Degerö stand for unstable and stable conditions, respectively. The light-green pentagons indicate the location of the flux towers.

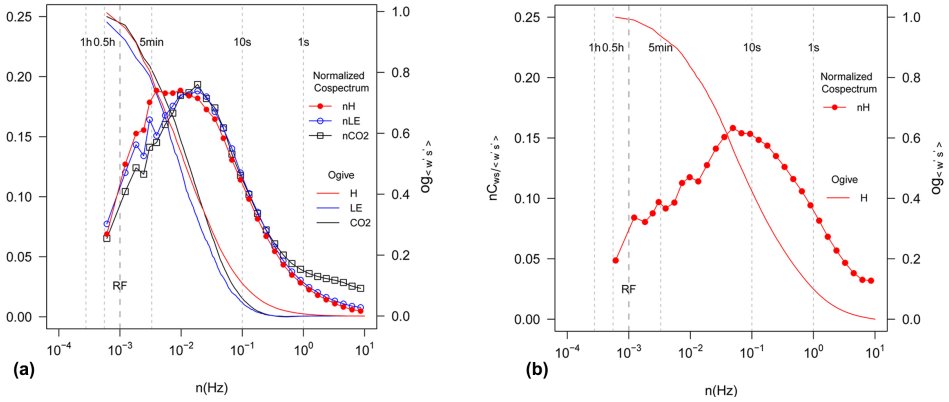

Figure 6. Normalized turbulence co-spectra (y axis, lines + symbols) and converging ogives (secondary y axis, lines) of sensible heat (red), latent heat (blue) and CO_2 flux (black) during unstable conditions for Basel **(a)** and Degerö **(b)**. The vertical line labeled as RF indicates the time constant of the applied high-pass filter. At Degerö only high-resolution air temperature data were used.

during the campaign was only a few millimeters due to the short vegetation (Sagerfors et al., 2008) and negligible when there was snow cover. During the Degerö campaign, the normalized turbulence spectra and ogives were derived for sensible heat flux during unstable conditions (Fig. 6b). Due to temporary technical problems regarding the LI-6262 closed-path infrared gas analyzer, CO_2 and latent heat flux data were not used for spectral analysis. In comparison to Basel the co-spectrum of the sensible heat flux was shifted significantly towards higher frequencies. The occurrence of more smaller eddies increased the fast-response valve switching interval (2.9 ± 0.7 Hz; mean $\pm$ SD) which increased with increasing u_* (Fig. S6). High-frequency losses at 10 Hz accounted for less than 5 % of the sensible heat flux. The ogive converged a constant value at RF and indicates that large eddies were sampled completely over the averaging period (Fig. 6b). At Degerö the integral damping factor for the REA flux was more than 20 % at high frequencies especially during stable and strong wind conditions. Simulated integral REA flux damping factors dependent on wind speed and stability conditions and cospectral density plots for site-averaged wind speeds are illustrated for Basel and Degerö in Figs. S7 and S8.

3.4 Atmospheric GEM concentrations

Mean $\pm$ SD atmospheric GEM concentration in Basel was $4.1 \pm 1\,\mathrm{ng\,m^{-3}}$. The average concentration difference between up and downdraft was $0.26 \pm 0.3\,\mathrm{ng\,m^{-3}}$ (median: $0.19\,\mathrm{ng\,m^{-3}}$) (Fig. 7). It might be possible that during the exceptionally cold period in Basel gas and oil-fired thermal power stations within the dense urban source area contributed to enhanced atmospheric GEM concentrations. In urban areas, total gaseous Hg concentrations were highest during heating season (Fang et al., 2004). Highest GEM lev-

Table 2. Summary of averaged, median and distribution of GEM fluxes, atmospheric GEM concentrations and environmental conditions during the measurement campaigns. Pearson correlation coefficients (r) between GEM flux and environmental parameters are given when statistically significant ($p < 0.05$).

Variable		Basel				Degerö			
	Unit	Mean	Median	10th/90th percentile	r	Mean	Median	10th/90th percentile	r
GEM flux	ng m^{-2} h^{-1}	15.4	34.9	−262/270	–	3.0	2.6	−71/67	–
GEM concentration	ng m^{-3}	4.1	3.9	3.3/5.6	−0.23	1.6	1.6	1.4/1.8	−0.14
Sensible heat flux (EC)	W m^{-2}	73.5	65	20/134	–	11.8	2.4	−17/58	0.23
Latent heat flux (EC)	W m^{-2}	12.3	10.6	1.8/24.5	0.26	–	–	–	–
CO_2 flux (EC)	µmol m^{-2} s^{-1}	0.02	0.01	0/0.04	0.36	–	–	–	–
Friction velocity	m s^{-1}	0.41	0.39	0.2/0.7	0.2	0.19	0.18	0.07/0.34	−0.23
Wind speed	m s^{-1}	2.6	2.5	1.3/3.9	0.13	2.9	2.7	1.0/4.8	−0.26
Solar radiation	W m^{-2}	78	–	0/312	−0.22	159	–	0/455	0.14
Air temperature	°C	−7.9	−8	−12/3.4	0.23	5.3	5.4	0.1/10.2	0.26
Soil temperature	°C	–	–	–	–	6.7	7	4.4/8.2	0.2
Relative humidity	%	62	60	40/85	−0.23	76	80	47/98	−0.3

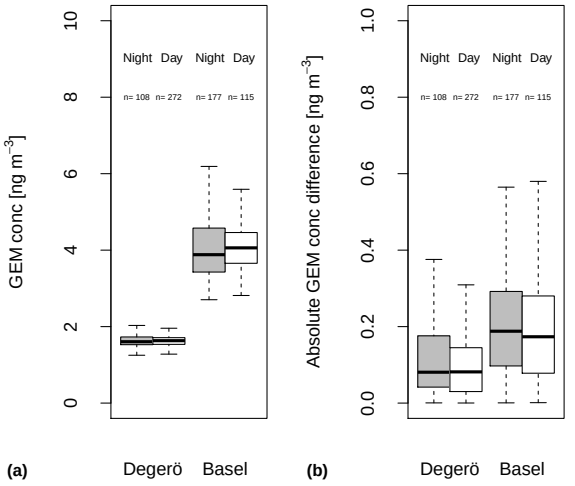

Figure 7. Box plots display atmospheric GEM concentrations **(a)** and the absolute GEM concentration differences between updraft and downdraft **(b)** during the day and night at Degerö and Basel.. Number of observations is indicated. The bold line in the box represents the median GEM concentration. The horizontal border lines indicate the 25th (Q1) and 75th (Q3) percentiles, from bottom to top. The lower whisker marks Q1 minus 1.5 times the interquartile range (IQR). The upper whisker marks Q3 plus 1.5 IQR. Outliers are not displayed.

els in Basel were observed during periods of low wind velocities ($u_* < 0.3$ m s^{-1}) and southern wind directions. Most likely additional GEM emissions from vehicular traffic along a highly frequented road contributed to elevated Hg concentrations during southerlies. GEM concentrations in the exhaust of motor vehicles in driving mode are elevated and range from 2.8 to 26.9 ng m^{-3} depending on fuel types (Won et al., 2007). The road runs in a north/south direction and is the major source of CO_2 (Lietzke and Vogt, 2013).

The average air concentration during snowmelt at Degerö was 1.6 ± 0.2 ng m^{-3}, comparable to observations made in 2009 by static chambers (Fritsche et al., 2014). Concentration difference in REA conditional samples collected at Degerö averaged 0.13 ± 0.2 ng m^{-3} (median: 0.09 ng m^{-2}) which is about a factor of 2 lower than the magnitude observed in Basel (Fig. 7). No significant concentration relationships were found with either wind direction or atmospheric stability.

3.5 GEM flux estimation in contrasting environments

Urban areas are of particular concern with respect to the global Hg cycle. Industrial sectors and anthropogenic combustion processes emit large quantities of Hg to the atmosphere (Walcek et al., 2003) where mostly gaseous oxidized Hg and particulate bound Hg deposit locally. Highly variable Hg air concentrations, the physically and chemically diverse nature of urban surface covers and urban meteorology (e.g., heat island effect) are suggested to create complex Hg flux patterns above cities (Gabriel et al., 2005). Up to now, just a handful of studies have described GEM emissions from urban environments (Kim and Kim, 1999; Feng et al., 2005; Gabriel et al., 2006; Obrist et al., 2006; Eckley and Branfireun, 2008). GEM fluxes measured in Basel showed a diurnal trend with a maximum deposition around noon and highest emissions around 7 PM (Fig. 8a). The mean flux ± SE of 15.4 ± 13.3 ng m^{-2} h^{-1} indicated that this urban area was a net source of atmospheric Hg during the study period. Similarly, for the same site in spring and fall, Obrist et al. (2006) observed average GEM emissions of 6.5 ± 0.9 ng m^{-2} h^{-1} (± SD) in the stable nocturnal boundary layer using the ^{222}Rn/Hg^0 method. Environmental variables, e.g., solar radiation, air and soil temperatures, are known to be major drivers of natural GEM emission (e.g., Schröder et

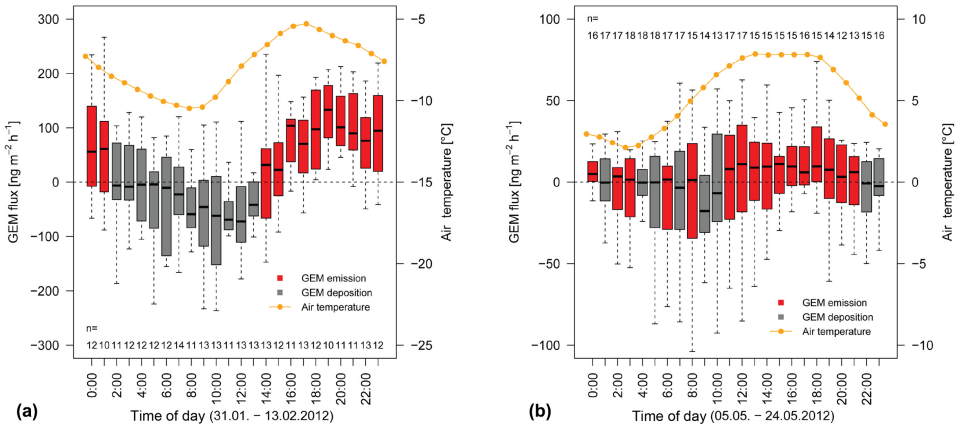

Figure 8. Diurnal patterns of GEM flux during the campaign in Basel **(a)** and Degerö **(b)** using the 6-hourly smoothed GEM flux time series. Red and gray colored box plots indicate median Hg emission and Hg deposition at different times of the day, respectively. Hourly averages of air temperatures are given (orange). Horizontal dashed line indicates the zero line of GEM flux and/or air temperature. Box plot description in caption of Fig. 7.

al., 1989; Steffen et al., 2002; Choi and Holsen, 2009). Correlations between GEM flux and its controlling factors for this study can be reviewed in Table 2. Northwesterly wind directions were associated with GEM deposition between 02:00 and 13:00. In contrast, emission events were linked to wind directions from the southeast.

Determination of GEM snow–air exchange has been a subject of interest since the first atmospheric mercury depletion events were observed (Schröder et al., 1998). Non-arctic GEM flux studies from snowpack report deposition as well as emission events with near zero net fluxes (Faïn et al., 2007; mean: 0.4 ng m^{-2} h^{-1}; Fritsche et al., 2008b; mean: 0.3 ng m^{-2} h^{-1}).

The mean GEM snow–air transfer observed at Degerö was 3.0 ± 3.8 ng m^{-2} h^{-1} ($\pm$ SE). It is the result of a balance between deposition prevailing from midnight to noon and vice versa during the rest of the day when emission predominates (Fig. 8b). REA fluxes varied strongly during both the day and night but revealed a significant difference between GEM fluxes during unstable (median: 8.7 ng m^{-2} h^{-1}), stable (median: -0.1 ng m^{-2} h^{-1}) and neutral conditions (median: -4 ng m^{-2} h^{-1}) (Mann–Whitney U test, $p < 0.05$). GEM concentrations in the surface snow layers were not determined in this study but in accordance with Faïn et al. (2013), GEM is likely enhanced during the course of daytime compared to ambient air due to sunlight-mediated processes. An impact of fresh snowfall and possible wet Hg deposition on GEM fluxes could not be observed with REA but precipitation events occurred regularly in the afternoon and might have contributed to GEM volatilized in the evenings together with GEM produced during dusk and night (Faïn et al., 2013).

GEM flux quantification is improved, compared to previous systems, by the synchronous sampling, as well the regular monitoring of GEM reference gas concentration and dry, Hg-free air. As demonstrated here, these improvements make REA feasible for measurements over tall buildings but also short vegetation and snow cover. At Degerö, however, higher abundance of smaller eddies increased the GEM flux variability. However, the REA technique remains better suited to assessing magnitudes and variability of fluxes rather determining the effects of short-term variability in environmental parameters on GEM fluxes (cf. Gustin et al., 1999).

For future long-term REA applications we have three suggestions: (i) a more regular determination of the bias between both sampling lines, either by a weekly check of the bias or by implementing an additional valve to switch up- and downdraft lines every hour (each cartridge would measure up- and downdraft); (ii) although Hg detector sensitivity due to rapid air temperature changes is corrected for, it could be avoided to a large extent by using a more effective temperature control unit; (iii) improvement of the accuracy in the air volumes sampled by installing mass flow meters for up- and downdraft lines.

4 Conclusions

The need to precisely determine GEM land–atmosphere exchange over long continuous periods is widely recognized. REA has the potential to do this more effectively than other methods. Therefore, several REA systems have been deployed, but their accuracy has been impaired by several design features such as the use of multiple detectors and non-synchronous sample collection. We developed a dual-inlet, single analyzer system that has overcome these shortcom-

ings and included new features such as the integrated GEM reference gas and Hg zero-air generator for continuous monitoring of GEM recovery, as well as blank measurements. The data acquisition and control system is fully automated and could be remotely controlled, which reduces the workload compared to other REA systems. We have demonstrated the system in contrasting environments to measure turbulent transport of GEM 39 m above ground level in Basel, Switzerland, and 1.8 m above a boreal peatland in Sweden during snowmelt. While the demonstration identified room for further improvements, we believe this novel design has the potential to facilitate the use of REA for measuring land–atmosphere Hg exchange for sustained periods in a variety of environments.

The Supplement related to this article is available online at doi:10.5194/amt-9-509-2016-supplement.

Acknowledgements. This research was funded by the Swedish Research Council (2009-15586-68819-37), the Department of Earth Sciences, Uppsala University, and the Department of Environmental Geosciences, University of Basel. We thank William Larsson and the late Lars Lundmark from Umeå University for technical assistance and engineering and Roland Vogt from the University of Basel's MCR lab for using the EC setup. The study at Degerö also received technical and maintenance support from the Svartberget Experimental Forest, Vindeln, Sweden. The study was also supported by the Swedish research infrastructures, ICOS Sweden (Integrated Carbon Observatory System) and SITES (Swedish Infrastructure for Ecosystem Science) at Degerö, both partly financed by the Swedish Research Council.

Edited by: M. Hamilton

References

Agnan, Y., Le Dantec, T., Moore, C. W., Edwards, G. C., and Obrist, D.: New constraints on terrestrial surface-atmosphere fluxes of gaseous elemental mercury using a global database, Environ. Sci. Technol., 50, 507–524, 2016.

Åkerblom, S., Bishop, K., Bjorn, E., Lambertsson, L., Eriksson, T., and Nilsson, M. B.: Significant interaction effects from sulfate deposition and climate on sulfur concentrations constitute major controls on methylmercury production in peatlands, Geochim. Cosmochim. Ac., 102, 1–11, 2013.

Alexandersson, H., Karlström, C., and Larsson-McCann, S.: Temperaturen och nederbörden i Sverige 1961–1990, The Swedish Meteorological and Hydrological Institute, Norrköping, Sweden, 1991.

Ammann, C.: On the applicability of Relaxed Eddy Accumulation and Common Methods for Measuring Trace Gas Fluxes, PhD Thesis, ETH Zürich, Zürich, 229 pp., 1999.

Ammann, C. and Meixner, F. X.: Stability dependence of the relaxed eddy accumulation coefficient for various scalar quantities, J. Geophys. Res., 107, 4071, doi:10.1029/2001JD000649, 2002.

Arnts, R. R., Mowry, F. L., and Hampton, G. A.: A high-frequency response relaxed eddy accumulation flux measurement system for sampling short-lived biogenic volatile organic compounds, J. Geophys. Res.-Atmos., 118, 4860–4873, 2013.

Baker, J. M., Norman, and Bland, W. L.: Field-scale application of flux measurement by conditional sampling, Agric. Forest Meteorol., 62, 31–52, 1992.

Bash, J. O. and Miller, D. R.: A note on elevated total gaseous mercury concentrations downwind from an agriculture field during tilling, Sci. Total Environ., 388, 379–388, 2007.

Bash, J. O. and Miller, D. R.: A relaxed eddy accumulation system for measuring surface fluxes of total gaseous mercury, J. Atmos. Ocean. Tech., 25, 244–257, 2008.

Bash, J. O. and Miller, D. R.: Growing season total gaseous mercury (TGM) flux measurements over an *Acer rubrum* L. stand, Atmos. Environ., 43, 5953–5961, 2009.

Bauer, D., Campuzano-Jost, P., and Hynes, A. J.: Rapid, ultrasensitive detection of gas phase elemental mercury under atmospheric conditions using sequential two-photon laser induced fluorescence, J. Environ. Monitor., 4, 339–343, 2002.

Brut, A., Legain, D., Durand, P., and Laville, P.: A relaxed eddy accumulator for surface flux measurements on ground-based platforms and aboard research vessels, J. Atmos. Ocean. Tech., 21, 411–427, 2004.

Businger, J. and Oncley, S.: Flux Measurement with Conditional Sampling, J. Atmos. Ocean. Tech., 7, 349–352, 1990.

Choi, H.-D. and Holsen, T. M.: Gaseous mercury fluxes from the forest floor of the Adirondacks, Environ. Pollut., 157, 592–600, 2009.

Cobos, D. R., Baker, J. M., and Nater, E. A.: Conditional sampling for measuring mercury vapor fluxes, Atmos. Environ., 36, 4309–4321, 2002.

Converse, A. D., Riscassi, A. L., and Scanlon, T. M.: Seasonal variability in gaseous mercury fluxes measured in a high-elevation meadow, Atmos. Environ., 44, 2176–2185, 2010.

Desjardins, R. L.: Energy budget by an eddy correlation method, J. Appl. Meteorol., 16, 248–250, 1977.

Eckley, C. S. and Branfireun, B.: Gaseous mercury emissions from urban surfaces: controls and spatiotemporal trends, Appl. Geochem., 23, 369–383, 2008.

Eckley, C. S., Gustin, M., Lin, C.-J., Li, X., and Miller, M. B.: The influence of dynamic chamber design and operating parameters on calculated surface-to-air mercury fluxes, Atmos. Environ. 44, 194–203, 2010.

Faïn, X., Grangeon, S., Bahlmann, E., Fritsche, J., Obrist, D., Dommergue, A., Ferrari, C. P., Cairns, W., Ebinghaus, R., Barbante, C., Cescon, P., and Boutron, C.: Diurnal production of gaseous mercury in the alpine snowpack before snowmelt, J. Geophys. Res., 112, D21311, doi:10.1029/2007JD008520, 2007.

Faïn, X., Moosmüller, H., and Obrist, D.: Toward real-time measurement of atmospheric mercury concentrations using cavity ring-down spectroscopy, Atmos. Chem. Phys., 10, 2879–2892, doi:10.5194/acp-10-2879-2010, 2010.

Faïn, X., Helmig, D., Hueber, J., Obrist, D., and Williams, M. W.: Mercury dynamics in the Rocky Mountain, Colorado, snowpack,

Biogeosciences, 10, 3793–3807, doi:10.5194/bg-10-3793-2013, 2013.

Fang, F., Wang, Q., and Li, J.: Urban environmental mercury in Changchun, a metropolitan city in Northeastern China: source, cycle, and fate, Sci. Total Environ., 330, 159–170, 2004.

Feigenwinter, C., Vogt, R., and Christen, A.: Eddy covariance measurements over urban areas, in: Eddy Covariance – a Practical Guide to Measurement and Data Analysis, edited by: Aubinet, M., Vesala, T., and Papale, D., Springer Science + Business Media B.V., Dordrecht, the Netherlands, 377–397, 2012.

Feng, X. B., Wang, S. F., Qiu, G. A., Hou, Y. M., and Tang, S. L.: Total gaseous mercury emissions from soil in Guiyang, Guizhou, China, J. Geophys. Res.-Atmos., 110, D14306, doi:10.1029/2004JD005643, 2005.

Foken, T.: Angewandte Meteorologie, Mikrometeorologische Methoden, 2. Auflage, Springer, Berlin, 2006.

Foken, T. and Wichura, B.: Tools for quality assessment of surface-based flux measurements, Agr. Forest Meteorol., 78, 83–105, 1996.

Foken, T., Leuning, R., Oncley, S. R., Mauder, M., and Aubinet., M.: Corrections and data quality control, in: Eddy Covariance – a Practical Guide to Measurement and Data Analysis, edited by: Aubinet, M., Vesala, T., and Papale, D., Springer Science + Business Media B.V., Dordrecht, the Netherlands, 85–131, 2012.

Fritsche, J., Obrist, D., Zeeman, M. J., Conen, F., Eugster, W., and Alewell, C.: Elemental mercury fluxes over a sub-alpine grassland determined with two micrometeorological methods, Atmos. Environ., 42, 2922–2933, 2008a.

Fritsche, J., Wohlfahrt, G., Ammann, C., Zeeman, M., Hammerle, A., Obrist, D., and Alewell, C.: Summertime elemental mercury exchange of temperate grasslands on an ecosystem-scale, Atmos. Chem. Phys., 8, 7709-7722, doi:10.5194/acp-8-7709-2008, 2008b.

Fritsche, J., Osterwalder, S., Nilsson, M. B., Sagerfors, J., Åkerblom, S., Bishop., K., and Nilsson., M.: Evasion of elemental mercury from a boreal peatland suppressed by long-term sulfate addition, Environ. Sci. Technol., 1, 421–425, 2014.

Gabriel, M. C., Williamson, D., Lindberg, S., Zhang, H., and Brooks, S.: Spatial variability of total gaseous mercury emission from soils in a southeastern US urban environment, Environ. Geol., 48, 955–964, 2005.

Gabriel, M. C., Williamson, D. G., Zhang, H., Brooks, S., and Lindberg, S.: Diurnal and seasonal trends in total gaseous mercury flux from three urban ground surfaces, Atmos. Environ., 40, 4269–4284, 2006.

Gaman, A., Rannik, Ü., Aalto, P., Pohja, T., Siivola, E., Kulmala, M., and Vesala, T.: Relaxed eddy accumulation system for size-resolved aerosol particle flux measurements, J. Atmos. Ocean. Tech., 21, 933–943, 2004.

Gillis, A. and Miller, D. R.: Some potential errors in the measurement of mercury gas exchange at the soil surface using a dynamic flux chamber, Sci. Total Environ., 260, 181–189, 2000.

Granberg, G., Sundh, I., Svensson, B. H., and Nilsson, M.: Effects of temperature, and nitrogen and sulfur deposition, on methane emission from a boreal mire, Ecology, 82, 1982–1998, 2001.

Grigal, D. F.: Inputs and outputs of mercury from terrestrial watersheds: a review, Environ. Rev., 10, 1–39, 2002.

Grönholm, T., Haapanala, S., Launiainen, S., Rinne, J., Vesala, T., and Rannik, Ü.: The dependence of the beta coefficient of REA system with dynamic deadband on atmospheric conditions, Environ. Pollut., 152, 597–603, 2008.

Gustin, M. S.: Exchange of mercury between the atmosphere and terrestrial ecosystems, in: Advances in Environmental Chemistry, and Toxicology of Mercury, edited by: Cai, Y., Liu, G., and O'Driscoll, N. J., John Wiley & Sons, Hoboken, NJ, USA, 423–452, 2011.

Gustin, M. S. and Lindberg, S. E.: Terrestrial Hg fluxes: is the next exchange up, down, or neither?, in: Dynamics of Mercury Pollution on Regional and Global Scales, edited by: Pirrone, N. and Mahaffey, K. R., Springer, New York, 241–259, 2005.

Gustin, M. S., Lindberg, S., Marsik, F., Casimir, A., Ebinghaus, R., Edwards, G., Hubble-Fitzgerald, C., Kemp, R., Kock, H., Leonard, T., London, J., Majewski, M., Montecinos, C., Owens, J., Pilote, M., Poissant, L., Rasmussen, P., Schaedlich, F., Schneeberger, D., Schroeder, W., Sommar, J., Turner, R., Vette, A., Wallschlaeger, D., Xiao, Z., and Zhang, H.: Nevada STORMS project: measurement of mercury emissions from naturally enriched surfaces, J. Geophys. Res.-Atmos., 104, 21831–21844, 1999.

Gustin, M. S., Lindberg, S. E., Austin, K., Coolbaugh, M., Vette, A., and Zhang, H.: Assessing the contribution of natural sources to regional atmospheric mercury budgets, Sci. Total Environ., 259, 61–71, 2000.

Gustin, M. S., Lindberg, S. E., and Weisberg, P. J.: An update on the natural sources and sinks of atmospheric mercury, Appl. Geochem., 23, 482–493, 2008.

Haapanala, S., Rinne, J., Pystynen, K.-H., Hellén, H., Hakola, H., and Riutta, T.: Measurements of hydrocarbon emissions from a boreal fen using the REA technique, Biogeosciences, 3, 103–112, doi:10.5194/bg-3-103-2006, 2006.

Hensen, A., Nemitz, E., Flynn, M. J., Blatter, A., Jones, S. K., Sørensen, L. L., Hensen, B., Pryor, S. C., Jensen, B., Otjes, R. P., Cobussen, J., Loubet, B., Erisman, J. W., Gallagher, M. W., Neftel, A., and Sutton, M. A.: Inter-comparison of ammonia fluxes obtained using the Relaxed Eddy Accumulation technique, Biogeosciences, 6, 2575–2588, doi:10.5194/bg-6-2575-2009, 2009.

Keeler, G. J. and Landis, M. S.: Standard Operating Procedure for Sampling Vapor Phase Mercury, University of Michigan, USA, 1994.

Kim, K. H. and Kim, M. Y.: The exchange of gaseous mercury across soil–air interface in a residential area of Seoul, Korea, Atmos. Environ., 33, 3153–3165, 1999.

Kim, K.-H., Lindberg, S. E., and Meyers, T. P.: Micrometeorological measurements of mercury vapor fluxes over background forest soils in eastern Tennessee, Atmos. Environ., 29, 267–282, 1995.

Kormann, R. and Meixner, F. X.: An analytical footrpint model for non-neutral stratification, Bound.-Lay. Meteorol., 99, 207–224, 2001.

Lee, X. H.: Water vapor density effect on measurements of trace gas mixing ratio and flux with a massflow controller, J. Geophys. Res.-Atmos., 105, 17807–17810, 2000.

Lietzke, B. and Vogt, R.: Variability of CO_2 concentrations and fluxes in and above an urban street canyon, Atmos. Environ., 74, 60–72, 2013.

Lindberg, S. and Meyers, T.: Development of an automated micrometeorological method for measuring the emission of mercury vapor from wetland vegetation, Wetl. Ecol. Manag., 9, 333–347, 2001.

Lindberg, S., Bullock, R., Ebinghaus, R., Engstrom, D., Feng, X., Fitzgerald, W., Pirrone, N., and Seigneur, C.: A synthesis of progress and uncertainties in attributing the sources of mercury in deposition, Ambio, 36, 19–32, 2007.

Mason, R. P. and Sheu, G.-R.: Role of the ocean in the global mercury cycle, Global Biogeochem. Cy., 16, 1093, doi:10.1029/2001GB001440, 2002.

Mauder, M. and Foken, T.: Documentation and Instruction Manual of the Eddy Covariance Software Package TK2, vol. 26, Arbeitsergebnisse, Universitat Bayreuth, Abteilung Mikrometeorologie, Bayreuth, 42 pp., ISSN 1614–8916, 2004.

McMillen, R.: An Eddy-correlation technique with extended applicability to non-simple terrain, Bound.-Lay. Meteorol., 43, 231–245, 1988.

MeteoSchweiz: Klimanormwerte Basel/Binningen, Normperiode 1961–1990, available at: http://www.meteoschweiz.admin.ch, last access: 10 January, 2016.

Meyers, T. P., Hall, M. E., Lindberg, S. E., and Kim, K.: Use of the modified Bowen-ratio technique to measure fluxes of trace gases, Atmos. Environ., 30, 3321–3329, 1996.

Meyers, T. P., Luke, W. T., and Meisinger, J. J.: Fluxes of ammonia and sulfate over maize using relaxed eddy accumulation, Agr. Forest Meteorol., 136, 203–213, 2006.

Milne, R., Beverland, I. J., Hargreaves, K., and Moncrieff, J. B.: Variation of the β coefficient in the relaxed eddy accumulation method, Bound.-Lay. Meteorol., 93, 211–225, 1999.

Milne, R., Mennim, A., and Hargreaves, K.: The value of the beta coefficient in the relaxed eddy accumulation method in terms of fourth-order moments, Bound.-Lay. Meteorol., 101, 359–373, 2001.

Moravek, A., Trebs, I., and Foken, T.: Effect of imprecise lag time and high-frequency attenuation on surface–atmosphere exchange fluxes determined with the relaxed eddy accumulation method, J. Geophys. Res.-Atmos., 118, 10210–10224, 2013.

Obrist, D., Conen, F., Vogt, R., Siegwolf, R., and Alewell, C.: Estimation of Hg^0 exchange between ecosystems and the atmosphere using ^{222}Rn and Hg^0 concentration changes in the stable nocturnal boundary layer, Atmos. Environ., 40, 856–866, 2006.

Olofsson, M., Ek-Olausson, B., Jensen, N. O., Langer, S., and Ljungström, E.: The flux of isoprene from a willow plantation and the effect on local air quality, Atmos. Environ., 39, 2061–2070, 2005a.

Olofsson, M., Sommar, J., Ljungstrom, E., Andersson, M., and Wängberg, I.: Application of relaxed eddy accumulation technique to quantify Hg^0 fluxes over modified soil surfaces, Water Air Soil Pollut., 167, 331–352, 2005b.

Panofsky, H. A. and Dutton, J. A.: Atmospheric Turbulence – Models and Methods for Engineering Applications, Wiley, New York, 397 pp., 1984.

Peichl, M., Sagerfors, J., Lindroth, A., Buffam, I., Grelle, A., Klemedtsson, L., Laudon, H., and Nilsson, M. B.: Energy exchange and water budget partitioning in a boreal minerogenic mire, J. Geophys. Res.-Biogeo., 118, 1–13, 2013.

Pierce, A. M., Moore, C. W., Wohlfahrt, G., Hörtnagl, L., Kljun, N., and Obrist, D.: Eddy covariance flux measurements of gaseous elemental mercury using cavity ring-down spectroscopy, Environ. Sci. Technol., 49, 1559–1568, 2015.

Rannik, U., Aubinet, M., Kurbanmuradov, O., Sabelfeld, K. K., Markkanen, T., and Vesala, T.: Footprint analysis for measurements over a heterogeneous forest, Bound.-Lay. Meteorol., 97, 137–166, 2000.

Ren, X., Sanders, J. E., Rajendran, A., Weber, R. J., Goldstein, A. H., Pusede, S. E., Browne, E. C., Min, K.-E., and Cohen, R. C.: A relaxed eddy accumulation system for measuring vertical fluxes of nitrous acid, Atmos. Meas. Tech., 4, 2093–2103, doi:10.5194/amt-4-2093-2011, 2011.

Richardson, A. D., Aubinet, M., Barr, A. G., Hollinger, D. Y., Ibrom, A., Lasslop, G., and Reichstein, M.: Uncertainty quantification, in: Eddy Covariance – a Practical Guide to Measurement and Data Analysis, edited by: Aubinet, M., Vesala, T., and Papale, D., Springer Science + Business Media B.V., Dordrecht, the Netherlands, 173–209, 2012.

Sagerfors, J., Lindroth, A., Grelle, A., Klemedtsson, L., Weslien, P., and Nilsson, M.: Annual CO_2 exchange between a nutrient-poor, minerotrophic, boreal mire and the atmosphere, J. Geophys. Res.-Biogeo., 113, G01001, doi:10.1029/2006JG000306, 2008.

Schröder, W. H., Lindquist, O., and Munthe, J.: Volatilisation of mercury from natural surfaces, Proc. 7th International Conference of Heavy Metals in the Environment, Geneva, Switzerland, September 1989, edited by: Vernet, J. P., CEP Consultants, Edinburgh, UK, 480–484, 1989.

Schröder, W. H., Anlauf, K. G., Barrie, L. A., Lu, J. Y., Steffen, A., Schneeberger, D. R., and Berg, T.: Arctic springtime depletion of mercury, Nature, 394, 331–332, 1998.

Shanley, J. B. and Bishop, K.: Mercury cycling in terrestrial watersheds, in: Mercury in the Environment: Pattern and Process, 1st edn., edited by: Bank, M. S., University of California Press, Berkely, CA, 119–141, 2012.

Skov, H., Brooks, S. B., Goodsite, M. E., Lindberg, S. E., Meyers, T. P., Landis, M. S., Larsen, M. R. B., Jensen, B., McConville, G., and Christensen, J.: Fluxes of reactive gaseous mercury measured with a newly developed method using relaxed eddy accumulation, Atmos. Environ., 40, 5452–5463, 2006.

Slemr, F., Brunke, E.-G., Ebinghaus, R., Temme, C., Munthe, J. Wängberg, I., Schroeder, W., Steffen, A., and Berg, T.: Worldwide trend of atmospheric mercury since 1977, Geophys. Res. Lett., 30, 1516, doi:10.1029/2003GL016954, 2003.

Sommar, J., Zhu, W., Shang, L., Feng, X., and Lin, C.-J.: A whole-air relaxed eddy accumulation measurement system for sampling vertical vapour exchange of elemental mercury, Tellus B, 65, 19940, doi:10.3402/tellusb.v65i0.19940, 2013a.

Sommar, J., Zhu, W., Lin, C.-J., and Feng, X.: Field approaches to measure Hg exchange between natural surfaces and the atmosphere – a review, Critical Reviews in Environ. Sci. Technol., 43, 1657–1739, 2013b.

Steffen, A., Schroeder, W. H., Bottenheim, J., Narayan, J., and Fuentes, J. D.: Atmospheric mercury concentrations: measurements and profiles near snow and ice surfaces in the Canadian Arctic during Alert 2000, Atmos. Environ., 36, 2653–2661, 2002.

Sutton, M. A., Milford, C., Nemitz, E., Theobald, M. R., Hill, P. W., Fowler, D., Schjoerring, J. K., Mattsson, M. E., Nielsen, K. H., Husted, S., Erisman, J. W., Otjes, R., Hensen, A., Mosquera,

J., Cellier, P., Loubet, B., David, M., Genermont, S., Neftel, A., Blatter, A., Herrmann, B., Jones, S. K., Horvath, L., Fuhrer, E. C., Mantzanas, K., Koukoura, Z., Gallagher, M., Williams, P., Flynn, M., and Riedo, M.: Biosphere-atmosphere interactions of ammonia with grasslands: Experimental strategy and results from a new European initiative, Plant and Soil, 228, 131–145, 2001.

United Nations Environment Programme: Minimata Convention on Mercury, available at: http://www.mercuryconvention.org (last access: 10 January 2016), 62 pp., 2013a.

United Nations Environment Programme: Global Mercury Assessment 2013: Sources, Emissions, Releases and Environmental Transport, UNEP Chemicals Branch, Geneva, Switzerland, 42 pp., 2013b.

Walcek, C., De Santis, S., and Gentile, T.: Preparation of mercury emissions for eastern North America, Environ. Pollut., 123, 375–381, 2003.

Wallschläger, D., Turner, R. R., London, J., Ebinghaus, R., Kock, H. H., Sommar, J., and Xiao, Z. F.: Factors affecting the measurement of mercury emissions from soils with flux chambers, J. Geophys. Res.-Atmos., 104, 21859–21871, 1999.

Won, J. H., Park, J. Y., and Lee, T. G.: Mercury emissions from automobiles using gasoline, diesel, and LPG, Atmos. Environ., 41, 7547–7552, 2007.

Zhu, W., Sommar, J., Lin, C.-J., and Feng, X.: Mercury vapor air–surface exchange measured by collocated micrometeorological and enclosure methods – Part I: Data comparability and method characteristics, Atmos. Chem. Phys., 15, 685–702, doi:10.5194/acp-15-685-2015, 2015a.

Zhu, W., Sommar, J., Lin, C.-J., and Feng, X.: Mercury vapor air–surface exchange measured by collocated micrometeorological and enclosure methods – Part II: Bias and uncertainty analysis, Atmos. Chem. Phys., 15, 5359–5376, doi:10.5194/acp-15-5359-2015, 2015b.

A.2 P4: Spatial Distribution of Sensible and Latent Heat Flux in the URBANFLUXES case study city Basel (Switzerland)

URBANFLUXES is a Horizon 2020 funded joint research project between Foundation for Research and Technology Hellas (Greece), the Deutsches Zentrum für Luft- und Raumfahrt (Germany), the Centre d'Etude Spatiale de la Biosphère (France) the University of Basel (Switzerland), the University of Reading (United Kingdom), the Göteborgs Universitet (Sweden) as well as experts on Science Communication Stichting Dienst Landbouwkunding Onderzoek (The Netherlands) and the industry represented by a spin-off company GEO-K s.r.l. (Italy). The goal is to determine the components of the urban energy budget by combining satellite imagery and conventional ground-based meteorological measurements in order to estimate the anthropogenic heat flux as a residual term. The remote sensing approach should enable the transfer of the results to any other city to quantify and monitor the urban heat budget. To develop the methods and models three case studies are conducted in Heraklion (Greece), Basel (Switzerland) and London (United Kingdom).

The following chapter is published as a research article in proceedings of the 2017 Joint Urban Remote Sensing Event (JURSE 2017):

Feigenwinter, C., E. Parlow, R. Vogt, **M. Schmutz**, N. Chrysoulakis, F. Lindberg, M. Marconcini, and F. del Frate (2017). Spatial distribution of sensible and latent heat flux in the URBANFLUXES case study city Basel (Switzerland). *In: 2017 Joint Urban Remote Sensing Event (JURSE 2017)*: Proceedings of a meeting held 6-8 March 2017, Dubai, United Arab Emirates. p. 4.

Spatial Distribution of Sensible and Latent Heat Flux in the URBANFLUXES case study city Basel (Switzerland)

Christian Feigenwinter, Eberhard Parlow, Roland Vogt, Michael Schmutz
Meteorology, Climatology, Remote Sensing
University of Basel
Switzerland
christian.feigenwinter@unibas.ch

Nektarios Chrysoulakis
Foundation for Research and Technology – Hellas (FORTH)
Heraklion, Crete, Greece

Fredrik Lindberg
Dept. of Earth Sciences
University of Gothenburg
Sweden

Mattia Marconcini
German Remote Sensing Data Center: Land Surface
German Aerospace Center (DLR)
Oberpfaffenhofen, Germany

Fabio del Frate
GEO-K s.r.l.
Rome, Italy

***Abstract*— Urban surfaces are usually complex mixtures of different land covers and surface materials; the relative magnitude of the surface energy balance components typically will therefore vary widely across a city. Eddy covariance (EC) measurements provide the best estimates of turbulent heat fluxes, but are restricted to their source area. To extrapolate to larger areas land surface modelling with earth observation (EO) data is beneficial as citywide information is possible. In this study, turbulent sensible and latent heat fluxes are calculated by a combined method using micrometeorological approaches (the Aerodynamic Resistance Method ARM), Earth Observation (EO) data and GIS-Techniques. Input data such as land cover fractions and surface temperatures are derived from Landsat 8 OLI and TIRS, urban morphology (mean building height, plan area index, aspect ratio) was calculated from high resolution digital building models and GIS-data layers. Input of meteorological data (e.g. air temperature, humidity, air pressure, wind speed and wind direction) was provided by measurements from flux towers and meteorological station networks. The spatial distributions of turbulent heat fluxes were analyzed for 22 for the city of Basel (Switzerland), covering all seasons and different meteorological conditions. Highest sensible heat fluxes were modelled for industrial areas, railway stations and areas with high building density. The magnitude of sensible heat flux strongly depends on the surface temperature, because the spatial variation of air temperature during daytime is small when limited to a satellite pixel view. For latent heat flux, the spatial distribution of the saturation deficit of vapor (e.g. above urban water bodies) and the (minimum) stomatal resistance of vegetation types show the largest influence on evapotranspiration rates. Seasonal variations in heat fluxes are strongly dependent on meteorological conditions, i.e. air temperature, water vapor saturation deficit and wind speed. Comparison of measured fluxes with modeled fluxes in the weighted source area of the flux towers is moderate due to known drawbacks in the modelling approach and uncertainties inherent to EC measurements, particularly also in urban areas.**

Keywords*— *Urban Energy Balance, Eddy Covariance, Earth Observation, Aerodynamic Resistance Method, GIS, URBANFLUXES

I. Introduction

The URBANFLUXES Horizon 2020 project (urbanfluxes.eu) aims to derive the anthropogenic heat flux from Earth Observation (EO) data. Each component of the energy balance (net radiation R_n, sensible (Q_H) and latent (Q_E) heat flux, and storage heat flux ΔQ_S) is evaluated in a separate work package [1]. This study concentrates on the fluxes of sensible and latent heat. These fluxes are strongly modified by the properties of the urban surface, i.e. 3D geometry, high roughness, impervious surfaces, complex source/sink distribution and injections of heat and water into the urban atmosphere by human activities (traffic, heating, waste management, etc.). The spatial variability of urban terrain complicates their estimation. The existence of various surface types and different exposures to solar radiation in a complex surface geometry lead to significant variations in heat fluxes over short distances. This problem is well-known, but for practical purposes various simplifications that assume homogeneous properties at the surface like Monin–Obukhov Similarity Theory (MOST) [2] are still widely used to estimate the sensible heat flux in meso-scale models, typically with the scalar roughness approach. Although MOST was originally derived for flat and homogeneous terrain, several studies have used it over heterogeneous terrain, including cities [2].

II. Methods

A. Flux calculation

In URBANFLUXES, the Aerodynamic Resistance Method (ARM) to estimate Q_H uses the simple relation (e.g. [3])

$$Q_H = \rho c_p \frac{T_s - T_a}{r_a} \tag{1}$$

where ρ is the density of air, c_p the specific heat of air at constant pressure, T_s is the surface temperature derived from satellite thermal infrared observations, T_a is the air temperature recorded by the meteorological stations, and r_a is the aerodynamic resistance. Analogously Q_E is expressed as

$$Q_E = \frac{\rho c_p}{\gamma} \frac{e_s^* - e_a}{r_a + r_s} \tag{2}$$

where e_s* is the saturation water vapor pressure at T_a, e_a is the atmospheric water vapor pressure, γ is the psychrometric constant and r_s is the stomatal resistance. Stomatal resistance is calculated after [4] using the simplified equation from [5]

$$\frac{1}{r_s} = \frac{f_1(T_a) f_2(PAR)}{r_{sMIN}} + \frac{1}{r_{cuticle}} \tag{3}$$

where PAR is the photosynthetic active radiation, r_{sMIN} is the minimum stomatal resistance and $r_{cuticle}$ is the canopy resistance related to the diffusion through the cuticle layer of leaves (10^5 s m^{-1}). Functions $f1$ and $f2$ are calculated as per [5] and r_{sMIN} can be determined for each vegetation type. Q_E is calculated by land cover type and weighted by fraction of water, vegetation and pervious surfaces with the respective r_{sMIN} in every pixel. Values for r_{sMIN} used in this study are listed in Tab. 1.

The aerodynamic resistance r_a for sensible heat in (1) can then be written as

$$r_a = \frac{1}{u_* k}\left[ln\left(\frac{z_{ref}-z_d}{z_{0m}}\right) - \psi_h\left(\frac{z_{ref}-z_d}{L}\right) + \ln\left(\frac{z_{0m}}{z_{0h}}\right)\right] \tag{4}$$

and

$$u_* = Uk\left[ln\left(\frac{z_{ref}-z_d}{z_{0m}}\right) - \psi_m\left(\frac{z_{ref}-z_d}{L}\right) - \psi_m\left(\frac{z_{0m}}{L}\right)\right]^{-1} \tag{5}$$

where u_* is the friction velocity, k is the von Kármán constant (0.4), z_{ref} refers to a reference height (usually the height of wind measurements), z_d is the zero-plane displacement height, L is the Monin-Obukhov length, z_{0m} is the roughness length for momentum, z_{0h} the roughness length for heat (accounting for the excess resistance when using radiometric surface temperatures [6]) and $\psi_{m,h}$ are the stability functions for momentum and heat, respectively, as documented in [7]. Equation (5) can be used to estimate u_* from wind velocity U by iteration, if no direct measurements of the friction velocity are available [8]. z_{0h} values are usually reported as the dimensionless number $k\beta^{-1}$, defined as

$$k\beta^{-1} = ln\left(\frac{z_{0m}}{z_{0h}}\right) \tag{6}$$

and z_{0h} can be calculated after [3] by

$$z_{0h} = z_{0m}\left(7.4\exp(-\alpha Re^{0.25})\right) \tag{7}$$

where Re is the roughness Reynolds number and α is a parameter that varies with surface. Re is calculated by $Re = z_{0m} u_*/\nu$ with a kinematic molecular viscosity ν of 1.461×10^{-5} m^2 s^{-1}.

TABLE I. Minimum stomatal resistances for land cover types used in this study

Land Cover type	$r_{s\,MIN}$ [s m^{-1}]
Bare soil	500
Low vegetation	100
Deciduous	60
Evergreen	70

To determine the input parameters for r_a, the approach of [9] is modified to the satellite data. Both, roughness length (for heat and momentum) and displacement height are needed in r_a calculation. Input for the calculation of roughness parameters, i.e. the morphometry, is derived from a digital surface model, including the heights of buildings and trees, in high spatial resolution (between 1 and 5 m) using the open source Geographic Information System software QGIS and the Urban Multi-scale Environmental Predictor (UMEP) [10]. UMEP output provides building heights (mean, standard deviation, maximum) and the morphological parameters plane area index and frontal area index aggregated to the chosen grid size. Roughness parameters z_{0m} and z_d are calculated by the real urban surfaces parameterization of [11] using UMEP results as an input.

B. Evaluation

The results are evaluated by the analysis of the calculated fluxes in 100 m spatial resolution in the footprint of the flux towers. For Q_H and Q_E the source area model of [12] is used. Fluxes are measured by the Eddy Covariance method and processed with standard methods [13, 14]. Since measured Q_H and Q_E may vary considerably between averaging intervals (normally 30 mins.), the mean value of three half-hourly fluxes centered at overpass time was taken for the evaluation and is listed in Tab. 2. Satellite derived surface temperatures are compared to the surface temperature T_{rad} calculated from the emitted longwave radiation in the radiation footprint of the flux towers. T_{rad} is calculated by

$$T_{rad} = \left[\frac{L\uparrow-(1-\varepsilon)L\downarrow}{\sigma\varepsilon}\right]^{0.25} \quad (8)$$

where $L\uparrow,\downarrow$ is the upwelling and downwelling longwave radiation, respectively, measured by the radiometer, ε is the emissivity of the surface in the radiation footprint (0.97) and σ is the Stefan Boltzmann constant (5.67×10^{-8} W m^{-2} K^{-4}). According to [15], 50% of the radiometer signal origins from an area below the sensor with a radius equal to the height a.g.l. of the sensor (fig.1). Because the original resolution of the Landsat 8 TIRS is 100 m we decided to take an area of 3 x 3 cells with the flux tower in the center. The center cell was weighted 20 % and the adjacent cells 10 % each for the evaluation of T_s.

Fig.1: Fisheye photograph from the BKLI flux tower in Basel, simulating the field of view (FOV) of the downward looking pyrgeometer. Contours refer to view factor, i.e. the percentage of received signal from the respective area. (photo courtesy of M. Schmutz)

III. Study Areas and Datasets

URBANFLUXES case study cities are Basel, Switzerland, London, U.K., and Heraklion, Greece. Here we present results from Basel (city population 200k, Basel agglomeration population 500k), a typical mid-sized mid-european city right at the border triangle France-Switzerland-Germany. Figure 2 shows the land cover map and the digital elevation model for the investigated area.

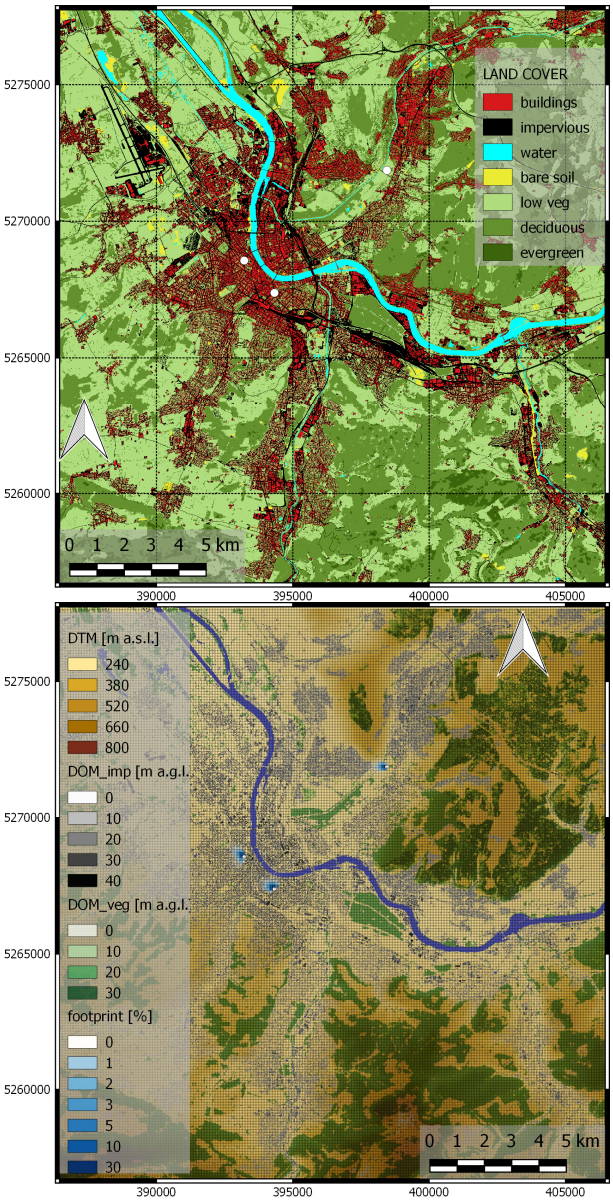

Fig.: Land cover map of Basel (top) and digital terrain and object model with overlayed 100 m grid (bottom). White points mark flux towers with footprints for 30 AUG 2015. DTM refers to terrain, DOM_imp to buildings and DOM_veg to vegetation.

Land Cover types (fig. 2) were derived from SPOT 5 data in 2.5 m resolution, land cover fractions used in (3) were aggregated to the URBANFLUXES standard 100 m grid. Surface temperatures were calculated from Landsat 8 TIRS in the same grid using the atmospheric correction software ATCOR [16]. Urban morphology parameters used for the calculation of atmospheric resistances in (4) are available in the same resolution. The reference height z_{ref} in (4) and (5) was

taken as 3 times the mean building height in the 100 m resolution UMEP output. For the parameter alpha in (7) we used a value of -0.8 for built-up areas as proposed for the city of Basel by [17] and the standard value of -2.46 from [3] for areas with low roughness, i.e. mean building/vegetation height < 1 m (mainly the low vegetation land cover class, e.g. agricultural land use and bare soil).

Q_H and Q_E were calculated for 22 Landsat 8 scenes between FEB 2013 and DEC 2015 for Basel (overpass time around 11:15 UTC+1). The analyzed scenes are listed in Table 2 sorted by season and with the most important meteorological measurements from the BKLI flux tower (fig. 6) during satellite overpass. This data is used as input for evaluation of the modelled heat fluxes in section IV.*B* and for the spatial extrapolation of T_a and u_*. Because the city of Basel is surrounded by the hills of the Black Forest in the North-East and the Jura mountains in the South, measured T_a was extrapolated to the standard grid using the dry adiabatic lapse rate of 0.0098 K m^{-1} to consider the topography ranging from 240 m to 800 m a.s.l. (fig. 2).

TABLE II. LANDSAT 8 SCENES ANALYSED FOR THE BASEL CASE STUDY AND MEASUREMENTS AT FLUX TOWER BKLI. *RN*, *RH* AND *WV* REFER TO NET RADIATION, RELATIVE HUMIDITY AND WIND VELOCITY, RESPECTIVELY

Date	Q_H	Q_E	Rn	Ta	RH	wv	u^*
YYYYMMDD	Wm^{-2}	Wm^{-2}	Wm^{-2}	K	%	ms^{-1}	ms^{-1}
20150210	249	12	298	1.7	32.8	0.85	0.23
20150226	187	44	384	5.9	29.0	3.24	0.57
20150314	176	16	413	5.5	31.7	1.88	0.46
20140320	182	41	483	15.1	41.0	4.82	0.77
20150408	251	32	540	11.3	22.4	1.07	0.36
20150415	303	79	578	20.8	24.6	2.28	0.53
20150424	300	96	596	17.5	25.6	1.16	0.37
20130425	287	47	601	20.7	41.0	0.72	0.37
20130605	268	63	665	19.3	52.4	1.14	0.35
20140608	153	172	632	29.8	31.3	1.08	0.33
20150611	367	44	639	23.0	39.7	0.97	0.41
20150704	154	69	622	31.9	34.6	1.08	0.33
20130714	286	51	621	22.7	51.6	1.19	0.39
20140717	237	136	645	26.6	37.3	1.76	0.49
20150805	251	69	612	25.1	40.7	1.86	0.44
20130815	343	85	582	20.0	51.6	1.42	0.33
20150821	244	125	582	22.1	36.1	2.00	0.39
20150830	187	143	544	29.3	32.9	1.77	0.47
20151001	192	42	404	9.7	35.0	3.92	0.59
20141014	145	98	409	17.9	41.1	3.38	0.58
20151102	183	10	310	10.2	43.8	3.37	0.57
20151220	69	6	182	7.8	41.5	2.03	0.4

Friction velocity u_* was extrapolated to the 100 m standard grid by iteration as in [8] using the measured wind speed and the Monin-Obukhov length L at the BKLI flux tower as starting values and 100 m grid roughness parameters z_{0m} and z_d. Note that measurements in the same season may vary considerably between different years (Tab. 2) with consequences for the modelled fluxes as shown in the overview in fig. 4. For example, R_n on 5 JUN 2013 and 8 JUN 2014 are of similar amount (665 and 632 W m^{-2}, respectively), but the partition between Q_H and Q_E is completely different, namely 268 and 153 W m^{-2} for Q_H to 63 and 172 W m^{-2} for Q_E, respectively, reflecting higher T_a and the higher saturation deficit on 8 JUN 2014.

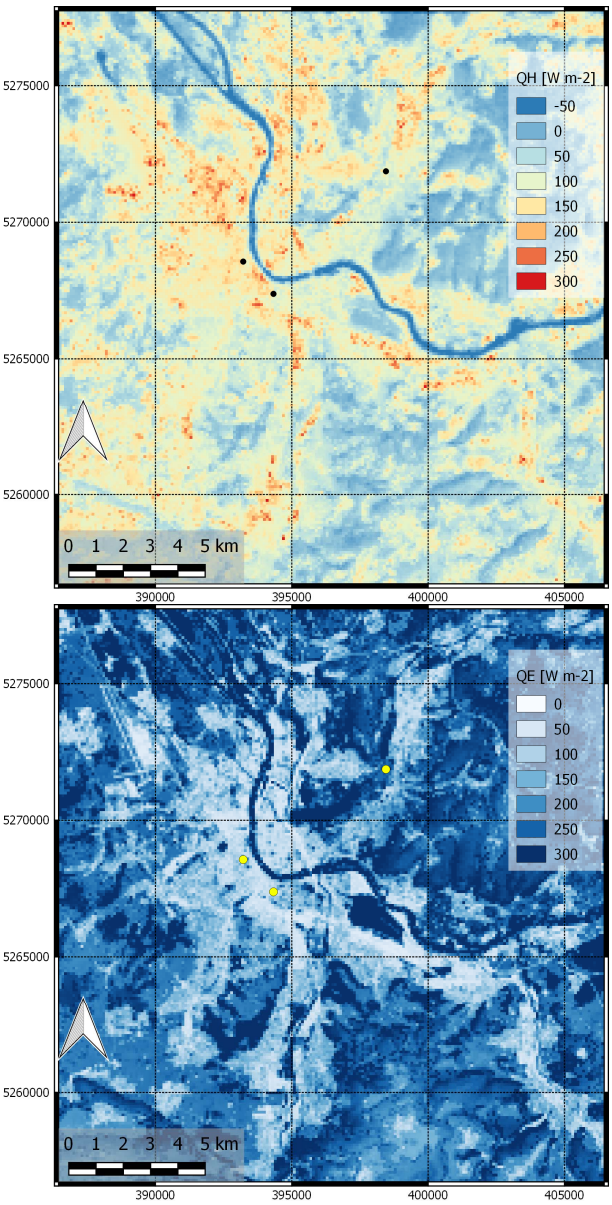

Fig. 2. Sensible heat flux (top) and latent heat flux (bottom) for Basel during Landsat 8 overpass from 30 AUG 2015. Black and yellow points mark flux towers BKLI, BAES and BLER (from left to right).

IV. RESULTS

A. Fluxes

Sensible and latent heat flux for the Basel study area are shown in fig. 2 for the Landsat overpass on 30 AUG 2015 at 1116 CET. Q_H shows highest values in the industrial areas, at the airport (NW of city center) and the railway stations (areas

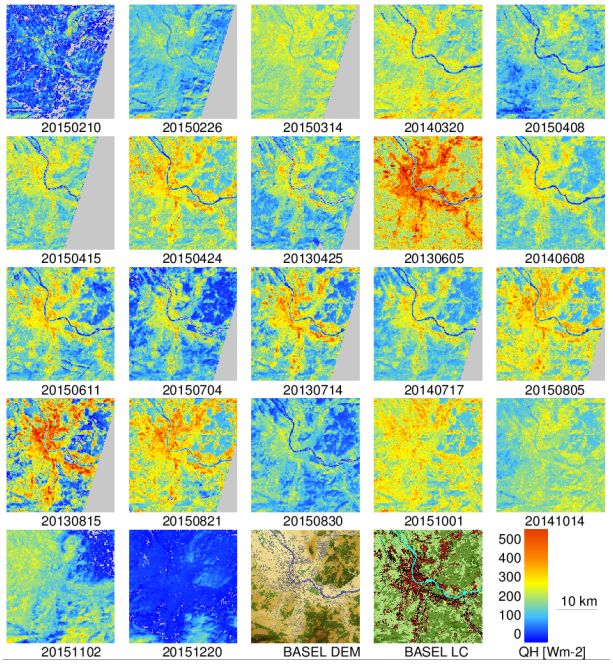

Fig. 3. Sensible heat flux for 22 scenes for Basel case study (sorted by season from upper left (FEB) to lower right (DEC) according to Table 2. Lower row additionally shows digital elevation model (DEM) and Land Cover map (LC).

with impervious land cover in fig. 2), in the inhabited areas in the city and in the densely populated valleys of the urban agglomeration. Negative values are calculated for River Rhine, because the surface temperature of water bodies is lower (25 °C) than the surrounding air temperature (29 °C). Dense forests also show low sensible heat flux, because the foliage temperature is close to air temperature.

Largest latent heat fluxes Q_E origin from water bodies and dense forests. Urban parks and areas with low building density (e.g. mansion districts) also show considerable amounts of evapotranspiration and may reach up to 200 W m^{-2}. Note that T_a on this day was very high for the season (29° C) causing a high saturation deficit which again leads to high Q_E.

Though the most important input to Q_H in the ARM method is the difference between surface temperature and air temperature, the correlation is not always straightforward, as can be seen by the comparison of the scenes in figs. 3,4 and 5. The general seasonal trend with highest fluxes for both, Q_H and Q_E, during the summer months is obvious, but interannual differences can be large when e.g. comparing the diffent scenes available for months April, June, July, August and October. A more detailed analysis of the interannual variability of flux distribution and partition may raise some interesting general relations between the modelled fluxes and atmospheric conditions, but this topic is out of the scope of this paper.

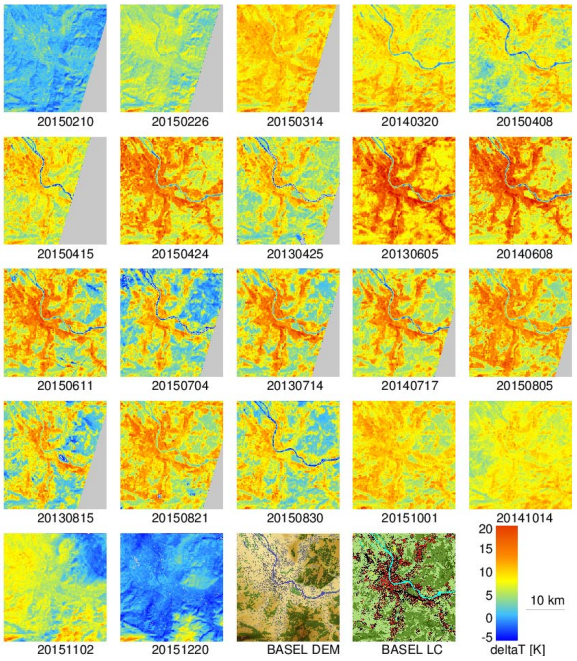

Fig. 4. As fig. 3 but for temperature difference T_s-T_a.

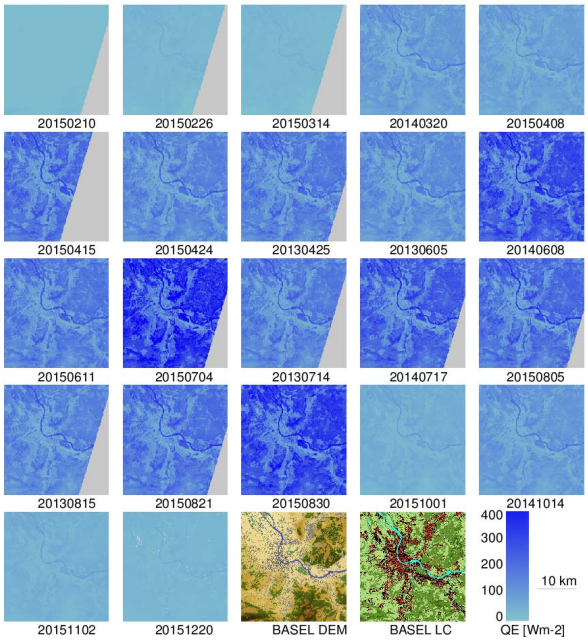

Fig. 5. As fig. 3 but for latent heat flux Q_E.

B. *Evaluation*

Modeled Q_H and Q_E from the 22 Landsat scenes are evaluated by comparison with the measured fluxes in the weighted source area of the three Basel flux towers. Figure 6 shows the locations and the weighted source areas for 30 AUG

2015 in the 100 m standard grid for Basel flux towers BKLI, BAES and BLER with underlayed Land Cover according to fig. 1. Note that Q_E is not measured at BLER.

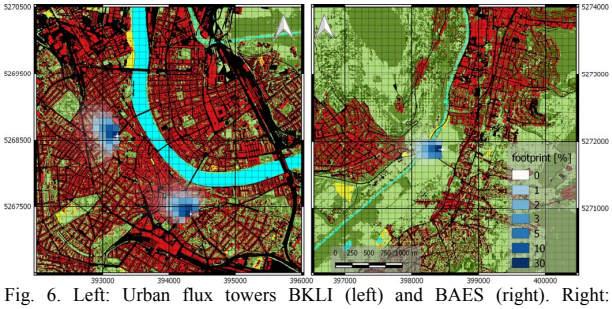

Fig. 6. Left: Urban flux towers BKLI (left) and BAES (right). Right: Rural/suburban flux tower BLER. Weighted footprint for 30 AUG 2015 satellite overpass (11:00 UTC+1). Reference system is UTM 32N.

The regression statistics of measured to modeled fluxes and tower T_{rad} to T_s are listed in Tab. 3. and shown in figs. 7 and 8. Agreement between measured and modeled fluxes is generally poor though flux maps in figs. 2, 3 and 4 show reasonable values. Modeled fluxes in the footprint of the flux towers do mostly underestimate the measured fluxes and the scatter is large. Relative underestimation of Q_E is larger than for Q_E but evaporative fluxes are of course lower in urban areas than in the rural surroundings. Some possible reasons leading to this results are discussed in section V.

TABLE III. REGRESSION STATISTICS FOR T_S, Q_H AND Q_E AT FLUX TOWERS

Flux tower	*slope*	*Offset*	*R2*
surface temperature			
BKLI	1.09	-27.81	0.988
BAES	1.09	-25.98	0.987
BLER	0.95	10.6	0.987
TOTAL	1.03	-11.42	0.963
Sensible heat flux			
BKLI	0.76	10.95	0.63
BAES	0.92	-17.97	0.68
BLER	0.58	40.60	0.63
TOTAL	0.76	15.88	0.71
Latent heat flux			
BKLI	0.58	16.00	0.65
BAES	0.42	13.34	0.64
TOTAL	0.54	12.76	0.65

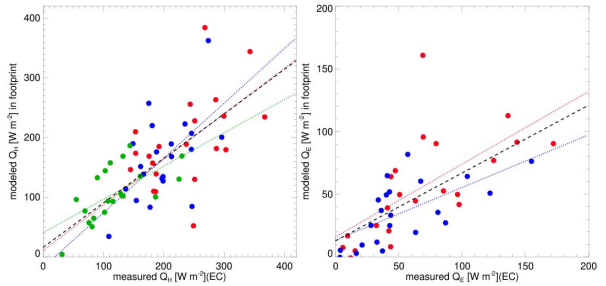

Fig. 7. Comparison of modeled (y-axis) and measured (x-axis) Q_H (left) and Q_E (right) for flux towers BKLI (red), BAES (blue) and BLER (green).

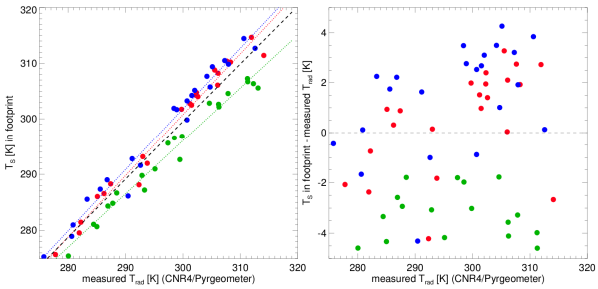

Fig. 8. Left: Measured surface temperature T_{rad} (x-axis) against satellite derived surface temperature T_s (y-axis) in the radiation footprint of flux towers BKLI (red), BAES (blue) and BLER (green) with regression lines. Black dashed line is the regression for all data. Right: Same as left panel, but for the differences $T_s - T_{rad}$.

Regression statistics for T_s are better than for the heat fluxes, nevertheless, differences may reach up to 4 K. Satellite derived T_s are higher at the urban flux towers BKLI and BAES and lower at the rural/suburban flux tower BLER. We address this to the different fields of view, i.e., the radiation sensor mounted on an urban flux tower "sees" a considerable amount of walls (fig. 9), which are more influenced by shadow effects and may lead to cooler T_{rad}. Additional uncertainty is introduced by the use of a bulk emissivity for EO derived T_s and atmospheric correction.

V. DISCUSSION AND OUTLOOK

The analysis of modeled Q_H and Q_E from 22 Landsat scenes for the URBANFLUXES case study city Basel shows reasonable results, but the validation with in-situ measurements is generally moderate. Since there is no alternative for the evaluation of EO-derived fluxes, possible reasons for the observed deviations are listed in the following:

- The uncertainty inherent to EC measurements may range from 10% for Q_H to up to 25 % for trace gases (e.g. [18], [19]). Representativeness of flux tower measurements in urban environments is reduced compared to rural areas due to the heterogeneity of urban neighbourhoods [13]. Large (inherent) variations in EC measurements between averaging intervals additionally increase this uncertainty. Using averages of the adjacent half hours (before and after the satellite overpass) for comparison with modelled fluxes reduce this uncertainty.
- Known drawbacks of the ARM method: input parameters (T_a, wv) have to be spatially derived from in-situ measurements (flux towers and/or sensor networks) and may differ from "true" values in certain areas during satellite overpass; further large uncertainties exist in the calculation of the aerodynamic resistance including $k\beta^{-1}$.
- Uncertainties in the calculation of flux tower source areas used for comparison with modelled fluxes [20].

- Difficulties to measure evapotranspiration in general and in urban areas in part. Spatial extrapolation of measured vapor saturation deficit.

Finally, modelled fluxes may be improved by examination of uncertainties in T_s related to emissivity, thermal anisotropy and atmospheric correction in urban areas.

As URBANFLUXES will model all terms of the urban energy balance independently to derive the anthropogenic heat flux, the next step within this project is to combine the presented results with EO derived storage term ΔQ_S and net radiation R_n and then analyze the energy balance closure.

ACKNOWLEDGMENT

The project leading to this application has received funding from the European Union's Horizon 2020 research and innovation program under grant agreement No 637519 (URBANFLUXES).

REFERENCES

[1] N. Chrysoulakis et al., "Urban Energy Budget Estimation from Sentinels: The URBANFLUXES Project," Mapping Urban Areas from Space, Frascati, Italy, 4-5 November 2015

[2] T. Foken, "50 Years of the Monin–Obukhov Similarity Theory", *Boundary Layer Meteorol.,* vol. 119, pp. 431-447, 2006.

[3] W. Brutsaert, "Evaporation into the atmosphere," D. Reidel Publ. Co. Boston. 1982

[4] S. Kato, Y. Yamaguchi, C.C. Liu, C.Y. Sun, "Surface heat balance analysis of Tainan City on March 6, 2001 using ASTER and Formosat-2 data," *sensors*, vol. 8, pp. 6026 – 6044, 2008.

[5] K. Nishida, R.R. Nemani, S.W. Running, J.M. Glassy, "An operational remote sensing algorithm of land surface evaporation,", *J. Geo. Res*, vol. 108, doi: 10.1029/2002JD002062

[6] J.A.Voogt, C.S.B. Grimmond, "Modeling surface sensible heat flux using surface radiative temperatures in a simple urban area," *J. Appl. Meteorol.*, vol. 39, pp. 1679-1699, 2000.

[7] U. Högström, "Non-dimensional wind and temperature profiles in the atmospheric surface layer: A re-evaluation," *Topics in Micrometeorology*. A Festschrift for Arch Dyer. Springer Netherlands, pp.55-78, 1988

[8] C.S.B. Grimmond and H.A. Cleugh, "A simple method to determine Obukhov Lengths for suburban areas," *J. Appl. Meteorol.,* vol. 33, pp. 435-440, 1994.

[9] D.F. Nadeau, W. Brutsaert, M.B. Parlange, E. Bou-Zeid, G. Barrenetxea, O. Couach, M.-O. Boldi, J.S. Selker, M. Vetterli, "Estimation of urban sensible heat flux using a dense wireless network of observations," *Environ. Fluid Mech.*, vol. 9, pp. 635-653, 2009.

[10] F. Lindberg, C.S.B. Grimmond, S. Onomura, L. Järvi, "UMEP - An integrated tool for urban climatology and climate-sensitive planning applications", International Conference on Urban Climatology (ICUC9), Toulouse, France, 2015.

[11] M. Kanda, A. Inagaki, T. Miyamoto, M. Gryschka, S. Raasch, "A new aerodynamic parametrization for real urban surfaces," *Boundary- Layer Meteorol.*, vol. 148, pp. 357-377, 2013

[12] R. Kormann, F.X. Meixner, "An analytical footprint model for non-neutral stratification," *Boundary-Layer Meteorol.,* vol 99, pp. 207-224, 2001.

[13] C. Feigenwinter, R. Vogt, A. Christen, "Eddy Covariance Measurements Over Urban Areas," pp. 377–397, in: Eddy Covariance A Practical Guide to Measurement and Data Analysis. Heidelberg, New York, Springer Atmospheric Sciences, p. 430. Springer. 2012

[14] X. Lee, W. Massman, B. Law (eds.), "Handbook of Micrometeorology", Heidelberg, New York, Springer, 2005.

[15] W.E. Reifsnyder, "Radiation geometry in the measurement and interpretation of radiation balance," *Agr. Meteorol.*, vol. 4, pp. 255-265, 1967.

[16] R. Richter and D. Schläpfer, "ATCOR-2/3 User Guide," Version 9.0.0. DLR & ReSe Applications, 2015.

[17] C.M. Frey and E. Parlow, "Determination of the aerodynamic resistance to heat using morphometric methods," *EARSel eProceedings* vol. 9:2, pp. 52-63, 2010.

[18] J. Wang, J. Zhung, W. Wang, S. Liu and Z. Xu, "Assessment of uncertainties in Eddy Covariance flux measurements based on intensive flux matrix of HiWATER-MUSOEXE," *IEEE Geos. Rem. Sens. Let.* vol. 12.2, pp. 259-263, 2015.

[19] A.D. Richardson et al., "Uncertainty Quantification," pp. 173–207, in: Eddy Covariance - a Practical Guide to Measurement and Data Analysis. Heidelberg, New York, Springer Atmospheric Sciences, p. 430. Springer. 2012

[20] A. Hellsten et al., "Footprint evaluation for flux and concentration measurements for an urban-like canopy with coupled Lagrangian stochastic and LES simulation models," *Bound.-Layer Meteorol.,* vol. 157.2, pp.157- 191, 2015

A.3 P5: Insights from More than Ten Years of CO_2 Flux Measurements in the City of Basel, Switzerland

This article is a summary of research focusing on carbon dioxide measurements that has been conducted in Basel. Basically, results from Lietzke and Vogt [2013], Lietzke et al. [2015] and Schmutz et al. [2016] are compiled and scientific highlights from one of the longest urban eddy covariance time series are presented.

The following chapter is published as an article in the Quarterly Newsletter of the International Association for Urban Climate, Urban Climate News:

C. Feigenwinter, **M. Schmutz**, R. Vogt, E. Parlow (2017): Insights from more than ten years of CO_2 flux measurements in the city of Basel, Switzerland. *Urban Climate News, Quarterly Newsletter of the International Association for Urban Climate 65*, 24-32.

Urban Projects 24

Insights from more than ten years of CO_2 flux measurements in the city of Basel, Switzerland

Introduction

Urban micrometeorology has a long tradition in Basel, Switzerland. Flux tower measurements started as early as in 1992 with the installation of a 15 m high tower on the terrace at the 5th floor of the former location of the institute of Meterorology, Climatology and Remote Sensing of the University of Basel (MCR) at Spalenring (BSPA in Fig. 1). Though the site was far from ideal (the building had a pitched roof and the chimney was pretty close to the sensors…) and latent heat flux was only sporadically measured, the tower was an important symbol for the institute's activities and attracted several urban climatology and turbulence projects.

In these early years, the main research topic was the vertical structure of turbulence in and above the urban canopy layer, also strongly influenced by the early work of M.W. Rotach in Zurich (e.g. Rotach, 1993a,b). With the help of Rotach's group, a 51 m high antenna tower (BMCH in Fig. 1) was equipped with sonics at three levels (z/h = 1.5, 2.1 and 3.2) on a 21 m high building at Messe Schweiz (BMCH in Fig. 1) between July 1995 and February 1996. Results of this campaign described for the first time the vertical dependence of velocity spectra in the urban roughness sub-layer (RSL) by the analysis of a large number of simultaneously measured multi-level turbulence time series (Feigenwinter et al., 1999). This study also confirmed that profiles of velocity variances and spectra of wind components could be parametrized within the framework of Monin-Obukhov similarity theory (MOST), if local scaling is applied. Feigenwinter and Vogt (2005) analyzed the same dataset with respect to profiles of coherent structures and showed that organized motions are not only a feature of vegetation canopies but can also be detected over rough urban surfaces.

With BUBBLE (Basel UrBan Boundary Layer Experiment) in 2002, Basel and MCR became definitely established in the Urban Climatology community. Despite no common funding, Roland Vogt and Andreas Christen accomplished to bring world leading urban climatologists to Basel for one of the longest and most detailed urban boundary layer programs (Rotach et al., 2005), including flux towers at Spalenring and Sperrstrasse (BSPA and BSPE in Fig. 1). The open data policy of BUBBLE led and still leads to numerous publications using the BUBBLE dataset, notably also for the validation of LES and CFD models (e.g. Gartmann et al., 2012). Christen and Vogt (2004) provide a comprehensive overview of the main findings of BUBBLE in terms of the urban energy and radiation balance. Within the framework of BUBBLE, research of MCR also started to focus on profiles of urban CO_2 concentration and fluxes. Vogt et al. (2006) tested the applicability of MOST to CO_2 flux-gradient relationships and found acceptable agreement for the top level at the upper boundary of the roughness sub-layer at 2 z_h (e.g. Feigenwinter et al., 2012). As a main conclusion they stressed the need for detailed analysis of surface properties (i.e. vegetation fraction) and anthropogenic CO_2 emissions (traffic, combustion) in the source area of flux towers when comparing with other urban studies.

As a consequence, research in Basel further concentrated on the analysis of CO_2 fluxes and concentrations with respect to the underlying urban structure. Simultaneously with the movement of MCR in 2003 to its present location, the flux tower from Spalenring was re-installed on the roof of the new building at Klingelbergstrasse (BKLI). An additional flux tower was installed on a slim 36m high building at Aeschenplatz (BAES) in 2009. In the following, the main findings from three papers analyzing data from the two flux towers BKLI and BAES are discussed, considering spatial scales from street canyon to neighborhood and temporal scales from months to years to decades.

Basel flux towers

Figure 1 shows the locations of active (BKLI and BAES) and former flux towers (BSPA-Spalenring, BSPE-Sperrstrasse and BMCH-Messe Schweiz) in the context of a digital object model (DOM) for buildings and trees. Footprints are calculated by the Kormann and Meixner (2001) algorithm and show the annual mean flux footprint of the respective flux tower. All flux towers were and are equipped with state of the art Eddy Covariance (EC) systems including an open path infrared gas analyzer (IRGA) and measurement devices for extended standard meteorology (temperature, humidity, wind and radiation (4 components)). At the BKLI site, numerous additional measurements are performed, including e.g. measurement of direct and diffuse radiation. Up to date instrumentation of BKLI and BAES flux towers is described in detail in Schmutz et al. (2016) and Lietzke et al. (2015), respectively; for further details about BMCH, BSPE and BSPA sites and instrumentation please refer to the respective papers.

The street canyon view

For the study of Lietzke and Vogt (2013) an additional 18 m high flux tower (B) with 5 levels of turbulence measurements was installed at the center of the adjacent

Figure 1. BASEL digital object model DOM with building heights (red), tree heights (green) and flux towers: former (blue) and active (yellow) towers with mean annual footprints. Light green areas refer to low vegetation (lawn), gray areas refer to impervious surfaces (roads, plazas) and railway tracks. Coordinate system is UTM 32N (EPSG: 32632).

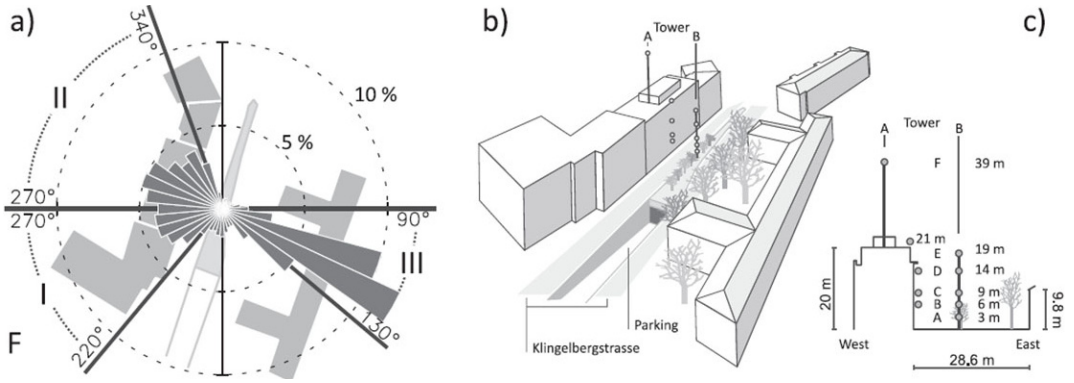

Figure 2. (a) BKLI Wind rose at 39 m (F) and plan area of the surrounding buildings. (b) 3D-view from the south. (c) cross section at the tower location (adapted from Lietzke and Vogt, 2013)

street canyon to BKLI flux tower (A), providing a full-year dataset for 2010. Figure 2 gives an overview of the experimental setup. The street canyon orientation (20°) is approximately perpendicular to the main wind directions. As a result, in-canyon air flow forms a vortex that shows a corkscrew-like lateral motion, the direction of which is dependent on the direction of the wind above. Eastern (90-130°) and western winds from less than 270° lead to northward flowing air masses inside the canyon whereas western winds from directions greater than 270° result in a southwards directed flow, as shown in Figure 3. The flow regime of wind coming from the area west of the site is expected to be 'skimming flow' (Oke, 1987) as the underlying building structure is relatively dense. The street canyon itself has a non-ideal cross section. The height to width ratio is 0.7 for the building to the west and 0.34 for the building to the east. Thus, the local flow regime for the canyon for east wind situations might be characterized as 'wake interference flow' (Oke, 1987).

CO_2 concentrations

Daytime in-canyon distribution of CO_2 concentration depends heavily on these vortex structures and traffic emissions. Mean diurnal courses of CO_2 concentrations are comparable to that of other cities but spatial differences reveal some interesting patterns. Basically, the concentration level is coupled to the height of the urban boundary layer. Traffic as the dominant CO_2 source in the street canyon has only a minor influence on absolute concentrations at all heights. However, traffic emissions result in a superimposed effect that is generally stronger closer to the ground. This fact is represented by the vertical differences between the bottom or top of the canyon and 39 m as shown in Figure 4. These differences reflect the diurnal course of traffic density well and also allow for a clear distinction between working day and weekend courses.

CO_2 fluxes

Traffic is obviously the determining factor for CO_2 fluxes (F_C) since mean diurnal courses of traffic density and F_C(19) in Figure 5 have almost identical characteristics. In accordance with traffic density, F_C(19) shows distinct working day/weekend differences and the one hour shift in morning traffic increase during periods with/without daylight saving time. Strong linear correlations support the assumption of a distinct relationship. We are well aware that F_C(19) is measured in the roughness sub-layer (RSL) and the influence of individual roughness elements cannot be avoided. A height dependency of turbulent fluxes in the urban canopy layer (UCL) was expected and the sensor at 19 m was intended to capture the influence of the traffic of this busy street and to see how far up this influence reaches. The excellent qualitative agreement of the F_C(19) flux patterns with the diurnal patterns of traffic confirms

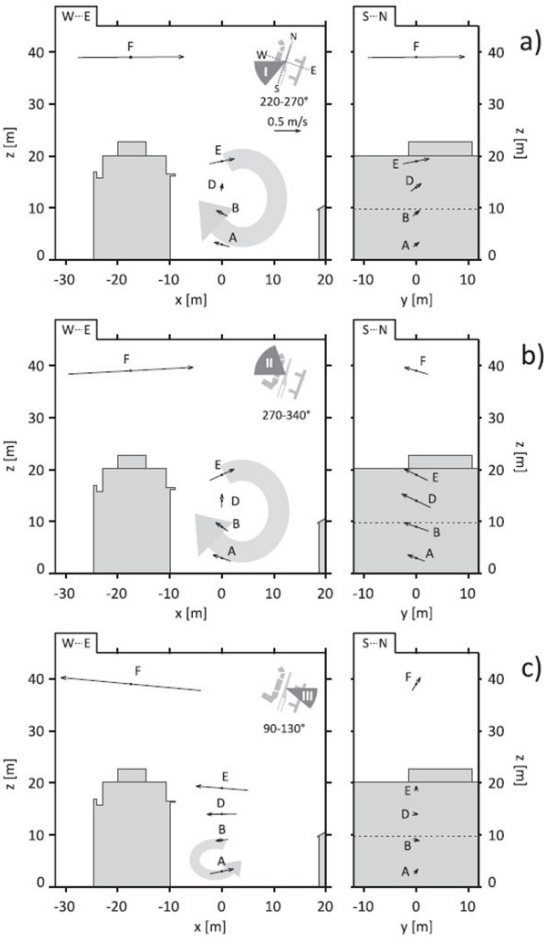

Figure 3. Cross (left column, W-E) and lateral (right column, S-N) sections of the street canyon for three different ambient wind sectors (a, b & c). Arrows depict average wind vector components in the respective planes at the measurement locations A, B, D, E and F. Typical expected vortex structures are shown for each wind sector (adapted from Lietzke and Vogt, 2013).

this approach and demonstrates the applicability of the EC method for such a specific purpose. Obviously sufficient mixing blends the traffic emissions to a representative flux.

As a first consequence, it can be argued that urban CO_2 fluxes at a height of approximately 2 z_h are extremely sensitive to the placement of the tower. A few tens of meters of horizontal displacement may lead to totally different diurnal regimes depending on prevailing wind directions combined with the given canyon orientation and configuration. The authors therefore stress the need for reliable source area determination in order to compare flux towers at different locations.

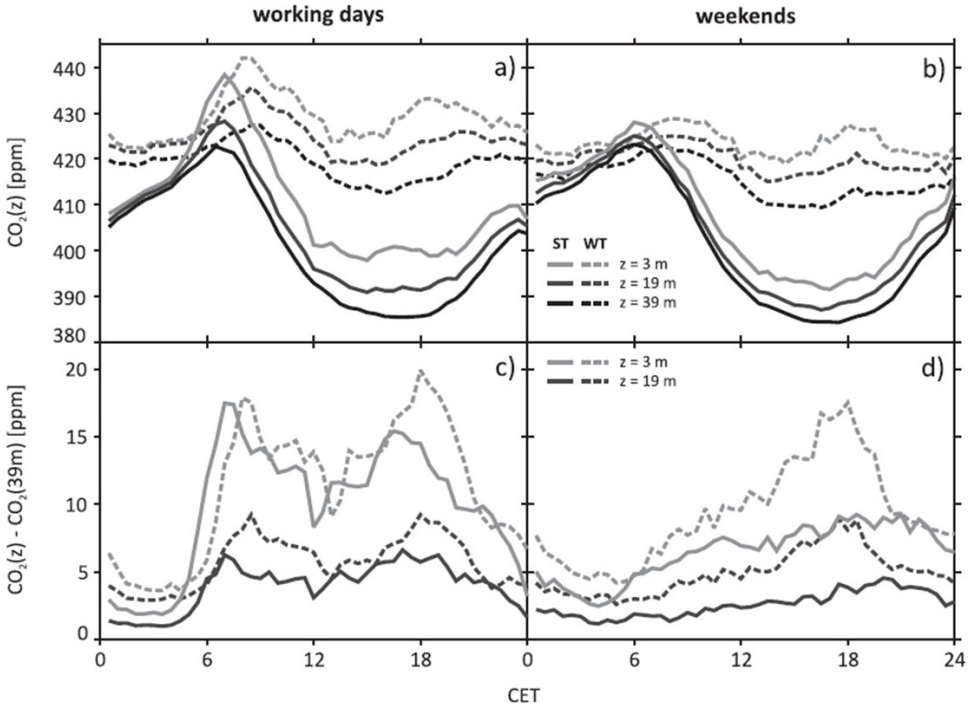

Figure 4. Mean diurnal courses of CO_2 concentrations at two heights in the canyon center and above the roof for working days (a) and weekends (b). Data is separated for summer-(ST) and wintertime (WT). (c) & (d): Corresponding differences relative to top level (adapted from Lietzke and Vogt, 2013)

The neighborhood view

Lietzke et al. (2015) analyzed the controlling factors responsible for the variability of urban CO_2 fluxes based on a 4-year dataset of Basel flux tower BAES. In their study the authors provide a review of more than 40 urban studies trying to find a common relationship between CO_2 flux, traffic density and land cover fraction (Figure 6). Despite the huge uncertainties resulting from non-standardized methods for measurement procedures (reference height, tower location, data processing) and for determination and classification of surface characteristics, even the greenest locations with high vegetation fractions show a positive CO_2 budget and fossil fuel emissions (traffic and heating related combustion) have a strong influence on the size of CO_2 fluxes.

In order to make results from different locations and different cities better comparable, the authors for the first time introduced the concept of "expected fluxes" eF_C based on the sectoral analysis of F_C. Ideally a dataset provides an equal representation of each sector, which is never the case in the real world. The method is based on the gap filling method with mean diurnal cycles (MDC) (e.g. Järvi et al., 2012), where missing F_C data are replaced based on a set of MDC for the existing data. Each MDC accounts for different conditions (e.g. season, working days/weekends, wind sectors, etc.). Sectoral eF_C is derived by splitting F_C into nine sectoral datasets and filling the missing values with MDC data derived for the respective sector. The average of all sectoral eF_C is the average expected flux and the sum of all sectoral *eNEE* ("Net (urban) ecosystem exchange") is the average expected *eNEE*, respectively. eF_C as an up-scaled measure is expected to give a more accurate average representation of the heterogeneous surroundings than F_C as the latter represents only a patchwork of single, temporally restricted and wind direction dependent images of the surroundings.

Relating sectoral eF_C instead of F_C to urban surface fractions of buildings and vegetation results in a better agreement (also with data from other studies), as shown in Figure 7.

Provided sufficient data availability (EC fluxes, Land Use/Land Cover maps (LULC), morphology, urban form, etc.) the concept of eF_C and *eNEE* may be of help for the interpretation of measured carbon fluxes at other urban sites, especially those surrounded by areas with different emission characteristics and unequally distributed wind directions. As eF_C relies on statistical up-scaling, its application is restricted to long-term measurement sites. An interesting option for future applications would be the combination with LCZ classification (Stewart and Oke,

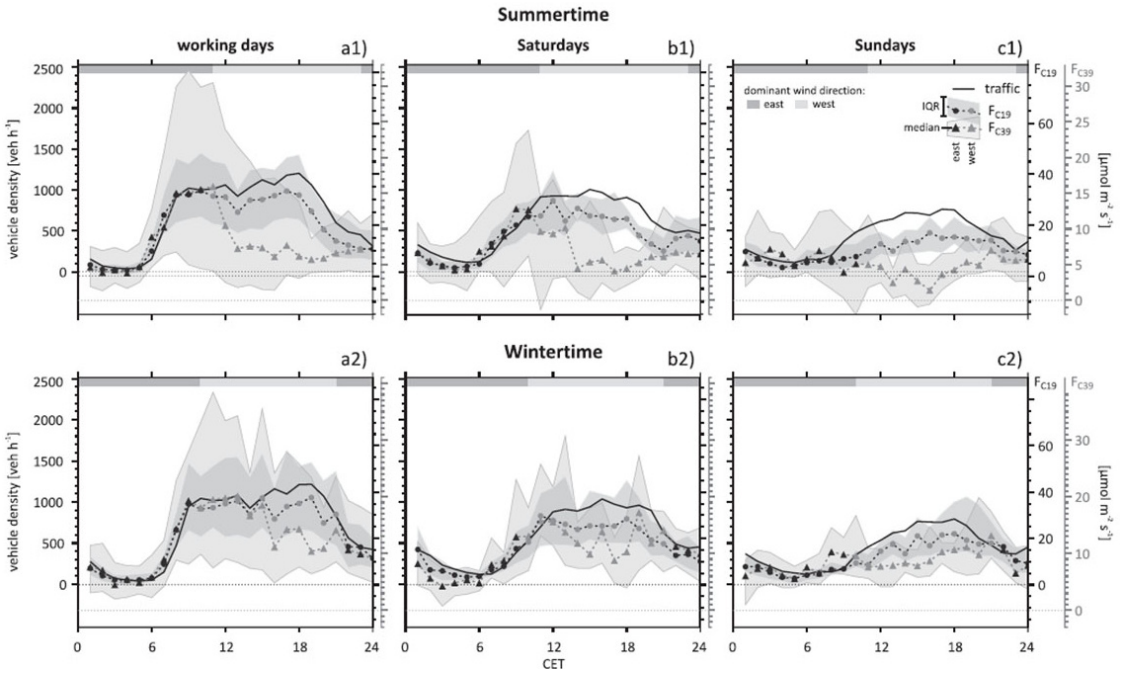

Figure 5. Average diurnal courses of vehicle density (black line), F_C(19) (circles) and F_C(39) (triangles) for ST (upper row) and WT period (lower row). Hourly averaged median data for (a) working days, (b) Saturdays and (c) Sundays. Shaded areas represent the interquartile ranges. The light gray bar at the top of each plot denotes > 50% winds from western directions (20-200°), the dark gray > 50% from eastern directions (200-20°). Correspondingly, F_C values measured under west wind (east wind) influence are marked with lighter gray (darker gray) symbols (adapted from Lietzke and Vogt, 2013)

2012) which could lead to a more standardized implementation.

The longterm view

After moving the flux tower from BSPA to its current location at Klingelbergstrasse BKLI in 2003, a lot of effort was put into maintenance work and sensor calibration. Numerous recalibrations of the EC system as well as several wind tunnel experiments with the sonic anemometer have been performed (Vogt & Feigenwinter, 2004), which made it possible to run the EC system without considerable gaps up to the present day, covering almost 14 years of continuous flux data. Schmutz et al. (2016) present results from the first decade of CO_2 flux measurements, which is the longest urban CO_2 flux time series currently published in literature.

Decadal trends of CO_2 flux and concentration

Comparing the CO_2 concentration at BKLI to regional background concentration records from Global Atmosphere Watch (GAW) stations Schauinsland (SAL, 40 km north of BKLI, 1205 m asl) and Jungfraujoch (JFJ, 120 km south of BKLI, 3580 m asl) reveals good agreement of the data in terms of seasonal patterns and long term trends (Figure 8). At all three sites an average linear trend near 2.0 ppm y^{-1} was calculated, which is in good agreement with results reported in the IPCC report 2013 (IPCC, 2013) derived from Mauna Loa and South Pole data. The seasonal course of the CO_2 concentration is mainly shaped by the varying photosynthetic activity of the vegetation. However, the average concentration level is around 10 ppm higher in the city compared to the reference sites. Interestingly, the coupling between local and background concentration follows a hysteresis, whereas the winter peak is delayed by up to three month and the summer peak by around one month at JFJ and SAL (Figure 9). This shows the time needed to mix the signal of the ongoing source and sink processes within the boundary layer into the lower troposphere during stable conditions in wintertime and convective conditions in summertime.

In order to analyze the long-term trend of F_C, the concept of "expected fluxes" introduced by Lietzke et al. (2015) was refined and further developed in Schmutz et al. (2016). The use of moving look-up tables increases the statistical robustness and eliminates the need of multi-year time series for the calculation of what is now called horizontal averages (denoted by angle brackets). While

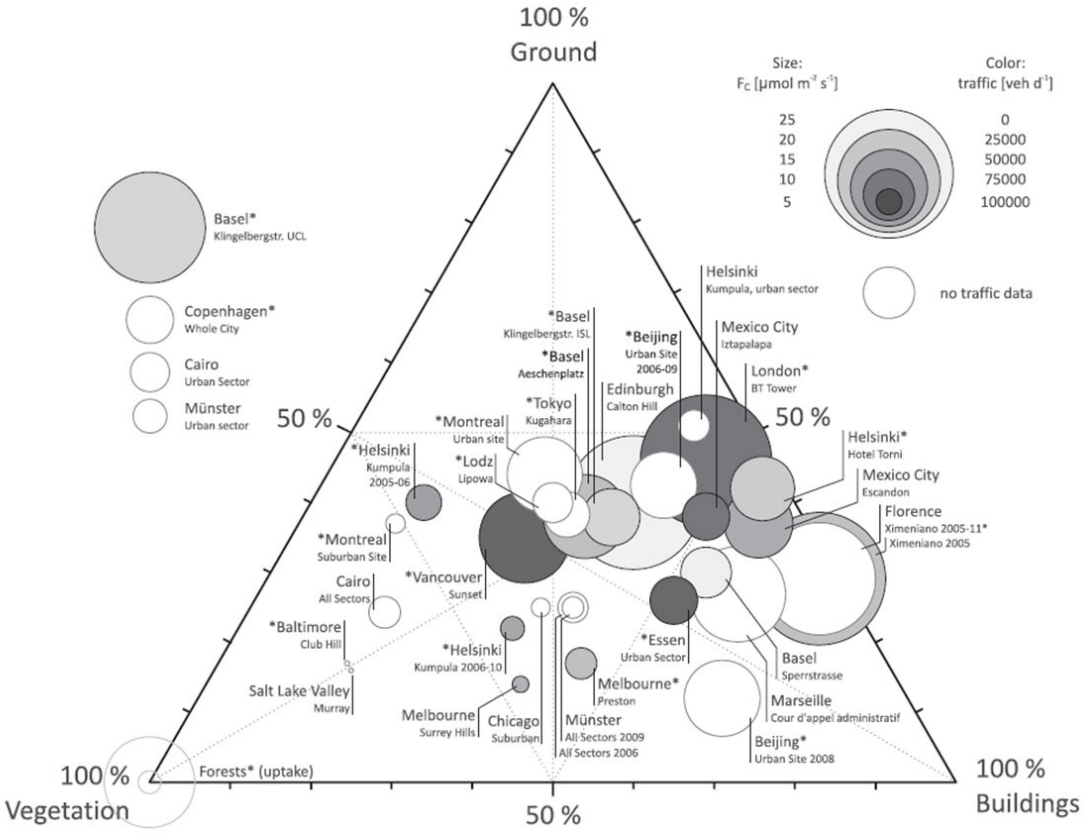

Figure 6. Ternary plot of selected urban studies. The centre point of each circle gives the plan area fractions. The size represents F_C and the gray tone represents the reported traffic density if available in vehicles per day (see legend). An asterisk indicates that the F_C data coverage was at least one whole year. Where only vegetation cover was listed, the remaining fraction was assumed to be equally split between buildings and ground. For circles outside the plot no plan area fractions were reported. Refer to Tab. 1 in Lietzke et al. (2015) for full references. (Adapted from Lietzke et al., 2015)

varying wind systems may considerably superimpose the measured CO_2 fluxes by advecting the signal of varying sources over the course of time, horizontal averages mostly eliminate this effect and reveal the effective variability and long-term trends at the measurement site. F_C at BKLI was thereby reduced by 5 % between 2005 and 2014, which can be explained by the reduced traffic volume around BKLI due to new city bypass roads. Still, the year-to-year variability of F_C is much larger than the calculated linear trend (compare Fig. 8), which makes it difficult to further discuss long-term tendencies of F_C at BKLI. Despite the large inter-annual variability, a lower limit of F_C was found around 5 µmol m^{-2} s^{-1} consistent over the entire measurement period. This implies a base-load of the urban metabolism during minimal source activity in early morning, especially in summertime, introduced by e.g. human respiration and the fact that main sources like traffic or heating activity are never zero.

Outlook

A short history and the most recent research from the flux towers in Basel, Switzerland, were presented. As the value of long-term flux measurements is evident, also considering the enormous efforts and investments in long-term infrastructure and monitoring programs like ICOS (www.icos-ri.eu) and NEON (www.neonscience.org), we are confident to find future funding to continue our high quality measurements in Basel. Long-term EC measurements in urban environments are essential for the assessment of urban climate models and remote sensing applications. Currently, the Basel flux towers BKLI and BAES provide invaluable data for the evaluation of satellite derived sensible and latent heat fluxes (Feigenwinter et al., 2017) in the frame of the Horizon 2020 URBANFLUXES project (Chrysoulakis et al., 2017; www.urbanfluxes.eu). Since the number of urban flux towers is still increasing and a lot of the permanent urban flux tow-

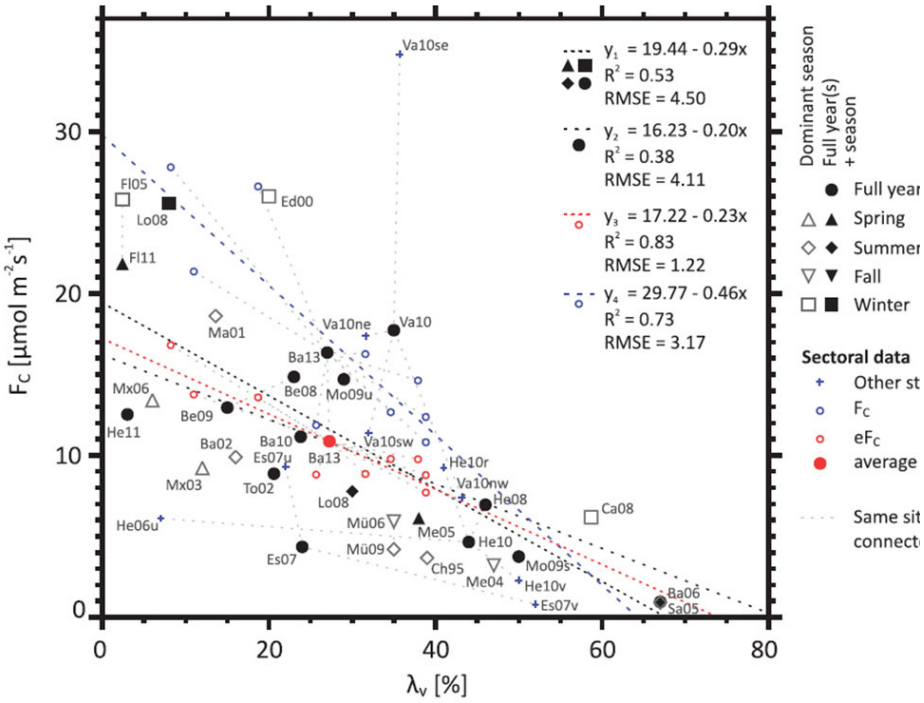

Figure 7. Average F_C as a function of vegetation fraction λv for selected studies. Open symbols define the season of measurements. Filled circles represent measurements of one or more full years, all other filled symbols stand for full years plus an additional part of the respective season. Sectoral average F_C and eF_C (derived from *eNEE*) of this study are denoted by the small open circles. Regression equations (y1-y4) are for the respective groups of data as labelled. Other dashed lines connect different results from one single site (e.g. for sectors or years) and show site-specific variability. (Adapted from Lietzke et al., 2015)

ers meanwhile have time series of more than a decade, it may be time for a refreshment of the URBAN FLUX NETWORK (see also IAUC Newsletter from June 2009), e.g. in form of a La Thuile–like synthesis dataset (http://fluxnet.fluxdata.org/data/la-thuile-dataset/).

Acknowledgements

This work has received funding from the EU FP7 (European Community's Seventh Framework Programme) project BRIDGE (grant agreement no. 211345), from the project "Urban Climate Study of Bucharest" (IZERZ0_142160) made possible by the Romanian-Swiss Research Program, and from the European Union's Horizon 2020 research and innovation programme URBANFLUXES (grant agreement no. 637519). The authors highly acknowledge the work of countless students, technicians and researchers involved in the installation, maintenance and data processing of the Basel flux towers since 1992.

References

Christen A, Vogt R. Energy and radiation balance of a central European city. *Int. J. Climatol*. 24, 1395–1421 (2004).

Chrysoulakis, N., Marconcini, M., Gastellu-Etchegorry, J-P., Grimmond, C.S.B., Feigenwinter, C., Lindberg, F., del Frate, F., Klostermann, J., Mitraka, Z., Esch, T,. Landier, L., Gabey, A., Parlow, E., Olofson, F. Anthropogenic heat flux estimation from space: results of the first phase of the URBANFLUXES project. Joint Urban and Remote Sensing Event (JURSE), Dubai, U.A.E., 2017. (http://ieeexplore.ieee.org/stamp/stamp.jsp?tp=&arnumber=7924591)

Feigenwinter, C., Parlow, E., Vogt, R., Schmutz, M., Chrysoulakis, N., Lindberg, F., Marconcini, M., del Frate, F. Spatial distribution of sensible and latent heat flux in the URBANFLUXES case study city Basel (Switzerland). Joint Urban and Remote Sensing Event (JURSE), Dubai, U.A.E., 2017. (http://ieeexplore.ieee.org/stamp/stamp.jsp?tp=&arnumber=7924594)

Feigenwinter, C., Vogt, R. Detection and analysis of coherent structures in urban turbulence. *Theor. Appl. Climatol*. 81, 219-230 (2005)

Feigenwinter, C., Vogt, R., Christen, A. Eddy covariance measurements over urban areas. In Eddy Covariance – A Practical Guide to Measurement and Data Analysis. Springer Atmospheric Sciences, Aubinet, M., Vesala, T.,

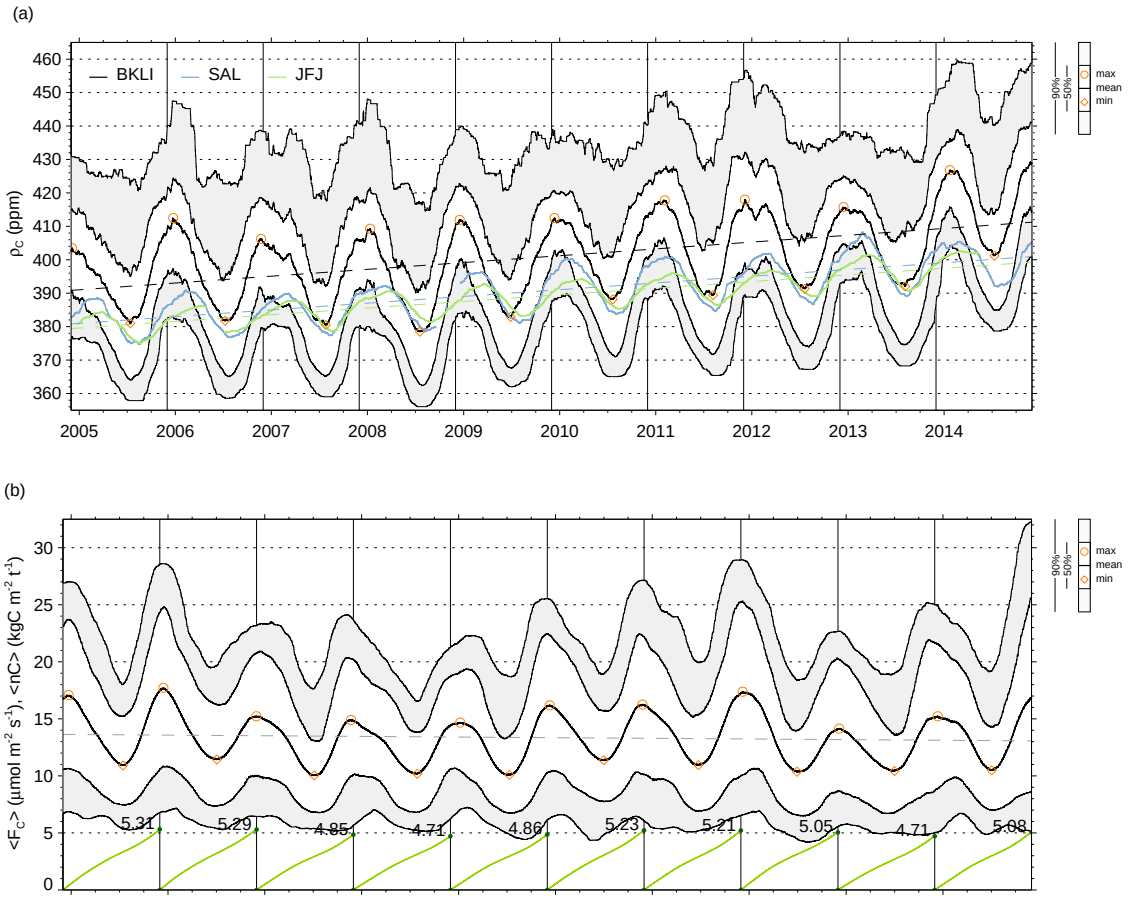

Figure 8. (a) Time series of CO_2 concentration at BKLI, Schauinsland (SAL), and Jungfraujoch (JFJ) and (b) time series of $<F_C>$ (horizontally averaged F_C) and yearly cumulative $<n_C>$ (green lines from 2005 until 2014). The solid lines are 90 days running means of half hourly data. Statistics for BKLI are indicated by grey shaded areas. The dashed lines show the linear regression for each time series. Additionally, winter maxima (circles) and summer minima (diamonds) are drawn (adapted from Schmutz et al. 2016).

Papale, D. (eds). Springer: Dordrecht, the Netherlands, 377–397 (2012).

Feigenwinter, C., Vogt, R., Parlow, E. Vertical structure of selected turbulence characteristics above an urban canopy. *Theor. Appl. Climatol*. 62, 51–63 (1999)

Gartmann, A., Mueller, M.D., Parlow, E., Vogt, R. Evaluation of numerical simulations of CO2 transport in a city block with field measurements, *Environmental Fluid Mechanics* 12, H.2, 185-200 (2012)

Intergovernmental Panel on Climate Change (IPCC). Climate Change 2013: The Physical Science Basis. Contribution of Working Group I to the Fifth Assessment Report of the Intergovernmental Panel on Climate Change, 1535 pp., Cambridge Univ. Press, Cambridge, U. K. (2013). doi:10.1017/CBO9781107415324.

Järvi, L., Nordbo, A., Junninen, H., Riikonen, A., Moilanen, J., Nikinmaa, E., Vesala, T. Seasonal and annual variation of carbon dioxide surface fluxes in Helsinki, Finland, in 2006–2010. *Atmos. Chem. Phys*. 120(3), 8355–8396, (2012). doi: 10.5194/acpd-12-8355-2012

Kormann, R., Meixner, F.X. An analytical footprint model for non-neutral stratification. *Bound.-Layer Meteorol*. 99, 207–224 (2001).

Lietzke B, Vogt R. Variability of CO2 concentrations and fluxes in and above an urban street canyon. *Atmos. Environ*. 74, 60–72 (2013).

Lietzke, B., Vogt, R., Feigenwinter, C., Parlow, E. On the controlling factors for the variability of carbon dioxide flux in a heterogeneous urban environment, *Int. J. Climatol*., doi:10.1002/joc.4255 (2015).

Oke, T.R. Boundary Layer Climates. Routledge, London (1987)

Rotach, M. W., Vogt, R., Bernhofer, C., Batchvarova, E., Christen, A., Clappier, A., Feddersen, B., Gryning, S.E., Martucci, G:, Mayer, H., Mitev, V., Oke, T.R., Parlow, E., Richner, H., Roth, M., Roulet, Y.-A., Ruffieux, D., Salmond, J. A., Schatzmann, M., Voogt J. A. BUBBLE – an Urban Boundary Meteorology Project. *Theor. Appl. Climatol.* 81, 231-261 (2005).

Rotach, M. W. Turbulence close to a rough urban surface. Part I: Reynolds stress. *Bound.-Layer Meteor.*, 65,1-28 (1993a).

Rotach, M. W. Turbulence close to a rough urban surface. Part II: Variances and gradients. *Bound.-Layer Meteor.*, 66, 75-92 (1993b).

Schmutz, M., Vogt, R., Feigenwinter, C., Parlow, E. Ten years of eddy covariance measurements in Basel, Switzerland: Seasonal and interannual variabilities of urban CO2 mole fraction and flux, *J. Geophys. Res. Atmos.*, 121, 8649–8667 (2016). doi:10.1002/2016JD025063

Stewart, I.D., Oke, T.R. Local climate zones for urban temperature studies. *Bull. Am. Meteorol. Soc.* 93, 1879–1900 (2012).

Vogt, R. and Feigenwinter, C. Sonic anemometers tested in a wind tunnel. 26th Conference on Agricultural and Forest Meteorology, Vancouver, BC, 2004.

Vogt, R., Christen, A., Rotach, M.W., Roth, M., Satyanarayana, A.N.V. Temporal dynamics of CO_2 fluxes and profiles over a Central European city. *Theor. Appl. Climatol.* 84, 117-126 (2006).

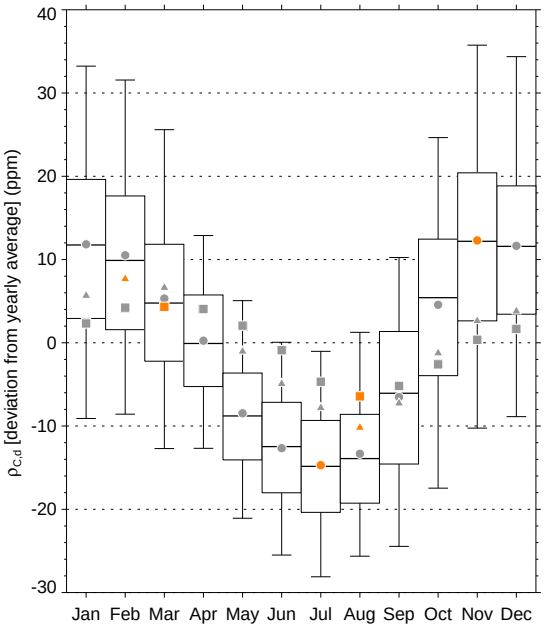

Figure 9. Average seasonal amplitude (deviation from yearly mean) of CO_2 concentration ($\rho_{C,d}$) for BKLI (circle), SAL (triangles), and JFJ (squares). Depicted are average monthly values of $\rho_{C,d}$ calculated from daily averages corrected for long-term trend of each station. Winter and summer peak values are marked in orange (adapted from Schmutz et al. 2016).




Christian Feigenwinter christian.feigenwinter@unibas.ch
Michael Schmutz mi.schmutz@unibas.ch
Roland Vogt roland.vogt@unibas.ch
Eberhard Parlow eberhard.parlow@unibas.ch

Meteorology, Climatology and Remote Sensing (MCR), Department of Environmental Sciences
University of Basel, Switzerland

This article is a basically a summary of three recent papers representative for the research on urban CO_2 fluxes and concentrations based on the Basel flux tower data: Lietzke & Vogt (2013), Lietzke et al. (2015) and Schmutz et al. (2016), but also shortly recapitulates the 25 years of flux measurements in the city of Basel, Switzerland. For more detailed information please refer to the full papers.

APPENDIX B

List of Publications and Conference Contributions

List of Publications:

Schmutz M., R. Vogt (2019): Flux similarity and turbulent transport of momentum, heat and carbon dioxide in the urban boundary layer. *Boundary-Layer Meteorology 172*(45), 45-65.

Feigenwinter C., **M. Schmutz**, R. Vogt, E. Parlow (2017): Insights from more than ten years of CO_2 flux measurements in the city of Basel, Switzerland. *Urban Climate News, Quarterly Newsletter of the International Association for Urban Climate*(65), 24-32.

Feigenwinter, C., E. Parlow, R. Vogt, **M. Schmutz**, N. Chrysoulakis, F. Lindberg, M. Marconcini, and F. del Frate (2017). Spatial distribution of sensible and latent heat flux in the URBANFLUXES case study city Basel (Switzerland). *In: 2017 Joint Urban Remote Sensing Event (JURSE 2017)*: Proceedings of a meeting held 6-8 March 2017, Dubai, United Arab Emirates. p4.

Schmutz, M., R. Vogt, C. Feigenwinter, and E. Parlow (2016). Ten years of eddy covariance measurements in basel, switzerland: Seasonal and interannual variabilities of urban CO_2 mole fraction and flux. *Journal of Geophysical Research: Atmospheres 121*(14), 8649-8667.

Osterwalder, S., J. Fritsche, C. Alewell, **M. Schmutz**, M. B. Nilsson, G. Jocher, J. Sommar, J. Rinne, and K. Bishop (2016). Adual-inlet, single detector relaxed eddy accumulation system for long-term measurement of mercury flux. *Atmospheric Measurement Techniques 9*(2), 509-524.

List of Conference Contributions:

AK Klima 2014 (Conference on climatological and meteorological topics)
Poster: Urban climate study of Bucharest
Talk: Seasonal and inter-annual variation of CO2-flux and concentration in Basel

ICOS-NEON greenhouse gas data training workshop 2015
Poster: Long term monitoring of urban carbon dioxide emissions

ICUC9 2015 - 9th international conference in urban climate

Talk: Seasonal and inter-annual variation of CO2 flux and concentration in Basel

Honoured by IAUC/AMS student presentation awards for best oral presentation